Investigation of the Excited-State Potentials of Ultracold RbYb

– Towards Light-Shift Spectroscopy –

Inaugural-Dissertation

zur Erlangung des Doktorgrades der
Mathematisch-Naturwissenschaftlichen Fakultät
der Heinrich-Heine-Universität Düsseldorf
vorgelegt von

Christian David Sillus

aus Düsseldorf

Düsseldorf, Juli 2025

Aus dem Institut für Experimentalphysik
der Heinrich-Heine-Universität Düsseldorf

Gedruckt mit der Genehmigung der
Mathematisch-Naturwissenschaftlichen Fakultät der
Heinrich-Heine-Universität Düsseldorf

Tag der mündlichen Prüfung: 22.08.25

Referent:	Prof. Dr. Axel Görlitz
Koreferent:	Prof. Dr. Thomas Heinzel

Summary

This thesis presents the latest results and technical advancements of the ultracold molecule experiment within the Görlitz group in Düsseldorf, originally initiated by Tobias Franzen [1] and subsequently extended by Bastian Pollklesener [2]. The overarching goal is to develop robust pathways for the formation of ground-state molecules composed of rubidium (Rb) and ytterbium (Yb) via photoassociation (PA). Ultracold RbYb ground-state molecules offer access to rich and tunable long-range interactions due to their electric and magnetic dipole moments, enabling new regimes of quantum simulation, precision measurements, and ultracold chemistry.

Our apparatus consists of three distinct vacuum chambers – two production and one science chamber – enabling independent preparation of each species, enhanced optical access, and improved maintainability. In the science chamber, a mixture of ultracold Rb and Yb is prepared, serving as the basis for all photoassociation experiments.

An extensive search for weakly bound molecular states near the intercombination line of Yb in ^{87}Rb^{170}Yb was carried out across a detuning range of 0.1–11 GHz, resulting in the discovery of a single resonance pair with binding energies of $-h \cdot 3057.2(3)\,\mathrm{MHz}$ and $-h \cdot 3074.3(3)\,\mathrm{MHz}$. One-photon photoassociation spectroscopy was performed in a bulk trap as well as in two- and three-dimensional lattices, achieving a maximum photoassociation rate of $K_{3D} = 1.0(2) \cdot 10^{-12}\mathrm{cm}^3/\mathrm{s}$ in a 3D lattice.

Two-photon photoassociation spectroscopy targeted the two least bound levels of the $^2\Sigma_{1/2}$ ground state potential, yielding binding energies of $E_B(\Delta v = -1) = -h \cdot 101.9(1)\,\mathrm{MHz}$ and $E_B(\Delta v = -2) = -h \cdot 1011.9(1)\,\mathrm{MHz}$. Dark resonance spectroscopy enabled the precise determination of free-bound and bound-bound Rabi frequencies.

For the realization of an ultracold molecule experiment, a diverse set of highly stable, tunable, and narrow-linewidth laser systems spanning a broad wavelength range is required. Core contributions of my individual work are new active and passive frequency stabilization techniques for the laser systems operating near the intercombination line of Yb, along with a stable laser system for efficient Yb slowing. These improvements significantly increase the experimental stability, a critical prerequisite for reliable photoassociation experiments.

A series of optical dipole traps is used for trapping, transport, and cooling of both species, including the production of quantum-degenerate Bose-Einstein condensates. A dual-species ultracold atomic mixture was realized through a complex merging process involving two independent crossed dipole traps and vertical transport via an optical lattice.

Several prospective improvements to the experimental apparatus are proposed to enhance the efficiency of photoassociation near the Yb intercombination line. In addition, the limitations of this method are critically evaluated and compared with earlier results obtained near the Rb D1 line. Combining the sharp spectral features of the intercombination line with the strong coupling strengths available at the D1 line promises substantial gains in the formation of ultracold molecules and the exploration of their interaction potentials.

The second major focus of my work involves the design of experimental configurations and accompanying theoretical considerations for implementing light-shift spectroscopy with this hybrid approach and theoretical estimations for potential energy curves and corresponding vibrational levels were made.

Due to the complexity of an ultracold molecule experiment, which demands continuous maintenance and the development of new experimental setups, this work is inherently a collaborative effort. Consequently, Tobias and Bastian have also contributed to or presented some of the results shown here.

Zusammenfassung

Diese Dissertation präsentiert die neuesten Ergebnisse und technischen Fortschritte des Ultrakaltmolekülexperiments in der Görlitz-Gruppe in Düsseldorf, das ursprünglich von Tobias Franzen [1] initiiert und anschließend von Bastian Pollklesener [2] erweitert wurde. Das übergeordnete Ziel ist die Entwicklung robuster Pfade zur Bildung von Molekülen im Grundzustand aus Rubidium (Rb) und Ytterbium (Yb) mittels Photoassoziation (PA). Ultrakalte RbYb-Moleküle im Grundzustand ermöglichen durch ihre elektrischen und magnetischen Dipolmomente Zugang zu komplexen und einstellbaren langreichweitigen Wechselwirkungen, wodurch neue Regime der Quantensimulation, Präzisionsmessungen und Ultrakaltchemie erschlossen werden können.

Unser Aufbau besteht aus drei separaten Vakuumkammern – zwei Produktionskammern und einer Wissenschaftskammer – was die unabhängige Präparation beider Spezies, einen verbesserten optischen Zugang sowie eine leichtere Wartung ermöglicht. In der Wissenschaftskammer wird eine Mischung aus ultrakaltem Rb und Yb präpariert, die die Grundlage aller Photoassoziationsexperimente bildet.

Eine umfangreiche Suche nach schwach gebundenen Molekülzuständen nahe der Interkombinationslinie von Yb in ^{87}Rb^{170}Yb wurde über einen Frequenzbereich von 0,1–11,GHz durchgeführt, was zur Entdeckung eines einzelnen Resonanzpaares mit Bindungsenergien von $-h \cdot 3057{,}2(3)\,\mathrm{MHz}$ und $-h \cdot 3074{,}3(3)\,\mathrm{MHz}$ führte. Ein-Photonen-Photoassoziationsspektroskopie wurde sowohl in einer Bulk-Falle als auch in zwei- und dreidimensionalen Gittern durchgeführt, wobei eine maximale Photoassoziationsrate von $K_{3D} = 1{,}0(2) \cdot 10^{-12}\mathrm{cm}^3/\mathrm{s}$ in einem 3D-Gitter erreicht wurde.

Zwei-Photonen-Photoassoziationsspektroskopie zielte auf die beiden am schwächsten gebundenen Zustände des $^2\Sigma_{1/2}$-Grundzustandspotentials ab und ergab Bindungsenergien von $E_B(\Delta v = -1) = -h \cdot 101{,}9(1)\,\mathrm{MHz}$ und $E_B(\Delta v = -2) = -h \cdot 1011{,}9(1)\,\mathrm{MHz}$. Dunkelresonanzspektroskopie ermöglichte die präzise Bestimmung von freien und gebundenen Rabi-Frequenzen.

Für die Realisierung eines Ultrakaltmolekülexperiments wird eine Vielzahl hochstabiler, abstimmbarer und schmalbandiger Lasersysteme über einen breiten Wellenlängenbereich benötigt. Wesentliche Beiträge meiner eigenen Arbeit bestehen in der Entwicklung neuer aktiver und passiver Frequenzstabilisierungstechniken für die Lasersysteme nahe der Interkombinationslinie von Yb sowie in einem stabilen Lasersystem zur effizienten Yb-Abbremsung. Diese Verbesserungen steigern die experimentelle Stabilität erheblich – eine entscheidende Voraussetzung für verlässliche Photoassoziationsexperimente.

Eine Reihe optischer Dipolfallen wird zum Fangen, Transportieren und Kühlen beider Spezies verwendet, einschließlich der Erzeugung entarteter Bose-Einstein-Kondensate. Eine Mischung aus beiden Atomarten wurde durch einen komplexen Zusammenführungsprozess zweier unabhängiger gekreuzter Dipolfallen und vertikalen Transports über ein optisches Gitter realisiert.

Mehrere mögliche Verbesserungen des experimentellen Aufbaus werden vorgeschlagen, um die Effizienz der Photoassoziation nahe der Yb-Interkombinationslinie zu steigern. Darüber hinaus werden die Grenzen dieser Methode kritisch bewertet und mit früheren Ergebnissen nahe der Rb-D1-Linie verglichen. Die Kombination der scharfen spektralen Eigenschaften der Interkombinationslinie mit den starken Kopplungsstärken der D1-Linie verspricht erhebliche Fortschritte bei der Erzeugung ultrakalter Moleküle und der Erforschung ihrer Wechselwirkungspotentiale.

Der zweite Hauptfokus meiner Arbeit liegt im Entwurf experimenteller Konfigurationen und begleitender theoretischer Überlegungen zur Implementierung von Light-Shift-Spektroskopie mit diesem hybriden Ansatz. Theoretische Abschätzungen für Potentialkurven und die zugehörigen Vibrationsniveaus wurden durchgeführt.

Aufgrund der Komplexität eines Ultrakaltmolekülexperiments, das eine kontinuierliche Wartung und die Entwicklung neuer experimenteller Aufbauten erfordert, ist diese Arbeit inhärent ein Gemeinschaftsprojekt. Dementsprechend haben auch Tobias und Bastian zu einigen der hier gezeigten Ergebnisse beigetragen oder diese präsentiert.

Contents

1

Introduction

Are you interested in the physics of ultracold atoms and molecules? Then it might be well worth staying tuned and letting yourself be drawn into this fascinating world over the following pages.

This thesis is part of the ultracold RbYb molecule experiment in the Görlitz group at the Heinrich-Heine-Universität Düsseldorf and will give the reader an overview of the progress made in the last several years since I joined the project. The long-term goal of the experiment is the production and investigation of ultracold RbYb molecules in their absolute rotational, vibrational, and electronic ground state.

One question I'm frequently asked is: *What's the point of all this?* This introduction aims to answer that by offering both context and motivation for our work with ultracold molecules – why we care, and what they might reveal.

Ultracold

As the reader may imagine, objects that are not moving have several advantages. We can take a better photograph, meaning it is better observable, we have more precise control and more time for measurements. When we consider a sample of these not (or slowly) moving objects in all three directions of space being in equilibrium, we speak of a low temperature. But what does that mean in atomic and molecular physics?

In our context, *ultracold* means temperatures in the sub-mK (or even sub-μK) regime. At such extremes, the kinetic energy of particles becomes so small that their de Broglie wavelengths become comparable to the interparticle distances. This regime makes quantum phenomena accessible and allows for controlled molecule formation at the level of single quantum states. While temperatures of $\sim 1\,\mathrm{K}$ can be achieved by cryogenic cooling, ultracold samples in the μK regime are produced with laser cooling techniques.

Ultracold Atoms

Following the advent of suitable laser sources for laser cooling, the pursuit of ultracold physics with neutral atoms began in the 1980s – and it remains an active and vibrant field to this day.

The new era was initiated by the first experimental realization of a Zeeman slower by Phillips and Metcalf in 1982 [3], and the subsequent trapping of neutral sodium atoms in a magneto-optical trap (MOT) by Raab et al. in 1987 [4]. These milestones launched an entirely new domain of physics. Even the Doppler limit in a MOT – typically a few hundred µK – was soon overcome through innovative cooling techniques such as polarization gradient cooling [5], Raman cooling [6], and evaporative cooling [7]. These developments culminated in the 1997 Nobel Prize in Physics awarded to S. Chu, C. Cohen-Tannoudji, and W. Phillips "for the development of methods to cool and trap atoms with laser light".

Building upon these achievements, the field rapidly expanded. In 1995, the first experimental realizations of Bose-Einstein condensates (BECs) were reported [8, 9], fulfilling a prediction made by Bose and Einstein in 1924 [10, 11]. A BEC represents a macroscopic quantum system in which individual atomic wavefunctions coalesce into a single, unified quantum state.

Today, ultracold atoms serve as powerful platforms for simulating quantum systems where no or only short-range interactions are required. Notable applications include studies of superconductivity [12] and the superfluid to Mott insulator phase transition [13].

Ultracold Molecules

When people hear the word 'molecule', many of them first think of chemistry. Indeed, ultracold chemistry is a key application of cold molecules [14], where the ultralow temperatures enhance the precision of molecular spectroscopy, enabling measurements at the level of the natural linewidth and providing detailed insights into molecular structure and formation.

From a physicist's perspective, the main appeal lies in the large electric dipole moments (order of several Debye) of polar, and thus heteronuclear molecules, and the corresponding long-range dipole-dipole interactions. When trapped in optical lattices, these interactions can become comparable in strength to the on-site interactions in atomic systems [15], enabling exploration of strongly correlated quantum phases such as supersolids [16–18], two-dimensional lattice-spin models [19], and other complex many-body systems [20–22].

Further advances include the use of bulk traps, where molecule-molecule collisions can be controlled via electric field shielding, allowing for direct thermalization and evaporative cooling [23].

In addition to these applications, ultracold polar molecules are promising candidates for quantum computing. Here, the qubits can be represented by the electric dipole moments of the molecules [24–28], offering a highly controllable and scalable platform.

Production of Ultracold Molecules

Given the growing interest in ultracold polar molecules, the natural question arises: *How can we produce them?*

Broadly speaking, there are two approaches. The first is **direct cooling**, wherein stable molecules are cooled and trapped using techniques similar to those applied to atoms. This method has seen substantial progress in recent years, leading to the successful laser cooling and trapping of several species including SrF [29], YbF [30], YO [31], CaF [32], SrOH [33], and CaOH [34]. Many more are under active investigation.

However, the complex internal structure of molecules makes this method challenging. (Quasi) Closed optical transitions are rare, and generating the necessary large number of repump lasers is technically demanding. Furthermore, the strong interaction complicates efficient (evaporative) cooling. As a result, the **indirect approach** – forming ultracold molecules from ultracold atoms – remains more practical for many experiments.

This indirect method benefits from the well-established techniques of atomic laser cooling and allows for the creation of dense ultracold atomic samples. The key challenge lies in associating atoms into molecules, which is typically achieved using magnetic Feshbach resonances [35] or photoassociation [36].

While magnetic Feshbach resonances work well for bi-alkali systems, they are less effective for combinations involving closed-shell atoms, where electron-spin coupling is absent. In such cases, photoassociation becomes the more promising technique in these experiments. Nonetheless, a growing number of experimental studies have already achieved such dipolar molecules [37–39] and both methods are discussed in detail in this thesis.

Ultracold RbYb Molecules

Recognizing the potential of polar molecules, one must choose a suitable atomic combination. While heteronuclear bi-alkali dimers have been extensively studied experimentally [40–44] – thanks to their single valence electron and accessible laser transitions – the field has matured significantly, motivating exploration of alternative molecular systems with richer internal structure and interacting properties. One disadvantage of bi-alkali molecules is that they have diamagnetic ground states and hence no permanent magnetic dipole moment.

To move toward paramagnetic molecules, we focus on a combination of an alkali atom and a closed-shell atoms. Our system of choice is rubidium (Rb) and ytterbium (Yb), forming a RbYb molecule with a paramagnetic ${}^2\Sigma_{1/2}$ ground state [45].

Both elements can be laser-cooled to quantum degeneracy using well-developed techniques and accessible laser systems [9, 46]. Rb has two stable bosonic isotopes, while Yb offers a rich spectrum of five bosonic and two fermionic stable isotopes. This variety enables flexible control over inter- and intraspecies scattering lengths and the formation of both bosonic and fermionic molecules. Yb also features a narrow intercombination line, facilitating high-resolution spectroscopy and achieving very low Doppler temperatures.

Other groups have investigated similar alkali-closed-shell combinations such as CsYb [47], RbSr [37], LiYb [38], and LiEr [39], and RbYb in our group at the University of Düsseldorf [2, 48–51].

Thesis Outline

When I joined the RbYb project in the Görlitz group at the University of Düsseldorf, the vacuum system and laser infrastructure for cooling and trapping both Rb and Yb were already in place, thanks to the foundational work of Tobias, who initiated the experiment, and Bastian. At that time, a Rb BEC had already been realized, and the transport of ^{174}Yb atoms was under preparation. The photoassociation experiments near the intercombination line of Yb were conducted in the first years of my thesis project in collaboration with Tobias and Bastian. The idea and initial realization of the novel light-shift spectroscopy method were developed independently later on.

This thesis presents the results of our work on photoassociation spectroscopy near Yb's intercombination line, its implications and limitations, and a novel pathway for exploring RbYb molecular structure.

The thesis is structured as follows:

- In Chapter 2, I provide the theoretical background required to understand molecule formation, covering molecular physics, scattering properties – motivating our choice of isotopes, atom-light interactions, and the photoassociation approach.

- Chapter 3 revisits earlier photoassociation spectroscopy of RbYb conducted with a previous apparatus, providing critical context for our current investigations.

- The experimental setup is detailed in Chapter 4, including the vacuum system, laser systems, and data acquisition infrastructure. Furthermore, the methods used to prepare ultracold atomic samples and the merging process for combining Rb and Yb is outlined. In this chapter, I will focus primarily on my contributions.

- Chapter 5 presents the extensive search for one-photon and two-photon photoassociation resonances close to the intercombination line of Yb.

- Chapter 6 summarizes the results related to the intercombination line of Yb and discusses their implications for our experiment. In this chapter, I present an alternative approach to probing the RbYb molecular structure based on light-shift spectroscopy, outlining the proposed experimental strategy and its initial implementation.

- Finally, in Chapter 7, I present short- to mid-term improvements to potentially enable efficient molecule formation and a forward-looking perspective on achieving efficient production of RbYb molecules in their absolute rovibronic ground state.

2

Basic Theoretical Aspects

This chapter provides the theoretical foundation necessary to understand the atomic and molecular physics relevant for this thesis. We begin in Section 2.1 with a theoretical description of diatomic molecules, with particular emphasis on potential energy curves and approximations for long-range interactions. In Section 2.2, we briefly examine atomic scattering properties, with a focus on the choice of the RbYb isotope combination. The discussion then turns to the interaction between atoms and light in Section 2.3, using the dressed-state picture, and introduces optical potentials and optical traps. Finally, Section 2.4 introduces the one- and two-photon photoassociation techniques used for molecule production in this work.

2.1 The Physics of Diatomic Molecules

This chapter will give an overview of the theory we will need to understand the formation of diatomic molecules starting with two ultracold single atoms [52]. A diatomic molecule exhibits a set of discrete electronic states, which arise from the interaction between the electronic configurations of the constituent atoms. Each electronic state is associated with a characteristic potential energy curve (PEC) $V(r)$, describing the potential energy of the molecule as a function of the internuclear distance r (see Section 2.1.2 and Section 2.1.3).

With a given electronic state, the molecule supports a set of vibrational levels (see Section 2.1.4), each of which is further split into rotational sublevels. These rovibrational states form the internal structure of the molecule and define the binding energies relevant for its dynamics and spectroscopy.

For the molecular binding of atoms, we need a mechanism that lowers the potential energy of the constituent atoms with their interatomic distance. Once a PEC is known, the rovibrational wavefunctions, eigenenergies, and binding energies can be determined by solving Schrödinger's equation [53]

$$\left(-\frac{\hbar^2}{2\mu}\frac{d^2}{dr^2} + V(r) + \frac{\hbar^2}{2\mu r^2}(J(J+1))\right)\Psi(r) = E\Psi(r). \tag{2.1}$$

Here, μ is the reduced mass, $\hbar$ the reduced Planck's constant, and J the rotational quantum number. In the ultracold regime, typically only the lowest-lying rotational levels are populated, and the rotational quantum number J is often equal to zero.

Photoassociation (PA), which plays a central role in this work (see Section 2.4), relies on optically coupling two colliding atoms into a weakly bound vibrational level of an electronically excited molecular state. The efficiency and photon frequency of the PA resonance are determined by the corresponding excited-state PEC. In the following, I will give the results for approximations of these PECs and for calculating the binding energies. The methods for these numerical calculations are part of theoretical chemistry and are not covered in this thesis. For more detailed information on molecular chemistry and the mathematical considerations, the following literature can be consulted [53–55].

2.1.1 Electronic States and Angular Momenta

Like atoms, molecules possess several angular momenta, which result from the combination of the angular momenta of their constituent atoms. Here, I will follow the commonly used naming and treatment as outlined in [52]

$\vec{L}$ – sum of the electronic angular momenta $\vec{l}_1 + \vec{l}_2$ of both atoms

$\vec{S}$ – sum of the spin angular momenta $\vec{s}_1 + \vec{s}_2$ of both atoms

$\vec{J}$ – total angular momentum $\vec{L} + \vec{S} + \vec{R}$

$\vec{N}$ – total angular momentum, without electron spin $\vec{J} - \vec{S}$

$\vec{R}$ – rotational angular momentum of nuclei $\vec{N} - \vec{L}$.

These angular momenta can couple in many different ways, which then give rise to the choice of good quantum numbers. An idealized treatment of these couplings was first introduced by F. Hund in 1926 [56] and is also covered in [52]. However, it will not be described here, as these coupling cases may not be applicable in the case of most molecules, particularly in the case of RbYb. We will instead focus on the molecular potentials in the following sections. However, for the naming conventions of electronic molecular states, we will still rely on the angular momenta. An electronic molecular state, for which these quantum numbers are good quantum numbers, is named as

$$^{2S+1}\Lambda^{\pm}_{\Omega_{g/u}},$$

which is similar to the naming convention in the atomic (L-S)-coupling. Here, Λ is the projection of the sum of the electronic angular momenta $\vec{L}$ on the internuclear axis and is labeled with Greek letters as Σ, Π, Δ etc., Σ the projection of the spin sum $\vec{S}$ and Ω is the sum of both $\Omega = |\Lambda + \Sigma|$. The index g/u (gerade/ungerade) describes the parity and the superscript ± the reflection symmetry of the wavefunctions along the internuclear axis and g/u is only defined for homonuclear molecules and ± only for states where $\Omega = 0$.

In the case of RbYb, we find the electronic ground state

$$^2\Sigma_{1/2}.$$

It should be noted that spin-orbit coupling leads to mixing between states of different multiplicities, making the $^{2S+1}\Lambda^{\pm}_{\Omega}$ term designation somewhat ambiguous – particularly for states at the asymptotic limit with a large extent. Here, the $(n)\Omega$ notation, where n labels the n-th state[1] with quantum number Ω, provides a more appropriate description [45]. In this notation, the electronic ground state is

$$1\,(\Omega = 1/2).$$

2.1.2 Lennard-Jones Potentials

In our case, where two ultracold atoms are brought together, the interaction is mostly determined by Van-der-Waals and dipole-dipole interactions. At these large interatomic separations, the electron cloud of the atoms is not yet disturbed and we can approximate the long-range part of the potential by a power law

$$V(r) \approx E_D + \sum_n \frac{C_n}{r^n}, \tag{2.2}$$

where E_D is the dissociation limit of the potential curve, r the interatomic distance, and C_n are specific constants, which are determined by the atoms' interaction mechanisms. For identical atoms, the long-range part of the potential can, for instance, be described using a C_3 coefficient, which comes from the resonant dipole-dipole interaction. In our case of a heteronuclear potential, the long-range part is described by a C_6 coefficient, which is the part of the potential we can access with photoassociation spectroscopy and which we are therefore interested in. Having the knowledge of these C_6 coefficients would simplify the search for photoassociation resonances; however, there is no simple way to predict them theoretically.

The short-range part of the potential of a heteronuclear interaction in terms of the approximation of power laws is due to the repulsive Van-der-Waals interaction, because the electronic wavefunctions are disturbed by the presence of a second nucleus and the corresponding inner electrons and are described by a C_{12} coefficient. This results in a Lennard-Jones potential of the form

$$V(r) = E_D + \frac{C_{12}}{r^{12}} + \frac{C_6}{r^6} \tag{2.3}$$

with C_6 being negative and C_{12} positive.

---

[1] Lower values of n correspond to states with lower energy.

The C_6 coefficient for the ground-state potential can be determined by two-photon photoassociation (see Chapter 3) and was derived for RbYb by Frank Münchow [57] by fitting the spectroscopy data to Equation (2.3).

2.1.3 Morse Potentials

In the short-range regime of diatomic molecules we find that another approach gives better results, the so-called Morse potential. A Morse potential can approximate various PECs by parameterizations and is given by

$$V(r) = D_E \cdot \left(1 - e^{-\omega_E \sqrt{\frac{\mu}{2D_E}}(r-R_E)}\right)^2 . \tag{2.4}$$

The parameters are here the potential depth D_E, the interatomic distance R_E, where the potential is minimized and the harmonic oscillation frequency at this point ω_E. The Morse potential is suitable for representing the deeply bound states of a molecule.

As one can imagine, neither of these approaches fulfills the required accuracy for an experimentalist when searching for the position of energy levels and thus ab-initio calculations often use combined approaches to approximate the potentials. For RbYb there have been a few attempts to calculate the corresponding potential energy curves. A comparison of three models is shown in Figure 2.1. The calculated Morse potential was done by Sørensen et al. by performing a high-level four-component coupled cluster calculation in 2009 [58]. The PEC of the Lennard-Jones approach is calculated with the C_6 coefficient of Münchow [57]. A more complex perturbation theory based calculation was performed by M. Shundalau [45]. It is clear that all potentials exhibit significant differences particularly in the short-range region (see also Section 6.2). By solving Schrödinger's equation Equation (2.1), the resulting vibrational levels would also show considerable variation and thus lead to substantial inaccuracies and long measurement times for experimentalists. Especially the Morse potential from Sørensen et al. differs from the others and only approaches them at large distances. Shundalau's and Münchow's calculations yield already comparable results for interatomic distances of about 11 Bohr radii.

2.1.4 Vibrational States

Unlike atoms, which can be described as point masses in motion, molecules have additional degrees of freedom, allowing them to both vibrate and rotate. As mentioned above, the vibrational energy of a diatomic molecule can be calculated by solving Schrödinger's equation (see Equation (2.1)) with the appropriate potential $V(r)$. If the complete potential is known, this can nowadays be solved relatively easily with numerical methods. Since the knowledge of the potentials is usually very limited, we require alternative methods to calculate the vibrational energy levels. By combining approximate potential energy curves with available experimental data, we can apply numerical methods to calculate the vibrational

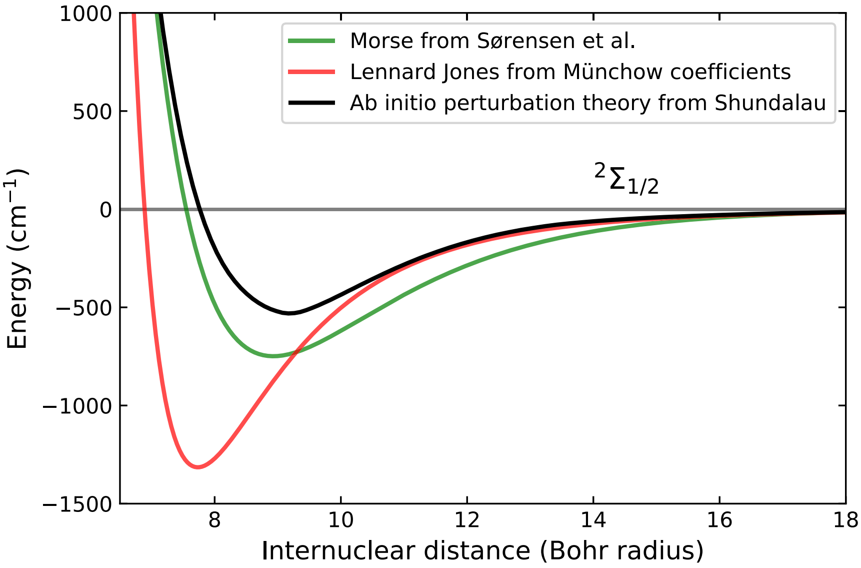

Figure 2.1.: Comparison of the modeled $^2\Sigma_{1/2}$ ground-state potential of RbYb. The green line shows the calculations done by Sørensen et al. [58], the black one the ab-initio calculations from Shundalau [45] and the red line a Lennard-Jones potential with the C_6 coefficient from Münchow [57].

energy levels with higher accuracy for short-range (deeply bound levels) and long-range (weakly bound levels) parts of the molecular potential. In the context of photoassociation, we are particularly interested in the long-range states, while deeply bound levels are relevant for molecule formation in the ground state. An example of a Lennard-Jones type potential energy curve with calculated wavefunctions for some vibrational states is shown in Figure 2.2.

Vibrational Quantum Numbers

Naturally, the vibrational quantum number v is counted from the vibrational ground state, where $v = 0$. For calculations and treatments of deeply bound states this convention is straightforward, but leads to issues for photoassociation measurements of weakly bound states, since the total number of bound vibrational states N is typically not known. In these cases, we use the quantum number $\Delta v = v - N$ starting from the dissociation limit, where $\Delta v = -1$ represents the least bound state. Vibrational levels of the electronically excited state are labeled with a prime as v' and $\Delta v'$.

Long-Range Vibrational Levels: LeRoy-Bernstein Approach

This thesis deals with the weakly bound molecular states of the long-range potential measured via photoassociation spectroscopy, and therefore, we require a method to determine

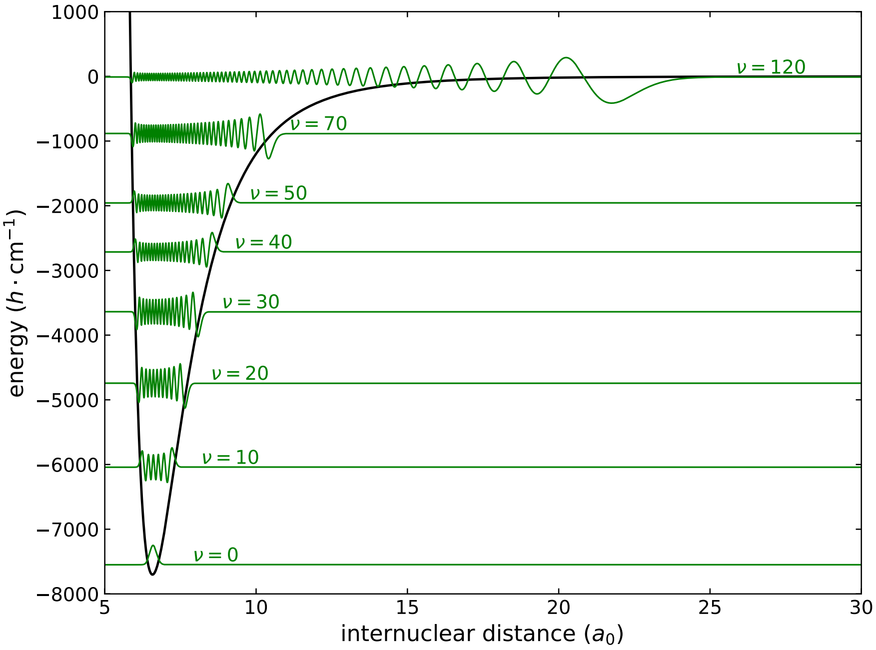

Figure 2.2.: Lennard-Jones type potential and corresponding selected wavefunctions with vibrational quantum number v. Adapted from [1].

these states. An accurate semi-classical approximation is the LeRoy-Bernstein formula for vibrational levels near the dissociation limit. In the following, I will give a short derivation of this formula, strictly following [52].

Starting from the Jeffreys-Wentzel-Kramers-Brillouin (JWKB) approximation for solving Schrödinger's equation for slowly varying potentials

$$v + \frac{1}{2} = \frac{\sqrt{2\mu}}{\pi\hbar} \int_{R_1}^{R_2} [E(v) - V(R)]^{1/2} dR, \tag{2.5}$$

where $E(v)$ is the energy of vibrational level v and R_1 and R_2 the inner and outer classical turning points of the potential $V(R)$, and differentiate with respect to $E(v)$, we come up with

$$\frac{dv}{dE(v)} = \frac{\sqrt{2\mu}}{2\pi\hbar} \int_{R_1}^{R_2} [E(v) - V(R)]^{-1/2} dR. \tag{2.6}$$

We can now insert the long-range approximation for the potential from Equation (2.2), which yields

$$\frac{dv}{dE(v)} \approx \frac{\sqrt{2\mu}}{2\pi\hbar} \int_{0}^{R_2} \left[E(v) - E_D + \frac{C_n}{R_n}\right]^{-1/2} dR. \tag{2.7}$$

After evaluating the integral, we obtain the final version

$$E(v) = E_D - \left[\frac{(n-2)\sqrt{\pi}\hbar}{C_n^{1/n}\sqrt{2\mu}} \frac{\Gamma(1+1/n)}{\Gamma(1/2+1/n)} \right]^{\frac{2n}{n-2}} (v_D - v)^{\frac{2n}{n-2}}. \tag{2.8}$$

Here, $\Gamma(...)$ is the Gamma function and v_D the fractional vibrational quantum number at the dissociation threshold E_D. Using experimental level energies obtained via photoassociation, this method provides an effective way to predict new vibrational levels and minimizing measurement time by reducing the search window. Since Equation (2.8) only allows us to calculate energy levels for a single C_n coefficient, there is an extended approach to add an additional term C_m, which may be necessary for the calculation of the potential [59].

Mass Scaling

In the Born-Oppenheimer approximation, we assume that the molecular potential $V(r)$ is independent of the specific isotope involved. Consequently, the binding energy in Equation (2.8) is modified solely by the reduced mass μ and the fractional vibrational quantum number v_D, which is given by [60]

$$v_D = \sqrt{\mu}\,\frac{\sqrt{8}}{h} \int_{R_1}^{\infty} \sqrt{-V(r)}dr, \tag{2.9}$$

where v_D scales with the square root of the reduced mass μ. Since both Yb and Rb are heavy atoms, the variation in their reduced mass is minimal, leading to only slight changes in the vibrational structure. By knowing the potential – characterized by the C_6 coefficient for one isotope pair – it is possible to predict the variation of the binding energies of other isotope combinations with high accuracy. This approach significantly reduces the measurement time required to determine binding energies for different isotopes. With these assumptions, we can predict the binding energies as follows:

$$E_x = \left(\frac{\mu_i}{\mu_x}\right)^{3/2} \frac{\left(\Delta_{frac}^{x} - \Delta v\right)^3}{\left(\Delta_{frac}^{i} - \Delta v\right)^3} E_i. \tag{2.10}$$

Here, the indices x and i denote the unknown and the known isotope combination, respectively, and Δ_{frac} the corresponding fractional part of the fractional quantum number v_D.

Deeply Bound Vibrational Levels

The long-term goal of the experiments with RbYb is to produce molecules in the rovibronic ground state. When dealing with deeply bound states, the LeRoy-Bernstein formalism fails

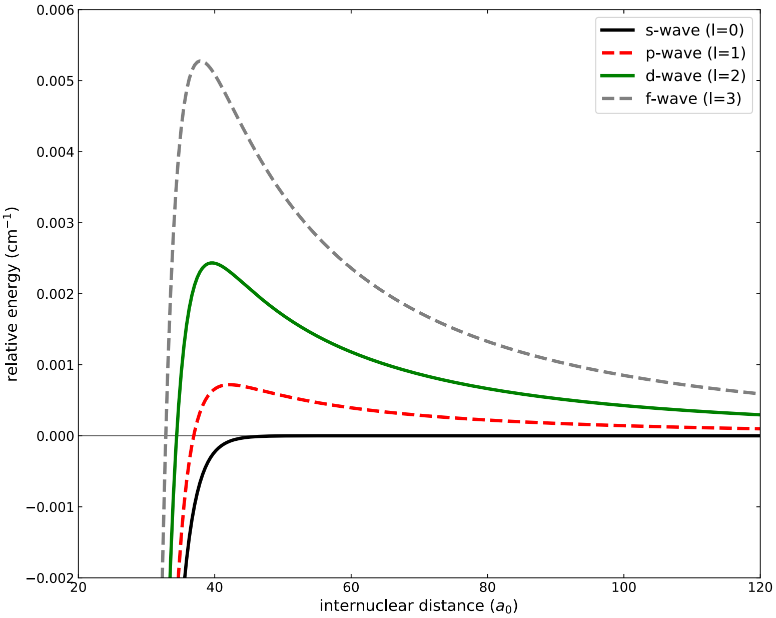

Figure 2.3.: Centrifugal barrier in Yb_2 for different partial waves of the scattering event. The centrifugal barrier allows for metastable states lying above the dissociation limit of a $l = 0$ scattering state. Taken from [1].

and we have to find a solution for the Morse potential from Equation (2.4), which is given by

$$E(v) = \hbar\omega_E \left(v + \frac{1}{2}\right) - \frac{\hbar^2\omega_E^2}{4E_D}\left(v + \frac{1}{2}\right)^2 \tag{2.11}$$

and is a good representation for the position of bound molecular states.

2.1.5 Rotation

As already shown in Schrödinger's Equation (2.1), molecules also have a rotational degree of freedom, which has to be included. The rotation of a molecule leads to an additional centrifugal term to the potential. The rotational energy is given by

$$E_{rot} = B_v\, J(J+1) = \frac{\hbar^2}{2\mu\, r_{bond}^2} J(J+1), \tag{2.12}$$

where B_v is the rotational constant and r_{bond} the effective bond length of the molecule. This term becomes more important for higher rotational quantum numbers J and leads to a centrifugal barrier of the potential, allowing for metastable vibration-rotation levels lying above the dissociation limit. An example of the centrifugal barrier of Yb_2 is shown in Figure 2.3.

For ultracold temperatures, J is generally small and we can assume only s-wave scattering, because the centrifugal barrier suppresses collisions with $l > 0$.

2.2 Scattering Length and Choice of Isotopes

With rubidium having two stable isotopes and ytterbium having seven, there is a broad range of possible mixtures that can in principle be explored, like Fermi-Bose or Bose-Bose mixtures. Unfortunately, there are restrictions, which are reducing the possible combinations in our experiment dramatically. The isotope selection for our experiment is already explained in detail in [1] and [2] and I will only reproduce the main results for understanding the choice of isotopes in our experiment. A more detailed treatment of collisions in ultracold atomic gases can be found in [61].

2.2.1 Scattering Length

As mentioned above, in the ultracold regime the scattering between two colliding ground state atoms can be described by the s-wave scattering length a, which describes the scattering process. The scattering length is given by

$$a = -\lim_{k \to 0} \frac{\tan \delta_0(k)}{k} \tag{2.13}$$

with k being the wavenumber and $\delta_0(k)$ the phase shift of the scattering wavefunction depending on the energy. From the scattering length, we can derive the scattering cross section as

$$\sigma = 4\pi a^2 \quad \text{for distinguishable atoms} \tag{2.14}$$

$$\sigma = 8\pi a^2 \quad \text{for identical bosons.} \tag{2.15}$$

The scattering length is typically given in units of the Bohr radius a_0. For a thermal gas with relative velocity v and density n, the elastic collision rate of ultracold atoms can be derived as [2]

$$\Gamma = n\, v\, \sigma \propto n\, v\, a^2. \tag{2.16}$$

A larger scattering length thus leads to a higher scattering rate. This in turn enables faster thermalization of the atomic ensemble through collisions, which is crucial for efficient evaporative cooling. However, it also increases three-body losses, which scale with a^4 [62]. The sign of the scattering length is not determining the cross section, but shows if the interaction is attractive (negative sign)[1] or repulsive (positive sign)[2]. Scattering lengths can be determined by photoassociation, because they can be related to the binding energy of the least bound state in the electronic ground state. These values were measured for Rb and Yb in [64] and [65].

---

[1] Negative a leads to collapsing of Bose-Einstein condensates for relatively small atom numbers

[2] Large positive a can lead to immiscibility, shown for ^{174}Yb and ^{87}Rb [63].

Yb Isotope	Abundance [67] [%]	a(Yb-Yb) [65] [a_0]	a(^{87}Rb-Yb) [64] [a_0]
168	0.1	252	39
170	3.0	64	-11
171 ($I = 1/2$)	14.3	-3	-59
172	21.8	-599	-161
173 ($I = 5/2$)	16.1	-200	-626
174	31.8	105	880
176	12.8	-24	217

Table 2.1.: Table of the seven stable Yb isotopes, their natural abundance, intraspecies scattering length and interspecies scattering length with ^{87}Rb.

2.2.2 Isotope Selection

Isotope selection primarily depends on the intra- and interspecies scattering lengths discussed above, though other key factors like natural abundance or hyperfine structure can also complicate experimental processes.

Rubidium

Rubidium has two stable bosonic isotopes, ^{85}Rb and ^{87}Rb. While ^{85}Rb has a natural abundance of 72 %, its intraspecies scattering length is with $a = -400\,a_0$ not suitable for cooling to quantum degeneracy[3] due to the attractive interaction and experiences a high three-body loss rate. The scattering length of $a = 100\,a_0$ of ^{87}Rb allows for efficient cooling to a Bose-Einstein condensate (BEC) and is therefore the workhorse in various cold atom experiments.

Ytterbium

Ytterbium has seven stable isotopes, as summarized in Table 2.1. ^{171}Yb and ^{173}Yb are fermions, possessing a nuclear spin of $I = 1/2$ and $I = 5/2$, respectively, while the remaining isotopes are bosons without any nuclear spin.

^{168}Yb:

The low natural abundance would lead to very long MOT loading times and would complicate frequency locking due to a weak spectroscopy signal.

^{171}Yb and ^{173}Yb:

---

[3] Stable BECs can be created by using magnetic Feshbach resonances [66] tuning the scattering length, but requires additional Feshbach coils at the experiment and is therefore not used.

Both isotopes are fermions and possess nuclear spin, which would complicate the spectroscopic data due to their hyperfine structure and cause problems with evaporative cooling, because a spin mixture has to be maintained [68].

^{172}Yb:

Has a large negative scattering length (see Table 2.1), leading to large inelastic losses and preventing it from Bose-Einstein condensation.

^{174}Yb:

A large positive interspecies scattering length with ^{87}Rb results in phase separation of both species, preventing the formation of a mixture [69]. This hinders photoassociation, as effective spatial overlap between the Rb and Yb clouds is essential.

^{176}Yb:

Has a small intraspecies scattering length, leading to slow thermalization and additional having a so-called Ramsauer-Townsend minimum at 25 µK [65]. This causes the scattering cross-section going to zero at a temperature, where the atoms get transferred from the MOT to the optical dipole trap, making the transfer ineffective.

^{170}Yb:

The best candidate for photoassociation in our experiment, ^{170}Yb, has a relatively low intraspecies scattering length of $a_{Yb,170} = 64\,a_0$, which results in longer thermalization times and makes it harder to achieve quantum degeneracy. However, these times are acceptable for our purposes. The low interspecies scattering length of $a_{Rb,Yb} = -11\,a_0$ limits efficient sympathetic cooling of Rb by Yb and prevents the quantification of spatial overlap of the two species through thermalization effects. However, the slight attractive interaction allows miscibility.

Although more suitable inter- and intraspecies scattering lengths would be preferable, photoassociation spectroscopy can still be achieved with the isotopes ^{87}Rb and ^{170}Yb. Possible approaches to overcome the above mentioned remaining issues will be briefly discussed in Chapter 6.

2.3 Atom-Light Interaction

For the description of a system consisting of atoms in a light field, it can be useful to employ a full quantum description, where both the atomic states and the light field are quantized. The concept of the coupling mechanism between atomic states and a (laser) light field can be expressed in the *Dressed-Atom Picture* [70, 71]. With this approach, it is possible to describe atom-light phenomena like light shifts, *Autler-Townes splitting* [72] and optical dipole potentials. In this chapter, I will give only a conceptual overview of the interaction between atoms and a light field. An exhaustive treatment can be found in [70] and [71]. Even though the picture here is explained using atomic states for simplicity, all explanations can be applied to arbitrary states coupled by a strong driving field, especially molecular ones.

2.3.1 Dressed States

In the dressed-state approach, we start with an (atomic) two-level system and a laser field. The uncoupled Hamiltonian describing this atom-light field system is then

$$\hat{H} = \hat{H}_A + \hat{H}_L, \tag{2.17}$$

where $\hat{H}_A$ describes the atomic Hamiltonian and $\hat{H}_L$ the light field Hamiltonian with the corresponding eigenstates

$$|a, N+1\rangle \quad \text{and} \quad |b, N\rangle\,. \tag{2.18}$$

$|a, N+1\rangle$ represents the ground state and $N+1$ photons with laser frequency ω_L and $|b, N\rangle$ the excited state with N photons. This notation also accounts for the fact that one photon is absorbed by the atom to be transferred into the excited state. The states $|a\rangle$ and $|b\rangle$ are also called *bare states*, as they are not coupled by the laser field.

In the dressed atom picture, we consider this as a fully coupled system, and the Hamiltonian can then be written as

$$\hat{H} = \hat{H}_A + \hat{H}_L + \hat{H}_I, \tag{2.19}$$

where $\hat{H}_I$ is now the interaction or coupling Hamiltonian between the atom and the driving field. This leads to new dressed eigenstates, which are denoted as

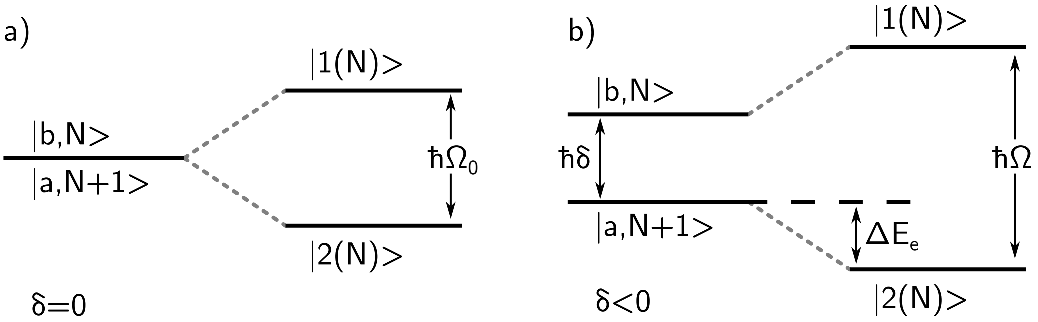

Figure 2.4.: Energies of two states in the dressed atom picture with the uncoupled (bare) states $|a, N+1\rangle$ and $|b, N\rangle$ and the coupled (dressed) states $|1(N)\rangle$ and $|2(N)\rangle$. a) shows the situation for a resonant driving field ($\delta = 0$) and b) the red detuned ($\delta < 0$) case. The energy difference between the dressed states is $\hbar\Omega$. Adapted from [70].

$$|1(N)\rangle \quad \text{and} \quad |2(N)\rangle\,. \tag{2.20}$$

The coupled $|2(N)\rangle$ state is the lower lying state.

The bare states have an energy difference of $\Delta E = \hbar\delta$, where $\delta = \omega_0 - \omega_L$ is the detuning of ω_L from the atomic resonance ω_0. For $\delta = 0$, the bare states are degenerate. An energy scheme of the bare and dressed states is shown in Figure 2.4. Figure 2.4 a) shows the energy splitting for $\delta = 0$ and b) for a red-detuned light field $\delta < 0$. For $\delta > 0$, the situation would be reversed with $|a, N+1\rangle$ being the higher lying state. The coupled states are now separated by $\hbar\Omega$ with Ω being the generalized Rabi frequency

$$\Omega = \sqrt{\Omega_0^2 + \delta^2} \tag{2.21}$$

and the resonant Rabi frequency Ω_0 which is proportional to $\sqrt{N+1}$ and therefore to the laser intensity (see Section 2.3.5). The resonant Rabi frequency is defined as [71]

$$\Omega_0 = \frac{|\vec{d} \cdot \vec{E}|}{\hbar} = \gamma\sqrt{\frac{I}{I_{sat}}} \quad \text{with} \quad I_{sat} = \frac{\pi h\, c\, \gamma}{3\lambda^3} \tag{2.22}$$

and $\vec{E}$ being the electric field, $\vec{d}$ the transition dipole matrix element, γ the decay rate of the transition and I_{sat} the saturation intensity in a two-level system. λ is the wavelength of the laser field, and h is Planck's constant.

This means that the splitting increases with increasing laser intensity and detuning δ, and also that the Rabi frequency is proportional to the transition dipole moment between $|a\rangle$ and $|b\rangle$. The energy shift ΔE_e shown in Figure 2.4 b) is nothing but the *AC-Stark* shift or light shift [72] and will be discussed in the following.

2.3.2 Three-Level Systems and Autler-Townes Splitting

For the explanation of effects like Autler-Townes splitting [72] and light-shift spectroscopy, we require a model of a three-level system with a strong coupling field ω_L and a weak probe field ω_p. The states are denoted as $|a\rangle$, $|b\rangle$ and $|c\rangle$, but only the transitions $|a\rangle \leftrightarrow |b\rangle$ and $|b\rangle \leftrightarrow |c\rangle$ are dipole allowed. In principle, there are three different types of such three-level systems: Cascade-, Λ- and V-schemes. Since Autler-Townes splitting and light-shift spectroscopy are Λ-schemes, it will be explained here. A simple picture of such a scheme is illustrated in Figure 2.6 a). The strong driving field ω_L couples the states $|a\rangle$ and $|b\rangle$, while the weak probe field ω_p probes the transition $|b\rangle \leftrightarrow |c\rangle$. The detuning $\delta = \omega_L - \omega_0$ is small compared to the transition frequencies ω_0 and ω_0'.

Due to the coupling of the bare states, the absorption of the probe field will be modified by changes in the coupling field parameters (intensity and detuning). Figure 2.6 b) illustrates the probing of the dressed states $|1(N)\rangle$ and $|2(N)\rangle$ from the higher lying unperturbed state $|c\rangle$. Because of the coupling between the unperturbed states $|a, N+1\rangle$ and $|b, N\rangle$, there are now two allowed transitions from $|c\rangle$ and the absorption spectrum becomes a doublet, which is called the Autler-Townes doublet.

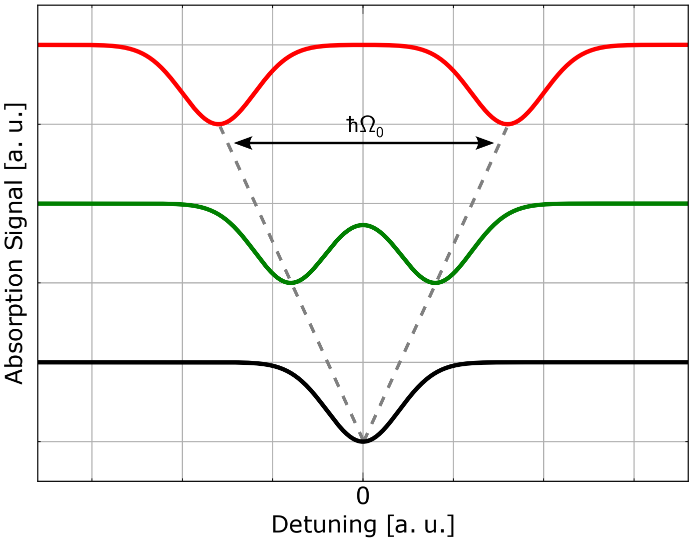

Figure 2.5.: Schematic absorption spectra illustrating the Autler-Townes splitting for increasing Rabi frequencies Ω_0 at fixed resonant driving laser frequency $\omega_L = \omega_0$. The bottom curve shows a single resonance peak in the absence of coupling. As the Rabi frequency increases (middle and top curves), the peak splits into a doublet with a separation of $\hbar\Omega_0$.

The minimum splitting of this doublet, $\hbar\Omega_0$, occurs when the driving field is resonant with the $|a\rangle \leftrightarrow |b\rangle$ transition and depends only on the resonant Rabi frequency. With this knowledge it is now possible to evaluate Rabi frequencies of certain transitions very precisely by spectroscopy with the weak probe laser. We refer to this method as Autler-Townes spectroscopy [72]. A schematic of such a doublet is presented in Figure 2.5, illustrating the absorption signal for three different Rabi frequencies at a fixed resonant driving frequency $\omega_L = \omega_0$. The Rabi frequency increases from bottom to top, resulting in a splitting of the absorption peaks by $\hbar\Omega_0$. In the lowest curve, where the coupling field is absent, a single unshifted spectroscopy peak is observed.

To understand the spectral behavior of the Autler-Townes doublets as the detuning varies, we can visualize an energy level diagram of the dressed states against the energy of a driving photon $\hbar\omega_L$ (see Figure 2.7). The horizontal lines in Figure 2.7 show the energy of the uncoupled states with N photons and their corresponding energies $\hbar\omega_0$ and $\hbar(\omega_0 - \omega_0')$ respectively, while the energy of the $|a, N\rangle$ ground state is set to zero. The dashed line with slope 1 is the ground state plus one photon and its energy increases with increasing photon energy. We see that $|a, N+1\rangle$ and $|b, N\rangle$ cross at the resonance frequency ω_0, which means that both states are degenerate on resonance. The curved solid lines represent the dressed states whose asymptotes are for a small coupling, e.g. large detunings, the bare states. We see that the coupled states repel each other and thus the coupling leads to an "anti-crossing". Since the third state $|c\rangle$ is not affected by the strong driving field, it is

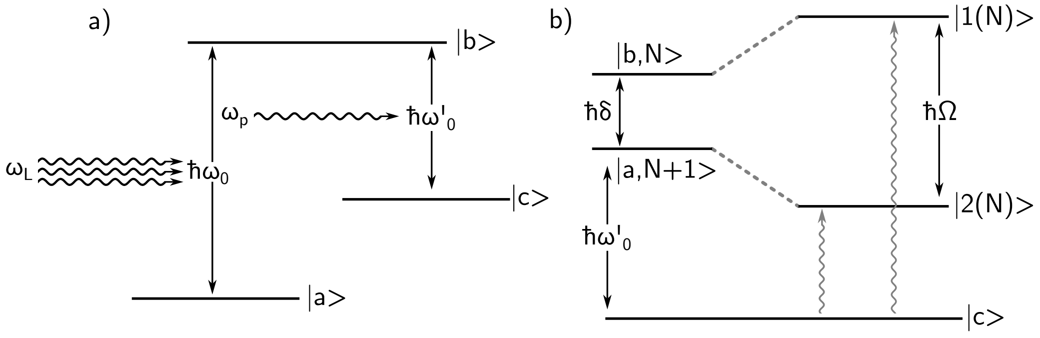

Figure 2.6.: A three-level Λ scheme. a): The states $|a\rangle$ and $|b\rangle$ are coupled with a strong, near resonant coupling field ω_L and $|b\rangle \leftrightarrow |c\rangle$ is probed by a weak probe field ω_p. The transition frequencies are ω_0 and ω_0', while the transition $|a\rangle \leftrightarrow |c\rangle$ is dipole forbidden. b): The eigenstates $|a, N+1\rangle$ and $|b, N\rangle$ of the free Hamiltonian are coupled due to ω_L. There are now two allowed transitions from $|c\rangle$ to either $|1(N)\rangle$ or $|2(N)\rangle$, the Autler-Townes doublet. Adapted from [70].

unperturbed and we can probe the above mentioned Autler-Townes doublets with a weak probe field ω_p as indicated by the wavy lines in Figure 2.7. The minimum splitting occurs at resonance $\omega_L = \omega_0$ and is $\hbar\Omega_0$ (see Figure 2.4). Off resonance we get one line close to ω_0' and the other line close to $\omega_0 + \omega_0' - \omega_L$.

At resonance, both lines have equal strength, but for large detunings of ω_L, the line near $\omega_p \approx \omega_0'$ becomes dominant. This can be demonstrated by analyzing the admixture of the $|b, N\rangle$ state of the dressed states and was done in [71]. The distance between the dressed states and the corresponding bare states (dashed lines in Figure 2.7) is then called light shift or AC-Stark shift.

The so-called Autler-Townes spectroscopy is a powerful tool for analyzing molecular transitions, as the Rabi frequency can be directly measured using the known intensity and detuning of the driving laser field. An additional important point derived from the previous explanations is the use of the light shift to determine the position of new molecular transitions, which will be further explored in the following section.

2.3.3 Light-Shift Spectroscopy in a Λ Three-Level System

Light-shift spectroscopy can be described as a three-level Λ-scheme and is shown in Figure 2.8 a). We consider only the $|1(N)\rangle$ state and thus a red-detuned light spectroscopy. All arguments are equally valid for a blue detuned coupling field, except that the sign of the light shift changes.

In our case, state $|c\rangle$ corresponds to the atomic scattering state, $|b\rangle$ is an intermediate weakly molecular bound state of the electronically excited potential, and $|a\rangle$ a bound molecular state of the ground-state potential. If we know the transition energy of $|c, N\rangle \leftrightarrow$

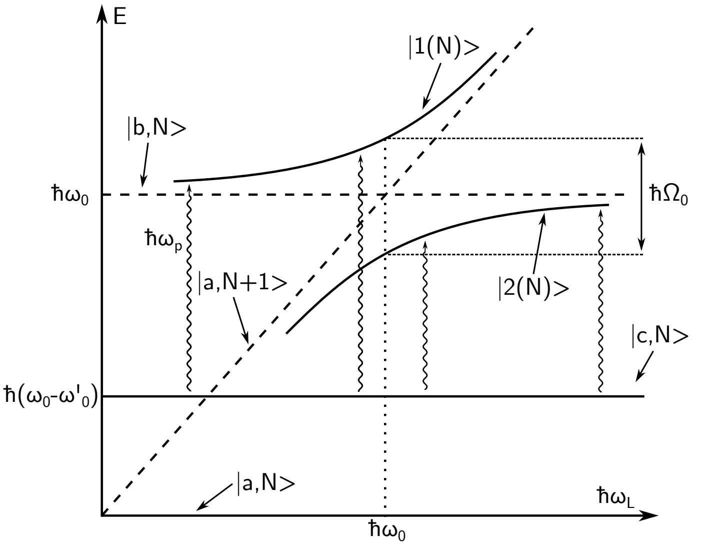

Figure 2.7.: Energy of the dressed states versus the driving field frequency. The bare state energies are illustrated by the dashed lines while the ground state $|a, N\rangle$ corresponds the the x-axis. The energy of the state $|a, N+1\rangle$ is shown as dashed line with slope 1 and crosses the energy of the uncoupled state $|b, N\rangle$ at the resonance frequency ω_0. The wavy lines indicate probe photons ω_p from the unperturbed state $|c, N\rangle$. The dressed states are illustrated as solid curved lines and show the anti-crossing at the energy $\hbar\omega_0$. The energy splitting of the Autler-Townes doublet at resonance is $\hbar\Omega_0$. Adapted from [70].

$|b, N\rangle$ and are interested in the position of one or more new transitions $|a_i, N\rangle \leftrightarrow |b, N\rangle$, we can utilize the light shift as follows (see Figure 2.9). A weak laser field at frequency ω_p is set to resonance and in the absence of a coupling field, we obtain a typical spectroscopy signal for a two-level system with a corresponding linewidth Γ. Then, we add a strong coupling field with an arbitrary frequency ω_L. If the driving field is far off-resonant with a transition $|a, N\rangle \leftrightarrow |b, N\rangle$, the corresponding states are not coupled and can be seen as bare states. This case is shown in Figure 2.8 b) on the left side. If the detuning is reduced, the states $|a, N+1\rangle$ and $|b, N\rangle$ begin to couple, mainly to $|1(N)\rangle$, and its eigenenergy increases. As the probe field frequency ω_p remains unchanged, the corresponding spectroscopic signal will vanish if the coupling field induced energy shift ΔE_e, i.e. the light shift, is larger than the spectroscopy linewidth Γ and can be calculated via the resonant Rabi frequency and the detuning [70]:

$$\Delta E_e = \frac{\hbar\Omega_0^2}{4\delta}. \tag{2.23}$$

A schematic spectroscopy signal is depicted in Figure 2.9. In the left panel, the frequency of the probe laser ω_p is scanned in the absence of the coupling laser. A typical atom loss signal is observed when the probe laser is resonant with the transition $|c, N\rangle \leftrightarrow |b, N\rangle$.

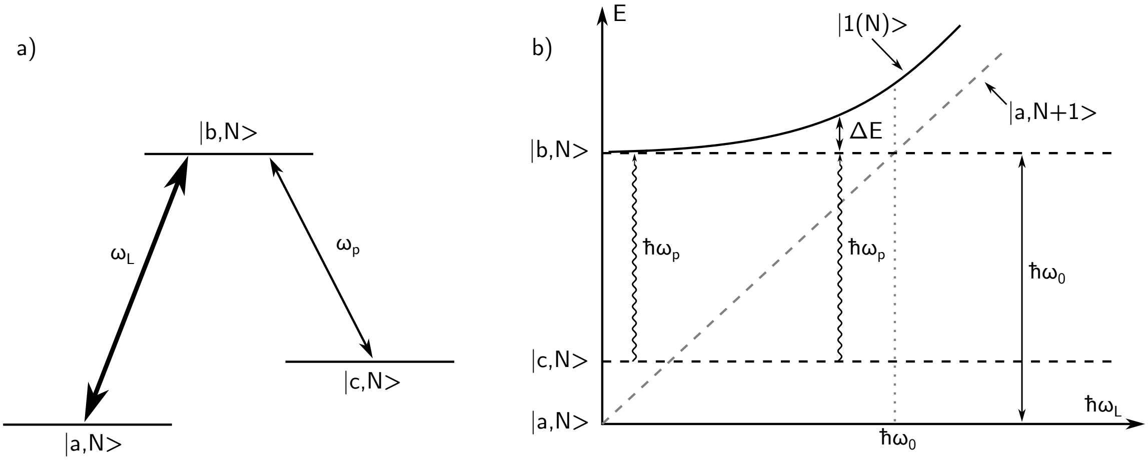

Figure 2.8.: A typical three-level Λ-scheme. The thicknesses of the arrows in a) indicate that the driving field intensity is larger compared to the probe field. b) shows the energy diagram of the Λ-scheme in the dressed-state picture. Only $|1(N)\rangle$ is shown for simplification and because for the light shift only large detunings are relevant.

Once this resonance is identified, the probe laser is fixed at that frequency, and the coupling laser frequency is scanned instead (right panel). As the light shift ΔE_e induced by the coupling field increases, the resonance condition is modified, and a characteristic loss-of-loss signal can be observed. The width of this signal is determined by the light shift as described in Equation (2.23).

Due to the typically limited knowledge of molecular potentials, the possible range for a transition can be quite broad, resulting in an extensive search. Thus, it is feasible to work with a large light shift on the one hand, and a narrow linewidth of the probing transition on the other hand. Since Ω_0 scales with $\sqrt{I}$ (see Equation (2.22)), the first step is to use high laser intensities for the driving field and, if possible, select a narrow transition for the probe field. Fortunately, both is possible in the case of photoassociation with Rb and Yb, which will be explained in Section 6.2.

2.3.4 Optical Dipole Potential

To reach ultracold temperatures below the mK (or even µK) regime, as well as to manipulate or transport atoms, most cold atom experiments make use of optical dipole traps (ODT) in forms of tweezers [73, 74] and lattices [75–77].

The optical dipole potential can also be explained in the dressed-atom picture, where the driving laser field is red-detuned $\delta < 0$, and has varying intensity, i.e. generalized Rabi frequency $\Omega(r)$, in space, as shown in Figure 2.10. Inside the high-intensity part of the laser beam, the separation of the dressed states is large, since ΔE_e is proportional to Ω. In the outer region, the splitting is small and the states approach the bare states. For a

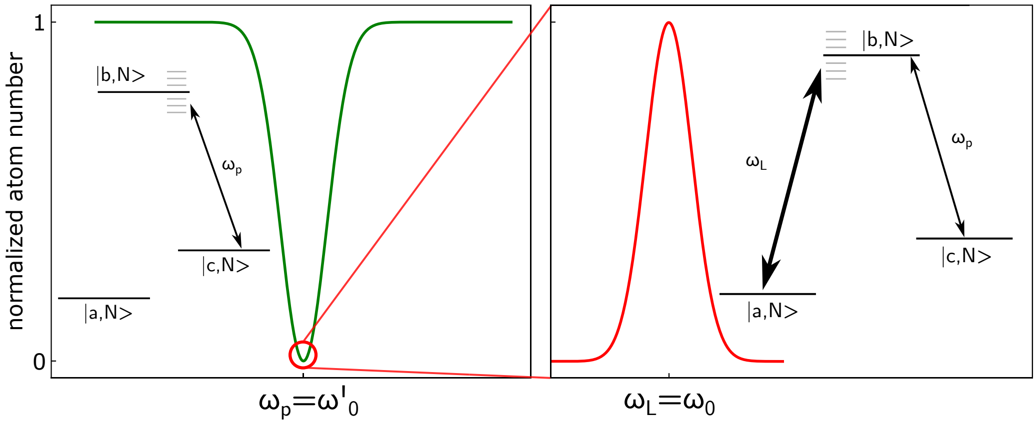

Figure 2.9.: Schematic illustration of a light-shift measurement. Left: Atom loss signal observed by scanning the probe laser frequency ω_p in the absence of the coupling laser. A resonance occurs when the probe laser drives the transition $|c, N\rangle \leftrightarrow |b, N\rangle$. Right: With the probe laser fixed on resonance, the coupling laser frequency is scanned. As the light shift ΔE_e increases, the original transition is shifted out of resonance, resulting in a loss-of-loss signal.

red-detuned laser field ($\omega_L < \omega_0$), we find that $|a, N+1\rangle$ is lying below $|b, N\rangle$ and in this case, the lower-lying dressed state $|2(N)\rangle$ corresponds to the bare ground state $|a, N+1\rangle$ (see Section 2.3.1).

Because of the position dependence of the dressed-state energy, an atom experiences a gradient force, which is indicated by the arrows in Figure 2.10. An atom in the $|2(N)\rangle$ state experiences a gradient force directed towards the region of the highest laser intensity. The higher-lying state $|1(N)\rangle$ is pushed outwards from the laser field. To calculate the net force, we need to average over the dressed states' occupation probabilities.

In Figure 2.10 we can see that, for a red-detuned laser field, the trapped state $|2(N)\rangle$ has significantly larger population than $|1(N)\rangle$. The reason is simply that the excited state $|b, N\rangle$ has a relatively short lifetime and with large δ, the probability of $|a, N+1\rangle$ absorbing a photon and transitioning to $|b, N\rangle$ is very low. Thus, the net force acting on a two-level atom in a red-detuned laser beam, with its maximum intensity at the center, is directed towards the center, allowing the atom to be trapped at the point of highest intensity. For a blue-detuned laser field, $|a, N+1\rangle$ is lying above $|b, N\rangle$ and the situation is reversed.

With the energy difference from Equation (2.23) being the optical potential, we can write the optical dipole force as

$$\vec{F} = -\vec{\nabla}\left(\Delta E_e\right). \tag{2.24}$$

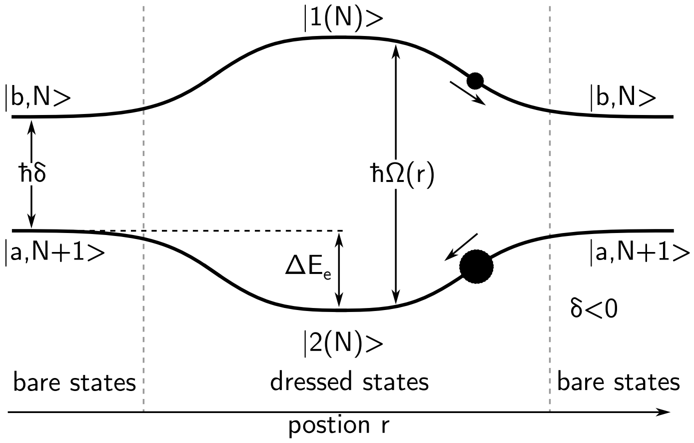

Figure 2.10.: Energy differences of two dressed states dependent on the position r along a red-detuned laser beam (and a varying laser intensity). In the beam's center, the states are coupled and experience an energy (light) shift ΔE_e from the bare state and the splitting of $|2(N)\rangle$ and $|1(N)\rangle$ is determined by the position-dependent general Rabi frequency $\Omega(r)$. Outside of the beam (denoted by vertical dashed lines), the states can be regarded as bare states, with the splitting being just the detuning $\hbar\delta$. Adapted from [70].

2.3.5 Semi-Classical Approach of an Optical Dipole Trap

An alternative explanation of optical dipole potentials is a semi-classical approach, where the atom is treated as a quantum mechanical oscillator driven by a classical radiation field. In most experiments with ODTs this approach is more suitable for a quantitative description, since the required parameters are mostly known. The results of this approach are, of course, the same as in the picture of dressed atoms. Here, I will only present the main results from [78], where a detailed derivation can be found.

A radiation field can also be seen as a time-varying electric field $\vec{E}$ with frequency ω_L. This electric field induces a dipole moment in the atom

$$\vec{p} = \alpha \vec{E}. \tag{2.25}$$

Here, α is the complex polarizability depending on ω_L. As with a classical induced dipole, we find the dipole potential to be

$$U_{dip} = -\frac{1}{2}\langle \vec{p}\vec{E}\rangle = -\frac{1}{2\epsilon_0 c}\mathrm{Re}\,(\alpha)\,I, \tag{2.26}$$

where $\langle ... \rangle$ denotes the time average over the oscillation. In Equation (2.26), we can see that the optical dipole potential is directly proportional to the driving field intensity I. With the atomic polarizability $\alpha\,(\omega_L)$ from [78] and a few simplifications, we end up with

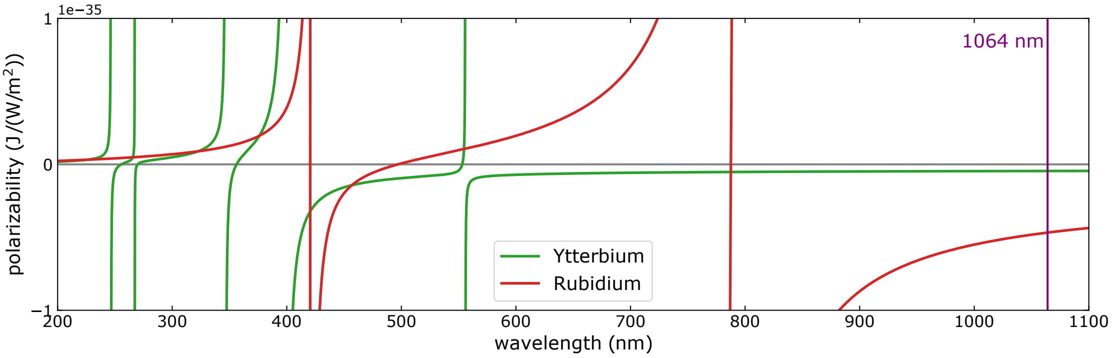

Figure 2.11.: Polarizabilities of Rb (red) and Yb (green) versus the wavelength. The vertical purple line shows the used trapping wavelength, where $\alpha_{Rb} \approx 10 \cdot \alpha_{Yb}$. Taken from [1].

an easy expression for the potential and the photon scattering rate of the driving photons

$$U_{dip}(\vec{r}) = \frac{3\pi c^2}{2\,\omega_L^3}\frac{\gamma}{\delta}\,I(\vec{r}), \tag{2.27}$$

$$\Gamma_{sc}(\vec{r}) = \frac{3\pi c^2}{2\hbar\omega_L^3}\left(\frac{\gamma}{\delta}\right)^2 I(\vec{r}). \tag{2.28}$$

Here, δ is the detuning from the atomic resonance and γ the corresponding decay rate of the excited state.

We see that the potential, respectively the dipole force, is strongest near an atomic resonance, which might suggest operating an ODT close to such a resonance. One advantage would be the relatively low intensities required for deep potentials. Unfortunately, at small detunings, the scattering rate is very large, which reduces the lifetime and induces significant heating in the trap. The required lifetimes in typical cold atom experiments can be up to several seconds, so the solution to this is to use a high-intensity far red-detuned optical dipole trap. As we can see in Equation (2.27) and Equation (2.28), the potential is proportional to $\frac{1}{\delta}$ and the scattering rate to $\frac{1}{\delta^2}$, making large detunings preferable.

We can also expand Equation (2.27) to a multi-level atom by summing over all optical transitions to get the full optical potential [78]

$$U_{dip}\left(\vec{r}\right) = \frac{3\pi c^2}{2\omega_L^3} I\left(\vec{r}\right) \sum_i \frac{\gamma_i}{\delta_i}, \tag{2.29}$$

where the index i denotes one atomic resonance, γ_i its decay rate and δ_i the corresponding detuning. These data are for most of the elements available in literature and thus the calculation of the optical dipole potential is straightforward.

By using Equation (2.23) and inserting Equation (2.21) and Equation (2.22), we obtain the same expression as in Equation (2.27), which means that the dipole potential is nothing but the light shift induced energy shift of a dressed state. Since the atomic data required for calculating the potential are available in the literature, it is common to use Equation (2.29) for designing an ODT.

The polarizabilities, which are proportional to the optical potential, of both ytterbium and rubidium are shown in Figure 2.11 as a function of the trap wavelength. The significant difference in polarizabilities between the two species is evident, meaning that a combined single-frequency ODT, where Rb and Yb experience the same potential, can only be achieved at the intersection of the green and red lines in Figure 2.11, where the polarizabilities are negative. Unfortunately, these points are located close to atomic resonances of either Rb or Yb, leading to extensive scattering losses and heating. This leads to challenging issues in merging the atoms in a combined trap that need to be overcome, which is also explained in [1] and [2] and will be shortly summarized in Section 4.9.3.1.

2.3.5.1 Single-Beam Traps

The simplest realization for a three-dimensional optical dipole trap is a red-detuned focused Gaussian laser beam. The intensity distribution of a Gaussian beam propagating in z-direction is given by

$$I(r,z) = \frac{2P}{\pi\, w^2(z)} \exp\left(-2\frac{r^2}{w^2(z)}\right), \tag{2.30}$$

with P being the total power, $w(z)$ the $1/e^2$ radius and r the radial coordinate. The radius along the z-axis is calculated via

$$w(z) = w_0\sqrt{1+\left(\frac{z}{z_R}\right)^2}, \tag{2.31}$$

with the so-called Rayleigh length $z_R = \frac{\pi w_0^2}{\lambda}$, the minimum beam radius w_0 at $z = 0$, and λ is the trapping wavelength. With Equation (2.30) and Equation (2.29) we can calculate the spatial optical potential of a single focused Gaussian laser beam.

The trap depth U_0 represents the maximum potential, obviously occurring at the point of highest intensity, $U_0 = U(r = 0, z = 0)$. Since $\frac{z_R}{w_0} = \frac{\pi w_0}{\lambda} > 0$, the potential in axial z-direction has always a much lower slope, resulting in a reduced confinement compared to the radial direction. Typical values for beam waists are in the range of a few tens of micrometers, leading to Rayleigh lengths on the order of a few mm.

In the limit of low temperatures compared to the trap depth atoms will be located at the bottom of the trap and thus, we can approximate the relevant optical potential of a single-beam focused Gaussian laser beam to

$$U_{ODT}(r,z) = -U_0\left[1 - 2\left(\frac{r}{w_0}\right)^2 - \left(\frac{z}{z_R}\right)^2\right], \tag{2.32}$$

which is a cylindrical harmonic oscillator with trap frequencies

$$\omega_r = \sqrt{\frac{4U_0}{m\,w_0^2}} \quad \text{and} \quad \omega_z = \sqrt{\frac{2U_0}{m\,z_R^2}}, \tag{2.33}$$

where m is the atomic mass of the trapped atom. Single-beam ODTs are typically loaded from magnetic or magneto-optical traps, enabling the transfer of atoms to a conservative potential. Additionally, they are used for transporting and spatially manipulating atoms, such as in optical tweezers [79]. A disadvantage of such a trap is the clearly anisotropic potential in the axial and radial direction. Due to the weak confinement along the axial directions, the atomic density in the trap remains low, which hinders efficient evaporative cooling by suppressing collisions.

2.3.5.2 Crossed Dipole Traps

To overcome the disadvantages of a single-beam ODT, the obvious solution is to implement a crossed optical dipole trap (CODT). In this configuration, two single red-detuned ODTs intersect with their waists at the same position and in general, we can sum the spatial intensity distributions of both beams and calculate the potential using Equation (2.29). If both beams have the same waist and cross at an angle of 90°, we obtain a nearly isotropic potential of the form [78]

$$U_{CODT}(x, y, z) \approx -U_0 \left(1 - \frac{x^2 + y^2 + 2z^2}{w_0^2}\right). \tag{2.34}$$

The effective potential depth is only U_0, since an atom with higher energy can leave the trap along one of the beams. CODTs are widely used for evaporative cooling, since the confinement is tight enough to ensure a sufficient collision rate on acceptable time scales, which enables the possibility of cooling in the nK regime and achieving quantum degeneracy.

2.3.5.3 Optical Lattices

An optical lattice is formed by a spatially periodic optical potential and can be used, for example, in quantum simulation of solid states and superconductivity [80, 81], and quantum computing [82, 83]. In our case, optical lattices are used for transport and combining ultracold atomic clouds of Rb and Yb and enhance photoassociation efficiency. This chapter follows the treatments of [84].

A periodic optical potential can be created by the interference of two superimposed counter-propagating beams, forming a standing wave, or by simply retro-reflecting a single-beam ODT. There are several geometries for optical lattices in either one, two, or three dimensions, depending on the incident angles of the beams, their wavelength, and beam shapes [85]. I will focus only on simple geometries, as these are used in our experiment.

1D Optical Lattice

The simplest way of realizing a one-dimensional optical lattice is by retro-reflecting a single Gaussian beam and creating a standing wave due to interference. Assuming the incoming and the retro-reflected beams propagate in z-direction have the same shape, power and are perfectly superimposed, the resulting periodical potential is given by

$$V(r,z) = -V_{lat} \cdot e^{-2r^2/w_0^2} \cdot \sin^2(kz) \simeq -V_{lat} \cdot \left(1 - 2\frac{r^2}{w_0^2}\right) \cdot \sin^2(kz). \tag{2.35}$$

Here, w_0 is the beam waist of the Gaussian beam, $k = 2\pi/\lambda$ the magnitude of the wave vector with laser wavelength λ and V_{lat} the lattice potential depth. Note that V_{lat} is four times the potential depth of a single-beam ODT, due to retro-reflection and constructive interference. The periodicity in such a potential is $\lambda/2$. In our case, with a lattice laser of 1064 nm, this results in a periodicity of 532 nm.

To determine the potential depth – in units of the photon recoil energy $E_{rec} = \hbar^2 k^2/2m$ – of a 1D lattice with large detuning, we can combine Equation (2.27) and Equation (2.30) at the center of the lattice beams, which gives

$$\frac{V_{lat}}{E_{rec}} = 4 \cdot \frac{2m}{\hbar^2 k^2} \frac{3\pi c^2}{2\omega_L^3} \frac{\gamma}{\delta} \frac{2P}{\pi w_0^2}. \tag{2.36}$$

Unlike a single-beam ODT, an 1D lattice provides strong confinement along the propagation direction, making it possible to trap atoms using only a vertical lattice. This setup allows us to transport atoms vertically, as will be discussed in Section 4.9.3.

3D Optical Lattice

The simplest three-dimensional lattice can be created by superimposing three mutually orthogonal one-dimensional lattices. By superimposing additional lattice beams, they can also interfere, leading to unwanted potential fluctuations of neighboring lattice sites and heating effects. This can be avoided by using orthogonal polarizations or distinct frequencies of the beams. We can write the resulting potential then as

$$V(x,y,z) = -V_x\, e^{-2\frac{y^2+z^2}{w_x^2}} \sin^2(kx) - V_y\, e^{-2\frac{x^2+z^2}{w_y^2}} \sin^2(ky) - V_z\, e^{-2\frac{x^2+y^2}{w_z^2}} \sin^2(kz), \tag{2.37}$$

with $1/e^2$ Gaussian beam radii w_x, w_y and w_z and the potential depths of the three 1D optical lattices V_x, V_y and V_z. In the trap center, where x, y and z are smaller than the beam radii, we can approximate the potential to a homogeneous periodic potential superimposed with a harmonic external potential as

$$V(x,y,z) \simeq V_x \sin^2(kx) + V_y \sin^2(ky) + V_z \sin^2(kz) + \frac{m}{2}\left(\omega_x^2 x^2 + \omega_y^2 y^2 + \omega_z^2 z^2\right) \tag{2.38}$$

with the trapping frequencies

$$\omega_x^2 = \frac{4}{m}\left(\frac{V_y}{w_y^2} + \frac{V_z}{w_z^2}\right), \quad \omega_y^2 = \frac{4}{m}\left(\frac{V_x}{w_x^2} + \frac{V_z}{w_z^2}\right), \quad \omega_z^2 = \frac{4}{m}\left(\frac{V_x}{w_x^2} + \frac{V_y}{w_y^2}\right). \tag{2.39}$$

In a deep lattice, we can approximate the potential at one lattice site with a harmonic potential, leading to trap frequencies of

$$\omega_{lat}^2 = V_{lat}\frac{2k^2}{m} = \frac{V_{lat}}{E_{rec}}\frac{\hbar^2 k^4}{m^2}. \tag{2.40}$$

Here, V_{lat} denotes the lattice depth along a single spatial direction. In the case of an isotropic lattice, all three directions are equivalent and we have $V_x = V_y = V_z = V_{lat}$.

Figure 2.12 shows a comparison of different trap geometries for Yb, which are used in our experiment. The chosen parameters for the trap depth calculation are: Beam waist $w_0 = 40\,\mu\text{m}$, ODT and CODT power $P_{ODT} = 20\,\text{W}$, lattice power $P_{lat} = 5\,\text{W}$ and trap wavelength $\lambda = 1064\,\text{nm}$. It is clearly visible that a single-beam ODT has only a tight confinement in the x and y-direction, while the confinement in the direction of propagation is very low. For a CODT, we already get a sufficient trap depth in all directions to successfully perform evaporative cooling. For the vertical transport of an ultracold Rb cloud, a vertical 1D lattice is used, which gives in the horizontal axes a typical potential of a single-beam ODT and only in the direction of propagation a periodical potential with periodicity of $\lambda/2 = 532\,\text{nm}$. The 3D lattice is shown at the trap center, where Equation (2.38) is used to calculate the potential, and from the outside, where the effective potential is simply the sum of three orthogonal single-beam ODTs with four times the trap depth due to retro-reflection and interference. We can see that the trap depths of these configurations are in the regime of a few hundred µK, which allows us to trap atoms with temperatures smaller than that.

2.4 Photoassociation

Photoassociation (PA) is a precise and widely used method for the production of weakly bound molecules and the investigation of long-range potentials via spectroscopy. The principle of a photoassociation process is that two colliding atoms absorb a photon γ and form a weakly bound molecule in an electronic excited state where the binding energy is given by the difference of the photon energy and the energy of the corresponding atomic transition. We can write that as follows

$$A + B + \gamma \rightarrow (AB)^*, \tag{2.41}$$

where A and B are the involved atoms. The parentheses indicates the molecular state and $*$ the electronic excitation of this state. A more comprehensive discussion on photoassociation can be found in [86]. The produced molecule $(AB)^*$ has typically a short lifetime and can decay due to spontaneous emission either to a molecule in the electronic ground state or a pair of free atoms.

$$(AB)^* \rightarrow A + B + \gamma' \quad \text{or} \quad (AB)^* \rightarrow (AB) + \gamma'. \tag{2.42}$$

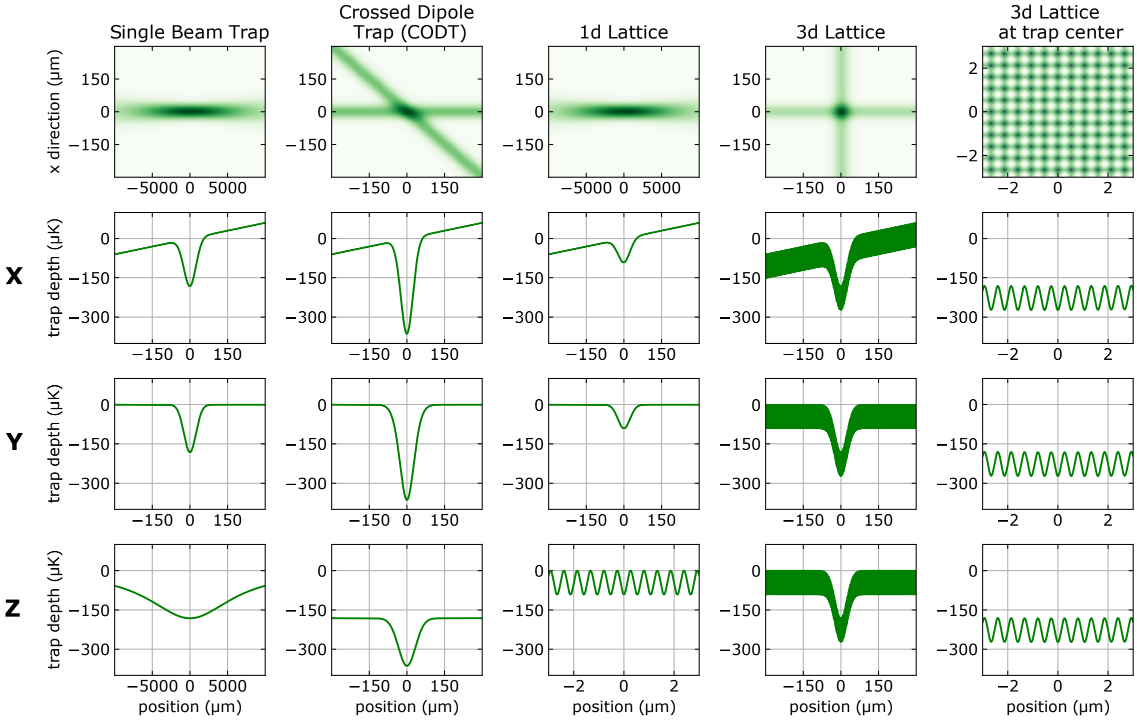

Figure 2.12.: Comparison of various trap geometries (for Yb) used in our experiment. The first row displays the intensity distribution of the optical dipole traps employed, with the CODT beam angle set to 45°, as in the experiment. Subsequent rows present the optical dipole potential along each axis, beginning with the vertical x-axis in the second row, where the tilt in the potential arises from the gravitational potential. The last row shows the potential in the z-direction, which corresponds to the propagation direction of the single-beam ODT or the 1D lattice. Note that the x-axis scaling may vary across several orders of magnitude, especially for the z-direction of the ODT and in the central region of a 3D lattice.

In ultracold atomic experiments these final products are no longer detectable, because the kinetic energy of the free atoms is too high and they can no longer be trapped. The differing energy level structure of molecules causes the imaging light to be off-resonant. However, both of these processes lead to a loss of atoms in the trap, which can be used to identify spectral lines. Due to the typical temperature of laser-cooled atomic samples below the mK regime, the kinetic energy distribution of the colliding atoms is comparable or even smaller than the lifetime of the excited state and therefore PA can be used as a high-resolution spectroscopy method for these molecular states. The average loss rate of such an event is given by [87]

$$K\left(\Delta, I, \vec{p}_c, \vec{p}_r\right) = \frac{\hbar\pi}{k_r\mu}\sum_{e,g}(2l+1)\frac{\Gamma_{pe}\Gamma_{eg}\left(I,\epsilon_r\right)}{\left[\Delta_{FB}\left(\Delta, I, \vec{p}_c, \vec{p}_r\right)\right]^2+\left[\Gamma_e\left(I,\epsilon_r\right)/2\right]^2} \tag{2.43}$$

and can be calculated by summing over all possible transitions from the electronic excited bound molecular state $|e\rangle$ to the ground state $|g\rangle$. Here, k_r is the magnitude of the atom's relative motion wave vector, μ the reduced mass, l the total angular momentum[1] of the two-atom system, $\vec{p_r}$ the momentum vector of the relative motion, $\vec{p_c}$ of the motion of the center of mass. Δ_{FB} is the total detuning from the PA resonance and can be formulated as [87]

$$\Delta_{FB} = \Delta + \epsilon_D + \epsilon_r - \Delta_e - \Delta E_e\left(I, \epsilon_r\right) - E_{rec} \tag{2.44}$$

with Δ being the detuning from the atomic resonance, ϵ_D the Doppler shift from the relative motion of atoms and light, ϵ_r the kinetic energy of the relative motion between two colliding atoms, Δ_e the detuning from the molecular transition $|e\rangle$ to $|g\rangle$, $\Delta E_e\left(I, \epsilon_r\right)$ the light shift and E_{rec} the shift due to photon recoil. $\Gamma_e\left(I, \epsilon_r\right) = \Gamma_{pe} + \sum_g \Gamma_{eg}(I, \epsilon_r)$ is the resonance's total width. Γ_{eg} is the loss induced by light and Γ_{pe} the loss due to other effects, i.e. the decay probability. In the case of predominantly radiative losses, this corresponds to the natural linewidth of the molecular state. For the light induced width Γ_{eg} we can use Fermi's golden rule as follows

$$\Gamma_{eg} = 2\pi |\langle \Psi_e | V_{las}(I) | \Psi_g^+(\epsilon_r)\rangle|^2. \tag{2.45}$$

The laser field operator V_{las} describes the optical coupling between the ground state $|g\rangle$ and the excited state $|e\rangle$. After some treatments done in [87] we end up with an expression for the light induced width

$$\Gamma_{eg} = \Gamma_{atom} \frac{3}{4\pi} \frac{I \lambda_{atom}^3}{c} f_{eg}^{rot} f_{eg}^{FC}. \tag{2.46}$$

Here, Γ_{atom} denotes the natural atomic width and λ_{atom} represents the wavelength of the atomic transition. f_{eg}^{rot} is the rotational line strength factor and depends on the angular momentum of $|e\rangle$ and $|g\rangle$. Finally, f_{eg}^{FC} is the Franck-Condon factor and describes the overlap integral of the vibrational wavefunctions ψ_e and ψ_g

$$f_{eg}^{FC}(\epsilon_r) = \left| \int_0^\infty dr\, \psi_e(r) \psi_g(r; \epsilon_r) \right|^2 = \left| \langle \psi_e(r) | \psi_g(r; \epsilon_r) \rangle \right|^2. \tag{2.47}$$

The Franck-Condon factor depends on the initial kinetic energy ϵ_r of the scattering state, making it suitable to perform experiments at ultra-low temperatures to avoid broadening of PA resonances. Using the reflection approximation we can further simplify the expression of the Franck-Condon factor to

$$f_{eg}^{FC}(\epsilon_r) = \frac{\partial E_e}{\partial n} \frac{1}{D_C} \left| \psi_g(r_C; \epsilon_r) \right|^2 \tag{2.48}$$

---

[1] l describes here the partial wave of the scattering event and is only > 0 for high collision energies. In most ultracold atom experiments $l = 0$.

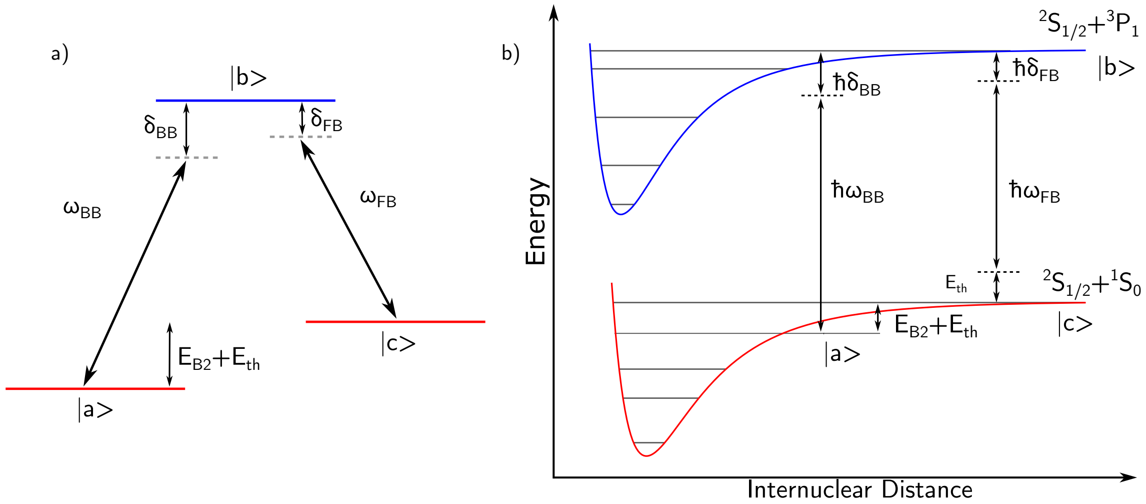

Figure 2.13.: Scheme of a 2-PA process. a) shows the typical Λ three-level system for 2-PA with the involved states and their corresponding detunings and transition frequencies. The energy difference between states $|c\rangle$ and $|a\rangle$ is the binding energy plus the thermal energy of the scattering state. b) shows the 2-PA process with involved potential energy curves and schematically drawn vibrational levels.

where the scattering wavefunction of the ground state is evaluated at the Condon point. $\frac{\partial E_e}{\partial n}$ is the spacing between vibrational levels and D_C the difference between the slopes of the effective potentials of the ground and excited state at the Condon point. In the reflection approximation, we can assume the Condon point being approximately the outer turning point of the excited state. The Condon point is the internuclear distance where the overlap between the wavefunctions of the ground and excited states reaches its maximum value [88].

2.4.1 2-Photon Photoassociation

Two-photon (or two-color) photoassociation spectroscopy (2-PA) enables probing of a molecular state via an auxiliary intermediate state. This technique opens pathways to several interesting phenomena, such as Autler-Townes splitting (see Section 2.3.2), *Electromagnetically Induced Transparency (EIT)* [89, 90], dark resonances [91], *Stimulated Raman Adiabatic Passage (STIRAP)* [92, 93] and, of course, provides information about the probed molecular potential [65, 94, 95].

A typical scheme of a 2-PA process is shown in Figure 2.13, where the intermediate state is a weakly bound state of the electronic excited potential, coupled to the scattering state of two individual atoms by a free-bound laser field ω_{FB}, corresponding Rabi frequency Ω_{FB} and detuning from 1-PA resonance δ_{FB}. In a 2-PA process an additional laser couples now this intermediate state to a bound state of the molecular electronic ground-state potential, which we call the bound-bound laser with parameters ω_{BB}, Ω_{BB} and δ_{BB}. As shown in Figure 2.13 a), we can directly link a 2-PA process to a Λ three-level system, coupled by two light fields, as explained in Section 2.3.2 and Section 2.3.3. We can now combine both explanations as follows:

$\|a\rangle$	(weakly) bound vibrational state of the molecular electronic ground state
$\|b\rangle$	weakly bound vibrational state of the molecular excited state
$\|c\rangle$	scattering state of two individual atoms
$\|a\rangle \leftrightarrow \|b\rangle$	2-PA transition probed by bound-bound laser ω_{BB}
$\|b\rangle \leftrightarrow \|c\rangle$	1-PA transition probed by free-bound laser ω_{FB}
$\|a\rangle \leftrightarrow \|c\rangle$	transition is dipole forbidden.

In this case, the binding energy (plus the thermal energy of the scattering state $|c\rangle$) of the molecular ground state can directly determined by the difference $E_{B2}+E_{th} = \hbar\omega_{BB}-\hbar\omega_{FB}$. For ultracold samples with low thermal energy, this method provides a precise measurement of the energies of vibrational levels of the electronic ground state and thus allows for modeling of the ground-state potential. There are two different ways of performing two-photon photoassociation spectroscopy.

a) $\delta_{\mathbf{FB}} = 0$:

The most obvious way is to start with the free-bound laser frequency set to a known 1-PA resonance ($\delta_{FB} = 0$) and scan the bound-bound laser frequency ($\delta_{BB} \neq 0$). As explained already in Section 2.3.3, for large detunings ($\delta_{FB} \gg \gamma$) and large bound-bound Rabi frequencies ($\Omega_{BB} \gg \Omega_{FB}$), we are in the regime of the AC-Stark shift and can perform light-shift spectroscopy (see Figure 2.14 left). The spectroscopic signal is then a loss-of-loss signal. The first laser causes a detectable loss of atoms in the trap, while the second laser shifts the energy of the excited state. When this shift is larger than the linewidth of the 1-PA resonance, the transition is detuned, preventing further 1-PA transitions. As a result, more atoms remain detectable in the trap. For small bound-bound Rabi frequencies but highly coherent laser fields ω_{BB} and ω_{FB}, the effect has to be treated in a quantum interference picture where different paths interfere destructive on resonance. This leads to a prevention of the population of the excited state $|b\rangle$ [91]. However, the spectroscopic signal in both cases is a loss-of-loss signal.

b) $\delta_{\mathbf{BB}} = 0$:

The second way of two-photon photoassociation spectroscopy is to set the bound-bound laser on a known resonance ($\delta_{BB} = 0$) and to scan the free-bound laser. For a strong

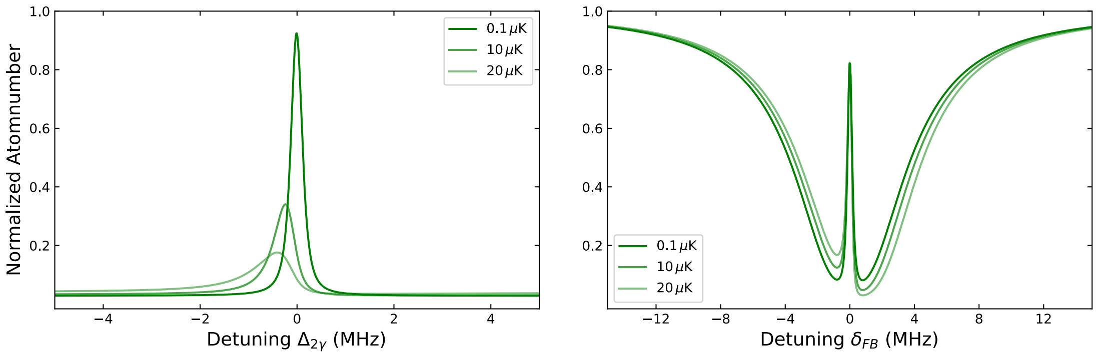

Figure 2.14.: Visualization of 2-PA resonances (Equation (2.49)) for $\delta_{FB} = 0$ (a) and $\delta_{BB} = 0$ (b). The temperature is included via averaging over the thermal Boltzmann distribution. Rabi frequencies for this illustration are: $\Omega_{BB} = 10\,\text{MHz}$ and $\Omega_{FB} = 10\,\text{kHz}$.

bound-bound laser field, e.g. large Ω_{BB}, the resonance splits into two lines, the Autler-Townes doublet (see Section 2.3.2), separated by the bound-bound Rabi frequency Ω_{BB}. By varying the laser field intensity and measuring the resulting Rabi frequency, we can easily determine the saturation intensity, and thus the decay rate, of a certain transition (see Equation (2.22)). The spectroscopy signal appears as a loss signal when the first PA laser is resonant with one of the Autler-Townes doublet lines (see Figure 2.14 right).

In the case of coherent lasers ω_{BB} and ω_{FB} and low bound-bound laser intensity, the signal shows a typical loss of atoms in the vicinity of $\delta_{FB} = 0$, but with a sharp peak at zero detuning. The width of this peak can be on the order of the natural linewidth of the atomic resonance. This effect has also be treated in the manner of quantum interference of the involved transitions and is called electronically induced transparency, where a coherent superposition of the molecular and the scattering state becomes a dark state [89].

For $\Omega_{BB} \gg \Omega_{FB}$ we can calculate the atom loss rate of a 2-PA Λ three-level system as follows [96]

$$\frac{\dot{N}}{N} = \frac{\Omega_{FB}^2 \left[4\Gamma\Delta_{2\gamma}^2 + \Gamma_{eff}\left(\Omega_{BB}^2 + \Gamma_{eff}\Gamma\right)\right]}{\left|\Omega_{BB}^2 + (\Gamma + 2i\delta_{FB})\left(\Gamma_{eff} + 2i\Delta_{2\gamma}\right)\right|^2} \tag{2.49}$$

with the decay rate of the excited state Γ, the effective decay rate Γ_{eff}, where the dark state's incoherence is included, and the two-photon detuning $\Delta_{2\gamma} = \delta_{FB} - \delta_{BB}$. The situation of $\Omega_{BB} \gg \Omega_{FB}$ is in a typical 2-PA process easily fulfilled, due to the Franck-Condon factors for bound-bound transitions being significant larger than those for free-bound transitions.

Both described cases are illustrated in Figure 2.14. In Figure 2.14 a), we see the scenario with $\delta_{FB} = 0$, where the bound-bound laser is scanned, resulting in a single Lorentzian peak. In contrast, Figure 2.14 b) shows a typical dark resonance observed at $\delta_{BB} = 0$.

The corresponding Rabi frequencies are $\Omega_{BB} = 10\,\mathrm{MHz}$ and $\Omega_{FB} = 10\,\mathrm{kHz}$. As already indicated in Figure 2.13 b), the scattering state $|c\rangle$ does not have a single defined energy due to its finite temperature. Instead, its energy is distributed according to a thermal Boltzmann distribution, which is included via averaging Equation (2.49) over the thermal Boltzmann distribution. The effect of the finite temperature is shown for $T = 0.1\,\mu\mathrm{K}$, $T = 10\,\mu\mathrm{K}$ and $T = 20\,\mu\mathrm{K}$. Larger temperatures result in broader and smaller 2-PA resonances and also shift the resonance to smaller detunings.

3

Previous Photoassociation at the D1 Line of Rb

In this chapter, I will provide an overview of previous photoassociation experiments conducted near the D1 line of Rb. Due to the larger oscillator strengths and broader linewidths, photoassociation experiments are often performed near the D1 line of an alkali atom. These studies were carried out by our group using the earlier experimental apparatus [50, 57, 97] and I will only reproduce the key results of their work, which are useful for our search for additional one- and two-photon photoassociation resonances in RbYb. While all experiments were done with ^{87}Rb, there are results for Yb isotopes 170, 172, 174 and 176, but most of the found lines correspond to ^{176}Yb. The initial experiments by N. Nemitz [97] and F. Münchow [57] were performed using a dual-species MOT. Later, C. Bruni [50] enhanced the setup by employing a combined hybrid conservative trap which consisted of a magnetic trap (MT) for Rb and an optical dipole trap for Yb. This advancement significantly reduced the temperatures, allowing only s-wave scattering. Consequently, only molecular states with $R = 0$ contribute to the observed spectra.

3.1 One-Photon Photoassociation near the D1 Line of Rb

Due to the lack of angular momentum of the ground state of Yb, the only possible excited molecular state close to the $^2\mathrm{P}_{\frac{1}{2}} + {}^1\mathrm{S}_0$ transition is $^2\Pi_{\frac{1}{2}}$. The main results, important for this work, are the binding energies for various isotopic combinations, the C_6 coefficient of the potential and the fractional parts Δ_{frac} of v_D (of the ground-state potential). The experimentally determined values are summarized in Table 3.3. A fit of the improved LeRoy-Bernstein formula gives a C_6 coefficient of $C_6 = (-5684 \pm 98)\, E_h a_0^6$ [97], where $E_h = \frac{\hbar^2}{m_e a_0^2}$ is the Hartree-energy.

The measured binding energies in Table 3.3 are relative to the $F = 1 \rightarrow F' = 2$ D1 transition in ^{87}Rb at $\Delta_{PA} = 12579.1037\,\mathrm{cm}^{-1}$[1] and cover the potential down to the vibrational

---

[1] As often used in literature, the binding energy is given in wavenumbers, where $\tilde{\nu} = 1/\lambda = \nu/c$ and $1\,\mathrm{cm}^{-1} = 29979\,\mathrm{MHz}$.

state $\Delta v' = -28$ and a corresponding binding energy of $\Delta_{PA} = -75\,\mathrm{cm}^{-1}$. $E_{B,ms176}$ denotes the calculated binding energy of the corresponding states with Equation (2.9) using the reduced mass μ and Δ_{frac} relative to the measured values of ^{176}Yb.

Unfortunately, the measured and calculated values differ by up to $h \cdot 1.8\,\mathrm{GHz}$. This is likely because the LeRoy-Bernstein fit was performed for ^{176}Yb, where the residuals also differ up to $h \cdot 1\,\mathrm{GHz}$ for certain vibrational quantum numbers (specifically for $\Delta v' = -6$ and $\Delta v' = -16$) [97]. Furthermore, the fractional part of v_D for ^{170}Yb was derived using only a single measured binding energy ($\Delta v' = -6$) and the C_6 coefficient for ^{176}Yb. As a result, the search for new PA resonances in ^{170}Yb requires scanning across an extensive frequency range. Knowing the position of a second vibrational level allows us to refine the LeRoy-Bernstein fit for ^{170}Yb, potentially reducing the uncertainty in Δ_{frac} and improving the accuracy of predicted positions for additional levels.

3.2 Two-Photon Photoassociation near the D1 Line of Rb

After conducting 1-PA, Münchow [57] also performed 2-PA spectroscopy near the D1 line of ^{87}Rb and several Yb isotopes[1]. In doing so, they identified the seven least-bound vibrational levels with binding energies up to $E_B = -h \cdot 58.5\,\mathrm{GHz}$. In collaboration with a theory group [64], they modeled the ground-state potential, provided accurate s-wave scattering lengths for all isotope combinations, and determined molecular transition probabilities using Autler-Townes spectroscopy.

For the purpose of the work presented here, the Autler-Townes spectroscopy results and binding energies of the ground state are of particular interest, as they provide insight into bound-bound Rabi frequencies – an essential parameter for our later investigations involving light-shift spectroscopy (see Section 6.2.3).

The 2-PA spectroscopy was conducted as described in Section 2.4.1: The free-bound laser was held on resonance, while the bound-bound laser was scanned. When the bound-bound laser was on resonance with a molecular transition, it induced a light shift that shifted the free-bound transition out of resonance, leading to a measurable increase in atom number. For more detailed information on the experiment, see [50, 57].

The intermediate states of the excited state used in these measurements were either $\Delta v' = -9$ ($E_B = -2.7287\,\mathrm{cm}^{-1}$) or $\Delta v' = -11$ ($E_B = -4.8958\,\mathrm{cm}^{-1}$)[2], chosen for their strong coupling.

3.2.1 The $^2\Sigma_{1/2}$ Ground State

With the measured binding energies of the $^2\Sigma_{1/2}$ ground state, the potential energy curve could be modeled, providing estimates for dispersion coefficients (C_6, C_8), potential depth

---

[1] Most of the data, as with 1-PA, were taken using ^{176}Yb.

[2] Here, the binding energies are given for ^{87}Rb^{176}Yb.

D_e, and number of supported vibrational states N. This modeling, performed in collaboration with the theory group [64], is summarized in Table 3.1.

The theoretical model combined ab-initio coupled-cluster calculations for the short-range potential with a long-range van der Waals potential of the form $-C_6/r^6 - C_8/r^8$, smoothly connected at around $20\,a_0$ using a switching function. Table 3.1 lists the parameters of the three best-fit potentials, each achieving good agreement with experimental data. These potentials allow predictions of binding energies for additional vibrational states and for other Yb isotopes via mass scaling. Notably, this approach yielded highly accurate predictions for ^{170}Yb (see Table 5.2).

N	D_e [cm^{-1}]	C_6 [$E_h a_0^6$]	C_8 [$E_h a_0^8$]
65	759.9	-2820.0	-4.47
66	787.4	-2837.2	-4.62
67	815.4	-2854.0	-4.75

Table 3.1.: Parameters of the three best fitting modeled potentials for the ground state [50, 64].

3.2.2 Autler-Townes Spectroscopy

As discussed in Section 2.3.2, Autler-Townes spectroscopy provides an elegant method for determining molecular Rabi frequencies – and thus transition probabilities. When a molecular state is strongly coupled with a laser field, it splits into a doublet with a separation directly related to the Rabi frequency. In this setup, the bound-bound laser remains resonant while the free-bound laser acts as the probe. Knowing the coupling laser intensity allows us to extract the Franck-Condon factor via:

$$f^{FC} = \left(\frac{\Omega_{BB}}{\Omega_{at}}\right)^2, \quad \text{with} \quad \Omega_{at} = \gamma\sqrt{\frac{I_{PA}}{2\,I_{sat}}}, \tag{3.1}$$

where I_{PA} is the laser intensity, I_{sat} the saturation intensity of the atomic transition, γ the linewidth of the atomic transition, and Ω_{BB} the bound-bound Rabi frequency.

In [57] and [50], large Autler-Townes splittings exceeding 100 MHz were observed for the $|F' = 2, \Delta v' = 11\rangle \rightarrow |F = 1, \Delta v = -6\rangle$ transition, even with a moderate coupling laser power of approximately 50 mW.

Measured Franck-Condon factors for various transitions in ^{87}Rb^{176}Yb are presented in Table 3.2. Although these values were not obtained for the ^{87}Rb^{170}Yb system, we expect similar behavior in coupling strengths for bound-bound transitions near the D1 line, which will be part of Section 6.2.

The main takeaway is that strong light shifts can be expected when coupling bound-bound transitions near the D1 line of Rb. This makes them highly suitable for use in

excited state $\Delta v'$	ground state Δv	Franck-Condon factor f^{FC}
-9	-5(F=1)	0.20
-11	-4(F=1)	0.03
	-6(F=1)	0.13
	-6(F=2)	0.07
	-7(F=1)	0.05
	-7(F=2)	0.05

Table 3.2.: Measured Franck-Condon factors of several molecular transitions [57].

light-shift spectroscopy (see Section 6.2.3).

3.3 Conclusion

The previous photoassociation measurements near the D1 line of Rb have yielded a wealth of useful information that can inform and enhance future experiments.

In particular, the characterization of the RbYb ground state and its binding energies significantly reduces the search range for 2-PA resonances near the intercombination line. Moreover, the measured transition strengths for both 1-PA and 2-PA provide a solid foundation for our proposed approach to light-shift spectroscopy. In Section 6.2, we will explore this further by leveraging the large bound-bound Rabi frequencies near the D1 line of Rb in combination with the narrow linewidth of a dark resonance on the intercombination line of Yb (see Section 5.2.2).

Yb Isotope	Δv	Δ_{PA} [cm^{-1}]	Δ_{frac}	μ [u]	$E_{B,ms176}$ [cm^{-1}]	ΔE_B [h·GHz]
170	-6	-0.783	0.13	57.501	-0.836	1.6
172	-6	-0.974	0.58	57.729	-1.028	1.6
174	-4	-0.4249	0.928	57.953	-	-
	-5	-0.72800			-0.706	-0.66
	-6	-1.1486			-1.193	1.3
	-7	-1.70310			-1.732	0.87
	-8	-2.43700			-2.449	0.36
	-10	-4.45900			-4.487	0.84
	-12	-7.38365			-7.443	1.8
176	-5	-0.49440	0.274	58.174		
	-6	-0.88090				
	-7	-1.32980				
	-8	-1.93810				
	-9	-2.7287				
	-10	-3.70710				
	-11	-4.8958				
	-12	-6.3333				
	-13	-8.0016				
	-14	-9.9589				
	-15	-12.1942				
	-16	-14.8096				
	-17	-17.6897				
	-18	-20.9236				
	-19	-24.5102				
	-21	-32.8616				
	-22	-37.6097				
	-23	-42.7869				
	-24	-48.3581				
	-25	-54.3464				
	-26	-60.7821				
	-27	-67.6306				
	-28	-74.9147				

Table 3.3.: Measured binding energies of $^{87}Rb^{x}$Yb for several vibrational quantum numbers Δv and the fractional part Δ_{frac}. All binding energies are for $F' = 2$ and $R = 0$. The reduced masses of the isotope combinations are given, as well as calculated binding energies using Equation (2.9) with the values of ^{176}Yb and the difference ΔE_B to the measured binding energy in $h\cdot$ GHz. The accuracy of the measured values is $\pm 5 \cdot 10^{-3}\,\mathrm{cm}^{-1}$. Values are taken from [50, 57, 97].

4

Experimental Apparatus for Photoassociation Spectroscopy of RbYb

In this chapter, I present the experimental apparatus for the production of ultracold atomic samples of Rb and Yb and for photoassociation spectroscopy of RbYb. Operating a complex ultracold dual-species molecule experiment while implementing improvements is time-consuming and thus typically conducted by a team. The construction of the experimental apparatus was initiated by Tobias Franzen before Bastian Pollklesener joined the project. When I started the work presented in this thesis, the vacuum system was already constructed and rubidium was cooled to a Bose-Einstein condensate. A ^{174}Yb MOT was implemented, and its transport into the science chamber was prepared. The experiment and its results are covered in detail in the Ph.D. theses of Tobias [1] and Bastian [2] and have also been published in [51]. Therefore, I will not explain the experiment in all its details, but will only highlight the important points necessary for understanding. Major changes and advancements done on the machine by me after Tobias and Bastian left the lab will be pointed out in the respective subchapter.

The Apparatus

Conducting an ultracold dual-species molecule experiment requires a complex array of laser systems, optics, electronics, and a vacuum system to cool, trap, and manipulate each atomic species. For this reason, the experiment is divided into two main parts. First, the *laser room*, where all laser systems for cooling and trapping of the atoms are set up, and second, the *science table*, where the vacuum chambers, necessary setups for the experiment, and the high-power lasers are located. The light from the laser room is transported via optical fibers to the experiment. This separation allows working on one side without interfering with the other. Potential sources of interference, such as mechanical beam shutters, are therefore placed in the laser room, ensuring they do not affect the data acquisition. We begin with a brief overview of the vacuum system in Section 4.1 and then move on to the laser systems for cooling and trapping the atoms in Section 4.2 and Section 4.3. Following that, I will explain the systems located at the science chamber necessary for transporting

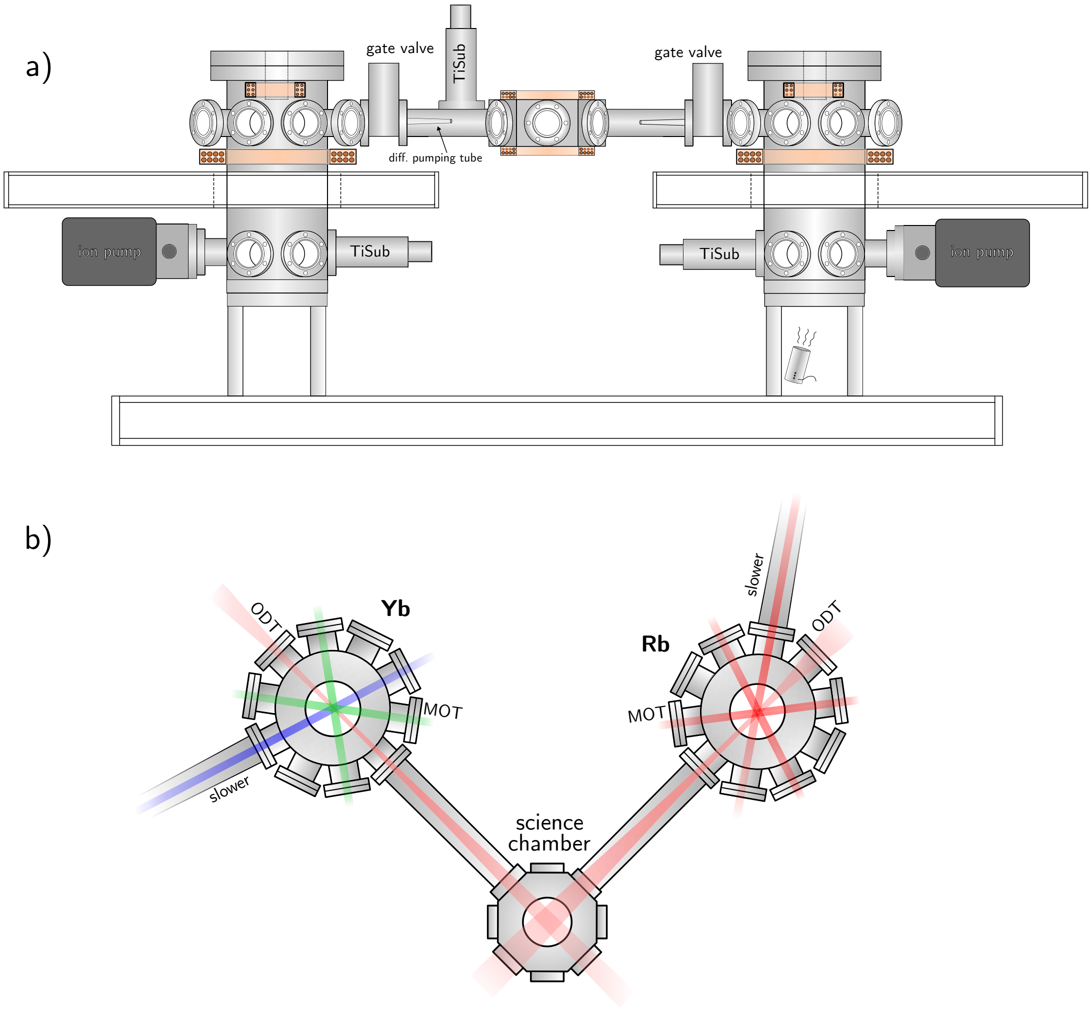

Figure 4.1.: Vacuum system of the RbYb molecule apparatus. a) shows the side view of the three chambers with connected ion getter and titanium sublimation vacuum pumps. The chambers are separated by pneumatic gate valves and differential pumping tubes. A microwave antenna is placed below the Rb production chamber, enabling forced microwave evaporation in the magnetic quadrupole trap. b) shows a top view of the chambers, including slower beams, horizontal MOT beams, and optical dipole traps. Part a) is adapted from [2].

and merging both atomic species in Section 4.6, and we conclude with the experimental control system and data analysis in Section 4.8.

4.1 The Vacuum System

The vacuum system consists of three connected chambers, as shown in Figure 4.1: two production chambers, where each species is prepared as an ultracold sample, and a science chamber, where the species are further cooled and combined within a shared trap. Each production chamber is connected to an atomic oven via a Zeeman slower. The connection to each chamber can be sealed off by pneumatic gate valves, allowing one chamber to be vented without affecting the pressure in the others, e.g. when refilling an atomic oven or upgrading the system.

4.1.1 Atomic Ovens

For Zeeman slowing, it is essential that the atoms are in the gas phase. This is achieved by heating elemental Rb and Yb until the vapor pressure becomes sufficiently high to generate an adequate atomic flux towards the Zeeman slower. The Rb oven remains unchanged from the setup described in [1] and operates at 125 °. The Yb oven, however, was replaced with a custom-built capillary oven tested and characterized in [98], and described in detail in [2]. It consists of 78 stainless steel capillaries (*MicroGroup Stainless Steel 304H22XX*) arranged in a triangular bundle. Capillary ovens like this are commonly used in other cold atom experiments [99, 100], as they reduce the emission angle of Yb atoms compared to a simple nozzle, thereby producing a more collimated beam. As a result, this design increases oven lifetime and reduces the need for frequent refilling.

4.1.2 Zeeman Slowers

For decelerating the atoms sufficiently to velocities low enough to trap them in a MOT, Zeeman slowers in increasing field geometry are used. Both are water-cooled and the designs can be found in detail in [101] (Rb) and [102] (Yb).

4.1.3 Production Chambers

The production chambers of Rb and Yb are shown in Figure 4.1. a) displays a side view of the entire vacuum system. The production chambers are cylindrical and span two levels on an optical table. The lower section houses ion getter pumps and titanium sublimation pumps, while the upper section is equipped with eight CF35 viewports that provide optical access for slowing, trapping, imaging, and transporting the atoms (see Figure 4.1 b)). Both chambers feature multiple coils for magnetic field control and compensation. To compensate magnetic stray fields (such as those from Zeeman slowers and Earth's magnetic field) or to shift the magnetic zero point, each chamber is provided with coils wrapped around two orthogonally positioned viewports. The coils used to generate the magnetic field gradient necessary for MOT and quadrupole trap (Rb) are shown in Figure 4.1 a). Pneumatic gate valves and conical differential pumping tubes[1] separate the production chambers from the science chamber.

---

[1] With a length of 150 mm and inner diameters of 14 mm (production) and 8 mm (science).

Both chambers exhibit minor differences, related to the specific production of ultracold samples of each species. Due to the low vapor pressure of Yb, atoms tend to deposit on surfaces at room temperature. As a result, we observed a deposition of Yb atoms on the inner glass surface of the viewport facing the oven. Over time, this deposition thickens and reduces the transparency of the viewport for the slower light. This effect has also been reported for Sr [103]. To enhance the viewport's lifetime, it is now constantly heated to 230 °, and since then, we have not observed further deposition. The pressure in the Yb production chamber, near the ion pump, is about $1 \cdot 10^{-11}$ mbar. Due to the heating of the viewport, the pressure at the location of the atomic cloud is significantly higher, but the lifetime of our optical dipole trap ($\sim 20\,\mathrm{s}$) remains long enough for trapping and transporting the atoms into the science chamber.

For forced microwave evaporation of Rb in the magnetic quadrupole trap (see Section Section 4.9.1.3), the Rb production chamber is equipped with a microwave antenna positioned beneath it, ensuring a direct line-of-sight to the trap. The pressure in this chamber is well below the measurement limit of the ion pump controllers of $1 \cdot 10^{-11}$ mbar[2].

4.1.4 Science Chamber

The science chamber (see Figure 4.1) is a spherical octagon with two ports connecting it to the production chambers. This configuration allows for the use of six viewports along the horizontal axis and two along the vertical axis, providing optical access for all required light fields[3]. The science chamber also features coils for magnetic field manipulation, as well as an ion pump and a titanium sublimation pump. The pressure in the science chamber is, like in the Rb production chamber, well below $1 \cdot 10^{-11}$ mbar.

4.2 Rb System

The rubidium laser system is unchanged from the extensive description of Tobias [1] and Bastian [2], and is therefore only briefly summarized here.

To cool and trap atoms, a closed cooling transition is required. For rubidium, the natural choice is the D2 line (${}^2\mathrm{S}_{1/2} \rightarrow {}^2\mathrm{P}_{3/2}$) at 780 nm, with a natural linewidth of $\gamma = 2\pi \cdot 5.7\,\mathrm{MHz}$ [104]. An energy level diagram with all necessary transitions of Rb is presented in Figure 4.2.

4.2.1 MOT, Slower and Imaging Light

The light used as MOT, slower, and imaging light is generated by a commercial (*Toptica* DL Pro) external cavity diode laser (ECDL). The laser is frequency stabilized using the

---

[2] The measured current of the ion pump is about four times smaller than that in the Yb production chamber.

[3] For crossed optical dipole traps, lattice beams, imaging light, and photoassociation beams.

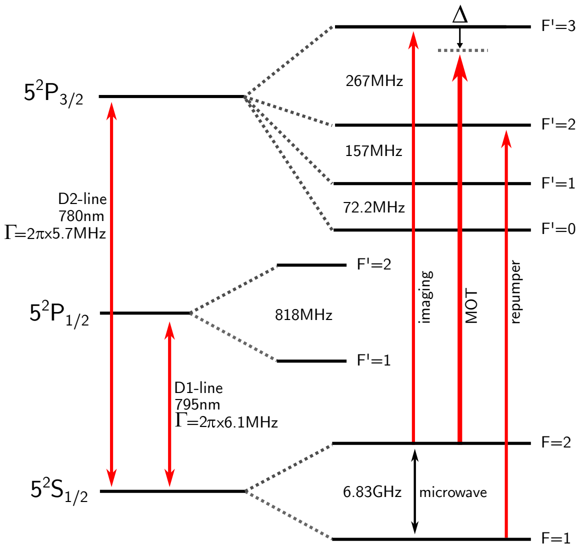

Figure 4.2.: ^{87}Rb energy level scheme with corresponding energy differences of the hyperfine states and linewidths. The arrows indicate the transitions used for imaging, MOT and slower operation and repumping light. Values are taken from [104].

lock-in technique to a compact saturated absorption spectroscopy of the $^2\mathrm{S}_{1/2}(F = 2) \rightarrow {}^2\mathrm{P}_{3/2}(F' = 3)$ cooling transition, with a red-detuning of about 360 MHz[1] and a corresponding wavelength of $\lambda = 780.246\,\mathrm{nm}$ [104][2].

The laser's total output power is $\sim 50\,\mathrm{mW}$, which must be divided among several paths, including spectroscopy, imaging, and beatnote locks. This leaves around 20 mW available for MOT and slowing operation, which is too little for sufficient performance. To address this, the laser is seeded into a tapered amplifier (TA, *DILAS TA-0780-1000*), amplifying the output to $\sim 600\,\mathrm{mW}$. The amplified light is then split into the MOT and slower beams. Both are frequency-shifted using AOMs and can be shuttered via mechanical shutters. Finally, the beams are coupled into optical fibers and directed to the science table.

4.2.2 Repumpers

Since rubidium exhibits a hyperfine structure, atoms can leave the cooling transition by decaying into the $F = 1$ hyperfine state. To ensure atoms remain in the cooling cycle, those entering the $F = 1$ state are pumped back using repumper lasers operating at the $F = 1 \rightarrow F' = 2$ transition at 780.232 nm [104]. For efficient cooling of a Rb MOT, two repumpers are employed.

The first repumper is spatially overlapped with the MOT laser, seeding the TA and thereby illuminating the entire MOT and slower. The second repumper, a so-called dark spot repumper, is coupled into a separate fiber and only illuminates the outer region of the

---

[1] The 360 MHz span is achieved by a double-pass AOM, which is also employed for the lock-in stabilization.

[2] Note that in earlier work of our group, this value was occasionally misreported as 780.250 nm.

MOT (see below). Both repumpers are self-built ECDLs based on interference filters [105, 106]. They use inexpensive *Sharp GH0781JA2C* laser diodes and provide an output power of $\sim 35\,\mathrm{mW}$.

Given the relatively small frequency difference between the MOT and repumping transition, it is possible to stabilize the repumper frequencies using a beatnote lock. This lock is performed by combining both lasers in an optical fiber, detecting the beatnote with a GaAs ROSA or a SFP+ (*Finisar FTLF1429P3BCE*) photodiode, and feeding the signal into an ADF4159 phase-locked-loop (PLL) board. The PLL provides an error signal for a simple PI controller, which acts on the laser piezo to maintain frequency stability. A detailed explanation of this locking technique is provided in Tobias' thesis [1].

4.2.3 Imaging Rb

Images of rubidium atomic clouds are captured using absorption imaging. At the end of the experimental sequence, the cloud is prepared in the $F = 2$ state by exposing the atoms to a short repumping pulse ($\sim 0.8\,\mathrm{ms}$). Subsequently, resonant imaging light is directed onto the atoms and then onto a camera. The atoms absorb this light, creating a typical absorption image, which can later be analyzed and fitted (see Section 4.7).

4.2.4 Microwave

As illustrated in Figure 4.2, the hyperfine splitting of the ^{87}Rb ground state is 6.83 GHz. This transition can be addressed using a microwave system for various applications. The frequency generation and antenna setup are extensively described in [1] and are briefly summarized here.

The hyperfine transition is utilized for forced microwave evaporation in a magnetic trap – performed in the production chamber – as well as for the preparation of Rb samples in different hyperfine and Zeeman states, which takes place in the science chamber. To achieve this, the microwave system must deliver several Watts of output power at 6.83 GHz. For evaporation and Landau-Zener sweeps, it must also allow for tunability over a range of $\sim 100\,\mathrm{MHz}$ and support short pulse generation. The fundamental principles of frequency generation, amplification, fast switching, tuning and the antenna design are similar for both microwave setups.

The microwave signal is generated by a VCO (*Minicircuits ZX95-6840C-S+*) and stabilized via an ADF4159 PLL board. The stability of the phase-locked loop depends on the quality of the reference oscillator. In the production chamber, a standard temperature-compensated crystal oscillator (TCXO) is used, whereas in the science chamber, higher frequency stability is required, necessitating the use of an oven-controlled crystal oscillator (OCXO) [107].

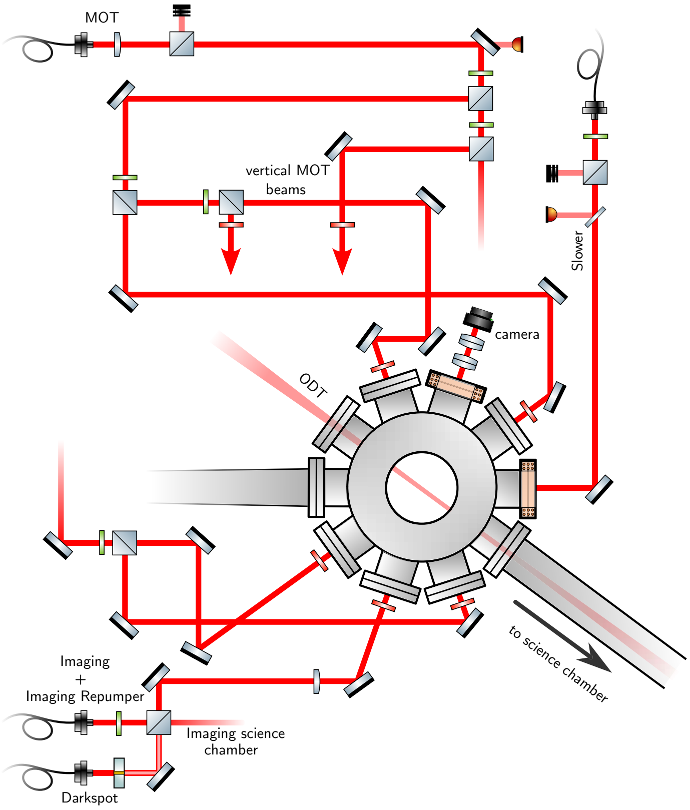

Figure 4.3.: Diagram of the optical setup and corresponding beam paths for MOT operation and imaging at the Rb production chamber. The setup is described in detail in the text.

The microwave signal is switched using an *HMC1118* solid-state switch and is subsequently amplified to 6 W by a *TERRASAT ED-0278-4* power amplifier.

Finally, the amplified signal is delivered to the respective chamber via a simple, sawed-off waveguide horn antenna [108].

4.2.5 MOT Setup

The MOT setup at the science table is illustrated in Figure 4.3. The MOT beam, delivering a power of $\sim 60\,\mathrm{mW}$, is polarization-cleaned using a polarization beam splitter (PBS), then split into six beams of equal power, and directed to the center of the vacuum chamber. The polarization of each MOT beam can be adjusted using $\lambda/4$ waveplates. Power stabilization is achieved via a photodiode that monitors the light leaking through a mirror. The polarization of the slower beam is similarly cleaned, and its power is stabilized by monitoring the reflection of a glass plate. The beam is guided through the chamber and slightly focused on the nozzle of the Rb oven with the out-coupling lens of the optical fiber.

Imaging light ($\sim 50\,\mathrm{\mu W}$) and imaging repumper light ($\sim 500\,\mathrm{\mu W}$), both coupled into single-mode optical fibers, are combined using a fused fiber combiner to ensure perfect spatial overlap. Resonant imaging light is derived from the MOT laser seed and undergoes an identical double pass as the spectroscopy light. When both double passes have the same radio frequencies (RF) for the AOMs, the imaging light is resonant with the transition used to lock the MOT laser's frequency.

The dark spot repumper, coupled out of a single-mode fiber, is generated by passing the light through an anti-reflection (AR) coated glass plate with a gold-coated spot in the center. This dark spot light is then spatially overlapped with the imaging path by a PBS[3]. The same PBS also splits the imaging light into two beams, enabling imaging in either the production or the science chamber.

4.2.6 Optical Tweezer for Rb

The optical tweezer utilizes 30 W of 1064 nm light to trap and transport Rb atoms from the production chamber to the science chamber. This power is generated by a commercial single-mode fiber amplifier (*Nufern NUA-1064-PB-0050-D0*), seeded with $\sim 14\,\mathrm{mW}$ from a spectrally multi-mode fiber laser (*IPG PYL-20M-LP*). The nominal output power of the amplifier is 50 W. For fast switching and precise intensity stabilization, an AOM (*Crystal Technology 3110-191*) is employed.

To achieve a sufficiently deep trapping potential, a tight focus with a waist of 40 µm is required due to the large detuning of the ODT beam. The beam is therefore expanded before passing the focusing lens ($f = 750\,\mathrm{mm}$), which is mounted on an air-bearing translation stage (*Aerotech ABL1500*) capable of traveling a distance of 500 mm. Once the atoms are trapped in the dipole trap, the focus can then be translated into the science chamber for further experiments.

The spectrum of the seed laser for both ODTs is intentionally broad (a few nm). Previous attempts using a single-frequency seed laser were unsuccessful due to etalon effects caused by reflections between parallel glass surfaces of opposite viewports. These effects induced intensity fluctuations during transport, resulting in significant atom losses. Using a broader-spectrum laser, with a reduced coherence length, effectively mitigates these issues and ensures stable transport.

4.3 Yb System

The preparation of ultracold Yb samples follows a process similar to that of Rb. Yb atoms are slowed using a Zeeman slower, which operates on the broad ${}^1\mathrm{S}_0 \rightarrow {}^1\mathrm{P}_1$ transition at 399 nm (blue), with a linewidth of $\Gamma = 2\pi \cdot 28\,\mathrm{MHz}$. This broad linewidth allows for fast and efficient slowing and is also utilized for imaging purposes. The MOT, on the

---

[3] This spatial overlap arises purely from practical considerations.

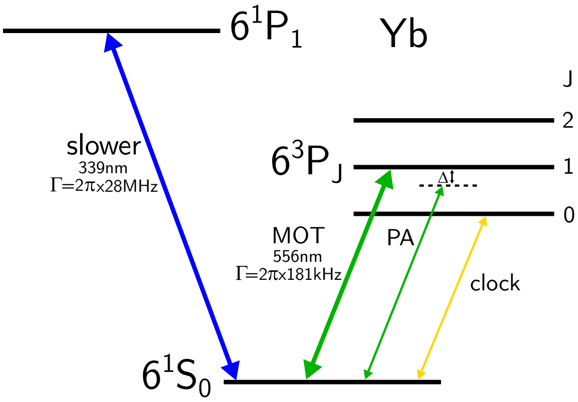

Figure 4.4.: Yb energy level scheme with all relevant transitions.

other hand, operates on the narrow intercombination line $^1\mathrm{S}_0 \rightarrow {}^3\mathrm{P}_1$ at 556 nm (green), which has a linewidth of $\Gamma = 2\pi \cdot 182\,\mathrm{kHz}$. Additionally, the photoassociation experiments described in this chapter are performed close to this intercombination line. Unlike Rb, Yb lacks hyperfine structure, which eliminates the need for repumping light. A more detailed explanation of the system can be found in [1] and [2].

This chapter describes the Yb laser setup used to obtain the presented data (see Sections 5.1 and 5.2). After Bastian left the lab, several modifications and advancements were made to the system. The generation of slowing and imaging light was renewed, and both the active and passive stability of the MOT light were improved. These changes and refinements to the experimental setup represent a central aspect of my independent work and are aimed at improving the system's overall stability and will be discussed in the respective chapters.

4.3.1 1st Generation Slower and Imaging Laser System

The light for Zeeman slowing and imaging of Yb atoms at 399 nm is generated with a self-built external cavity diode laser (ECDL) based on an interference filter. This ECDL seeds another laser diode, which functions as an amplifier to achieve the necessary output power for efficient slowing. This laser system was constructed by Bastian during his Bachelor's thesis and is described in detail in his work [109]. It should be noted that this laser was used for the photoassociation measurements near the intercombination line described in Chapter 5. Subsequently, the 2nd generation setup described in Section 4.3.2 was implemented.

4.3.1.1 Seed Laser

The seed laser is based on an AR-coated (*Nichia NDUA116T*) laser diode, providing an output power of ∼ 10 mW at 399 nm. A portion of its light is directly injected into the amplifying laser diode, while another portion is frequency-shifted using a double-pass AOM.

This shifted light is then used for absorption imaging and for frequency stabilization via spectroscopy.

4.3.1.2 Amplifier

The amplifier is a *Nichia NDV4313E* laser diode, collimated using a lens, with free-running center wavelength of 401 nm. Its output power of ~ 40 mW is then coupled into an optical fiber with coreless endcaps and directed to the experiment. This choice of optical fiber is made to address the degradation of the input fiber surface over time, even at relatively low power levels. Since the frequency and power of the slower beam are not adjusted during the experiment and fast shuttering is not required, the beam is switched using a mechanical shutter.

4.3.1.3 Frequency Stabilization

To keep the 399 nm light in resonance with the atomic transition[1], the seed laser is stabilized to a Yb fluorescence spectroscopy using a lock-in technique. After passing through a double-pass AOM (for frequency shifting and modulation), the beam enters a vacuum chamber containing an atomic beam of Yb[2]. To mitigate Doppler shifts, the beam is retro-reflected by a concave mirror. Permanent neodymium magnets are placed around the vacuum chamber to separate the spectroscopy peak of the desired ^{170}Yb isotope from the neighboring ^{171}Yb isotope. Due to the nuclear spin of the fermionic ^{171}Yb isotope, it exhibits a magnetic moment and is thus shifted by the generated magnetic bias field.

4.3.2 2$^{\text{nd}}$ Generation Slower and Imaging Laser System

The 1$^{\text{st}}$ generation 399 nm system described above is highly sensitive to perturbations and requires frequent maintenance, such as re-locking the seed laser to the spectroscopy peak, readjusting the injection beam or finding the required injection current of the amplifier laser diode to ensure single-mode operation. Additionally, the output power of 40 mW before the optical fiber results in only ~ 15 mW of usable light after coupling, due to the challenges of fiber coupling with blue light. Therefore, I have implemented an entirely new setup for the blue system, utilizing a commercial grating-based ECDL (*Toptica DL pro HP*) with a nominal output power of 100 mW at 399 nm. The linewidth is less than 1 MHz and the mode-hop free tuning range extends to about 20 GHz. The complete setup is illustrated in Figure 4.5. To avoid inefficient fiber coupling, the new system is positioned on the science table, with the main output beam sent free space to the Zeeman slower.

When we measured the quality of the laser beam in the near field, we observed a "hole" in its center. This hole was incidentally imaged with a magnifying telescope to the location

---

[1] Or within the required detuning for slower operation.

[2] Generated by a Yb oven working at ~ 450 °

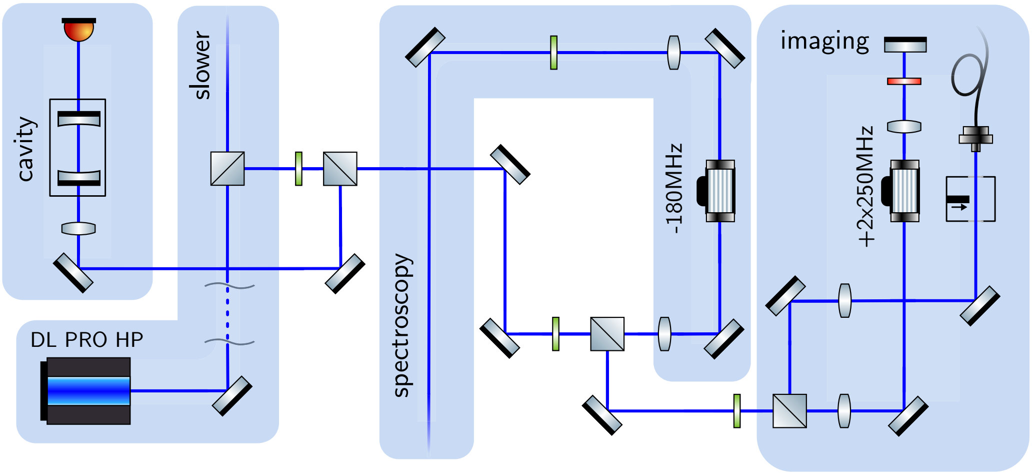

Figure 4.5.: Scheme of 399 nm laser system including slower, monitor cavity, spectroscopy, and imaging path. An extension distance of 2 m is indicated with dashed lines. Spectroscopy light and imaging light are frequency-shifted via single- and double-pass AOMs, respectively. The imaging light is coupled into an optical fiber and can be shuttered via a mechanical shutter.

of the Zeeman slower. To address this, we implemented an extension distance of approximately 2 m, as indicated with dashed lines in Figure 4.5. The beam is then collimated and split into multiple paths for slowing, monitoring, spectroscopy, and imaging, using polarization beam splitters and $\lambda/2$ waveplates.

A small portion of the light is coupled into a scanning low-finesse cavity, which serves as a monitor for the laser's single-mode behavior. The remaining light is divided into the spectroscopy and the imaging paths.

The light for spectroscopy passes through a single-pass AOM with an RF-frequency of -145 MHz before entering the same spectroscopy setup used in the previous configuration.

The imaging light passes through a double-pass AOM with an RF-frequency of 2×250 MHz and is then coupled into an optical fiber. For fast switching of the imaging light, the AOM can be used. Since a small portion of the light passing through an AOM is always deflected into the first order, a mechanical shutter is additionally employed to completely block the beam.

4.3.2.1 Frequency Stabilization

For frequency stabilization, we still use the lock-in technique along with a slow PI controller. However, unlike in the previous setup, we no longer lock to the desired (but very weak) ^{170}Yb transition. Instead, we now lock to the ^{172}Yb transition, which is much stronger. To maintain the same absolute frequencies for the slower and imaging light, the RF-frequencies of the AOMs are adjusted as described above. With these changes, we are able to increase

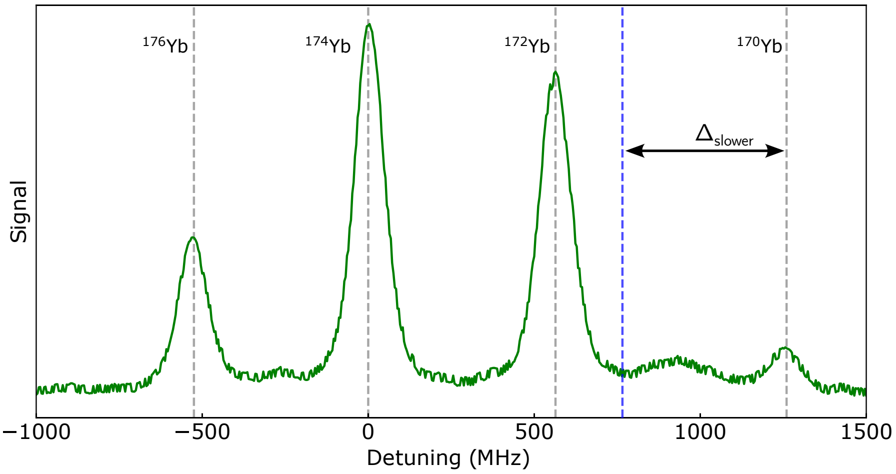

Figure 4.6.: Spectroscopy signal of the $^1\mathrm{S}_0 \rightarrow {}^1\mathrm{P}_1$ transition of Yb at 399 nm. Detunings are relative to the ^{174}Yb transition and only bosonic isotopes are labeled. The slower is locked with an offset of 180 MHz relative to the ^{172}Yb transition.

the usable optical power for the Zeeman slower, as the power required for spectroscopy is significantly reduced by using a single-pass AOM and a stronger spectroscopy peak. A typical spectroscopy signal is shown in Figure 4.6. As a result, the new 399 nm system provides about 45 mW of usable optical power for the slower operation, representing a threefold increase compared to the 1st generation setup. This increase facilitates faster loading of the MOT and, coupled with the intrinsic stability of the laser, results in a much more stable system that requires fewer adjustments or interventions throughout the day. Given that a stable MOT is critical for the success of any ultracold atom experiment, these improvements significantly enhance the overall performance and reliability of the apparatus.

4.3.3 1st Generation MOT Laser System

After slowing the Yb atoms in the Zeeman slower, they are directly captured in a narrow-line ($2\pi \cdot 182$ kHz) MOT at 556 nm. This light is generated using an amplified fiber laser at 1112 nm, which is frequency-doubled via a periodically poled lithium niobate (PPLN) waveguide, providing about 200 mW output power at 556 nm. The amplifier is a home-built fiber amplifier at the edge of the gain spectrum, and the entire light generation setup is described in detail in [110] and [1].

After leaving the doubling crystal, the light passes an AOM for fast frequency adjustment and intensity stabilization. A mechanical shutter is employed to completely block the beam. Finally, the light (~ 40 mW) is coupled into an optical fiber and directed to the science table.

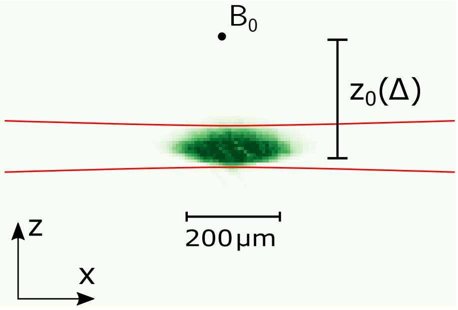

Figure 4.7.: Scheme of the experimental situation for loading of the ODT from the Yb MOT. B_0 indicates the magnetic zero point where a standard MOT is located. Here, $z_0(\Delta)$ shows the location of the MOT center where the gravitational force is compensated by the radiation pressure force, see Equation (4.3). The ODT beam is represented by the two red lines.

Stabilization of the MOT Laser using the MOT Position

This section outlines the frequency stabilization of the MOT laser using a reference cavity, complemented by an in-situ measurement of the vertical MOT position, which is directly correlated with the laser detuning (see Section 4.3.3.5). The stability of the vertical MOT position is essential for efficient loading into the optical dipole trap, making it a critical factor for the success of subsequent experimental stages. The experimental apparatus is first introduced in Section 4.3.3.1, followed by a description of the laser setup in Section 4.3.3.2. The implementation of the reference cavity and the experimental sequence are discussed in Section 4.3.3.3 and Section 4.3.3.4, respectively. The stabilization technique itself is detailed in Section 4.3.3.5, and the results of the 1^{st} generation MOT laser setup are presented in Section 4.3.3.6. This system was developed and improved later on (see Section 4.3.4) by the author during the course of the Ph.D. project.

This section has previously appeared in [111] and is reproduced with minor editing.
Reproduced from:
Active position stabilization of an atomic cloud in a narrow-line magneto-optical trap using a Raspberry Pi. C. Sillus, T. Franzen, B. Pollklesener, and A. Görlitz. Review of Scientific Instruments, 92(3):033204, 2021., with the permission of AIP Publishing.

4.3.3.1 Experimental Setup

A crucial step during an experimental sequence is the transfer of the Yb atoms from the MOT operating on the intercombination line into the ODT (see Section 4.3.6) and

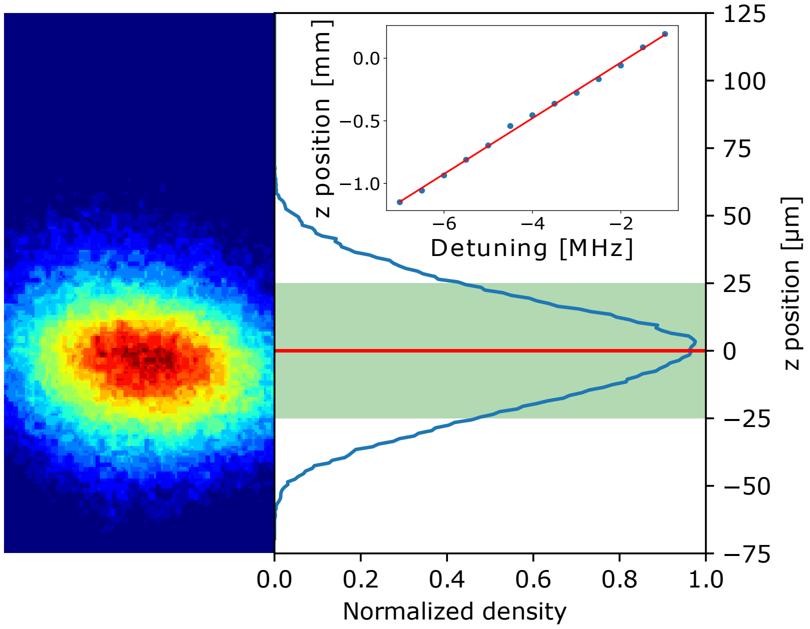

Figure 4.8.: (Left) False color picture of the fluorescence recorded by a *Raspberry Pi* camera. (Right) Normalized vertical profile of the density of the MOT. The green shaded background indicates the range of acceptable positions for transfer into an ODT while the red line indicates the optimal position of the MOT center.
Inset: Dependence of the vertical MOT position on the frequency detuning from the atomic resonance. The MOT shifts downwards with increasing absolute value of the detuning. The red line is a linear fit to the data with a slope of $\mathrm{d}z/\mathrm{d}\Delta = (223 \pm 4)\,\mu\mathrm{m} / (2\pi{\cdot}\mathrm{MHz})$.

Figure 4.7. Figure 4.8 shows a false color picture of the compressed MOT and a plot of a normalized vertical density distribution. The full width at half maximum (FWHM) of a typical MOT is $(38 \pm 1)\,\mu\mathrm{m}$, which is comparable to the $1/e$ diameter of the ODT of $(41 \pm 3)\,\mu\mathrm{m}$. The ODT loading efficiency vs. MOT position is shown in Figure 4.9 and emphasizes the required stability for a stable loading performance.

4.3.3.2 Laser Setup

The MOT laser in our experimental setup is a fiber laser (DFB fiber laser module system, *Koheras Boostik*) with a wavelength of 1112 nm and a linewidth of 0.1 MHz, which is amplified by a home-built fiber amplifier and subsequently frequency-doubled in a periodically poled lithium niobate (PPLN) waveguide to 556 nm [110]. The laser is locked at the fundamental wavelength via the *Pound-Drever-Hall* method [112] to a Fabry-Pérot reference cavity with low-loss mirrors. To avoid temperature and pressure fluctuations, which lead to changes in the free spectral range (FSR), the cavity is placed inside a vacuum chamber which is held at a pressure of 10^{-7} mbar. The cavity is mounted on a

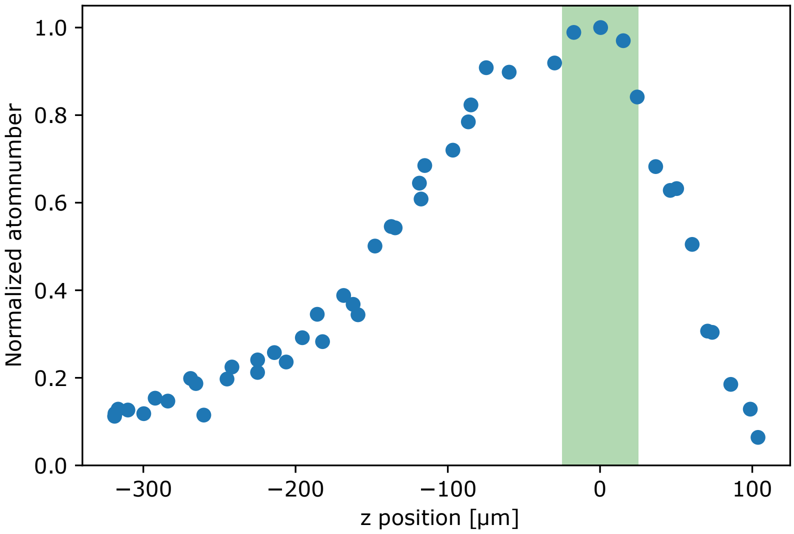

Figure 4.9.: ODT loading performance: The MOT position is changed by adjusting the frequency (see inset in Figure 4.8). The green shaded background indicates the desired loading position. The asymmetric edges of the graph are caused by an asymmetric MOT shape during ODT loading. The asymmetric shape of the MOT is due to gravity which not only affects the position of the MOT but also its shape.

temperature-stabilized copper plate. To reduce the sensitivity of the cavity to temperature fluctuations, the cavity mirrors are glued to a *Zerodur* spacer with a length of 105 mm and a thermal expansion coefficient (CTE) of $0 \pm 0.100 \cdot 10^{-6}\,\mathrm{K}^{-1}$. The nominal reflectivity of the cavity mirrors is $R = 0.99995$, resulting in a cavity linewidth of 25 kHz which is much smaller than the linewidth of the laser and is not limiting the locking performance. For fine-adjustment of the laser frequency a 200 MHz acousto-optical modulator (AOM) in double-pass configuration is installed in the beam path before the cavity.

4.3.3.3 Reference Cavity

The temperature of the reference cavity is stabilized using a PID-controller, which controls the temperature of the copper plate using a negative thermal coefficient (NTC) thermistor as a sensor. For monitoring the actual temperature an additional NTC is attached directly to the *Zerodur* spacer inside the vacuum chamber. Direct stabilization of the spacer temperature is not feasible due to the thermal inertia of the spacer material and the correspondingly large time constant.

The frequency stability that is required to control the MOT position to 10 µm is approximately 50 kHz, equivalent to roughly a quarter of the linewidth of the Yb MOT transition. This requires that the cavity length has to be stable to within a few pm, which corresponds to a temperature stability of around 2 mK. Though the temperature control loop can reach this stability as measured at the copper cooling plate, a diurnal temperature variation with an amplitude of 0.5 K between the two temperature sensors is observed, indicating that the temperature of the reference cavity is drifting. These temperature variations are attributed to periodic temperature fluctuations in our laboratory which radiatively couple from the unstabilized vacuum enclosure to the cavity spacer. In addition to the diurnal variations, we observe a long-term drift of the cavity length, which probably stems from an aging process of the *Zerodur* spacer. We determined this drift to be 0.2 MHz per day corresponding to a relative length change of $\frac{\Delta L}{L} = -3 \cdot 10^{-7}\,\mathrm{y}^{-1}$, which is in good agreement with the results of Riehle et al. [113]. The negative sign indicates that the cavity shrinks.

The temperature variations of the reference cavity lead to a change of the cavity length and hence the laser frequency, which in turn, affects the position of the MOT. A typical position drift of the MOT center is shown in the blue curve in Figure 4.12 where a drift of approx. 0.4 mm/h has been observed.

4.3.3.4 Experimental Sequence

The overall goal of our experimental study is the formation of ultracold RbYb molecules using photoassociation. An Rb and a Yb MOT are prepared in different vacuum chambers and loaded into ODTs. For the creation of an ultracold atomic mixture both species are transported into a science chamber using translation stages which move the focusing lenses of the ODTs. In the science chamber, the traps are merged in a crossed ODT or an optical lattice. For molecule formation via photoassociation either the Rb D1 transition [48, 114] or the intercombination line of Yb can be used. The total duration of an experimental cycle from the start of MOT loading to merging of the two atomic species in the science chamber is approximately 40 s.

The crucial step of the experimental procedure which is relevant for the stabilization method described in this manuscript is the loading of Yb atoms from the MOT into the ODT inside the Yb production chamber. The ODT for Yb consists of a far red-detuned 1064 nm high-power home-built fiber amplifier seeded by an *IPG PYL-20M-LP* laser. The trapping beam has a power of approx. 16 W and a $1/e$ diameter of $\omega = (41 \pm 3)$ µm. The method presented here stabilizes the position of the MOT operating on the ${}^1\mathrm{S}_0 \rightarrow {}^3\mathrm{P}_1$ intercombination line of ${}^{170}\mathrm{Yb}$ by acting on the MOT laser frequency. The linewidth of the intercombination transition is $\Gamma = 2\pi \cdot 182\,\mathrm{kHz}$ and its saturation intensity is $I_{sat} = 0.138$ mW/cm^2.

A partial scheme of the experimental sequence from the MOT capturing phase to the ODT loading phase can be seen in Figure 4.10. The atoms are first captured from a Zeeman slower operating on the ${}^1\mathrm{S}_0 \rightarrow {}^1\mathrm{P}_1$ line (with a linewidth of $2\pi \cdot 28\,\mathrm{MHz}$). In this loading phase, the saturation parameter for the upward MOT beam is $s = \frac{I_{up}}{I_{sat}} = 90$, and the detuning of the MOT laser from resonance is $-10\,\Gamma$. After 20 s of loading approximately

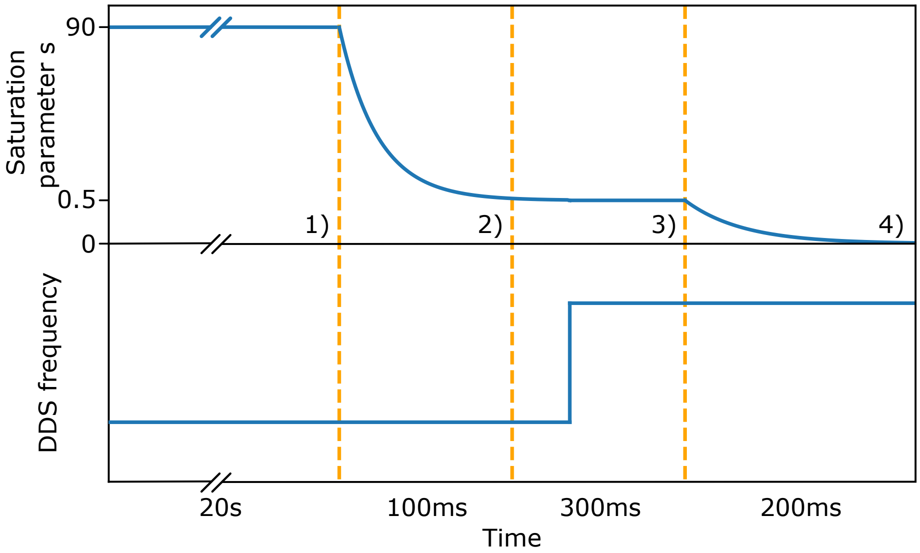

Figure 4.10.: Partial scheme of the experimental loading sequence for Yb: (Top) Saturation parameter $s = \frac{I_{up}}{I_{sat}}$ for the vertical MOT laser beam. (Bottom) Frequency of the MOT laser.
(1) The MOT is loaded for a duration of 20 s. (2) The intensity is ramped down to $s = 0.5$ in 100 ms, cooling the atoms to $T_1 \approx 30\,\mu\text{K}$. (3) For thermalization the MOT is held for 300 ms. In this step the MOT is imaged and subsequently the MOT laser frequency is adjusted. For efficient loading of the MOT into the ODT, the MOT laser intensity is ramped down to zero (4).

$3 \cdot 10^7$ atoms (Figure 4.10 (1)) are captured in the MOT. For further cooling we ramp down the intensity to $s = 0.5$ and lower the magnetic field gradient leading to an atomic sample with $2 \cdot 10^7$ atoms at a temperature of 30 µK (Figure 4.10 (2)). After this cooling step, the MOT is held at the final laser parameters for 300 ms (Figure 4.10 (3)) to allow for complete thermalization. During this thermalization phase, the vertical MOT position is measured and adjusted as described in the following section. After adjustment of the MOT position, the Yb atoms are transferred into the ODT by smoothly ramping down the MOT laser intensity.

4.3.3.5 Stabilization of the MOT Position

The stabilization method reported in this manuscript is based on an extension of the standard description of a MOT, which includes effects due to the interplay between the narrow linewidth of the intercombination line and gravity [115, 116]. In the regime of low scattering rates, i.e. low laser intensities, the MOT does experience a gravitational sag if the gravitational force becomes comparable to the radiation pressure force of the MOT beams. The gravitational sag may be derived quantitatively if one considers a situation where only the upward MOT beam is interacting with the atoms. The radiation pressure force on an atom at rest is then given by

$$\vec{F}_{rad} = \frac{\hbar k \Gamma}{2} \frac{s}{1 + s + \left(\frac{\Delta - \Delta_{Zeeman}(z)}{\Gamma/2}\right)^2} \vec{e}_z \tag{4.1}$$

where Δ is the detuning of the laser from the atomic resonance, $k = \frac{2\pi}{\lambda}$ the wavenumber, s the saturation parameter of the upward MOT beam and

$$\Delta_{Zeeman}(z) = \frac{g_j m_j \mu_B dB_z z}{\hbar} \tag{4.2}$$

the Zeeman shift of the MOT transition at position z. Here $\hbar$ is Planck's constant, dB_z the MOT magnetic field gradient along the z-axis, μ_B Bohr's magneton, g_j the Landé factor and m_j the magnetic quantum number of the excited state. In the case of ^{170}Yb, $g_j = 1.49$ and $m_j = 1$.

The MOT center will be located at the position z_0 where the radiation pressure force and the gravitational force $\vec{F}_g = -mg\,\vec{e}_z$ compensate each other leading to

$$z_0 \approx \frac{\hbar \Delta}{g_j m_j \mu_B dB_z} \pm \frac{\hbar \Gamma}{2 g_j m_j \mu_B dB_z} \sqrt{(R-1)s - 1}\ . \tag{4.3}$$

where $R = \frac{\hbar k \Gamma}{2mg}$ is the ratio of the maximum radiation pressure force and gravity. For ^{170}Yb this ratio has the value $R = 478$. In a 3D MOT Equation (4.3) only holds if $\Gamma\sqrt{1+s} << \Delta_{Zeeman}(z_0)$, otherwise the interaction with the downward MOT beam has to be included. Within the validity range of Equation (4.3), the vertical MOT position z_0 depends linearly on the detuning with a slope given by [115]

$$\frac{\mathrm{d}z_0}{\mathrm{d}\Delta} = \frac{\hbar}{g_j m_j \mu_B \mathrm{d}B_z}. \tag{4.4}$$

For the experimental situation considered here, where $dB_z = (20 \pm 3)$ G/cm, the theoretically calculated value is $\mathrm{d}z/\mathrm{d}\Delta = (240 \pm 32)$ µm/(2π·MHz). The measured MOT position in our experimental setup is shown in the inset of Figure 4.8 where the red line is a linear fit to the data with a slope of $\mathrm{d}z/\mathrm{d}\Delta = (223 \pm 4)$ µm/(2π·MHz). This is in good agreement with the theoretical value considering the accuracy with which the magnetic field gradient is known. In addition to the described shift of the position of the MOT center, the influence of gravity also leads to a distortion of the cloud shape. This can be seen in Figure 4.9 where the loading efficiency of an ODT is shown as a function of the MOT position. The reason for the observed asymmetry is that the lower edge of the MOT is much sharper than the top edge.

The frequency dependence of the MOT position as described by Equation (4.3) is used as means to keep the MOT at the optimal position for loading of the ODT. A scheme of the complete setup of the active stabilization system is depicted in Figure 4.11. The control

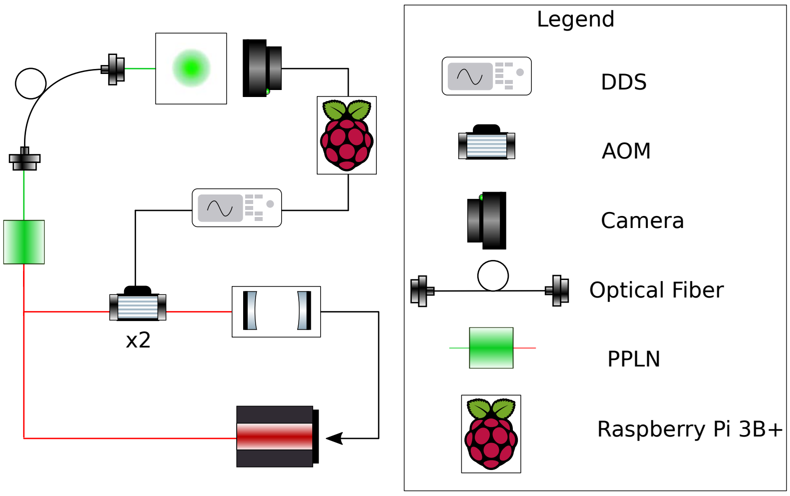

Figure 4.11.: Scheme of the active MOT position stabilization system: The MOT laser is prestabilized to a *Zerodur* cavity using the Pound-Drever-Hall technique to lock the fundamental wavelength at 1112 nm. Since it is not possible to tune the cavity length, a 200 MHz double pass AOM is used to shift the laser frequency to the desired value. The main part of the infrared light is frequency-doubled by a fiber coupled PPLN to 556 nm and is sent to the experiment using optical fibers. The camera takes a picture of the MOT during the thermalization phase (see Figure 4.10) and the *Raspberry Pi* is used to automatically determine the required frequency shift which is then sent to the AOM via a DDS.

loop consists of a *Raspberry Pi camera v2*, a *Raspberry Pi*, a direct digital synthesizer (DDS, *AD9910*), a radio frequency amplifier, and an AOM. During the thermalization phase (see Figure 4.10) the camera first takes a fluorescence picture of the MOT. Using the *OpenCV* python library the image is integrated horizontally yielding a 1D array from which the center of gravity is calculated. We confirmed that the center of gravity determined this way is in excellent agreement with the vertical position of the MOT as measured using absorption imaging. It should be noted that absorption imaging can only be used for calibration and is not suitable for the in-situ stabilization scheme due to its destructive nature. For active stabilization of the vertical MOT position, the required frequency to shift the MOT to the predefined position for loading of the ODT is calculated by the *Raspberry Pi*. This frequency is in turn generated using the DDS and fed to the AOM in the light path which is used for stabilization of the fundamental light at 1112 nm to the reference cavity. This has the advantage that the light path for the 556 nm MOT light and hence the fiber coupling is not affected by a change of the laser frequency. The whole stabilization takes place during the 300 ms thermalization time, so that the position of the MOT is adjusted for each experimental cycle individually. After the position adjustment,

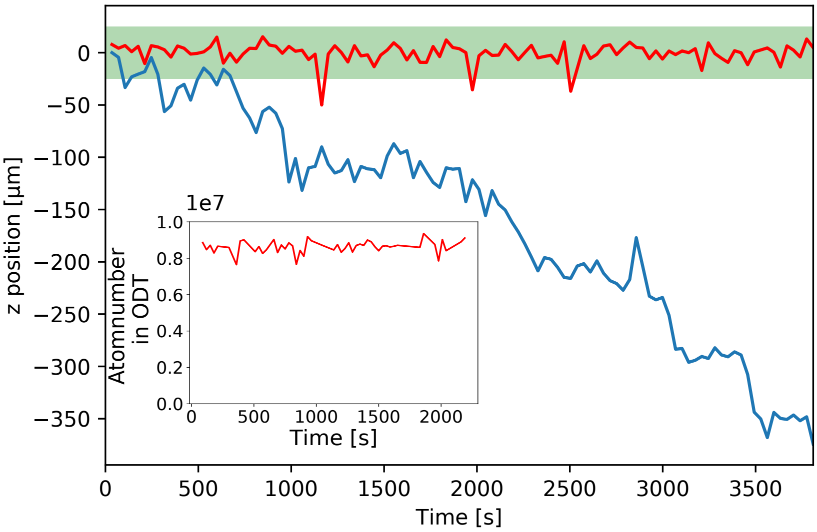

Figure 4.12.: Stability of the MOT position with (red line) and without (blue line) active stabilization: The green shaded background indicates the range over which a sufficient ODT loading performance can be achieved. Without active stabilization the MOT is kept in the desired range for only ≈ 200 s. (Data points are connected by lines to guide the eye.)
Inset: Loading performance of the ODT with stabilized MOT position as a function of time. (The data are obtained from a different measurement.)

the MOT can be loaded smoothly into the ODT by ramping the MOT laser intensity to zero (Figure 4.10, (4)).

For finding the starting point at the beginning of an experimental campaign the temperature of the reference cavity is read out using the *PyVisa* library and a digital multimeter. With an empirical relationship between temperature of the reference cavity and MOT laser frequency a start value is determined. This step is only needed after alignment changes or long experimental pauses. The set value for the vertical MOT position is obtained by determining the maximum loading efficiency of the ODT using a MOT laser frequency scan.

4.3.3.6 Results

Figure 4.12 shows a comparison of the unstabilized and the actively stabilized vertical MOT position for a period of 1 h. The unstabilized MOT position (blue line) exhibits a typical linear drift of approx. 0.4 mm/h. By comparison of Figure 4.9 and Figure 4.12 one can see that without active stabilization a sufficient loading performance can be achieved for less than 200 s, which is on the order of 5 complete experimental cycles. The observed drift leads to a fast degradation of the number of atoms in the ODT making systematic studies of e.g. photoassociation spectroscopy of RbYb almost impossible.

In contrast, the position of the stabilized MOT (red curve in Figure 4.12) stays within the green shaded background area where optimal loading of the ODT can be achieved. The few data points outside the shaded area are due to an overcompensation of transient external perturbations. Even if the position of the MOT is outside the desired region, the stabilization method is able to return it to the desired value within the next experimental cycle. As the outliers can be easily identified from the images taken by the stabilization system, these shots can be excluded from a measurement by post selection. The RMS deviation of the stabilized MOT position is 7 µm if the outliers are excluded. While Figure 4.12 only shows data taken over an hour to be able to compare the stabilized and the unstabilized performance directly, the position stabilization system operates reliably over a whole day without the need to re-locking or manual frequency readjustments. The inset of Figure 4.12 shows the loading performance from the MOT into the ODT. Except for a few outliers due to the mentioned overcompensation the number of atoms transferred into the optical dipole trap is stable to within an RMS deviation of 4 %, e.g. $(8.6 \pm 0.3) \cdot 10^6$ atoms, which is a good starting point for further experiments. To obtain a more accurate position stability the timing of the MOT image, which currently exhibits a jitter on the order of 0.1 s, would have to be improved since the position of the MOT center slightly shifts during the thermalization step where the image is taken. This could be achieved by using a camera capable of accepting a hardware trigger input. Furthermore, fast varying magnetic background fields, e.g. related to the AC power line, would have to be shielded or controlled more accurately.

In conclusion, we have developed a stable and reliable stabilization system for the vertical position of a Yb MOT operating on the intercombination line. This system which stabilizes the MOT position to 7 µm can in principle be adapted to any experiment where external perturbations lead to fluctuations of the vertical position of a narrow-linewidth MOT.

4.3.4 2nd Generation MOT Laser System

Although the system described in the previous subchapter ensures stable frequency stabilization and reliable ODT loading performance, certain challenges still hinder the optimal operation of our Yb system. Accordingly, I have developed an upgraded version of the frequency and position stabilization, incorporating improved active and passive stability measures, which is described in the following.

4.3.4.1 Upgraded Camera

To mitigate the above-mentioned timing jitter on the order of 0.1 s, a new camera (*GetCamera MER2-503-36U3M*) with a hardware trigger and global shutter has been implemented.

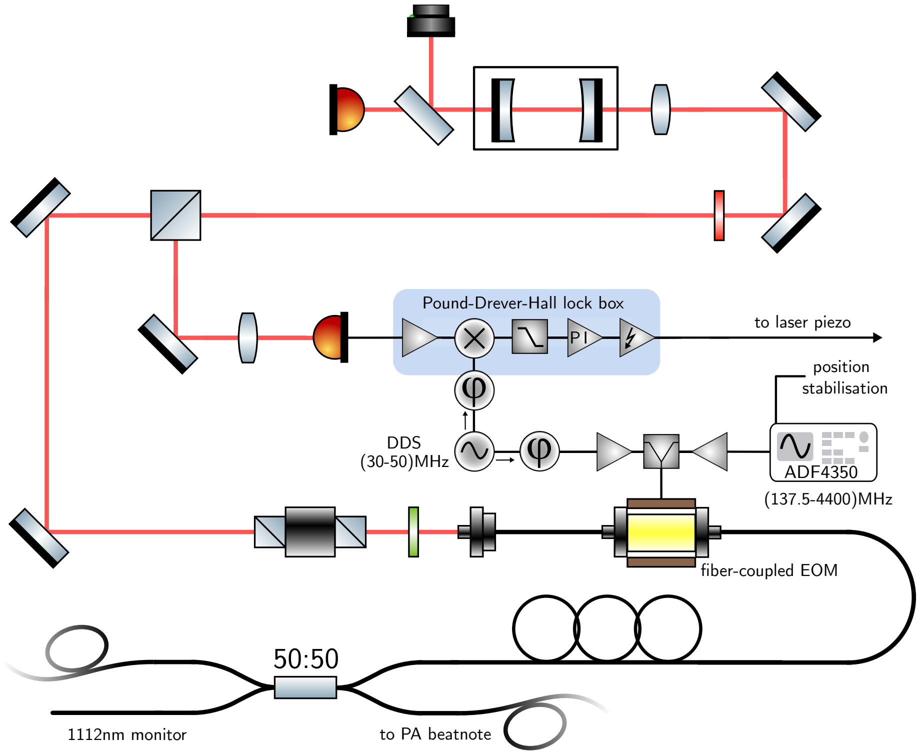

Figure 4.13.: Scheme of the new Pound-Drever-Hall sideband locking setup. The monitor signal of the 1112 nm fiber amplifier is polarization controlled, fed into a fiber-coupled EOM and then directed in free space to a Zerodur cavity. The reflected light is used for PDH-locking. For monitoring the transmission signal and transversal cavity mode, a photodiode and a camera are installed behind the cavity. The RF signals are derived from a direct digital synthesizer (for PDH lock) and an ADF4350 PLL synthesizer board (for sidebands). These signals are separately amplified and combined with a power combiner.

The camera is now triggered by a TTL-signal from the experimental control system. The delay between the trigger signal and the actual frequency shift of the position stabilization is now around 10 ms. The remaining timing jitter is now primarily determined by the difference in the runtime of the Python program for image evaluation and calculation of the desired frequency, and is on the order of 1 ms.

4.3.4.2 Fiber Electro-Optical Modulator

Another drawback of the previous stabilization system was the use of the double-pass AOM optical path. First, the optical power from the monitor output of the fiber amplifier was significantly reduced due to inefficient deflection. Additionally, the deflection efficiency varies with the RF frequency, leading to power fluctuations. As a result, the power before the cavity was only on the order of 50 µW, which is barely sufficient for effective lock performance. Another issue is that the free-spectral range of the cavity used is 1.42 GHz, while the typical RF tuning range of an AOM is around 100 Mhz. This discrepancy necessitates frequent modifications of the setup, such as using different AOMs or changing the deflection order to achieve the correct absolute frequency due to the described constant drift of the cavity frequency. Lastly, the used free-space electro-optical modulator (EOM) introduces amplitude modulation, causing a DC offset in the error signal, which shifts the lock point. The new setup is illustrated in Figure 4.13.

The monitor output of the 1112 nm fiber amplifier is now routed through a 50:50 fiber splitter. One half is directed to a beatnote lock box for frequency stabilization of the photoassociation laser (see Section Section 4.5), while the other half is sent to the stabilization setup for the MOT laser. Since the amplifier is not polarization-maintaining, the polarization not well-defined. To address this, a 3-paddle fiber polarization controller is connected to the fiber. This controller leverages stress-induced birefringence by wrapping the fiber around three spools, effectively functioning as three independent fractional waveplates to adjust the polarization for subsequent use.

The monitor output from the 1112 nm fiber amplifier is fed into a fiber-based EOM (*JENOPTIK PM1170*) with a rise time (10/90) of 0.2 ns, corresponding to a −3 dB bandwidth of around 1.75 GHz, and insertion loss of 4.3 dB. This high bandwidth, which exceeds the FSR of the cavity, allows the system to utilize a sideband locking technique.

4.3.4.3 Radio Frequency Generation

The Pound-Drever-Hall frequency ω_{PDH} is generated from a *JOY-IT JT-PSG9080* dual-channel programmable function generator with a tuning range of 0.1–80 MHz and adjustable phase relationship. The optimum frequency of ω_{PDH} was empirically found to be 30.85 MHz and the RF power is set to +16 dBm.

The tuning frequency ω_{tune} is generated via an *ADF4350* frequency synthesizer mounted on an *EVAL-ADF4350EB2Z* evaluation board from *Analog Devices*. The ADF4350 chip is a fractional-N and integer-N phase-locked loop (PLL) synthesizer covering an output frequency range of 137.5-4400 MHz and maximum RF output power of +5 dBm, which is amplified by a *Mini Circuits ZX60-V83MP-S+* wide band amplifier to +27 dBm. The evaluation board is connected to the Raspberry Pi via the *Serial Peripheral Interface (SPI)*, which can then set the desired frequency for the sideband lock.

Subsequently, both RF signals are combined using a *Mini Circuits ZFSC-2-372-S+* power combiner and fed into the EOM for light modulation.

4.3.4.4 Sideband Pound-Drever-Hall Locking

Unlike standard Pound-Drever-Hall locking [117], where the laser frequency is locked directly to a cavity mode, sideband locking provides the flexibility to stabilize the laser at an

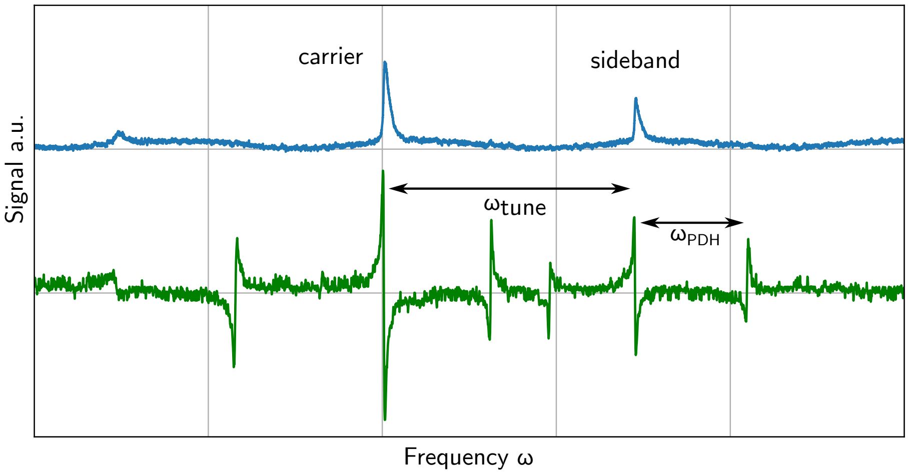

Figure 4.14.: Signal of sideband locking: The blue data represent the transmission through the cavity as the laser frequency is scanned, measured with a photodiode. The transmission signal is primarily used to monitor the cavity's coupling efficiency. The peak asymmetry arises from the slow response of the photodiode. The carrier signal indicates the laser frequency, while the sideband is generated by modulation of the EOM with a frequency of ω_{tune}. The green data show the dispersive Pound-Drever-Hall signal measured by the photodiode, which monitors the cavity's reflection. In addition to the dispersive signals at the carrier and the sideband, additional dispersive signals are observed, which are separated from the sideband by ω_{PDH}.

arbitrary frequency offset relative to the cavity mode. This is achieved by driving the fiber EOM with an RF frequency ω_{tune}, generating sidebands at $\omega_{Laser} \pm \omega_{tune}$. A secondary RF frequency $\omega_{PDH} << \omega_{tune}$ is then applied to modulate these sidebands for PDH-locking. The cavity transmission signal and the PDH sideband signal are illustrated in Figure 4.14.

This sideband locking approach allows the laser to be locked to any desired frequency within the range defined by ω_{tune}. However, challenges can arise if the targeted frequency falls near a higher-order transverse cavity mode, as overlapping signals from multiple sidebands can interfere with the locking process. This issue is mitigated by locking to a sideband associated with a neighboring longitudinal cavity mode $(n \pm 1)$ and changing the sign of ω_{tune}.

The light reflected from the cavity is focused onto a photodiode and subsequently amplified. The resulting signal is mixed with the (phase shifted) PDH modulation frequency ω_{PDH} to produce the error signal for a PI controller, which regulates the laser's piezo for frequency stabilization.

This upgraded setup enables coverage of an entire FSR of the cavity, allowing any desired wavelength within this range to be accessed. Additionally, the fiber pigtail monitor output connects seamlessly to the fiber pigtailed EOM, providing a robust and stable system with minimal susceptibility to alignment disturbances.

Using the improved setup described above, the optical power available before the cavity has been increased by a factor of 10, now exceeding 500 µW. This improvement enhances the locking system's signal-to-noise ratio and therefore ensures a more reliable and precise stabilization.

4.3.4.5 Improved Temperature Stabilization of the Reference Cavity

Although the active position stabilization ensures a stable frequency for further experiments, its relatively poor passive stability poses challenges if the stabilization cannot be used for certain reasons. The active position control is only effective if all preceding steps – such as MOT loading, Zeeman slowing, compression and cooling – are functioning properly. This creates a problem if adjustments to these initial steps are needed, as the unstabilized MOT laser frequency drifts rapidly.

If the MOT laser frequency is actively stabilized during these adjustments, changes in parameters like the magnetic field gradient cause a vertical shift of the magnetic field zero. Since the lock system stabilizes the position, it counteracts these shifts, making it nearly impossible to fine-tune the earlier stages of the Yb MOT for optimal performance.

To address this issue, we designed a new setup aimed at improving the temperature stabilization of the Zerodur cavity, with precision comparable to the aging process of the Zerodur spacer, thus improving the passive frequency stability of the MOT laser. This new system is inspired by the work of [118] and has been adapted to our system, as depicted in Figure 4.15.

To ensure optimal temperature stability and minimize temperature gradients within the Zerodur spacer, the new cavity is housed within a copper cylinder, isolated from direct thermal contact with the copper by two *Viton* rings. Once the cavity is inserted, the cylinder is sealed with copper covers on both sides, allowing light to reach the cavity mirrors through small apertures. This setup thermally decouples the Zerodur from the copper shield. The cylinder is then mounted on a copper stamp, and the entire setup is placed inside a vacuum chamber maintained at a pressure of around 10^{-7} mbar.

Temperature stabilization of the entire copper system is achieved using a 10 kΩ negative temperature coefficient (NTC) thermistor, located at the bottom of the copper stamp, and a PI controller that regulates the temperature of a Peltier element placed below. To monitor the ambient temperature of the cavity, which is primarily determined by the copper shield's temperature, another NTC thermistor is installed inside of the vacuum chamber on the shield with an electrical feed-through.

Our laboratory experiences diurnal temperature fluctuations of approximately 1 K[3], which affect the temperature of the vacuum chamber and consequently the radiative cou-

---

[3] These fluctuations are strongly influenced by external temperatures, daily weather patterns, and seasonal variations.

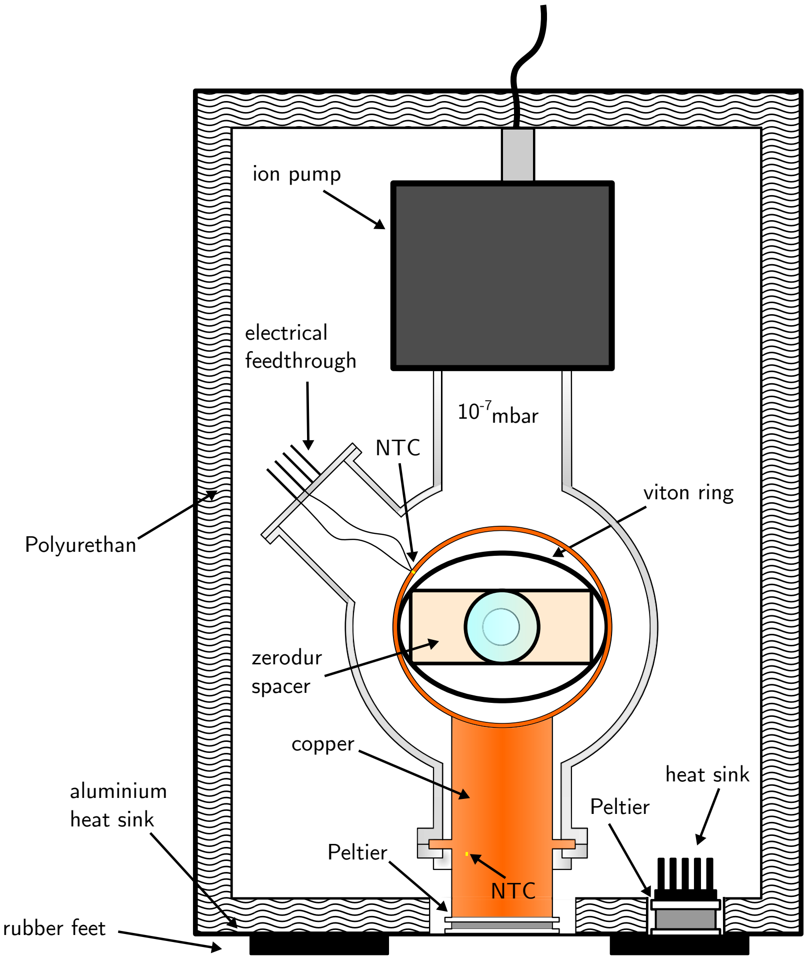

Figure 4.15.: Scheme of the new cavity system. The Zerodur spacer is placed inside a copper cylinder and thermally decoupled via Viton rings. The cylinder is covered by copper covers with small apertures. The cylinder is mounted on a copper stamp, which is temperature stabilized using a Peltier element. The entire system is placed inside a vacuum chamber with a pressure of around 10^{-7} mbar. The vacuum chamber is housed in a temperature stabilized aluminum box covered from the inside with polyurethane.

pling to the copper shield. Due to the relatively large distance between the NTC used for temperature regulation and the cavity itself, temperature gradients develop between the two points. As a result, the cavity experiences temperature variations despite the temperature of the NTC being held constant.

To mitigate this, the entire vacuum chamber is enclosed within an aluminum box, mounted on rubber feet. The aluminum structure also serves as a heat sink for the Peltier elements, while the inner walls of the box are lined with polyurethane to enhance thermal insulation and are held at 25 °C.

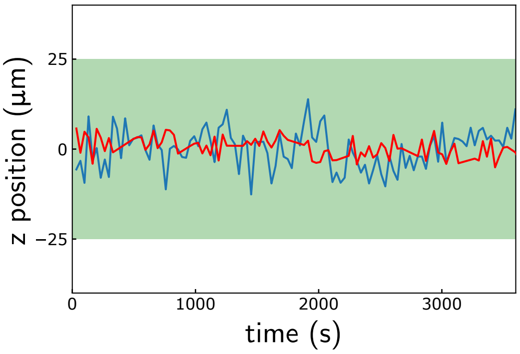

	unstabilized (red)	stabilized (blue)
slope	$(4.3 \pm 0.3)\ \frac{\mu\mathrm{m}}{\mathrm{h}}$	$(0.7 \pm 0.2)\ \frac{\mu\mathrm{m}}{\mathrm{h}}$
σ_{mean}	3.0 µm	5.4 µm
σ_{lin}	2.6 µm	5.4 µm

Figure 4.16.: Left: Vertical position stability for a stabilized (blue) and unstabilized (red) MOT with the 2^{nd} generation setup. Right: Slope of a linear fit to the data, standard deviation σ_{mean} and deviation from linear fit σ_{lin}.

The temperature of this box is monitored by a separate NTC located at the vacuum chamber, and its temperature is controlled via a PI controller that regulates a Peltier element with an attached heat sink serving as a radiator. A small fan ensures that the surrounding air is evenly distributed, preventing the formation of temperature gradients.

The temperature stability inside the box is now ±50 mK, which is an improvement by an order of magnitude compared to the average diurnal temperature variation in our laboratory. The temperature of the copper shield is 24.4 °C and remains stable within ±1.5 mK[4], and we expect the decoupled cavity's temperature to be even more stable, as fluctuations faster than the thermal coupling time constant of ∼ 3.65 h are effectively averaged out.

4.3.4.6 Performance of the 2^{nd} Generation Yb MOT Laser Stabilization

Figure 4.16 illustrates the stability of the vertical Yb MOT position over a period of 1 h, measured with the new setup. The red curve represents the vertical position of an unstabilized MOT, while the blue curve corresponds to an actively stabilized MOT (see Section 4.3.3). The green shaded region, indicating sufficient loading efficiency into the ODT, remains at 50 µm, as in Figure 4.12. The results, summarized on the right in Figure 4.16, clearly demonstrate a significant improvement over the previous setup, particularly for the unstabilized MOT position.

A linear fit to the data reveals a drift of $(4.3 \pm 0.3)\ \frac{\mu\mathrm{m}}{\mathrm{h}}$, marking a reduction by a factor of ∼ 100. This enhanced passive stability allows for experimental operation and MOT adjustments without requiring the active stabilization – something that was previously impossible. Furthermore, the standard deviation $\sigma_{\mathrm{mean}} = 3.0\ \mu\mathrm{m}$ and the deviation from the linear fit $\sigma_{\mathrm{lin}} = 2.6\ \mu\mathrm{m}$ are more than halved compared to the previously stabilized measurement of $\sigma_{\mathrm{old}} = 7\ \mu\mathrm{m}$. This improvement stems from the absence of the active position

---

[4] The temperature is measured with the upper NTC in Figure 4.15.

stabilization, where another camera is used for stabilization as for the data acquisition. Occasional overshooting of the stabilization mechanism contributed to the larger standard deviation observed in the 1^{st} generation system.

The MOT position is determined via a fit to the atomic cloud using absorption imaging, with the effective pixel size of the camera being 20.1 µm. Given this limitation, a standard deviation of 3 µm approaches the measurement resolution limit. It is worth noting that the unstabilized MOT position measurements were taken on a relatively calm day, without significant temperature fluctuations. Under different conditions, the drift could be slightly larger, potentially requiring slow active stabilization or manual frequency adjustments throughout the day.

The new active position stabilization system, featuring a hardware-triggered camera, also exhibits slight improvements over the previous one. The standard deviation is reduced to 5.4 µm and outliers caused by overcompensation are effectively eliminated. Since the measurements approach the resolution limit, the slightly higher standard deviation in the active stabilization case likely arises from discrepancies in position determination between the two cameras. Even small variations in the center of gravity calculation can induce laser frequency shifts during a crucial stage of MOT preparation, despite the frequency being more stable during an experimental sequence.

Assuming short-term laser frequency fluctuations are smaller than position determination uncertainties, this issue could be mitigated by calculating the desired frequency and applying adjustments only in subsequent experimental runs.

The newly developed stabilization system ensures reliable MOT performance, even during early-stage adjustments. Additionally, the implementation of a broadband fiber EOM reduces maintenance requirements, as it covers an entire free spectral range of the stabilization cavity.

4.3.5 Yb MOT Setup

The Yb MOT setup on the science table is depicted in Figure 4.17. The slowing light (blue) enters through the slower viewport and is focused on the oven's aperture. To prevent Yb deposition, the viewport is heated to 230 °C, and a compensation coil is located in front. The polarization of the slower beam is adjusted via a $\lambda/4$ waveplate placed before the chamber.

The MOT light (green) is collimated using achromatic doublets, and its polarization is cleaned with a PBS. A logarithmic photodiode monitors the transmission through the first mirror, enabling active intensity stabilization of the MOT beams. The beams are split into three parts and distributed orthogonally within the vacuum chamber. Circular polarization is achieved using $\lambda/4$ waveplates positioned before each viewport.

Due to the relatively low optical density of the Yb MOT, the beams are retro-reflected by mirrors placed behind the chamber, with orthogonal polarization ensured by a $\lambda/4$

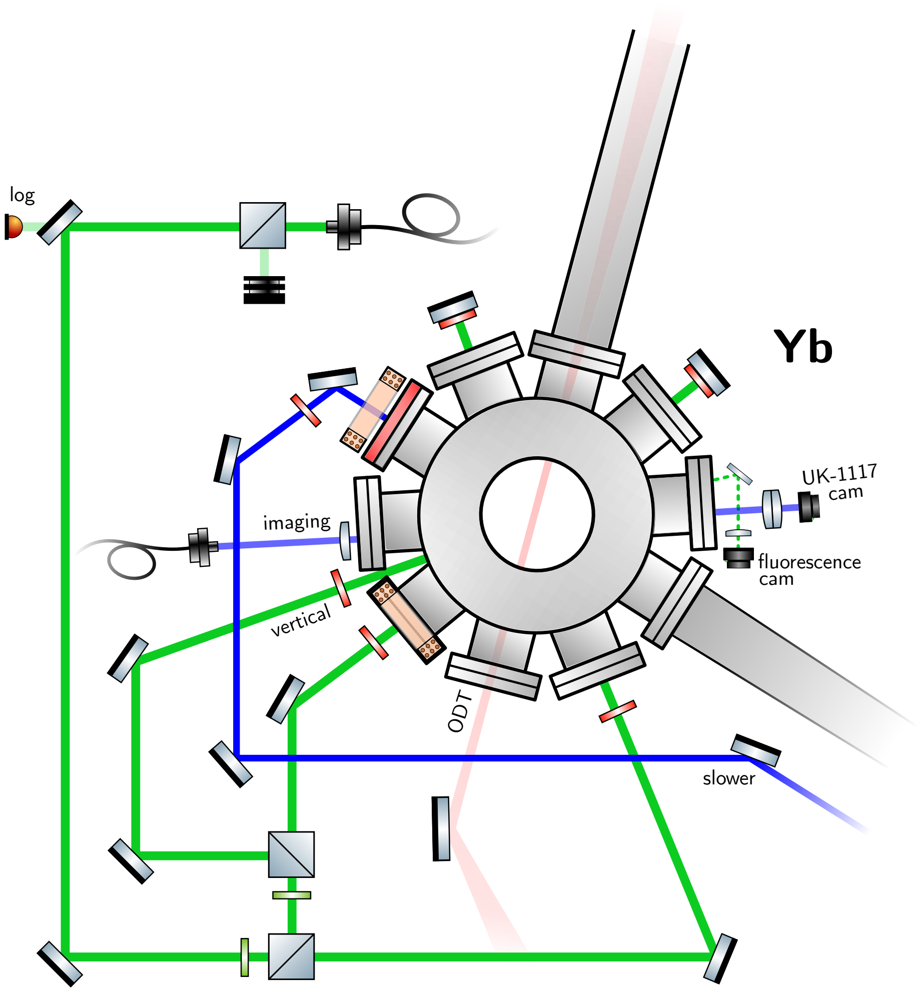

Figure 4.17.: Scheme of the Yb MOT setup at the science table. The MOT beams (green) are split by a polarization beam splitter and retro-reflected behind the chamber. Slower beam and imaging light are indicated in blue. The ODT beam (red) has a focus in the center of the vacuum chamber. Two coils for magnetic field manipulation are positioned at the viewports.

waveplate.

Both the imaging light and green fluorescence exit the chamber through the same viewport and are captured by a *UK-1117* camera and the *Raspberry Pi camera v2* (see Section 4.3.3) (or the later *GetCamera MER2-503-36U3M*, see Section 4.3.4.1).

4.3.6 Optical Tweezer for Ytterbium

The optical dipole trap setup for Yb, illustrated in Figure 4.17, is similar to the one for Rb, but with a few modifications. The trapping light is produced by a self-built high-power fiber amplifier, delivering up to 30 W at 1064 nm. This amplifier, constructed by Bastian, is thoroughly detailed in his thesis [2]. It is seeded with the same spectrally multi-mode *IPG PYL-20M-LP* laser employed in the Rb ODT system.

As in the Rb setup, the amplifier output is collimated, expanded and subsequently focused using a lens mounted on an identical translation stage (*Aerotech ABL1500*). For Yb, a lens with a focal length of $f = 1000\,\mathrm{mm}$ is used, compensating for the increased distance between the lens and the center of the vacuum chamber compared to the Rb system. The resulting focus has a $1/e$ diameter of $(41 \pm 3)\,\mu\mathrm{m}$[5].

Fast switching and intensity stabilization of the ODT are achieved using an AOM (*Gooch & Housego 3080-198*) operating at a center frequency of 80 MHz. Unlike in the Rb system, the AOM's driving frequency can also be dynamically shifted and modulated. This frequency is generated via a voltage-controlled oscillator (VCO) and amplified using a self-built RF amplifier. Adjusting the VCO's DC voltage alters the driving frequency, thereby modifying the deflection angle of the first-order diffracted beam[6]. This allows the horizontal position of the ODT to be shifted by several hundred micrometers within the vacuum chamber.

In addition to the DC offset, the RF frequency applied to the AOM can be modulated, which alters the beam profile and, consequently, the trap geometry. When the frequency modulation exceeds the trap frequencies, the atoms experience a time-averaged potential. For beam shape modulation, we apply the function described in [119], specifically designed to generate a harmonic potential[7]. The modulation waveform, produced by an arbitrary waveform generator, controls the VCO's input voltage. Both the modulation waveform and the corresponding beam shape are illustrated in Figure 4.18[8].

4.3.7 New Optical Tweezer for Ytterbium

Unfortunately, we observed a decline in the loading efficiency from the MOT to the optical dipole trap, likely due to a defective outcoupling isolator. This resulted in an increased beam waist ($1/e$ diameter) of up to $\sim 200\,\mu\mathrm{m}$. A magnification of a factor of five in beam diameter leads to a reduction of a factor of 25 in potential depth, which was no longer deep enough for efficient trapping of Yb atoms.

To address this issue, we constructed a new fiber amplifier capable of delivering up to 50 W of optical output power without an outcoupling isolator. This amplifier closely resembles the previous 30 W design [2] and will be described in detail in the thesis of the new Ph.D. student Arne Kallweit.

---

[5] Note that the beam shape illustrated in Figure 4.18 is measured with the new Yb ODT beam.

[6] This adjustment is possible because the beam is collimated rather than focused within the AOM crystal. Focusing the beam in the AOM would project the focus directly onto the atom's position.

[7] This holds if the beam waist is significantly smaller than the modulation depth. In practice, the potential results from a convolution of the harmonic modulation with the Gaussian beam profile.

[8] Note that the beam profiles in c) and d) are measured with the new Yb ODT.

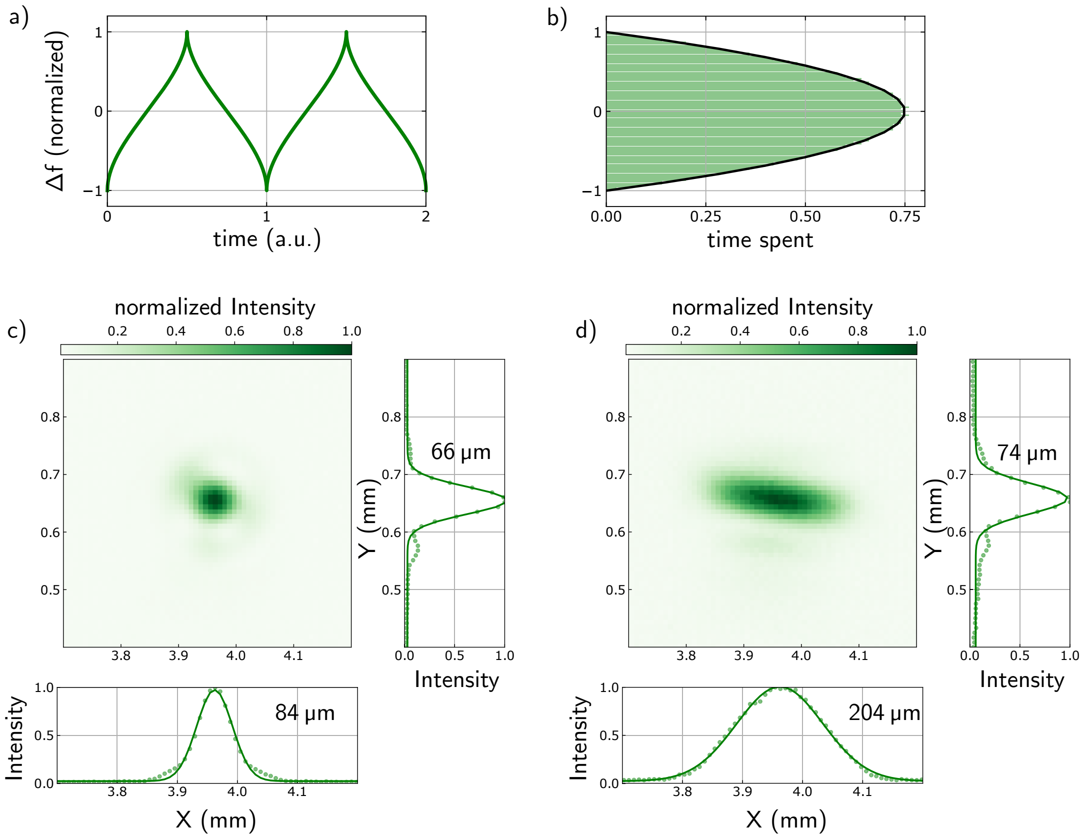

Figure 4.18.: Scheme of the beam shape modulation of the Yb ODT laser beam. a) shows the 'onion'-shaped modulation of the AOM frequency. b) shows a histogram of Δf from a), representing the time-averaged beam shape for an ideal point-like beam. c) shows the measured beam profile of the new ODT beam without (left) and with (right) modulation, along with the corresponding $1/e$ diameters.

The beam is outcoupled using a *Castech HPCOL-N-50-0-1064-C-6-A49* expanded beam collimator, producing a beam diameter of (6 ± 0.5) mm, which is subsequently reduced to 2 mm. The remaining optical path remains unchanged from the previous ODT configuration.

With this new amplifier and collimator, the beam waist ($1/e$ diameter) at the focus is now $\sim 70\,\mu$m, providing a sufficiently deep potential well of around $300\,\mu$K for efficient trapping and transport of Yb atoms.

4.4 Lattice Laser System

In this chapter, I will provide a brief overview of the lattice laser setup for the optical lattice, which can be used to create 1, 2, and 3-dimensional lattice configurations. The lattice consists of three orthogonal beams originating from the same laser source. These beams are retro-reflected behind the chamber, creating a standing-wave interference pattern that serves as the optical lattice.

The lattice light is generated by an *Innolight Mephisto* Nd:Yag non-planar ring oscillator (NPRO) laser and subsequently amplified using a self-built fiber amplifier. As with the ODTs, the operating wavelength is 1064 nm. To establish a stable optical lattice with a standing-wave interference pattern with retro-reflected laser beams, the laser's coherence length must be significantly larger than the optical path length. With a spectral linewidth of less than 3 kHz, the seed laser achieves a coherence length of over 30 km, which is well above the required threshold.

The seed laser is amplified in a self-built fiber amplifier, developed in the scope of [120]. While the principle is the same as for the ODT amplifiers, for small-linewidth lasers special attention must be paid to stimulated Brillouin scattering (SBS) [121], which limits the output power in our case to 6 W. Further amplification could be achieved using a double-stage amplifier.

Since an optical lattice relies on precisely aligned retro-reflected beams, optical feedback into the amplifier poses a potential issue. To address this, the output passes through a double-stage isolation before being coupled out onto an optical table for further manipulation.

The light is then split into three separate paths using PBS cubes and each beam is controlled by an AOM for intensity stabilization and switching. The VCO driving frequencies are set to distinct values with a minimal separation of 2 MHz. This frequency separation ensures that any interference effects between the beams are time-averaged over timescales much faster than the trap frequencies.

The beams are then coupled into single-mode fibers and routed to the science chamber. There, the beams are focused to $\sim 100\,\mu\mathrm{m}$ and retro-reflected using cat-eye setups, which offers greater stability against alignment shifts. The transmission through these retro-reflectors is monitored via photodiodes, providing feedback for active intensity stabilization. Depending on how many standing waves are operated simultaneously 1- to 3-dimensional optical lattices can be produced in the experiment.

4.5 Photoassociation Laser System

For the investigation of (weakly) bound molecular states (see Section 2.4), a photoassociation laser system with precise frequency stability is needed. This laser setup is illustrated in Figure 4.20. Since we perform photoassociation near the $^3\mathrm{P}_1 + {}^2\mathrm{S}_{1/2}$ asymptote of RbYb*, the Yb MOT laser serves as perfect reference for stabilization of the PA laser. This chapter will describe the laser system as well as the frequency stabilization for both the first photon and the second photon and is also explained in [1] and [2]. A schematic overview of the relevant PA and MOT laser frequencies is shown in Figure 4.19. The MOT

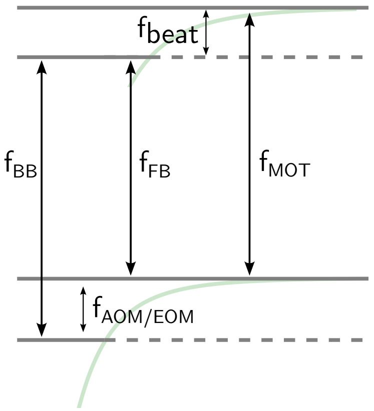

Figure 4.19.: Scheme of the photoassociation and MOT laser frequencies with their relative detunings.

laser frequency f_{MOT} serves as a stable reference for a beatnote lock of the free-bound laser (see Section 4.5.2), which is always red-detuned relative to the MOT frequency. The bound-bound laser frequency f_{BB} is derived via an AOM or EOM operating at $f_{AOM/EOM}$ (see Section 4.5.3) and can be tuned either red- or blue-detuned with respect to the MOT frequency, depending on the targeted molecular bound state.

4.5.1 Free-Bound Laser

The light required for 1-photon PA at the intercombination line is generated by a commercial frequency-doubled fiber laser/amplifier system from *Menlo*, as described in [122], and was implemented into the experiment as part of [123]. The setup consists of a seed fiber laser module (*NKT Koheras BASIK*), which is amplified in a fiber amplifier[1] and subsequently frequency-doubled using an *NTT* PPLN waveguide module, similar to the one used for the MOT laser. At the time of delivery, the system provided up to 16 mW of output power at 556 nm, but over time, a gradual decline in power was observed. Eventually, the output dropped below 1 mW, necessitating modifications to the laser system:

- Replacement of the defective pump diode in the seed module with a PM fiber coupled distributed Bragg reflection (DBR) pump diode at 976 nm (*Telebrook 3SP 3CN01794DA*).
- Repair of faulty temperature control of the heated active fiber in the amplifier.
- Repair of the temperature control for the PPLN waveguide module.
- Realignment of graded-index (GRIN) lenses for in- and out coupling to PPLN waveguide.

---

[1] The amplifier operates with a heated active fiber, similar to our MOT laser [110].

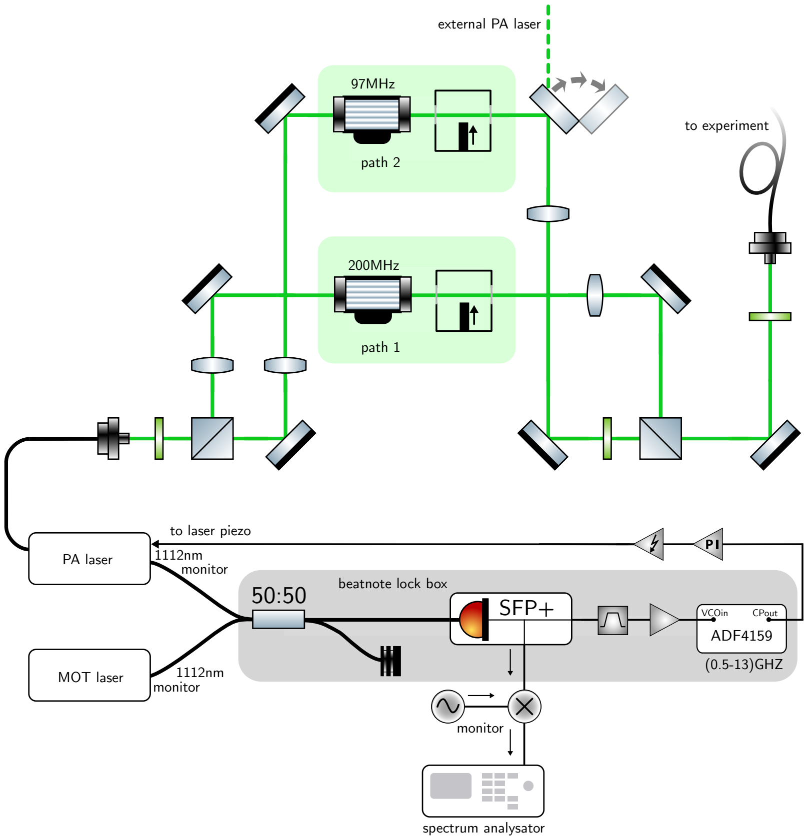

Figure 4.20.: Scheme of the photoassociation laser system. The upper part shows the 556 nm optical path for the first and the second photon, respectively. The lower part shows the frequency stabilization of the fundamental monitor output via a beatnote lock.

After these modifications, the laser system now delivers an output power of $\sim 10\,\mathrm{mW}$.

The 556 nm light is coupled out via a single-mode PM fiber onto an optical breadboard (upper part of Figure 4.20), while a portion of the fundamental light is extracted as a monitor signal for frequency stabilization (lower part of Figure 4.20). For intensity control, frequency shifting, and shuttering, the beam is sent through an AOM and a mechanical shutter before being coupled into an optical fiber for delivery to the science chamber.

4.5.2 Frequency Stabilization

A detailed explanation of frequency stabilization via beatnote locks can be found in [1]. Since the detuning of the two least bound states in the excited $^3\mathrm{P}_1 + {}^2\mathrm{S}_{1/2}$ potential of RbYb* from the intercombination transition of Yb is expected to be smaller than 10 GHz, the PA laser can be frequency stabilized via the beatnote-lock technique, similar to the Rb repumper lasers (see Section 4.2.2). The lock setup is illustrated in the lower part of Figure 4.20.

The monitor outputs of both the MOT laser and the PA laser are combined via a 50:50 fused fiber coupler and then sent to a *small formfactor pluggable SFP+ Finisar FTLF1429P3BCE* photodiode module with a bandwidth of $> 12\,\mathrm{GHz}$. This module includes a limiting amplifier, which provides a stable output signal at $-6\,\mathrm{dBm}$. The beatnote signal is then passed through a bandpass filter[2] and subsequently amplified. The amplified signal is then fed into the VCOin port of an *ADF4159* PPL board, which operates within a frequency range of 0.5–13 GHz. This PLL board generates an error signal proportional to the frequency difference between the beatnote signal and the set frequency. A typical PI controller processes this error signal and adjusts the laser piezo for frequency stabilization.

With these components, we can stabilize the PA laser at frequency offsets of $\sim 13\,\mathrm{GHz}$ with respect to the MOT frequency. Since the fundamental laser output at 1112 nm is used for the lock, the effective PA frequency range is doubled. The locking range can be further improved using high-end photo detectors and PLL boards, extending up to $\sim 30\,\mathrm{GHz}$ or by implementing a frequency comb, which allows for arbitrary frequency offsets.

For beam adjustments and calibration purposes, it is useful to be able to achieve zero PA detuning relative to the MOT beam. This is realized using appropriate AOMs before the frequency lock.

4.5.3 Bound-Bound Laser

While the first photon bridges the unknown frequency gap from the unbound scattering state to the electronically excited state of the RbYb* molecule, the second photon probes the ground-state potential and has to be blue-shifted with respect to the free-bound photon. Since the binding energies of the least bound states of the ground-state potential have been measured in previous works [50, 124] (see Chapter 3), the search range for these states is significantly reduced. Depending on the required detuning, various methods for light generation can be employed, each precisely tailored to the specific detuning's needs, as described in this chapter.

For coherent two-photon processes such as STIRAP and dark resonance spectroscopy, minimizing the relative linewidth of both laser sources is crucial. For small detunings, this can be achieved by frequency shifting or modulating the PA laser with AOMs or EOMs. For detunings exceeding the GHz range, a second laser – ideally phase-locked to the free-bound laser – must be used.

4.5.3.1 AOM for $\Delta v = -1$

The least bound state has a binding energy of $E_B = -h \cdot 102\,\mathrm{MHz}$, making it an ideal frequency gap for the use of AOMs. The optical setup for this purpose is illustrated in

---

[2] The used filters have a bandwidth of $\sim 1\,\mathrm{GHz}$ and are exchanged depending on the desired frequency range.

Figure 4.20. A portion of the PA laser beam is split via a PBS, sent through an AOM, and then recombined with the main beam using a second PBS[3].

The frequency shifts of the two AOMs are chosen such that $\Delta f_{path1} - \Delta f_{path2} = E_B/h$, i.e. that path 1 drives the bound-bound transition while path 2 addresses the free-bound transition. Since both paths originate from the same laser, the relative linewidth is determined solely by the RF sources, allowing for exceptionally narrow linewidths.

Moreover, using two AOMs enables independent intensity control for each path, which is particularly relevant for future experiments using STIRAP.

4.5.3.2 EOM for $\Delta v = -2$

Since the frequency gap achievable with AOMs is limited to a few hundred MHz, addressing the second least bound state at $E_B = -h \cdot 1018\,\mathrm{MHz}$ requires an alternative approach. A relatively simple and cost-effective solution is the use of an EOM to generate sidebands at $\Delta f_{EOM} = E_B/h$. This method offers the advantage of reducing the relative linewidth, as it depends only on a single RF source. However, a major drawback is the inability to independently control the intensities of the sidebands and the carriers. As a result, this technique is suitable for photoassociation spectroscopy but not for STIRAP. Additionally, besides the desired first-order sideband, higher-order sidebands are inevitably produced, reducing the usable power in the first order and potentially interfering with other atomic or molecular transitions.

For this reason, instead of using an expensive fiber-coupled EOM with GHz-range modulation bandwidths, we designed a free-space phase modulator setup. To achieve the required efficiency for the first-order sideband, a voltage of $100\,\mathrm{V}$ (corresponding to $200\,\mathrm{W}$ at $50\,\Omega$) would be needed, which is impractical for GHz-range frequencies. To overcome this limitation, our setup is based on a split-ring resonator [125]. A hollow conductive cylinder (made of copper foil) is split, and the EOM crystal is inserted into the resulting gap. The cylinder acts as an inductance, while the crystal-filled gap forms a capacitance, together creating a resonant circuit. The resonance frequency depends on the cylinder's radius and can be fine-tuned via inserting magnetic or dielectric materials. The RF signal is coupled via a single-loop antenna.

With this setup and a driving power of $1\,\mathrm{W}$, we achieve $\sim 20\,\%$ of the optical power in the first-order sidebands at $1018\,\mathrm{MHz}$, with a tuning range of $\sim 60\,\mathrm{MHz}$. Tobias gives a detailed explanation of this setup in his thesis [1].

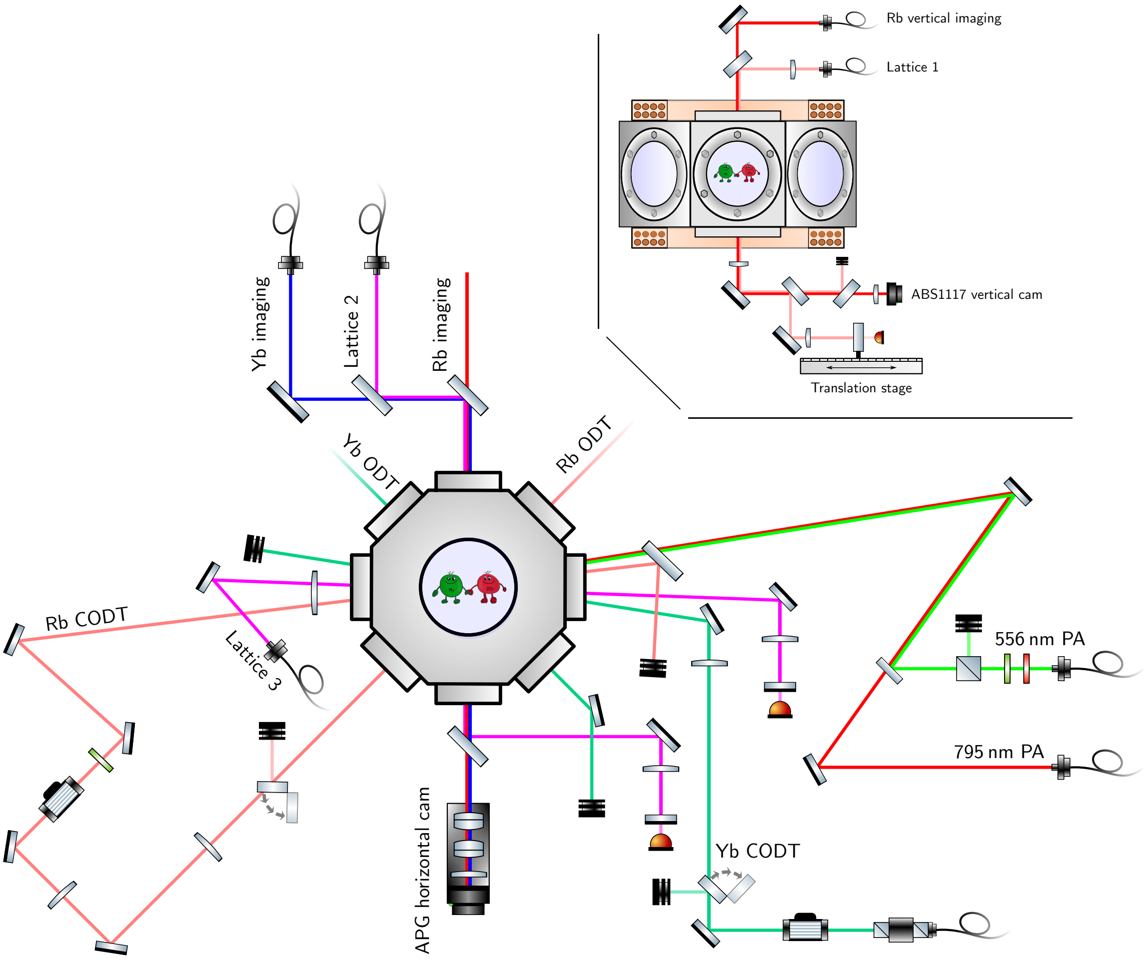

Figure 4.21.: Scheme of the science chamber and the surrounding optical paths. Bottom: Top view of the chamber including horizontal imaging, crossed optical dipole traps, horizontal lattice beams and PA beams. Top right: Side view of the chamber including vertical imaging for Rb and the vertical lattice beam with its translation stage.

4.6 The Science Chamber

The heart of the experiment, where all previously explained setups join together and the physics is done, is the science chamber, which is illustrated, including all optical paths, in Figure 4.21. Since the setup is extensively explained in [1] and [2], I will only give a brief overview of the experimental setup.

---

[3] Note that the laser polarizations become orthogonal after recombination. If the same polarization is required, the transmission through a PBS at the science chamber can be used, though at the cost of usable intensity.

4.6.1 Crossed Optical Dipole Traps

To achieve high phase-space density (PSD) and efficient evaporative cooling of both Rb and Yb samples, two crossed optical dipole traps (CODT) are utilized. A CODT (see Section 2.3.5.2) consists of the ODT beam, which transports the atoms to the science chamber, and an intersecting beam. To avoid interference and overlap between the beams corresponding to the different atomic species, the CODTs for Rb and Yb are positioned in horizontal planes with a vertical displacement.

4.6.1.1 Rb CODT

The Rb CODT is created by folding the ODT beam behind the chamber and directing it through another viewport. During the loading and transport of Rb with the ODT, the beam is blocked using a flip mirror mounted on a servo, preventing unwanted interference during transport. The beam is then directed through an AOM for intensity control and, as in the Yb ODT setup, to shift the horizontal position of the crossing. Interference between the two beams is avoided by rotating the polarization by 90 ° with a $\lambda/2$ waveplate and selecting the appropriate AOM driving frequency[1]. Finally, the beam (40 % of the ODT's power) is focused to $\sim 100\,\mu\mathrm{m}$ at the center of the science chamber.

4.6.1.2 Yb CODT

Unlike the Rb setup, the Yb CODT is formed from the ODT and a second independent laser source. This laser is a self-built fiber laser/amplifier system that generates up to 30 W non-polarized light at 1064 nm, as described in detail in [2]. The use of an independent laser source allows for higher power in the crossing beam, independent intensity control and eliminates interference effects due to the lack of coherence between both lasers.

As with the Rb CODT, an AOM is employed for intensity control and horizontal shifting of the crossing. The beam is then focused to 100 µm and directed to the center of the science chamber.

Unfortunately, the power of the amplifier dropped to 10 W, which is still enough for the merging sequence, but prevents a stable production of an Yb Bose-Einstein condensate (see Section 4.9.2). We assume a defective output isolator or an aged splice within the amplifier.

4.6.2 Optical Lattice and Lattice Elevator

To enhance photoassociation efficiency, an optical lattice plays a crucial role in later stages of the experiment. The light generation for the optical lattice is explained in Section 4.4

---

[1] The modes of the seed laser are separated by 4 MHz, and interference between closely spaced modes can reduce the lifetime of the CODT.

and was developed and integrated into the experiment as part of the works of [120, 127] and is thus only briefly described here.

The orthogonal lattice beams are focused to waists of 100 µm, re-collimated and retro-reflected behind the chamber. The reflected beam is then refocused to 100 µm.

Given that both CODTs have a vertical offset, it becomes necessary to bring them into the same vertical plane at later stages of the experiment. This is achieved by using the vertical lattice arm (lattice 1) as an elevator. For this purpose, the retro-reflecting mirror is mounted on a DC-driven servo translation stage (*Thorlabs DDSM100*), capable of a translation distance of up to 100 mm. As the retro-reflector is translated, the optical standing wave is also moved, resulting in a translation of the lattice sites. Since the confinement is much stronger in the axial direction compared to a single-beam ODT, it is possible to elevate the Rb atoms by several millimeters in the vertical direction.

4.6.3 Photoassociation Lasers

Since photoassociation is possible near the D1 line of Rb (at 795 nm) and near the intercombination line of Yb (at 556 nm), both paths are integrated into the setup. They originate from independent single-mode fibers, with their polarizations cleaned using waveplates and PBS. Using additional retardation plates, the polarization of the PA lasers can be adjusted to address polarization-sensitive transitions. Both lasers are then overlapped and focused onto the center of the science chamber. The resulting beam waists ($1/e$ diameter) are 0.16 mm (556 nm) and 0.99 mm (795 nm).

4.7 Imaging of Ultracold Atoms

Almost all of our data consist of images of atomic samples taken via absorption imaging, from which relevant information is extracted using nonlinear fitting.

Absorption imaging is a straightforward yet destructive method for visualizing atomic samples. The atoms are illuminated by a resonant beam (tuned to the cycling transition) with a large beam diameter, and the remaining light is captured by a camera equipped with an imaging system. To determine the column density of an atomic cloud, three images are recorded: an absorption image (I_{abs}) with both atoms and light present, a bright image (I_{bright}) with only the imaging light, and a dark image (I_{dark}) with neither light nor atoms. The dark image is subtracted from the other two to correct for residual light and the camera's dark current. Using these processed images and the absorption cross-section $\sigma_{abs} = 3\lambda^2/(2\pi)$, the pixel-wise column density along the imaging axis (z) is calculated as follows:

$$n(x,y) = \int n(x,y,z)\mathrm{d}z = -\frac{1}{\sigma_{abs}} \ln \frac{I_{abs} - I_{dark}}{I_{bright} - I_{dark}}. \tag{4.5}$$

Images are typically taken after a time-of-flight (TOF) expansion of typically 0.1–20 ms, during which all trapping and cooling lasers are switched off, allowing the atomic sample to expand freely.

The atom number, particularly crucial for trap-loss spectroscopy, is determined by integrating $n(x, y)$. To further analyze the atomic sample, density profiles are fitted to the measured distributions. For a thermal cloud, this profile follows a 2D Gaussian distribution, while for a degenerate quantum gas, a bimodal combination consisting of a thermal and a Thomas-Fermi distribution is used [128]. These fits provide information about the sample's spatial width, and together with the temperature, which can be determined via a series of images with different TOFs (TOF series) or the knowledge of the trap frequency, we now have the necessary information of our atomic samples for optimization and data acquisition.

4.7.1 Imaging System

The imaging system at the science chamber, depicted in Figure 4.21, consists of two cameras. The horizontal plane is imaged by a cooled CCD camera (*Apogee Ascent A185*), which can capture images of both atomic species[1]. It features an effective pixel size of 7.2 µm and a chip size of 10 × 8 mm. To facilitate long TOF series, the longer axis is orientated vertically, with the zero TOF position of the atoms aligned near the top of the chip.

The imaging lens system is designed to minimize chromatic aberrations and is based on broadband-coated achromatic doublets. However, a slight focal shift between different wavelengths remains, which must be considered when aligning the CODTs to the same position.

The second camera, aligned along the vertical axis, is primarily used for imaging Rb but can also be utilized for Yb, especially for CODT alignment. This camera (*ABS UK-1117*) is a simpler CCD model with an effective pixel size of 8.3 µm and a chip size of 7.48 × 6.15 mm.

4.8 Experimental Control System

The experimental control system is based on *Cicero Word Generator* and *Atticus Server*, developed by [129], which manage multiple analog and digital (TTL) output channels provided by *National Instruments* IO boards. Additionally, various devices are controlled via GPIB, TCP/IP and USB interfaces. The computer architecture for the experimental control, the database and visualization is illustrated in Figure 4.22[1].

---

[1] To prevent unwanted non-resonant background light, the imaging light for the non-imaged species is blocked.

[1] Note that our computers are named after (semi-)successful German soccer clubs for historical reasons.

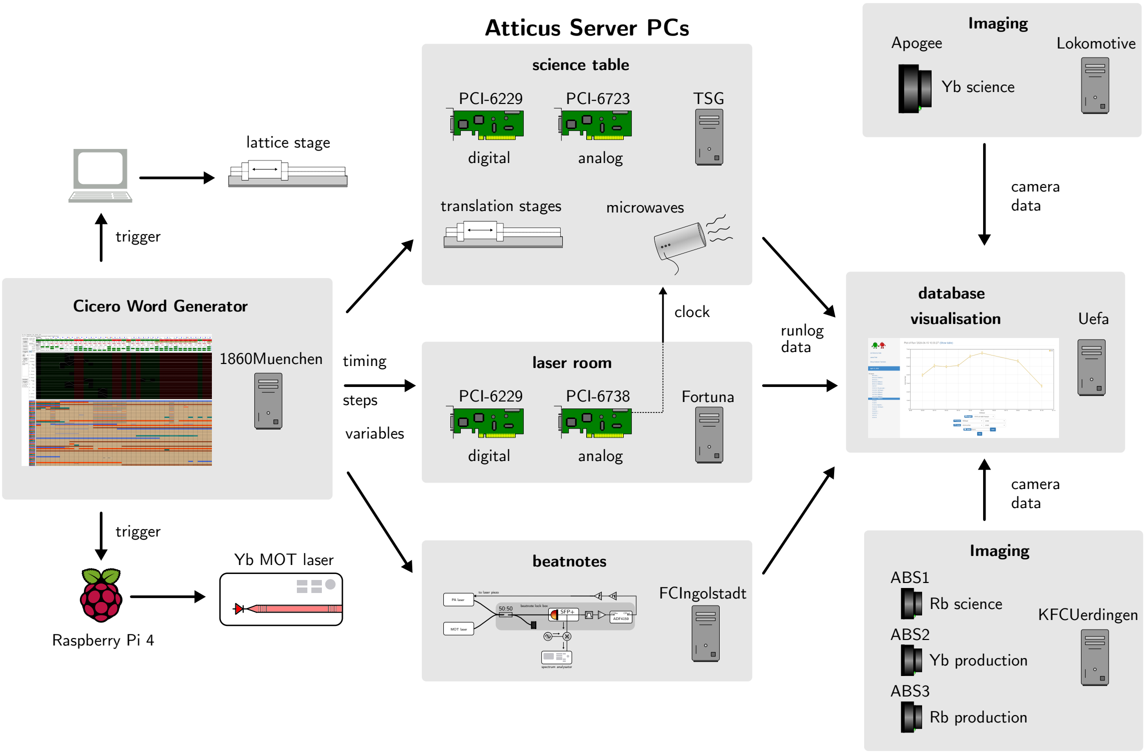

Figure 4.22.: Scheme of the experimental control. Computer for digital and analog signal generation, timing, data acquisition and visualization are shown.

Experimental sequences are created using the graphical user interface *Cicero*, running on *1860Muenchen*. Here, each output channel can be configured and experimental sequences with varying parameters can be generated.

The actual execution of output signals is handled by synchronized *Atticus* servers. The first computer, *Fortuna*, located in the laser room, is equipped with a digital *PCI-6229* and an analog *PCIe-6738* IO board, providing 32 digital and 32 analog output channels with a resolution of 16 bit (−10-10 V). The *PCIe-6738* board also supplies the experiment's sample clock, operating at a clock rate of 20 kHz.

The second computer, *TSG*, is situated at the science table and features a digital *PCI-6229* along with an older analog *PCI-6723* board. Although its analog resolution is only 13 bit, it remains sufficient for our purposes. *TSG* also controls the translation stages for optical transport and the Rb microwave systems.

FCIngolstadt manages the *ADF4159* boards, responsible for beatnote locking and frequency sweeping of the PA lasers.

The translation stage for the lattice elevator has its own hardware trigger and the Raspberry Pi for active position stabilization (see Section 4.3.3) is triggered in the old version only with software. Since the new camera is equipped with a hardware trigger, a digital TTL signal is used in the new experiments.

While the IO board outputs are hardware based and time synchronized, commands sent via GPIB, TCP/IP and USB rely on software, introducing timing inaccuracies. To mitigate this, digital triggers are used whenever possible.

As our data acquisition relies on absorption imaging of atomic clouds, dedicated imaging computers are required. *KFCUerdingen* handles both cameras for the production chambers and the vertical imaging in the science chamber, while *Lokomotive* is responsible for horizontal imaging in the science chamber. The use of two separate computers is solely due to practical reasons. The cameras are controlled by an ancient *LabView* program, which also handles data storage.

The collected image data are processed by the data server *Uefa*, which records the data alongside the Runlog in a database. A web interface provides real-time visualizations and basic fitting of these data.

4.9 Preparation of an Ultracold Atomic Mixture

This chapter describes the preparation of ultracold Rb and Yb samples, as well as their combination in a crossed optical dipole trap (CODT). It covers the simultaneous yet spatially separated preparation of ultracold Rb (see Section 4.9.1) and Yb (see Section 4.9.2), their transport into the science chamber, further evaporative cooling in crossed optical dipole traps and the final merging in a single CODT (see Section 4.9.3). Since these steps were optimized together with Tobias and Bastian and are described in detail in their theses [1, 2], I will only summarize the key aspects here.

4.9.1 Rubidium

The preparation of ultracold Rb samples follows standard procedures used in many experiments with ultracold alkali atoms. Hot Rb atoms emerging from the oven are slowed by a Zeeman slower and captured in a (dark spot) MOT. From there, they are transferred into a magnetic quadrupole trap before being loaded into an optical dipole trap and transported to the science chamber. Further evaporative cooling in a crossed optical dipole trap leads to the formation of a Bose-Einstein condensate (BEC).

4.9.1.1 Bright MOT

Zeeman-slowed ^{87}Rb atoms are cooled and trapped in a standard magneto-optical trap (MOT) operating at the D2 line at $780\,\mathrm{nm}$[1] using a detuning of $-3\,\Gamma$ and a magnetic field gradient of $15\,\mathrm{G/cm}$. Within a loading time of $8\,\mathrm{s}$, we achieve approximately $5 \cdot 10^9$ atoms at a temperature of $\sim 1\,\mathrm{mK}$.

---

[1] With a linewidth of $\gamma = 2\pi \cdot 5.7\,\mathrm{MHz}$ and Doppler temperature $T_D = 146\,\mu\mathrm{K}$.

4.9.1.2 Dark Spot MOT

To efficiently load atoms from the MOT into the quadrupole magnetic trap (MT), the density must be increased, and the spatial extent must be matched to the size of the MT. This is achieved by compressing the MOT by linearly increasing the magnetic field gradient to 44 G/cm in 30 ms. Simultaneously increasing the detuning to $-9\,\Gamma$ reduces the scattering rate and enhances cooling via Sisyphus sub-Doppler cooling [5].

During this compression, the repumper light in the MOT laser beams is switched off and the dark spot repumper is activated, creating a repumper-free region at the trap center. Within this dark region, Rb atoms enter the $|F = 1\rangle$ hyperfine state through off-resonant excitation, where they no longer interact with the MOT light operating on the $|F = 2\rangle \rightarrow |F' = 3\rangle$ transition. As a result, the atomic density at the trap center significantly increases. Atoms leaving the dark region are optically pumped back into the cycling transition and can be recaptured.

The compressed dark spot MOT reaches a temperature of about 100 µK and good overlap with the subsequent MT.

4.9.1.3 Quadrupole Trap and forced evaporative Cooling

For efficient transfer to the optical dipole trap, the atomic sample must be further cooled. This is achieved through forced microwave evaporation in a conservative magnetic quadrupole trap.

Since the magnetic field gradient in the dark spot MOT is already sufficient for trapping Rb, the MT is primarily loaded with atoms in the $|F = 1\rangle$ manifold. Within this trap, only atoms in the $|F = 1, m_F = -1\rangle$ state remain confined, while atoms in the other states are lost.

After switching off all laser beams, the magnetic field gradient is exponentially increased to 290 G/cm over 1 s using the same coils as the MOT. This results in adiabatic compression [130], yielding a sample of $\sim 1 \cdot 10^9$ atoms at 0.5 mK.

To ensure efficient loading into the ODT, the temperature of the magnetically trapped atoms must be reduced below 50 µK. This is accomplished via forced microwave evaporation [131], by driving the hyperfine transition from the trapped $|F = 1, m_F = -1\rangle$ state to the untrapped $|F = 2, m_F = -2\rangle$ state using microwave radiation.

The evaporation begins with a detuning of 120 MHz and is linearly ramped down to 20 MHz over 3.2 s, which ends up into a Rb cloud of $1.2 \cdot 10^8$ atoms at 40 µK. Evaporation to even lower temperatures is prevented by Majorana flip losses [132], occurring in simple quadrupole traps. These losses could be mitigated using a magnetic offset field at the trap center generated in different trap geometries [133] or a hybrid trap [134]. However, in our case, this is unnecessary, as a sufficient number of atoms can already be transferred into the ODT at the temperatures reached in the magnetic quadrupole trap. The ODT is kept

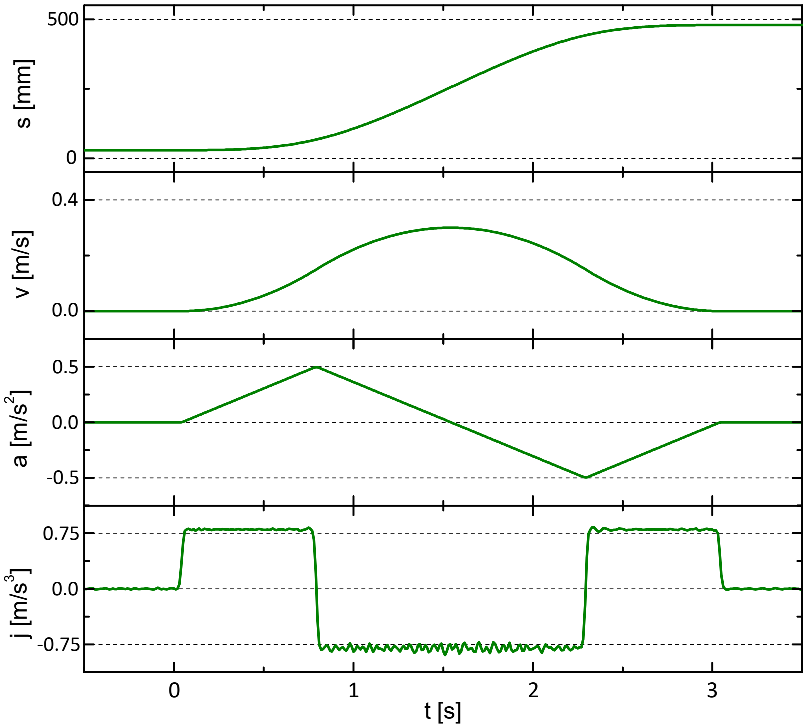

Figure 4.23.: Motion profile for transporting Rb atoms in the ODT from the production chamber to the science chamber. The Yb transport follows a similar profile with slightly adjusted parameters. Taken from [2].

on at 6 W during microwave evaporation[2].

4.9.1.4 Optical Dipole Trap for Rb

The transfer from the magnetic trap (MT) to the optical dipole trap (ODT) is achieved by smoothly ramping down the MT over 1 s while simultaneously increasing the ODT power to its maximum value of 16 W[3]. This process allows for an adiabatic expansion of the MT, improving mode matching with the ODT and facilitating additional evaporative cooling. As a result, we obtain $\sim 7 \cdot 10^7$ atoms at 30 µK, with a lifetime of ~ 30 s in the production chamber.

Once the atoms are successfully transferred into the ODT, they are transported to the science chamber by translating the ODTs focus over a distance of 450 mm, following a minimum-jerk motion profile, as illustrated in Figure 4.23. Due to the relatively small axial trap frequency of $\sim 2\pi \cdot 4$ Hz, the transport duration is limited to 3 s – still significantly shorter than the lifetime in the production chamber. Finally, $3 \cdot 10^7$ atoms at 21 µK and a

---

[2] The laser remains on to minimize thermal lensing effects, but its power is reduced to prevent trapping of atoms in the $|F = 2, m_F = -2\rangle$ state.

[3] This is the laser power at the position of the atoms and is therefore lower than the 30 W mentioned earlier.

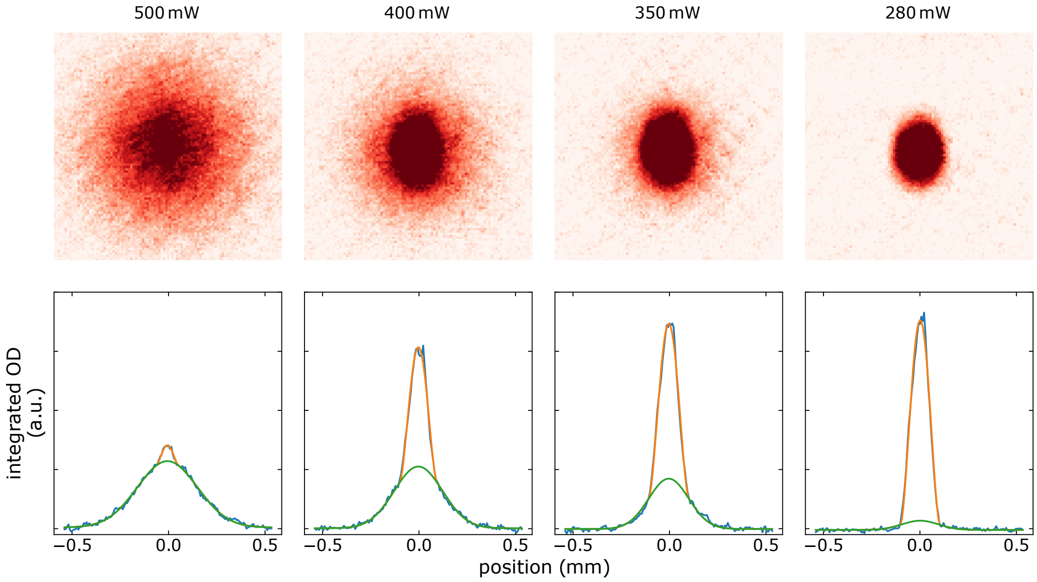

Figure 4.24.: Evaporation to quantum degeneracy of ^{87}Rb in a crossed optical dipole trap. The upper section displays false-color absorption images of the atomic sample with a time-of-flight of 30 ms. During evaporation, the initially round thermal cloud transitions into an anisotropic shape. The lower section presents a bimodal fit of the cloud's optical density, where the green fit represents the thermal (Gaussian) component, and the orange fit corresponds to the condensed fraction. Data from [2].

lifetime of $\sim 45\,\mathrm{s}$[4] arrive in the science chamber.

4.9.1.5 Crossed Optical Dipole Trap and Quantum Degeneracy

Since the axial confinement of a single-beam ODT is inherently weak, limiting the efficiency of evaporative cooling, a CODT is implemented upon arrival in the science chamber.

To transition from the single-beam ODT to the CODT, the power of the crossing beam is increased following a cubic ramp over 0.2 s, while the power of the original ODT beam is simultaneously reduced to 10 W.

Evaporative cooling in the CODT is performed by gradually ramping down the ODT power (and consequently the folded CODT beam power) according to:

$$P(t) = P_0 \left(1 + \frac{t}{\tau}\right)^{-3.5}, \tag{4.6}$$

following the approach outlined in [135]. The optimal time constant $\tau = 6\,s$ was determined experimentally. To achieve different final temperatures of the Rb sample, the total evaporation time is adjusted accordingly. A typical evaporation sequence for different final

---

[4] The lifetime is pressure-limited and corresponds to the pressure of $< 1 \cdot 10^{-11}$ mbar displayed at the ion getter pump controller for the science chamber.

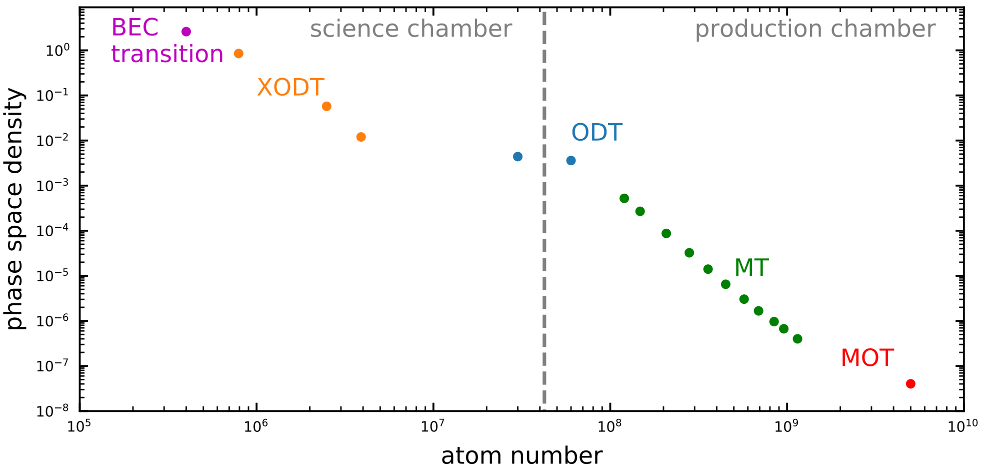

Figure 4.25.: Phase-space density trajectory for the cooling and transport steps for Rb during one experimental sequence. Taken from [2].

CODT powers is shown in Figure 4.24. After evaporation, the trap is held at the final power for 0.5 s to allow full thermalization of the sample. False-color absorption images of the Rb cloud visualize the optical density (OD), where a bimodal fit to the OD data reveals the fraction of Bose-Einstein condensed and thermal atoms. Finally, we achieve the creation of a pure BEC containing $2.5 \cdot 10^5$ atoms.

The atom number and corresponding phase-space density throughout the entire cooling and transport sequence are shown in the phase-space density trajectory in Figure 4.25.

4.9.2 Ytterbium

The Yb cooling sequence is similar to that of Rb, with some modifications due to its atomic properties: As with Rb, Yb atoms are evaporated in an atomic oven, slowed using a Zeeman slower and captured in a magneto-optical trap. The MOT is then compressed, and the atoms are transferred into an ODT before being transported to the science chamber. There, a crossed optical dipole trap provides further confinement, and forced evaporative cooling leads to the formation of a Bose-Einstein condensate.

4.9.2.1 Yb MOT

Unlike in Rb, where both the slowing and the MOT beams drive the same D2-transition, Yb utilizes two separate transitions: the broad ${}^1\mathrm{S}_0 \rightarrow {}^1\mathrm{P}_1$ ($\lambda = 399\,\mathrm{nm}$ and $\Gamma = 2\pi \cdot 28\,\mathrm{MHz}$) for slowing and the narrow – spin-forbidden – intercombination transition $\left({}^1\mathrm{S}_0 \rightarrow {}^3\mathrm{P}_1\right)$ for the MOT beams. The narrow linewidth of $\Gamma = 2\pi \cdot 182\,\mathrm{kHz}$ at 556 nm results in a Doppler temperature of $T_D = 4.4\,\mu\mathrm{K}$, which is crucial for Yb since its ground state is non-magnetic.

Consequently, magnetic trapping is not possible and the ODT must be loaded directly from the MOT[5].

The full implementation of the narrow-linewidth Yb MOT is detailed in Section 4.3.3, so only key aspects are summarized here.

- During the MOT loading phase, approximately $3 \cdot 10^7$ ^{170}Yb atoms are accumulated with 20 s using a magnetic field gradient of 3 G/cm and a detuning of $-10\,\Gamma$.
- To increase the phase-space density, the MOT is then compressed and further cooled by raising the magnetic field gradient to 19 G/cm while reducing the MOT beam intensity to $0.5\,I_{sat}$. This results in $\sim 2 \cdot 10^7$ atoms at a temperature of $\sim 25\,\mu$K.

4.9.2.2 Optical Dipole Trap for Yb

As discussed in Section 4.3.3, efficient loading of the ODT is a critical step in the Yb preparation sequence. Stability is ensured by active position stabilization of the Yb MOT, which was only recently improved by improving the passive frequency stability of the MOT laser system (see Section 4.3.4).

Since the intra-species scattering length of ^{170}Yb is relatively small ($64\,a_0$, see Section 2.2), a high initial atom number – and thus density – in the ODT is essential for efficient evaporative cooling in the science chamber. Considerable effort was devoted to optimizing the loading process to maximize atom transfer to the ODT.

Since the shape of the cooled MOT is rather oblate than spherical (see Figure 4.7), mode matching is achieved by a beam shape modulation of the ODT beam described in Section 4.3.6. The beam shape modulation almost triples the loading efficiency from the compressed MOT into the ODT, which is shown in Figure 4.26.

Using these methods, we are able to transfer up to 50 % of the atoms from the compressed MOT into the ODT, yielding $\sim 8 \cdot 10^6$ atoms at $30\,\mu$K.

The transport from the production chamber to the science chamber follows a similar procedure to that of Rb. However, due to the lower axial trap frequencies at the trapping wavelength of 1064 nm, the process is more sensitive. Despite some inevitable losses, we successfully transport around $4 \cdot 10^6$ atoms to the science chamber in 5.5 s and observe a lifetime of ~ 45 s in the science chamber.

4.9.2.3 Crossed Optical Dipole Trap and Quantum Degeneracy

As with Rb, Yb is transferred into a crossed optical dipole trap upon arrival in the science chamber. While the Rb CODT is formed by folding the ODT beam behind the chamber, the Yb CODT follows a different approach. Initially, we attempted to create the Yb CODT

---

[5] While the fermionic isotopes exhibit a weak magnetic moment, it is not strong enough to allow for magnetic trapping.

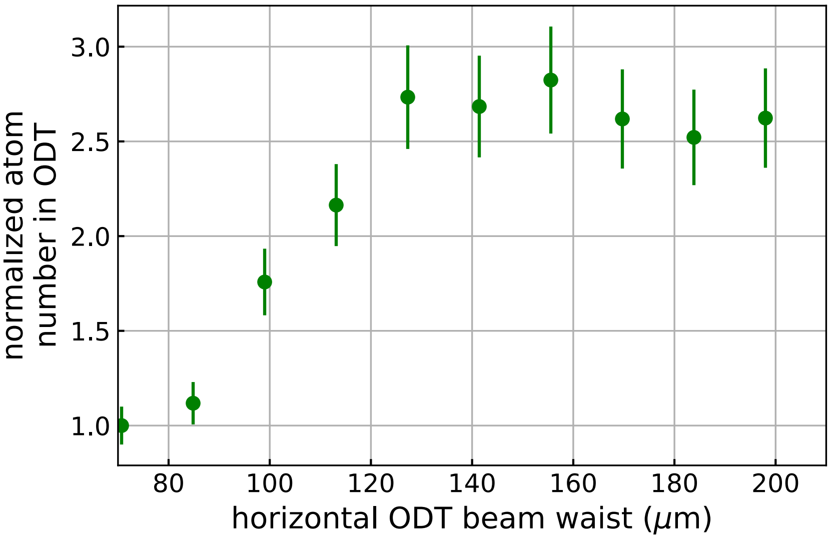

Figure 4.26.: Normalized atom number transferred from the compressed MOT into the ODT versus the horizontal beam waist of the ODT, which is generated by the trap shape modulation. An increase from 70 µm to 150 µm ($1/e$ diameter) almost triples the loading efficiency. Note that these data are taken with the new ODT setup presented in Section 4.3.7. For the old ODT, the increase is only a factor of 2.

using the Rb ODT as the crossing beam. However, since this method is incompatible with simultaneous evaporation of both species in the experiment, it serves primarily as proof of concept, ultimately enabling the formation of an almost pure BEC. Once the optimal evaporation parameters were determined, we transitioned to using the dedicated laser setup illustrated in Figure 4.21.

To produce a Yb BEC, the power of the Yb ODT is ramped down to 6 W over 3 s, while the Rb ODT remains at its maximum power of 16 W. This step collects atoms from the ODT wings into the crossing region, resulting in $\sim 10^6$ atoms being confined at the intersection. Subsequently, both beams are ramped down proportionally according to Equation (4.6) until the desired final power is reached. The trap is then held for 0.5 s to allow full thermalization. Due to the smaller intra-species scattering length of ^{170}Yb, its evaporation time constant is typically longer than that of Rb, with a characteristic value of $\tau = 10\,\mathrm{s}$. Using this method, we achieve the formation of a Yb BEC containing $3.6 \cdot 10^4$ atoms. The transition from a thermal cloud to an almost pure BEC is depicted in Figure 4.27, with the bimodal fit (orange) and the anisotropic expansion clearly indicating the phase transition. Since the Rb ODT cannot serve as a crossing beam in experiments involving both species, Rb and Yb are evaporated in separate CODTs for dual-species operation. In the case of PA experiments, reaching full BEC is, due to the low atom

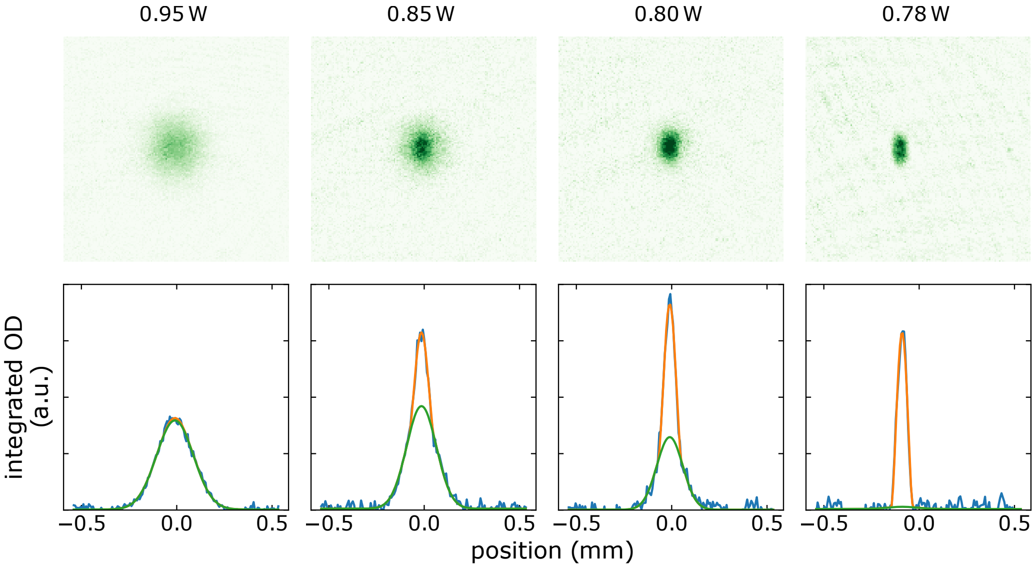

Figure 4.27.: Evaporation to quantum degeneracy of ^{170}Yb in a crossed optical dipole trap using the Rb ODT as crossing beam. The upper section displays false-color absorption images of the atomic sample. During evaporation, the initially round thermal cloud transitions into an anisotropic shape. The lower section presents a bimodal fit of the cloud's optical density, where the green fit represents the thermal (Gaussian) component, and the orange fit corresponds to the condensed fraction. Data from [2].

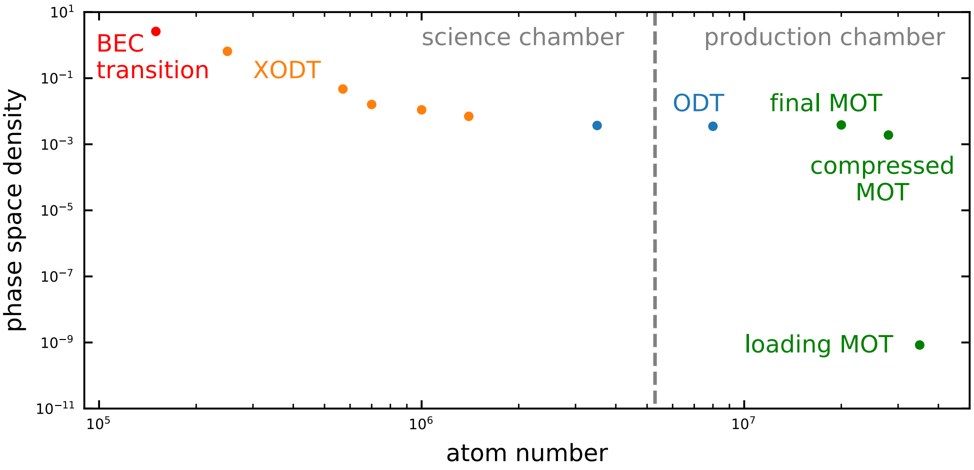

Figure 4.28.: Phase-space density trajectory during the cooling and transport steps for Yb within an experimental sequence. Note that the axes scales differ from those used for Rb. These experiments were conducted with the Rb ODT as crossing beam. Taken from [2].

number, not feasible and an alternative approach proves to be more effective. The crossing beam is ramped up to its maximum power of 9 W during Yb transport to the science chamber, after which the Yb ODT beam is ramped down to transfer the atoms from the wings into the crossing region. Both beams are then simultaneously ramped down to 0.8 W (ODT) and 0.6 W (crossing)[6] over 5 s – a much faster evaporation sequence compared to full BEC formation, yet optimized for efficient merging.

Under these conditions, Yb evaporation in the CODT yields $3 \cdot 10^5$ atoms in a thermal cloud at a temperature of 0.3 µK, with a lifetime of 16 s.

As with Rb, we can visualize the phase-space density evolution throughout the entire experimental sequence, as illustrated in Figure 4.28.

4.9.3 Simultaneous Preparation of a Dual Species CODT

While evaporative cooling in a CODT is a well-established technique, demonstrated in numerous ultracold atom experiments, merging two different atomic species within optical potentials presents several challenges:

- Simultaneous preparation of both species must be ensured. To achieve this, most of the preparation is carried out in separate production chambers. For instance, microwave evaporation of Rb in a MT can take place simultaneously with loading the Yb MOT. Performing both processes in the same chamber would be infeasible due to the fundamentally different magnetic field gradients required and due to limited optical access for necessary laser beams.

- Final evaporation must occur in separate CODTs within the science chamber. Transferring such cooled samples back into a single-beam ODT would result in lower atomic densities.

- Using the same CODT for evaporation of both species would lead to the complete loss of Yb since, at the trap wavelength of 1064 nm, the trap depth for Rb is roughly ten times higher than for Yb.

- Evaporation in two separate CODTs within the same vertical plane leads to beam interference. If both species start with equal trap depths, the required intensity of the Yb CODT beams must be significantly higher than that of Rb, effectively creating a deep trap for Rb and unintentionally collecting Rb atoms into the Yb CODT.

- Sympathetic cooling of Yb with cooled Rb is, due to the low inter-species scattering length between ^{87}Rb and ^{170}Yb, not feasible.

---

[6] The best final powers depend strongly on the initial performance of Yb, especially on the atom number, and can thus be slightly different from day to day.

To overcome these challenges, the initial cooling stages are performed in separate CODTs aligned in different vertical planes, with a slight horizontal offset. Subsequently, the lower-lying Rb sample is transferred into a vertical 1D optical lattice and elevated to the Yb plane (see Section 4.6.2). Finally, the Yb CODT is shifted using a frequency shift of the Yb ODT AOM to the position of the Rb cloud and the optical lattice is switched off. Following the combining sequence described in Section 4.9.3.1, this procedure results in a combined Rb-Yb mixture within the same trap.

4.9.3.1 Combining Rb and Yb

The experimental sequence for elevating and merging Rb and Yb is illustrated in Figure 4.29.

1. Initial transport (a): The atoms are first transported into the science chamber at different heights using their respective optical dipole traps.
2. Evaporative cooling (b): The crossing beams are then activated and forced evaporative cooling is performed for both species. Fortunately, Rb evaporates more quickly, allowing sufficient time to ramp up the vertical lattice beam (c) while gradually ramping down the entire Rb CODT laser power.
3. Lattice elevation (d): As a result, an ultracold Rb cloud is transferred into the optical lattice, which is then elevated by approximately 1 mm, aligning Rb within the same horizontal plane as Yb. However, transferring a Bose-Einstein condensate (or an extremely cold cloud) into an optical lattice leads to high atomic densities at the lattice sites, increasing three-body losses. To mitigate this, the trap volume of the CODT is expanded by slightly shifting the ODT beam focus away from the crossing region by moving the translation stage before loading the lattice[7]. This adjustment increases the number of occupied lattice sites, thereby reducing local density and minimizing losses. Additionally, to prevent heating of Yb due to the movement of the periodic potential, Yb is initially positioned with a slight 0.2 mm horizontal offset.
4. Final merging (e-f): At the end of the merging sequence, the Yb CODT is shifted onto the Rb cloud via a frequency shift of the ODT AOM driver and the lattice is ramped down. This results in both species being confined within the same CODT, where photoassociation experiments can be conducted.

4.9.3.2 Merging Optical Dipole Traps with different Trap Depths

A crucial step in the experiment is the merging sequence, where special care must be taken to avoid excessive heating of Rb or Yb. At the beginning of this sequence (see Figure 4.29

---

[7] Since the crossing beam is generated by folding the ODT beam behind the chamber, its focus is also translated out of the CODT region.

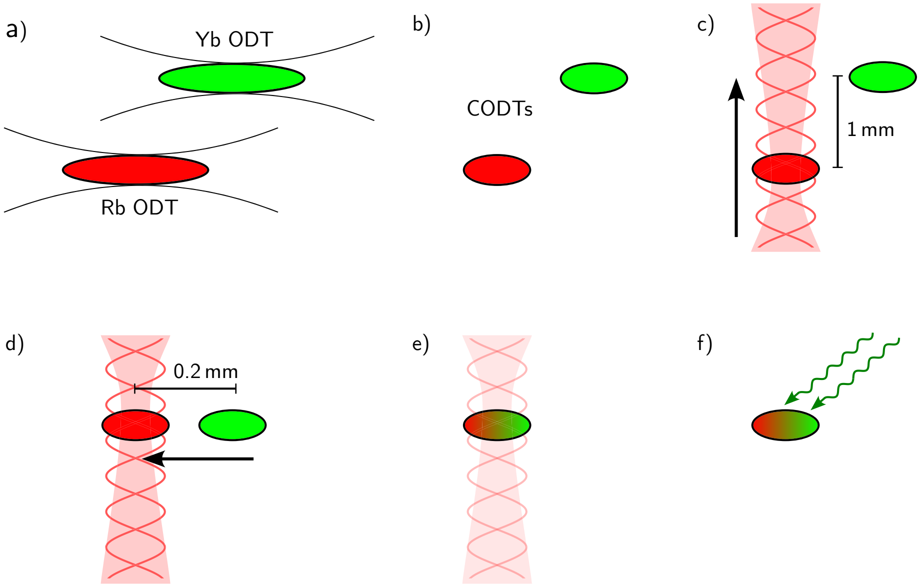

Figure 4.29.: Scheme of the simultaneous preparation and combination of Rb and Yb. a) Initial transport to the science chamber in separate ODTs. b) Separate evaporation of both clouds. c) Optical lattice elevation of Rb to the height of Yb. d) Shifting Yb CODT onto the Rb cloud. e)-f) Switching off the optical lattice and merging the traps for subsequent photoassociation experiments.

(e)), the elevated Rb sample and Yb are positioned at different positions within the Yb CODT beam. The corresponding CODTs are formed with the vertical lattice beam (Rb) and the Yb ODT beam (Yb).

Side note: The Yb CODT setup evolved over the course of this thesis. In the early stages, as described by Tobias [1], the CODT was created by folding the ODT beam behind the chamber, similar to the setup used for Rb. In this configuration, the merging sequence differed from the one described here and in [2]. Previously, Rb and Yb were located along the Yb ODT beam, and the Yb CODT beam was shifted onto Rb to merge the traps. The search for RbYb 1-PA (see Chapter Section 5.1) resonances and the detection of 2-PA lines (see Chapter Section 5.2) were conducted with this setup.

Using the same laser for both beams had several disadvantages, including heating due to mode beating of the multi-mode seed laser during the merging sequence. Additionally, the higher intensity of the ODT beam compared to the CODT beam led to heating of Rb while it was elevated into its potential. Furthermore, independent intensity adjustments were not possible with a folded CODT beam.

To address these issues, an additional Yb laser was implemented, as described in Section 4.6.1.2 and [2]. The merging sequence and final trap discussed here reflect this improved setup. A detailed explanation of the process can be found in [2]. The new

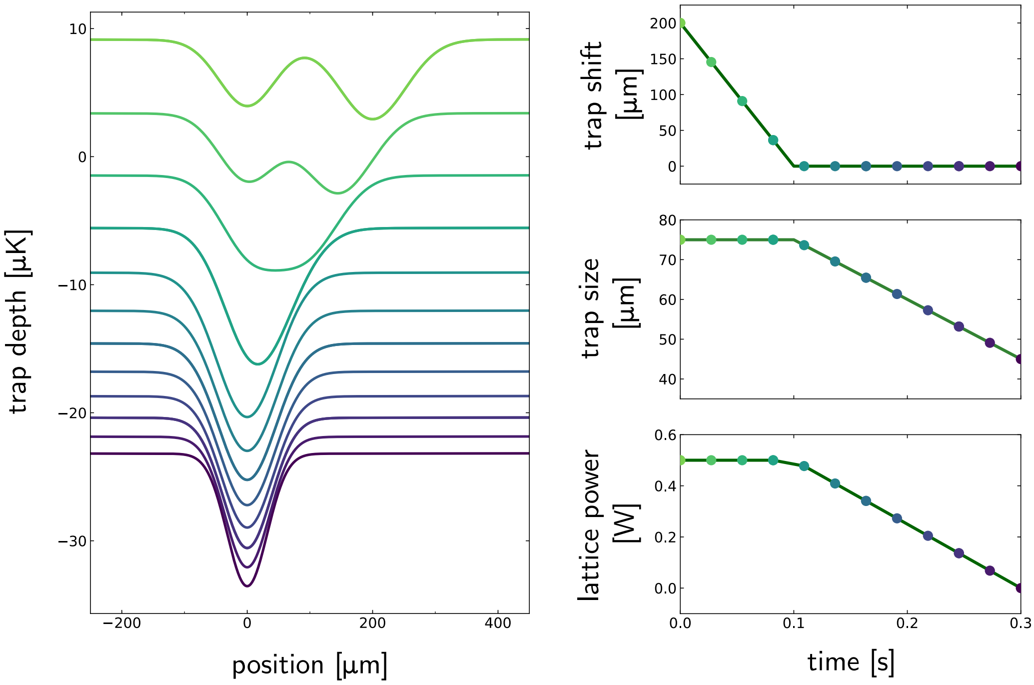

Figure 4.30.: Calculated optical potentials for Yb (same for Rb only with a scaling factor) during the merging sequence of Rb and Yb (left) and corresponding trap parameters (right). The potentials are vertically offset for better visibility. Before shifting the Yb CODT, which can be modulated such as the Yb ODT (see Section 4.3.6), the beam shape is enlarged to match the lattice beam waist. After shifting, the beam shape is reduced to its minimum value, and the lattice beam intensity is ramped down to zero. The used Python script is from [1].

configuration led to improved performance and flexibility, while maintaining comparable final trap parameters.

The merging sequence is illustrated in Figure 4.30, showing the evolution of the calculated potential for Yb (left) and of the corresponding trap parameters (right). The potential for Rb differs only by a scaling factor of approximately 10. The goal of the merging process is to transfer both species in the same trap with minimal loss and heating. For photoassociation near the intercombination line of Yb, maintaining a large Yb atom number is also beneficial, as it suffers from off-resonant scattering losses.

To achieve a quasi-adiabatic merge, the trap depths and shapes must be carefully matched [136, 137]. This is accomplished by adjusting the Yb CODT trap shape using the modulation technique described in Section 4.3.6[8]. Before shifting the Yb CODT

---

[8] Here, the ODT beam is not modulated.

onto the Rb trap, the Yb CODT trap shape is modified to match the lattice beam waist. After shifting, the trap shape is reduced to its original form without modulation, and the lattice power is ramped down to zero.

The potentials and parameters depicted in Figure 4.30 may vary from the actual experimental conditions and can fluctuate from day to day. Since the goal is to achieve an optimal mixture of Rb and Yb in terms of atom number and temperature, experimental conditions may necessitate adjustments to the merging parameters. Despite measurements of beam parameters, slight misalignments in beam position, intensity or focus size can alter the expected outcomes.

Thus, at the start of a measurement, the parameters are experimentally adjusted to optimize the mixture of Rb and Yb. As a result, the actual values presented in Figure 4.30 should be interpreted as a guide for the experimental procedure.

4.9.3.3 The Final Trap

After the merging process is completed, both species are trapped in the final potential, where the photoassociation experiments are conducted. Efficient photoassociation requires high atomic densities and significant spatial overlap between the species. Various configurations can be used for the final trap, which will be discussed in this section. A straightforward approach is to use the CODT described in the previous chapter as the final trap. However, to achieve higher densities and improved spatial overlap, a 3D optical lattice can also be employed.

4.9.3.4 CODT

A monochromatic CODT for both species represents the simplest setup for photoassociation experiments. Most of the data presented in the following sections were obtained using this configuration.

During the elevation of Rb, three-body collisions lead to an increase in its temperature to approximately 5 μK. Given the small inter-species scattering length of $a_{RbYb} = -11\,a_0$, thermalization occurs on relatively long timescales (on the order of several seconds), minimizing the impact on the lifetime of Yb, which is lost from the trap at lower temperatures due to the lower trap depth for this species. Unfortunately, the slow thermalization also makes direct observation of interactions between the two species difficult, complicating the verification of spatial overlap via thermalization measurements.

The optical potential for Yb in the final CODT and the corresponding spatial density distributions along the vertical axis are shown in Figure 4.31. Due to its approximately two times higher mass and the lower trap frequencies, Yb experiences a significantly larger gravitational sag than Rb, leading to a spatial mismatch in the density distributions. The left panel of Figure 4.31 represents the typical parameters used in our final CODT, where

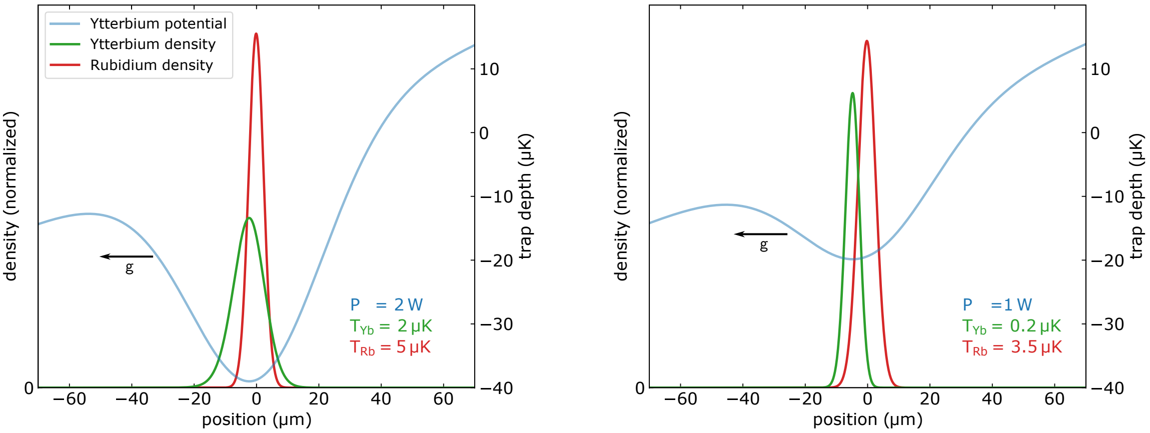

Figure 4.31.: Simulated optical potentials (for ^{170}Yb) for ODT beam powers of $P_{ODT} = 2\,\mathrm{W}$ (left) and $P_{ODT} = 1\,\mathrm{W}$ (right), shown along the vertical axis, along with the corresponding atomic densities for Rb and Yb with typical temperatures. The power of the CODT beam is set to $0.75 \cdot P_{ODT}$. In the left graph, Rb and Yb exhibit good spatial overlap, whereas in the right graph, the gravitational sag of Yb is clearly visible. The Python script for the simulation is from [1], using new values for the trap parameters. Note that the trap depths are just calculated and not measured.

Rb and Yb remain well overlapped. However, when the trap depth is reduced (right panel), the gravitational sag of Yb becomes pronounced, resulting in diminished spatial overlap and, consequently, lower PA rates.

Typical parameters for Rb and Yb in the final CODT are listed in Table 4.1. While this setup already provides a solid basis for photoassociation spectroscopy, further increasing atomic densities and spatial overlap is expected to enhance PA rates. This can be achieved by implementing a 3D optical lattice, which will be introduced in the following paragraph.

	Rb	Yb
Atom number	$5 \cdot 10^5$	$7 \cdot 10^4$
Temperature [µK]	5.3	2.0
Trap Frequencies [Hz]	$2\pi\,[372, 1208, 1264]$	$2\pi\,[83, 269, 279]$
Peak Density [cm^{-3}]	$\approx 10^{13}$	$\approx 10^{12}$

Table 4.1.: Typical values of Rb and Yb in the final CODT with beam powers of 2 W (ODT) and 1.5 W (CODT).

4.9.3.5 3D Optical Lattice

Compared to the relatively broad potential well of a CODT – determined by the beam waists – the potential wells of individual sites in a 3D optical lattice are on the order of the laser wavelength, while maintaining comparable trap depths. This results in increased atomic density and improved spatial overlap, as illustrated in Figure 4.32. The left panel of Figure 4.32 shows the density distributions of Rb and Yb confined in a 3D optical lattice along the vertical axis, along with the corresponding optical potential for all lattice beams at a power of 0.5 W. Since the atoms are localized in discrete lattice sites, the overall spatial overlap of the atomic distributions can be optimized by carefully adjusting the vertical position of Rb during the elevation and merging step (see Figure 4.29).

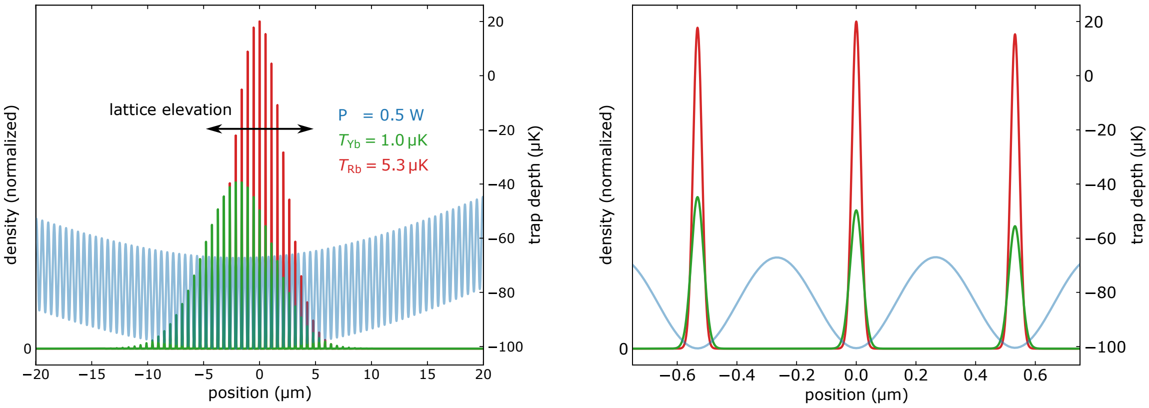

Figure 4.32.: Left: Potential for Yb in a 3D optical lattice with each beam having a power of 0.5 W and atomic density of both species along the vertical direction. The vertical position of Rb can now be adjusted by the final position of lattice elevation, ensuring better spatial overlap. Right: Yb potential at individual lattice sites and atomic density distributions on these sites. The spatial overlap is significantly increased compared with a CODT. Taken from [2].

The right panel highlights the confinement at individual lattice sites, where the absence of a noticeable gravitational sag leads to a significantly enhanced spatial overlap. This increased overlap and higher atomic densities are expected to enhance PA rates. Typical values for a 3D optical lattice are shown in Table 4.2, which show an increase of the peak atomic density of a factor of 1000 (see Table 4.1) and initial PA experiments using a 3D optical lattice have already been conducted and will be discussed in Section 5.1.3.8.

	Rb	Yb
Atom number	$4.3 \cdot 10^5$	$1.6 \cdot 10^5$
Temperature [μK]	6	12
Trap Frequencies [kHz]	$2\pi\,[120, 120, 120]$	$2\pi\,[26, 26, 26]$
Peak Density [cm^{-3}]	$\approx 10^{16}$	$\approx 10^{15}$

Table 4.2.: Typical values of Rb and Yb in the final 3D optical lattice with beam powers of 0.5 W. Values from [2].

However, several challenges arise in this configuration:

- In a deep optical lattice, tunneling between sites is strongly suppressed, leading to isolated atoms that may lack a reaction partner for photoassociation.
- The loading process into the lattice is not perfectly adiabatic, which can introduce heating.
- High atomic densities at individual lattice sites increase the likelihood of collisional losses in deep potentials.

These factors contribute to shorter lifetimes for both species in the optical lattice compared to the CODT [2].

Nonetheless, adiabatically loading a quantum degenerated mixture of Rb and Yb into a 3D optical lattice offers a promising route to significantly enhance PA rates. In a Mott insulator state, the heteronuclear combination of ^{87}Rb and ^{170}Yb is energetically favored over homonuclear Yb-Yb or Rb-Rb pairings. During the lattice ramp-up, the degenerate mixture initially remains in a superfluid state, allowing for tunneling and an energetically favorable redistribution of the atoms. Once the lattice depth surpasses the Mott insulator transition, the ideal scenario is that lattice sites become filled with Rb-Yb pairings, ensuring that each atom has a partner for photoassociation.

A further advantage of the lattice is the ability to prepare atoms in the motional ground state of the lattice sites. This results in discrete energy levels, effectively eliminating thermal broadening of 2-PA resonances from the continuum of scattering states (see Figure 2.14).

5

Photoassociation Spectroscopy near the Intercombination Line of Yb

This chapter describes our one- and two-photon photoassociation spectroscopy measurements performed near the intercombination line of Yb.

5.1 One-Photon Photoassociation near the Intercombination Line of Yb

After achieving a mixture of cold Rb and Yb atoms in a combined trap, we are now prepared to conduct photoassociation measurements and search for the first photoassociation resonances near the $^1\mathrm{S}_0 \rightarrow {}^3\mathrm{P}_1$ intercombination line of Yb. The search for these least bound states, as well as the analysis of the (unfortunately only) detected resonance, was carried out during Tobias' [1], Bastian's [2], and my thesis, and is also published in [51] in a collaborative effort.

Since the spin-forbidden intercombination line has a very narrow linewidth of $2\pi{\cdot}182\,\mathrm{kHz}$, it is highly suitable for high-precision photoassociation spectroscopy.

Given the lack of experimental data on the relevant excited Π-manifold of the $^2\mathrm{S}_{1/2} + {}^3\mathrm{P}_1$ asymptote, it is useful to first consider some preliminary theoretical aspects, which are discussed in the following. Subsequently, the actual search with a search range of 0.1–11 GHz is presented and the observed resonance at approximately 3 GHz is analyzed.

5.1.1 Preliminary Considerations

Since a typical experimental sequence lasts about one minute and linewidths of photoassociation resonances are expected to be on the order of the natural linewidth of the intercombination transition ($\sim 2\pi \cdot 182\,\mathrm{kHz}$), these measurements are highly time-consuming. Thus, a shot in the dark does not seem to be the best choice here.

To guide our search, we rely on theoretical studies of RbYb [45, 58, 138, 139] and insights from both theoretical and experimental work on RbSr [140, 141], given that Sr shares a similar electronic structure with Yb.

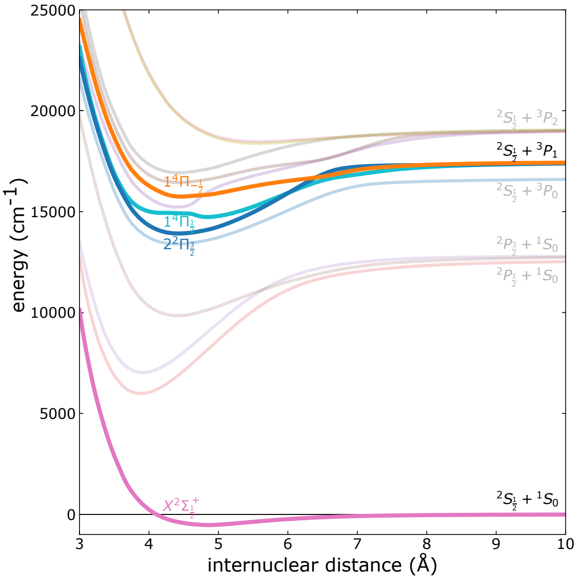

Asymptote	$\|\Omega\|$	Exp.	Theory [139]
$^2S_{1/2} + {}^1S_0$	1/2	2837(13) [64]	2837(57)
$^2P_{1/2} + {}^1S_0$	1/2	5684(94) [97]	7607(114)
$^2S_{1/2} + {}^3P_1$	1/2	–	3955(160)
$^2S_{1/2} + {}^3P_0$	3/2	–	4460(180)

Figure 5.1.: Left: Ab-initio potential energy curves for RbYb from [45]. The highlighted curves correspond to the potentials near the intercombination line of Yb. Right: C_6 coefficients for different potentials of RbYb obtained from experiment and theory. All values are given in units of $E_H\, a_0^6$.

The relevant molecular states at short range are denoted as $1^4\Pi_{1/2}$, $2^2\Pi_{3/2}$, and $1^4\Pi_{-1/2}$, while their corresponding long-range states are labeled $5(\Omega = 1/2)$, $1(\Omega = -1/2)$, and $2(\Omega = 3/2)$ [45].

To estimate the positions of the least bound states in the excited potential, we are interested in its long-range part, described by the C_6 coefficient and the fractional part Δ_{frac} of the fractional quantum number v_D. Ab-initio calculations for the potential energy curves and C_6 coefficients are presented in Figure 5.1. Using this information in combination with the LeRoy-Bernstein formula (see Equation (2.8)), we can estimate the locations of bound molecular states. However, predicting Δ_{frac} without experimental data is impossible, and even theoretically derived C_6 coefficients can show significant deviations from reality. This is evident from comparisons between calculated and experimental values for the excited potential near the D1 line at the $^2P_{1/2} + {}^1S_0$ asymptote, where discrepancies of approximately 25 % occur (see also deviation in Morse parameters in Table 6.1).

Nonetheless, approximate values for C_6 coefficients allow us to estimate the density of vibrational states in the long-range part of the potential. Taking $C_6 = 4200\, E_H\, a_0^6$ (mean value from $\Omega = 1/2$ and $\Omega = 3/2$ [139]), considering a ±20 % uncertainty and taking all possible values for Δ_{frac} into account, we expect five to six bound vibrational states with binding energies of $|E_B| < h \cdot 10\,\mathrm{GHz}$, which falls within our experimentally achievable range.

To refine the search strategy, an estimate of the expected line strengths is essential. This

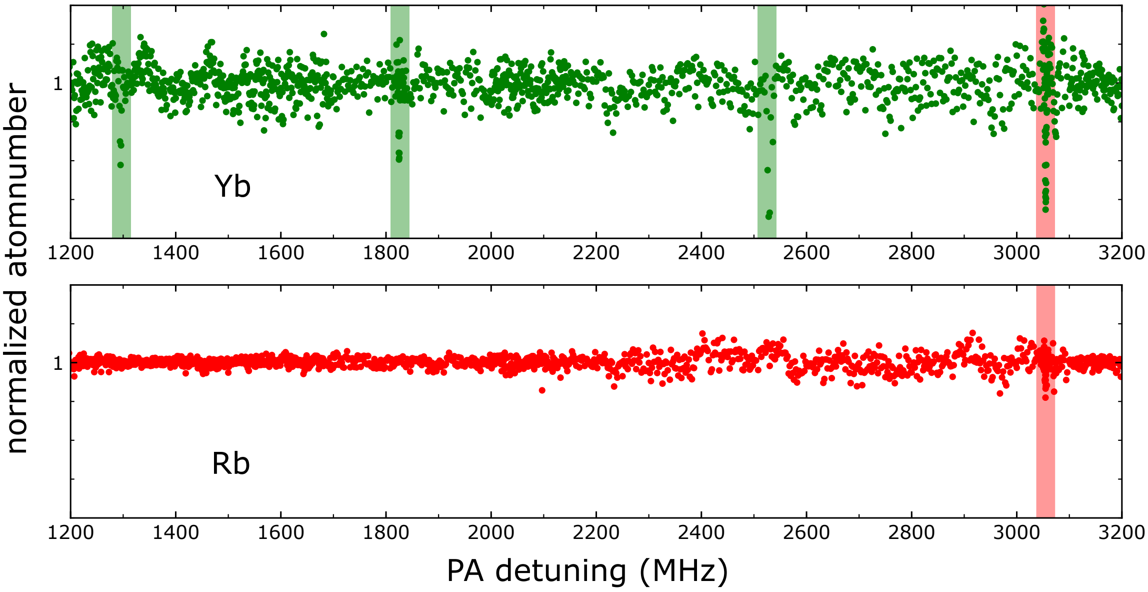

Figure 5.2.: Normalized atom numbers of Rb and Yb during photoassociation measurements covering a range of 1.2–3.2 GHz. While vertical green shaded areas show Yb_2 lines, the red shaded one shows the location of the RbYb resonance at ~ 3.1 GHz, which is the only one we could detect. (The figure previously appeared in [1] and [2].)

helps to determine the appropriate PA laser detuning step size, as well as the optimal pulse duration and intensity. Unfortunately, no experimental or theoretical data are available, so we rely on results for RbSr [140, 142–144], which has a similar molecular structure. Theoretical calculations [143] predict a rapid decrease in photoassociation rates near the asymptote. Since the intercombination transition is dipole-forbidden, line strengths are weak in this region, and the dipole moment only increases due to additional perturbations from the interaction of the electronic clouds of Rb and Yb.

Despite the significantly smaller linewidth of Sr ($\gamma = 2\pi \cdot 7.5\,\mathrm{kHz}$) compared to Yb, we expect similar photoassociation behavior. The detection of multiple resonances in [142] suggests that at least some resonances should be observable in our system as well.

5.1.2 Search for Photoassociation Resonances

The search for photoassociation resonances of RbYb at the $^2\mathrm{S}_{1/2} + {}^3\mathrm{P}_1$ asymptote was conducted during the theses of Tobias, Bastian, and the one presented here. We investigated a frequency range from 0.1–11 GHz, with an unfortunate gap between 3.2–3.7 GHz. Due to the small step size required to detect weak lines, with predicted linewidths on the order of $2\pi \cdot 1\,\mathrm{MHz}$, the search extended over several days and nights of measurements.

There are several factors that can reduce the sensitivity of the measurements:

- For PA detunings less than $\sim 2\,\mathrm{GHz}$, the maximal usable intensity and pulse duration are significantly reduced due to off-resonant scattering at the atomic transition of Yb.
- With a typical step size of $2\pi \cdot 1\,\mathrm{MHz}$, resonances with smaller linewidths are hard to detect
- Off-resonant excitation near Yb_2 lines reduces the usable intensity of the PA beam.

Nonetheless, we estimate – using Yb_2 lines as reference – that despite limitations, we are able to detect resonances with a PA rate constant of $K_{PA} \gtrsim 2 \cdot 10^{-14}\,\mathrm{cm}^3/\mathrm{s}$.

After confirming spatial overlap of the atomic samples through thermalization and properly adjusting the PA laser beam by resonantly exciting Yb atoms and thus removing them from the trap, the search for resonances could begin. The PA laser described in Section 4.5 was directed onto the combined CODT with a power in the range of 1–3 mW and a pulse duration in the range of 0.5–2 s, depending on the regions mentioned above.

An exemplary scan of the range from 1.2 GHz to 3.2 GHz, where three Yb_2 transitions and one RbYb transition were found, is shown in Figure 5.2. Note that the absolute atom number of Rb is about five times larger than that of Yb, which results in a much better visibility for the PA signal in Yb. Thus, careful verification is required when detecting a loss of Yb atoms. Yb_2 transitions can be verified by repeating the scan without Rb atoms present. Another potential cause of atom loss is an experimental failure, so any suspicious atom loss was checked by performing multiple scans over the dedicated region.

Despite all the effort, we were only able to identify a single pair of RbYb PA resonances. This will be analyzed in the following section.

Yb_2 Photoassociation Lines

During the search for RbYb resonances, several photoassociation lines of homonuclear Yb_2 molecules were observed. While these are not the primary focus of this work, they allow for a direct comparison with literature values and serve as a benchmark for the sensitivity of our experimental apparatus, demonstrating detection capabilities down to PA rates of $K_{PA} \gtrsim 2 \cdot 10^{-14}\,\mathrm{cm}^3/\mathrm{s}$. Additionally, we were able to expand the set of previously known one-photon transitions in $^{170}\mathrm{Yb}_2$. A detailed discussion of these resonances can be found in [1]; here I present the results in Table 5.1 for completeness.

5.1.3 A Pair of Photoassociation Resonances at 3 GHz

After identifying the first PA transition in Figure 5.2, we now take a closer look at this line and characterize it. A close-up view is shown in Figure 5.3, revealing that it actually consists of a pair of lines, labeled (a) and (b), with distinct linewidths and Zeeman shifts.

$\Delta v'$	Detuning [MHz]	Theory [87] [MHz]	Takahashi [87, 145] [MHz]
-9	-34(2)	-31.0	–
-10	-60(2)	-57.3	–
-11	-103(2)	-99.9	–
-12	-169(2)	-166.1	–
-13	-269(2)	-265.4	-268(3)
-14	-416(2)	-410.4	-413(3)
-15	-620(2)	-616.6	-619(3)
-16	-908(2)	-903.9	-906(3)
-17	-1297(2)	-1296.9	–
-18	-1827(2)	-1826.5	–
-19	-2531(2)	-2525	–
-20	–	-3428	–
-21	-4662(2)	-4616	–
-22	-6215(2)	–	–
-23	-8202(2)	–	–
-24	-10720(2)	–	–

Table 5.1.: Observed photoassociation resonances of homonuclear Yb_2 molecules during the search for RbYb lines. The table lists vibrational levels from $\Delta v' = -9$ to $\Delta v' = -24$, covering a detuning range of up to $\sim 11\,\mathrm{GHz}$.

5.1.3.1 Line Strength

Next, we examine the PA line strengths via the photoassociation rate constant $K_{PA}(I)$, which depends on the PA beam intensity, temperatures, and pair density. The PA rates can be determined using the following rate equations for the atomic densities n_{Yb} and n_{Rb}:

$$\dot{n}_{Yb} = -n_{Yb} \cdot K_{Yb} - n_{Rb} \cdot n_{Yb} \cdot K_{PA} \tag{5.1}$$

$$\dot{n}_{Rb} = -n_{Rb} \cdot K_{Rb} - n_{Rb} \cdot n_{Yb} \cdot K_{PA}. \tag{5.2}$$

Here, K_{PA} is the PA rate constant, while K_{Yb} and K_{Rb} represent the individual loss rates of each atomic species, which stem from trap loss and off-resonant (atomic) excitation. To determine these rates, we measure the atom numbers for different PA durations, comparing data with the laser on resonance to data with a detuning large enough to avoid photoassociation (see Figure 5.4). This approach is necessary since the off-resonant scattering loss of Yb is comparable in magnitude to the PA-induced loss. By numerically fitting the rate equations to the data, we obtain a PA rate constant of $K_{PA} \approx 5 \cdot 10^{-13}\,\mathrm{cm}^3/\mathrm{s}$ per Yb

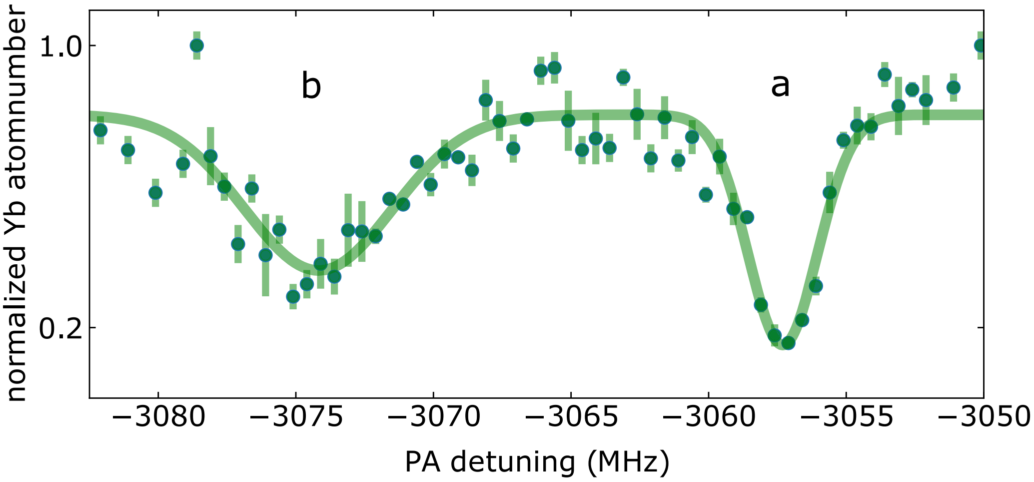

Figure 5.3.: Photoassociation measurement of the only detected resonance pair. For frequencies with multiple data points, the mean value was calculated, and the error bars represent the standard deviation from this mean. The solid line corresponds to a Gaussian fit, serving as a guide to the eye. Data published in [51] and previously reported in [1] and [2].

atom[1].

The PA rate constant observed for the transition in RbYb is several orders of magnitude larger than the predicted values for RbSr in [140], yet still significantly lower than those observed for the D lines of Rb.

5.1.3.2 Free-Bound Franck-Condon Factors

Although we are confident that we conducted a thorough search for PA transitions, we can consider additional factors to explain why other lines may be weaker and therefore undetectable with our experimental setup. One approach is to calculate (or estimate) the relative free-bound Franck-Condon factors (FCFs), which provide insight into the line strengths. To do this, we need to calculate the scattering wavefunction in the ground state and the desired first bound wavefunctions, then determine the overlap integral at the Condon point.

Due to the limited knowledge of the potential energy curves (PECs), certain assumptions are required. For both PECs, we use a Lennard-Jones type potential, which is appropriate since we are concerned with the long-range part of the potential (see Section 2.1.2). The ground state is modeled using the C_6 coefficient determined by Münchow, and the C_{12} coefficient is chosen such that the scattering length and the location of the least bound states match the potential [124]. The excited potential is modeled with $C_6 = 4466\, E_H\, a_0^6$,

---

[1] This value is an order of magnitude higher than previous measurements reported in [1] and published in [51].

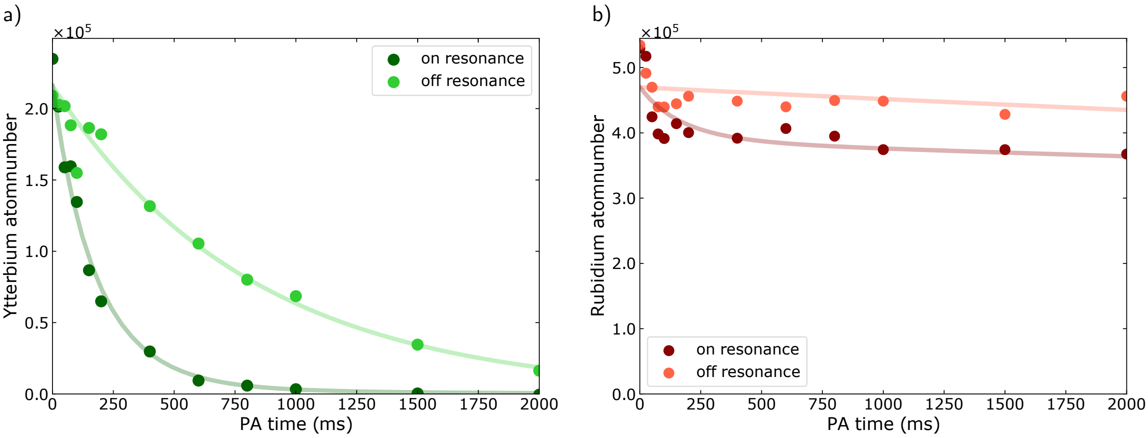

Figure 5.4.: Measurement of PA rate constant. a) shows the Yb atom number versus the PA time with the laser being on resonance (dark) and detuned from resonance (bright). The same measurement for Rb (b) shows smaller decay due to the higher initial Rb atom number, but the difference is of the same order. Previously reported in [2].

as calculated by [139] for $|\Omega| = 3/2$. C_{12} is then adjusted based on the information from the location of the found transition. The results are shown in Figure 5.5. The modeled PECs, the scattering wavefunction of the ground state with a thermal energy offset (red), and the four least bound wavefunctions of the excited states (green) are displayed. The calculated Franck-Condon factors for transitions within our search range are shown on the right side, along with the corresponding binding energies. A rapid decrease of the FCFs is observed for more deeply bound states.

Since these calculations are based on a number of assumptions, the results should be interpreted with caution. Nevertheless, they offer valuable insights and help to explain why additional transitions were not detected during our scan.

Although the FCFs for states more weakly bound than the one we found are significantly larger, their predicted binding energies lie very close to relatively strong Yb_2 resonances (see Section 5.1.2), complicating detection. Furthermore, off-resonant scattering in the region $< h \cdot 2\,\mathrm{GHz}$ reduces our sensitivity significantly.

For the more deeply bound states, the FCFs are significantly smaller, which may explain the difficulty in detecting these. The predicted increase in FCFs for deeply bound states due to electron cloud perturbations, as described by [45], only has a significant effect for binding energies larger than $h \cdot 1\,\mathrm{THz}$, which is beyond the reach of our laser system.

Despite all the assumptions made, these factors provide a plausible explanation for the unsuccessful search for additional lines.

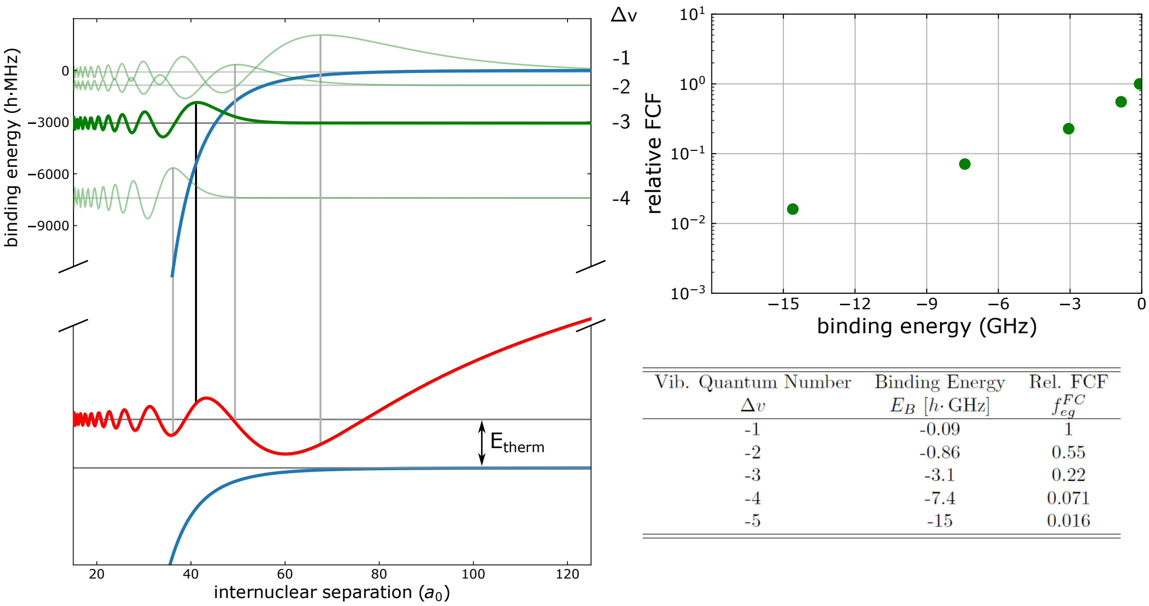

Vib. Quantum Number Δv	Binding Energy E_B [$h\cdot$ GHz]	Rel. FCF f_{eg}^{FC}
-1	-0.09	1
-2	-0.86	0.55
-3	-3.1	0.22
-4	-7.4	0.071
-5	-15	0.016

Figure 5.5.: Left: Potential energy curves of Lennard-Jones type potentials for the ground and excited state, including numerically calculated wavefunctions for the scattering state (ground state) and the least bound states in the excited potential. Right: FCFs relative to the first bound state FCF and the corresponding binding energies. The Python script used for the calculations is from [1].

5.1.3.3 Zeeman Shift

Since we now have to settle for a single pair of photoassociation lines, we can characterize its behavior in external magnetic fields and determine the Zeeman shift of each transition. The magnetic field is generated by bias coils attached to the science chamber, reaching field strengths up to 30 G, calibrated via microwave spectroscopy of Rb.

To determine the Zeeman shift of the excited PA lines, we first recall the Zeeman shifts of the ground state of the individual atoms. Since Yb is prepared in the non-magnetic $^1\mathrm{S}_0$ ground state, it remains unaffected by magnetic fields and the Yb ground state does not contribute to the shift of the PA resonance line. Rb, on the other hand, is prepared in the $|F = 1, m_f = -1\rangle$ Zeeman state, which shifts by 0.70 MHz/G [104] and must therefore be considered when determining the Zeeman shift of the excited molecular state, as shown in Figure 5.6. Accounting for the Rb ground-state shift, a linear fit to each peak yields Zeeman shifts of the molecular state of 0.59(3) MHz/G for peak (a) and 0.28(3) MHz/G for peak (b).

From this, we also determine the zero field transition frequencies to be −3057.5(3) MHz for peak (a) and −3074.3(3) MHz for peak (b), confirming that the lines remain split at zero field with a separation of approximately 17 MHz, i.e. that there are two distinct excited states.

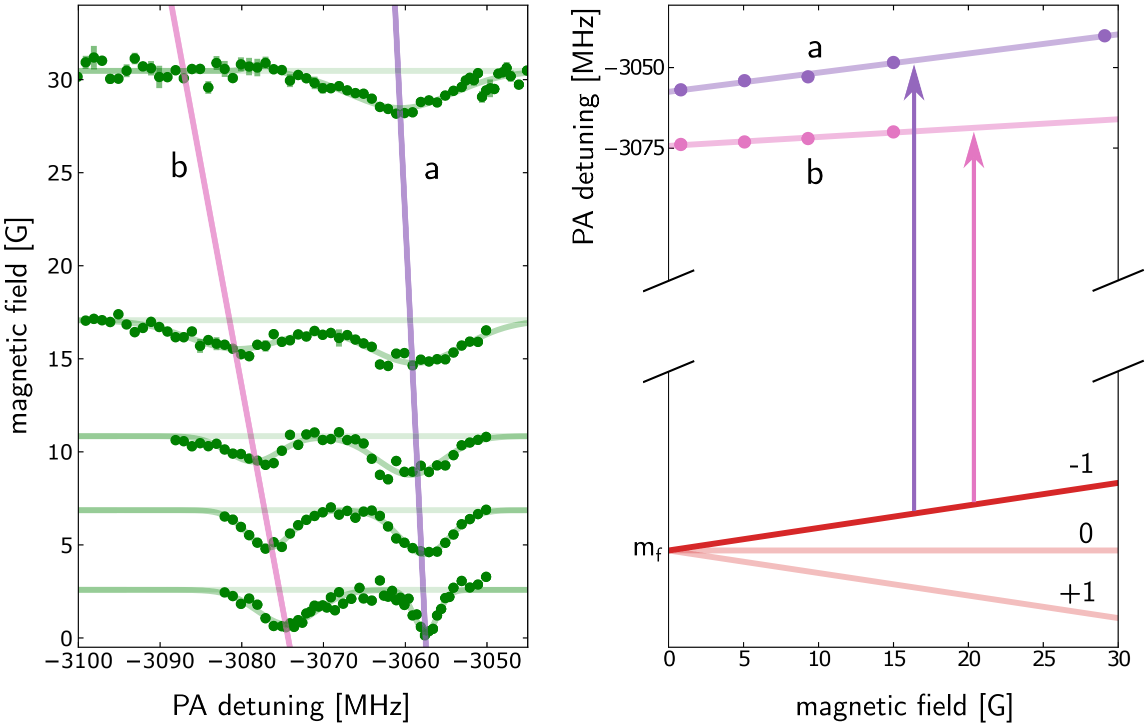

Figure 5.6.: Left: Both PA resonances in varying magnetic fields up to 30 G. The pink and purple lines represent linear fits to the peak positions of the lines (a) and (b). Right: Comparison of the atomic Zeeman shift for the $|F = 1, m_f = -1\rangle$ Rb ground state and the actual shifts of the excited molecular states. Data published in [51] and previously reported in [1] and [2].

Beyond the shift in magnetic fields, we also observe a broadening of the lines as the field strength increases. This broadening appears similar for both lines. At low magnetic fields, the FWHM is 3.0(3) MHz for line (a) and 6.3(7) MHz for line (b), with a broadening rate of 0.4(2) MHz/G and 0.5(2) MHz/G, respectively. Due to the decreasing line strength at higher fields, the fits exhibit relatively large uncertainties, making these broadening values less precise. However, the trend of increasing linewidth with field strength is evident.

5.1.3.4 Line Assignment

Tobias [1] and Bastian [2] made several attempts to explain the occurrence of a pair of resonances and the corresponding Zeeman shift. They considered various approaches, including Hund's coupling cases (c) and (e), angular momentum decoupling in magnetic fields, dipole-dipole interaction of magnetic moments, and Ω-doubling.

Unfortunately, none of these approaches fully explain the observed behavior, so I will not elaborate on them here. A comprehensive understanding requires further experimental and theoretical investigations, which are beyond the scope of this thesis.

5.1.3.5 Thermal Shift

Since the atoms are prepared in a thermal sample at finite temperatures, the thermal energy of collisions induces a shift in the transition frequency, which must be considered when determining the binding energy. The mean collision energy is given by

$$E_{therm} = \frac{3}{2}\mu k_B \left(\frac{T_{Rb}}{m_{Rb}} + \frac{T_{Yb}}{m_{Yb}} \right), \tag{5.3}$$

where μ is the reduced mass and k_B the Boltzmann constant. For typical experimental conditions ($T_{Rb} = 5\,\mu\mathrm{K}$ and $T_{Yb} = 1\,\mu\mathrm{K}$), this thermal shift amounts to $E_{therm} \approx h \cdot 0.2\,\mathrm{MHz}$.

5.1.3.6 Light Shift

As discussed in Section 2.3, transitions experience an AC-Stark shift (or light shift) due to the presence of both the trapping laser and the photoassociation laser.

Assuming that the molecular light shift is the sum of the individual atomic light shifts, the light shift induced by the trapping laser is already compensated, since the PA laser frequency is referenced to the atomic resonance measured in the same trap. However, determining the precise magnitude is valuable for estimating uncertainties arising from laser-induced fluctuations.

To quantify the light shift, we vary the trap intensity, which in turn affects the temperature and, consequently, the thermal shift described by Equation (5.3). After compensating for this effect, measuring the resonance shift at different trap powers yields a light shift coefficient of $-0.14(1)\,\mathrm{MHz/W}$ in the CODT configuration. Since the available power of the PA laser is very limited ($\sim 2\,\mathrm{mW}$ at the position of the atoms) and just sufficient to induce photoassociation, we were unable to measure the light shift caused by this laser. However, we assume it to be smaller than our measurement accuracy.

5.1.3.7 Linewidth

The above mentioned linewidths of 3.0(3) MHz and 6.3(7) MHz are more than one order of magnitude larger than the atomic linewidth of 182 kHz, which leads to the question where this effect comes from.

Since the linewidth is not further decreased by reducing the PA laser intensity, saturation broadening can not be the reason for this. Additionally, the Yb_2 resonances found during the search have smaller linewidths comparable to the atomic linewidth[2], so systematic broadening effects due to experimental conditions can be ruled out.

A possibility is that the broadening is introduced by additional decay channels, which can be of either radiative or non-radiative nature.

---

[2] The measured Yb_2 linewidths ranged from 1–5 MHz, but were probably saturation broadened, since we were searching for much weaker RbYb transitions.

Non-radiative Decay

One possible explanation for the broadening of PA lines is non-radiative decay within the ^{3}P manifold of Yb, such as transitions from ^{3}P$_1$ to ^{3}P$_0$.

A similar effect has been reported for inelastic predissociation from the ^{3}P$_2$ state in the context of magnetic Feshbach resonances for RbYb molecules [146]. The study found that these states exhibit significantly reduced lifetimes on the order of a few microseconds at most, leading to noticeable line broadening.

In addition to lifetime reduction due to predissociation, a decrease in line strength with increasing magnetic field has been observed. This can be attributed to Zeeman mixing of states with different j (but equal m_j) quantum number [147]. However, the calculations focused only on the ^{3}P$_0$ and ^{3}P$_2$ states. Further theoretical work is needed to determine whether a similar decay mechanism is responsible for the line broadening observed in our experiment. If the ^{3}P$_1$ state exhibits comparable behavior, this could also explain the broadening and reduced visibility of other PA transitions within our search range.

Radiative Decay

An alternative explanation for the increased linewidth is strong radiative decay from the excited RbYb* potential into the electronic $^2\Sigma_{1/2}$ molecular ground state [142]. Unlike non-radiative decay, which has no direct application to our experiment, radiative decay could lead to molecule formation in the electronic ground state. Although this process is non-coherent, identifying the specific vibrational states involved would provide valuable insights into the molecular ground state and guide future experiments. However, without a direct detection method or any clear indication of the decay pathways, we cannot confirm this hypothesis.

A key argument for this effect is the increasing transition dipole moment (TDM) for decreasing internuclear distances at the ^{3}P$_1$ asymptote, as calculated by [45]. This behavior stands in strong contrast to that observed near the Rb D1 line. An estimation of this effect conducted by Tobias [1], using these TDMs, suggests that the increase in TDM across all excited potentials is less than 10 % of the atomic dipole moment. This was deemed insufficient to fully explain the observed linewidth broadening in our measurements.

5.1.3.8 1-PA in optical Lattices

After completing the measurements in the CODT, we implemented optical lattices (1,2, and 3D) as final traps and performed photoassociation within these configurations. Since the results are discussed in detail in [2], I will summarize only the key findings for the −3057 MHz (a) line.

As outlined in Section Section 4.9.3.5, PA rate constants are expected to increase in optical lattices. However, in our experiments, significant heating within the lattice was observed ($T_{Rb} = 6\,\mu\text{K}$ and $T_{Yb} = 12\,\mu\text{K}$). Additionally, the estimated lattice filling remains below one atom per site (0.5 for Rb and 0.2 for Yb), limiting the number of atom pairs available for PA.

Despite these limitations, we obtained the following PA rate constants for 2D- and 3D optical lattices[3]:

$$\begin{aligned} K_{2D} &= 8.5(1) \cdot 10^{-13}\text{cm}^3/\text{s} \\ K_{3D} &= 1.0(2) \cdot 10^{-12}\text{cm}^3/\text{s}, \end{aligned} \tag{5.4}$$

corresponding to a factor-of-two increase in the 3D lattice compared to the CODT.

To achieve a significant increase in PA rates, lattice loading must be improved. A promising approach would be to load a dual-species BEC into the lattice and perform PA in a mixed Mott insulator [2].

5.1.3.9 Conclusion

Our study on 1-PA of RbYb near the intercombination line of Yb covered a frequency range of 0.1–11 GHz, with a gap between 3.2 and 3.7 GHz due to a temporary deterioration of overall experimental stability. Given that the observed resonance is located at 3.1 GHz, and based on the considerations in Section 5.1.1, we assume that no additional line exists within this gap and are confident that we have identified the strongest resonance. This resonance appears as a closely related pair, suggesting a strong connection between the two lines. However, despite our efforts, we were unable to provide a conclusive explanation for this splitting.

We characterized the identified lines by analyzing their shifts (Zeeman, AC-Stark and thermal), determining their linewidths, and discussing their relative strengths. From these measurements, we established the binding energies in zero-field as −3057.2(3) MHz and −3074.3(3) MHz.

Thanks to the lower temperatures and improved atomic sample preparation in the CODT, we achieved a PA rate coefficient an order of magnitude higher than the results reported in [51], which could be further increased in a 3D optical lattice.

For a coherent transfer of individual atoms to the molecular ground state – such as via a STIRAP process (see Section 7.2.1) – high Rabi frequencies are required. The feasibility of efficient molecule production near the $^3\text{P}_1$ asymptote, as well as the achievable Rabi frequency, can be assessed through two-photon photoassociation spectroscopy, which is the focus of the following chapter.

---

[3] PA in an 1D lattice did not lead to higher PA rates.

5.2 Two-Photon Photoassociation of the $^2\Sigma_{1/2}$ ground State of RbYb

After an extensive search for one-photon photoassociation lines, we have finally identified a suitable resonance. This allows us to perform two-photon photoassociation spectroscopy to investigate the $^2\Sigma_{1/2}$ ground state of ^{87}Rb^{170}Yb, as detailed in Section 2.4.1.

In this chapter, I present the results of two-photon photoassociation spectroscopy near the intercombination line of Yb, using the identified 1-PA resonance at 3.1 GHz as the intermediate state. We have located the two least bound states, determined their energy shifts, conducted dark resonance spectroscopy, and analyzed Rabi frequencies.

We follow the notation of Section 2.4.1, where the lasers are labeled as free-bound (FB) and bound-bound (BB).

Thanks to previous work on photoassociation near the D1 line of Rb (see Chapter 3 and [50, 57, 64]), we have a relatively precise knowledge of the ground state. Although these measurements were not performed with the ^{170}Yb isotope, Borkowski et al. [64] predicted the binding energies for the ^{87}Rb^{170}Yb combination with high accuracy, which reduced search time significantly. The predicted values and our experimental values are listed in Table 5.2.

Δv	v	E_B [h·GHz]		exp. E_B [h·GHz]
		F=1	F=2	F=1
-1	65	-0.103	-0.103	-0.113(15)
-2	64	-1.019	-1.017	-1.029(16)
-3	63	-3.675	-3.673	
-4	62	-9.018	-9.013	
-5	61	-17.997	-17.990	

Table 5.2.: Predicted binding energies for the five least bound vibrational states (R=0) [64] and measured data for the two least bound states for F=1.

5.2.1 Two-Photon Photoassociation near the Intercombination Line

The straightforward approach for 2-PA is to begin with the case $\delta_{FB} = 0$ (see Section 2.4.1), meaning the free-bound laser is on resonance while the bound-bound laser is scanned. The experimental procedure closely follows that of 1-PA, but now both lasers remain on during the whole PA step. The data were obtained using the stronger 1-PA resonance at -3057 MHz, though the experiment could also be conducted using the other line.

With this approach, we identified the two least bound vibrational states $\Delta v = -1$ and $\Delta v = -2$, using the laser setups described in Section 4.5. Both states are shown in

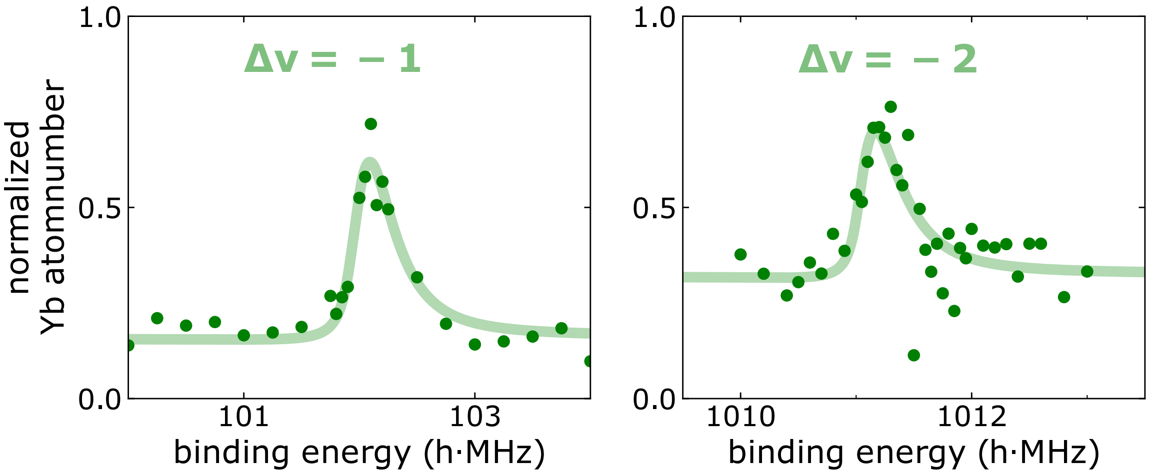

Figure 5.7.: Two-photon photoassociation spectra with fits based on Equation (2.49). Data published in [51] and previously reported in [1] and [2].

Figure 5.7, where the fit follows Equation (2.49)[1].

The observed Lorentzian peaks are centered at 101.97(1) MHz ($\Delta v = -1$) and 1011.0(1) MHz ($\Delta v = -2$), with linewidths of 0.17(2) MHz and 0.23(2) MHz, respectively. The observed linewidths are similar to the natural linewidth of the atomic Yb transition, since the intermediate molecular state is discrete and free from the thermal broadening associated with atomic scattering states. The measured binding energies are in agreement with the theoretical predictions, although the data at the D1 line, which served as an input to the theoretical predictions, had huge uncertainties due to the broader linewidth and the wavemeter used. Unlike the broader 1-PA lines, these linewidths are comparable to the natural linewidth of the Yb intercombination transition.

5.2.2 Dark Resonance Spectroscopy

Now that we identified the locations of the two least bound vibrational states, we can perform a dark resonance spectroscopy as described in Section 2.4.1. In this approach the bound-bound laser is held on resonance ($\delta_{BB} = 0$) while the free-bound laser is scanned. The results of these measurements are shown in Figure 5.8.

As we scan the free-bound laser, we observe the characteristic dark resonance feature: a sharp peak emerging within the loss spectrum of the 1-PA resonance. This peak is fitted using Equation (2.49), incorporating the thermal distribution of scattering states.

A key advantage of dark resonance spectroscopy is that it provides access to both Rabi frequencies, Ω_{FB} and Ω_{BB}, which are crucial for evaluating coherent processes such as *STIRAP*. The fitted values for both transitions are $\Omega_{FB} \approx 2\pi\cdot 1\,\text{kHz}$ and $\Omega_{BB} \approx 2\pi\cdot 1\,\text{MHz}$. The corresponding laser powers are $P_{FB} = 0.5\,\text{mW}$ and $P_{BB} = 0.1\,\text{mW}$ ($\Delta v = -1$) and

---

[1] For $\delta_{FB} = 0$, this corresponds to a Lorentzian line shape.

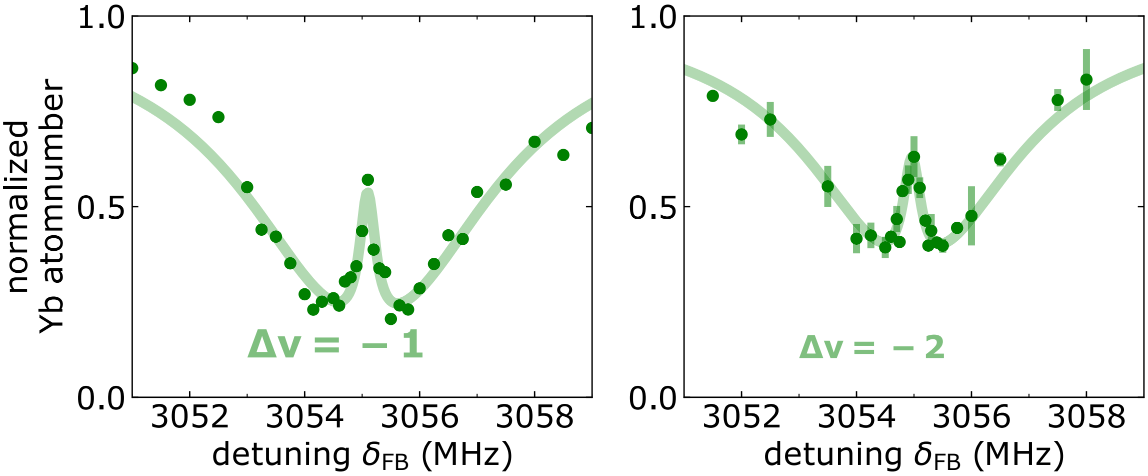

Figure 5.8.: Dark resonance spectroscopy of the two least bound states of the RbYb ground potential. Data published in [51] and previously reported in [1] and [2].

$P_{BB} = 0.02\,\mathrm{mW}$ ($\Delta v = -2$).

For bound-bound Rabi frequencies significantly exceeding the transition linewidth, Autler-Townes splitting (see Section 2.3.2) would be expected. This effect is commonly used to determine Rabi frequencies and Franck-Condon factors. However, due to the limitations imposed by off-resonant scattering, the available laser power was insufficient to reach this regime.

5.2.3 Shifts

As in the case of 1-PA, we examine line-shift mechanisms to determine precise values for the binding energies.

5.2.3.1 Zeeman Shift

The Zeeman shift was determined by scanning both transitions under increasing magnetic fields and found to be 0.7(1) MHz/G. This indicates that the least-bound states of the ground-state potential experience the same Zeeman shift as the scattering state—namely, that of the $|f = 1, m_f = -1\rangle$ hyperfine level of Rb, which shifts by 0.7 MHz/G. Moreover, the absence of additional spectral lines suggests that the bound-bound laser does not couple to other magnetic Zeeman or hyperfine states of Rb.

5.2.3.2 Thermal Energy

Since thermal effects predominantly impact the scattering state, the thermal energy was estimated to be on the order of $h \cdot 0.2\,\mathrm{MHz}$, as discussed for 1-PA in Section 5.1.3.5. This contribution manifests in the asymmetric shape of the fits in Figure 5.8 and broadens the dark resonance, hindering an accurate determination of the dark state's lifetime which is expected to be significantly longer. In the analysis shown here, the thermal energy is not treated as a free fit parameter but is assumed to be of the aforementioned magnitude, consistent with typical experimental conditions and in good agreement with the observed data.

5.2.3.3 Light Shift

Due to the nearly identical polarizabilities of the scattering state and the least bound states, the light shift caused by the trapping light effectively cancels out, unlike in the case of the excited state (see Section 5.1.3.6). However, for more deeply bound states, changes in polarizability may introduce light shifts that need to be taken into account.

5.2.4 Franck-Condon Factors

Using the Rabi frequencies obtained from dark resonance spectroscopy (see Section 5.2.2), we can now estimate the bound-bound Franck-Condon factors. Assuming that the dipole matrix elements remain similar to atomic values, we use the intensity of the photoassociation laser I_{PA}, derived from the power and the measured beam waist of 110 µm ($1/e^2$ radius).

The Franck-Condon factors are then given by:

$$f^{FC} = \left(\frac{\Omega_{BB}}{\Omega_{at}}\right)^2, \quad \text{with} \quad \Omega_{at} = \gamma\sqrt{\frac{I_{PA}}{2\,I_{sat}}}. \tag{5.5}$$

Here, I_{sat} is the atomic saturation intensity and γ the natural linewidth of the atomic transition. Assuming perfect alignment of the PA beam, we estimate the Franck-Condon factors as:

$$\begin{aligned} &f^{FC}(\Delta v = -1) \approx 0.02 \\ &f^{FC}(\Delta v = -2) \approx 0.08. \end{aligned} \tag{5.6}$$

These values provide a lower bound for the Franck-Condon factors, as they assume ideal beam alignment.

5.2.5 Limitations

Operating at relatively small detunings from atomic transitions, our setup is primarily limited by off-resonant excitation. For both 1-PA and 2-PA, higher laser intensities would result in significant losses, preventing an increase in Rabi frequencies.

Using an EOM to generate sidebands for the second photon introduces additional complications, as higher-order sidebands may lie close to atomic transitions. For instance, in the $\Delta v = -2$ transition, the third sideband appears at $3 \cdot f_{-2} = 3.03\,\text{GHz}$, only detuned by 0.02 GHz from the atomic line. Similarly, for the $\Delta v = -3$ transition at approximately -3.7 GHz, the bound-bound laser is detuned only by ~ 0.6 GHz, significantly reducing the lifetime.

For these reasons, achieving either a stronger free-bound transition or utilizing more deeply bound states in the ground potential would be highly desirable. This would require an additional independent laser source, such as an ECDL (see Section 4.5).

5.2.6 Conclusion

We have measured and analyzed the two least bound vibrational states of the $^2\Sigma_{1/2}$ ground-state potential of ^{87}Rb^{170}Yb using two-photon photoassociation spectroscopy. Additionally, we conducted dark resonance spectroscopy to determine Rabi frequencies and estimate the corresponding Franck-Condon factors. Including shift effects, we determined the binding energies to be $E_B(\Delta v = -1) = -h \cdot 101.9(1)\,\mathrm{MHz}$ and $E_B(\Delta v = -2) = -h \cdot 1011.1(1)\,\mathrm{MHz}$, in good agreement with theoretical predictions [64]. Finally, we outlined the limitations of our experimental approach.

6

Lessons Learned for RbYb Production – Light-Shift Spectroscopy near the D1 Line of Rb

After the presentation of our photoassociation experiments and the analysis of the results, I will now turn to a discussion of the implications of our results for the next steps on the experimental agenda. I will explore how the gained knowledge could lead to promising pathways for efficient molecule production in the ground state using the intercombination line of Yb.

Building on ideas that have emerged from the work of Tobias [1] and Bastian [2], I will develop a plan on how the use of light-shift spectroscopy near the D1 line of Rb to proceed towards our goal of creating dipolar ground-state RbYb molecules.

6.1 Evaluation of Possible Ground-State Production Using the Intercombination Line

We will first recap our results from photoassociation spectroscopy of ^{87}Rb^{170}Yb near the ^{1}S$_0$ → ^{3}P$_1$ intercombination line of Yb and in what manner this can help to produce RbYb molecules in the absolute ground state.

We have reported on the extensive search of 1-PA resonances with a range of 0.5–11 GHz detuning from the atomic line in Section 5.1.2 and the observation of a single pair resonance in Section 5.1.3, which was analyzed in the manner of shifts and especially line strengths.

The key aspect for the path towards ground-state production is that we do not expect to find a stronger 1-PA transition in this region, and even if we would implement the possible improvements explained above and also in [1, 2], we are limited by off-resonant scattering, preventing higher free-bound Rabi frequencies. An efficient STIRAP process also requires two transitions with similar Rabi frequencies, which is not the case here.

As a result, we, unfortunately, do not expect to achieve efficient molecule production using the intercombination line of Yb.

Nevertheless, the observation of a narrow dark resonance led us to think of a new approach by combining the features of intercombination and D1 line spectroscopy, where we make use of the narrow linewidth of the dark resonance and the strong coupling strengths at the D1 line of Rb. With this approach, I have developed a method to explore the potential of the excited state near the $^2\mathrm{P}_{1/2} + {}^1\mathrm{S}_0$ asymptote and the ground state in detail. This light-shift spectroscopy method will be explained in the next chapter.

6.2 Light-Shift Spectroscopy near the D1 Line of Rb

This section introduces a novel approach to our path to the absolute rovibronic ground state of RbYb using light-shift spectroscopy. The method combines the strong Rabi frequencies achievable near the D1 line of Rb (see Chapter 3) with the narrow dark resonance observed close to the intercombination line of Yb (see Section 5.2).

Due to the negligible wavefunction overlap, a direct two-photon transition from the atomic scattering state to the rovibronic ground state is not feasible. Therefore, a four-photon process is proposed. This approach begins with a (coherent) two-photon process (see Section 7.2), creating a weakly bound molecule in the ground-state potential. A third laser then couples this intermediate state to a more deeply bound state in the excited potential, from which a fourth laser can transfer the molecule to the absolute ground state. This scheme is illustrated in Figure 6.1.

While several vibrational levels near the dissociation limits of both potentials are known (see Chapter 3), coherent population transfer into a vibrational level of the ground state has not yet been realized. Therefore, we aim to explore the excited state potential further – particularly the location of deeply bound levels that can serve as an intermediate state[1] for molecule production.

6.2.1 The Third Photon

Predicting the absolute binding energies of deeply bound states – and thus the wavelength of the third laser needed to access them – is a nontrivial task.

To simplify understanding the multi-photon nature of the process, we first introduce consistent labeling for the involved molecular states:

$|0\rangle$ – Atomic scattering state.

$|1\rangle$ – Weakly bound excited state near the dissociation threshold, coupled from the scattering state via 1-PA laser (quantum number $\Delta v'$).

$|2\rangle$ – Weakly bound ground state, addressed via 2-PA (quantum number Δv).

$|3\rangle$ – Deeply bound excited state, addressed via the third laser (quantum number v').

---

[1] Labeled as transition (3) in Figure 6.1.

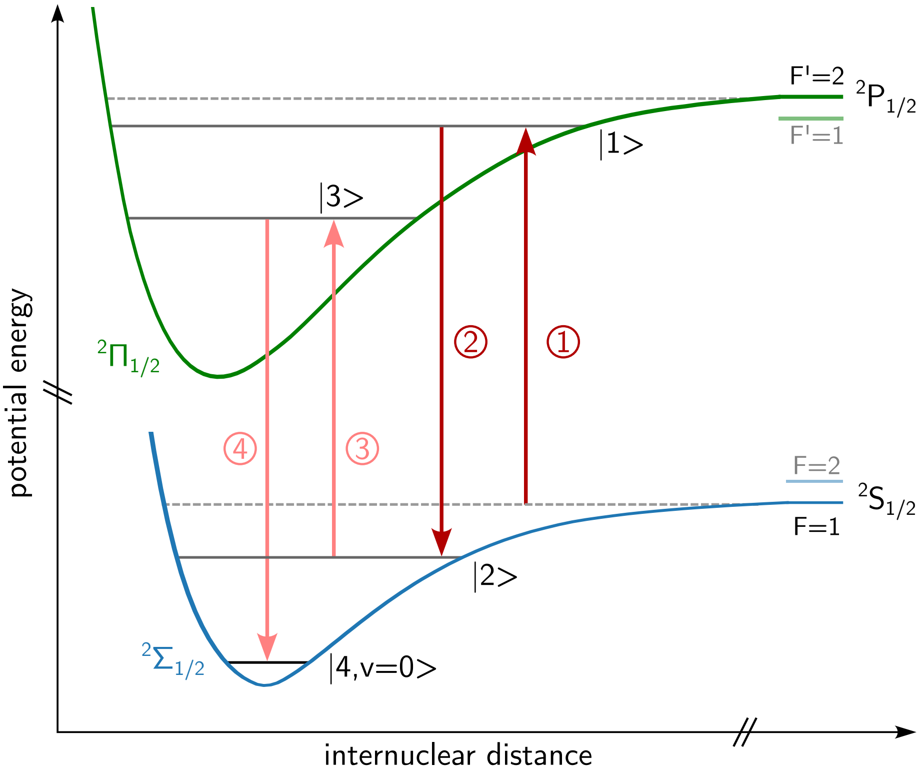

Figure 6.1.: Scheme of a fully optical pathway to the rovibronic ground state of RbYb. Potential energy curves of the $^2\Sigma_{1/2}$ ground state and the $^2\Pi_{1/2}$ excited state near the Rb D1 line. The horizontal dashed lines indicate the dissociation threshold. Dark red arrows (1 and 2) represent the 1-PA and 2-PA transitions; Pink arrows (3 and 4) represent transitions to the deeply bound vibrational levels.

$|4\rangle$ – Absolute rovibronic ground state (quantum number $v = 0$).

Note that vibrational quantum numbers for weakly bound states are referenced to the dissociation limit and are denoted as Δv or $\Delta v'$, while those for deeply bound states are counted from the bottom of the potential and labeled v and v'.

Münchow [124] proposed a method for molecule formation and estimated a suitable wavelength range for the third photon by evaluating Franck-Condon factors for the ^{87}Rb^{176}Yb isotope combination. Castor confirmed these predictions in her master's thesis [149], and constructed a laser system capable of driving this transition.

For efficient molecule production, both excited states ($|1\rangle$ and $|3\rangle$) must exhibit good Franck-Condon overlap with their respective ground states. This requires maximizing the product of the two FCFs involved.

Transitions (1) and (2) in Figure 6.1 were characterized experimentally by [57]. The strongest usable transitions to $|1\rangle$ are either $|F' = 2, \Delta v' = -9\rangle$ or $|F' = 2, \Delta v' = -11\rangle$. The corresponding FCFs for state $|2\rangle$ have been calculated by [124] and are listed in

State	Parameter	Shundalau [45]	Borkowski [64]	Sørensen [58]	Meyer [150]	Tohme [138]
$^2\Sigma_{1/2}$	$D_E\,[\mathrm{cm}^{-1}]$	531.1	704.5	844	193	700
	$R_E\,[a_0]$	9.178	9.014	8.882	10.22	9.447
	$\omega_E\,[\mathrm{cm}^{-1}]$	36.40	26.58	29.46	12.6	27.82
$^2\Pi_{1/2}$	$D_E\,[\mathrm{cm}^{-1}]$	6592.8	—	7688	3590	—
	$R_E\,[a_0]$	7.334	—	7.389	7.389	—
	$\omega_E\,[\mathrm{cm}^{-1}]$	73.939	—	69.441	70.9	—

Table 6.1.: Morse potential parameters from various theoretical models for the $^2\Sigma_{1/2}$ ground state and the $^2\Pi_{1/2}$ excited state of the RbYb molecule.

Table 3.2, with maxima observed at $|\Delta v = -5\rangle$ (FCF = 0.2) or $|\Delta v = -6\rangle$ (FCF = 0.13).

Unfortunately, no experimental data are currently available for deeply bound states, which can be used to estimate the value of FCFs and thus the transition matrix. Therefore, to identify a suitable intermediate state $|3\rangle$, with strong coupling to both $|2\rangle$ and $|4\rangle$, theoretical potential energy curves must be used. Münchow used ab-initio calculations for the ground state and a Lennard-Jones potential for the excited state with $C_6 = -5684\,E_h\,a_0^6$ and $C_{12} = 2.28105{\cdot}10^8\,E_h\,a_0^{12}$. In contrast, Castor applied Morse potentials, while Sørensen et al. [58] used a relativistic coupled-cluster approach.

The optimal intermediate state $|3\rangle$ is the one for which the product $f_4^{FC}\cdot f_3^{FC} = |\langle 4|3\rangle|^2\cdot|\langle 2|3\rangle|^2$ has to be maximized. Here, I will give the numerical procedure for finding the vibrational levels and the corresponding wavelength, following the treatments in [149] using Morse potentials.

6.2.1.1 Modeling Potentials

The first and most crucial step in predicting the energy (and thus the transition wavelength) of the optimal intermediate state $|3\rangle$ is selecting a suitable model for the potential energy curves of both the ground and excited state. Since we are now focusing on more deeply bound molecular states, we employ Morse potentials, as introduced in Section 2.1, and described by:

$$V(r) = D_E \cdot \left(1 - e^{-\omega_E\sqrt{\frac{\mu}{2D_E}}(r-R_E)}\right)^2. \tag{6.1}$$

The Morse potential is characterized by three parameters: the harmonic frequency ω_E, the potential depth D_E, and the equilibrium interatomic distance R_E, where the potential reaches its minimum. Several theoretical studies have proposed values for these parameters [45, 58, 64, 138, 150] and are provided in Table 6.1. As seen in the table, the predicted values vary significantly across models – particularly those from Meyer, which deviate

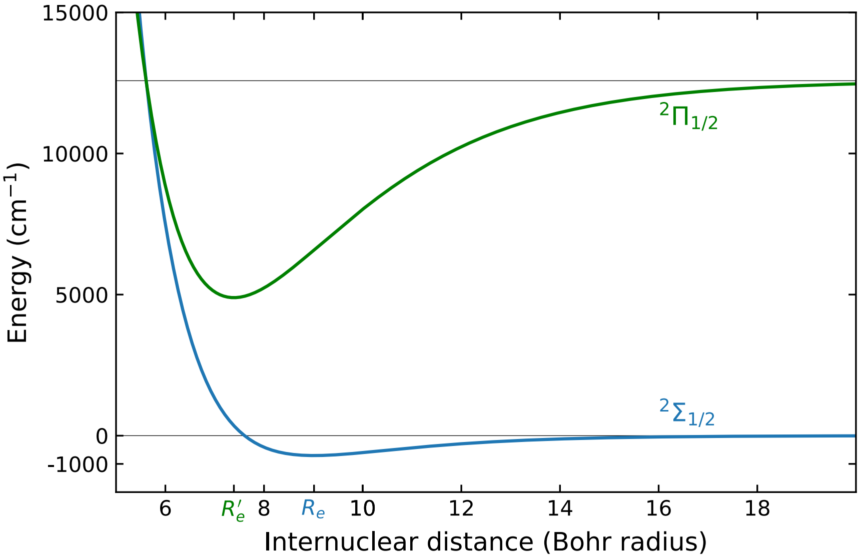

Figure 6.2.: Morse potential energy curves for the $^2\Sigma_{1/2}$ ground state (blue) and $^2\Pi_{1/2}$ excited state (green) of the RbYb molecule, using parameters from Borkowski [64] and Sørensen [58], respectively.

notably from the others. This spread in results highlights the need for further experimental data to validate and refine these theoretical models.

For the purpose of this work, we adopt the Morse parameters from Borkowski [64] for the $^2\Sigma_{1/2}$ ground state – since these have been obtained using experimental data – and for the $^2\Pi_{1/2}$ excited state, we use Sørensen's results [58] which are based on the most elaborate numerical calculation. This model potential reproduces the binding energies of the excited-state potential to within approximately $1\,\mathrm{cm}^{-1}$, whereas a potential based on, for example, Shundalau's parameters shows deviations of up to about $3\,\mathrm{cm}^{-1}$. The resulting potential energy curves are shown in Figure 6.2.

6.2.1.2 Solving Schrödinger's Equation

Once suitable models for the potential energy curves have been selected, we proceed to solve the Schrödinger Equation (2.1) to determine the vibrational states and calculate their energies. This is done numerically by discretizing the spatial coordinate r onto a finite grid. Using a second-order finite-difference approximation for the second derivative, we obtain the discretized form of the Schrödinger equation:

$$-\frac{\hbar^2}{2\mu}\frac{\Psi_{i+1}-2\Psi_i+\Psi_{i-1}}{(\Delta r)^2}+V_i\Psi_i=E\Psi_i, \tag{6.2}$$

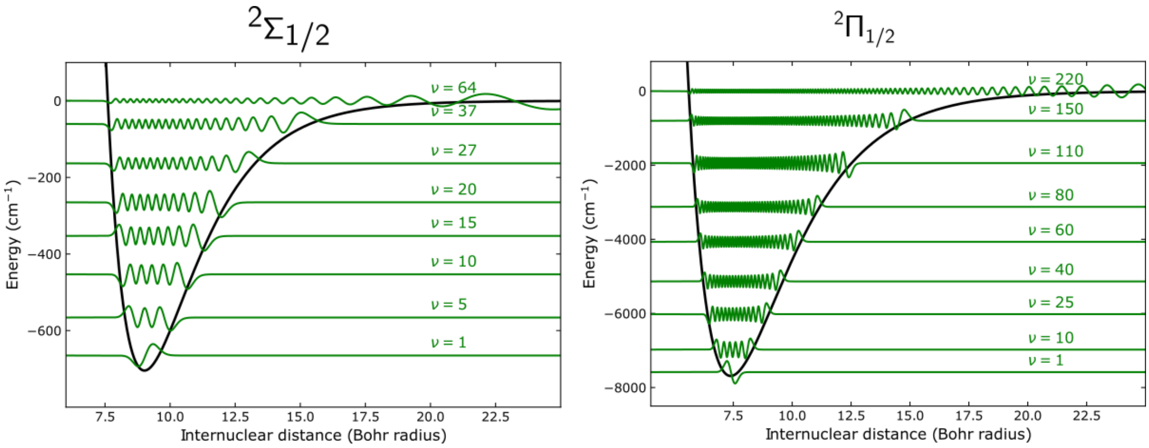

Figure 6.3.: Potential energy curves and selected wavefunctions of the ground (left) and excited state (right).

where Ψ_i denotes the wavefunction evaluated at the i-th grid point and Δr is the grid spacing. This equation can be reformulated as tridiagonal matrix equation:

$$\begin{pmatrix} \frac{\hbar^2}{\mu(\Delta r)^2}+V_1 & -\frac{\hbar^2}{2\mu(\Delta r)^2} & 0 & 0 & \dots \\ -\frac{\hbar^2}{2\mu(\Delta r)^2} & \frac{\hbar^2}{\mu(\Delta r)^2}+V_2 & -\frac{\hbar^2}{2\mu(\Delta r)^2} & 0 & \\ 0 & -\frac{\hbar^2}{2\mu(\Delta r)^2} & \frac{\hbar^2}{\mu(\Delta r)^2}+V_3 & -\frac{\hbar^2}{2\mu(\Delta r)^2} & \\ \dots & & & & \dots \end{pmatrix} \Psi(r) = E\Psi(r). \tag{6.3}$$

This eigenvalue problem is then solved numerically using the `scipy.sparse.linalg.eigsh` Python package, yielding the vibrational eigenstates (wavefunctions), the associated energies, and the number of bound states supported by each potential. The resulting potential energy curves and several representative wavefunctions are shown in Figure 6.3. The number of bound vibrational states obtained in this model is $N_g = 53$ for the ground state and $N_e = 222$ for the excited state. It should be noted that the actual number of ground-state levels is closer to ~ 66, according to Borkowski. This discrepancy arises, because the Morse potential used here does not accurately reproduce the long-range behavior of the potential. Borkowski instead employs a Lennard-Jones-type potential to better capture the asymptotic form. Nevertheless, since the level spacing near the dissociation limit is small, this approximation does not significantly affect our goal of estimating the wavelength region for the third photon. With the wavefunctions at hand, we can now compute the Franck-Condon factors and identify a suitable intermediate state $|3\rangle$.

6.2.1.3 Franck-Condon Factors

As outlined above, the optimal intermediate state $|3\rangle$ is the one that maximizes the product $f_4^{FC} \cdot f_3^{FC}$. We begin calculating the FCFs f_4^{FC} from the ground state $|4, v = 0\rangle$ to the various intermediate states $|3, v'\rangle$, as shown in Figure 6.4. The maximum occurs at $v' = 26$,

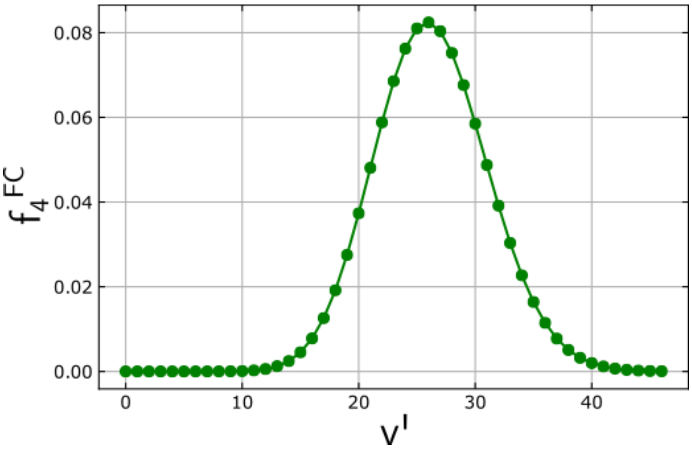

Figure 6.4.: Franck-Condon factors f_4^{FC} for the transition $|4, v = 0\rangle \rightarrow |3, v'\rangle$. The maximum FCF occurs at $v' = 26$.

and states with FCFs with a value of more than half of the maximum value lie in the range of $v' = 21 - 31$.

Recalling the results from two-photon photoassociation experiments by Münchow (see Chapter 3 and Table 3.2), the initial state is expected to be either $|2, \Delta v = -5\rangle$ or $|2, \Delta v = -6\rangle$, corresponding to $v = 49$ or $v = 48$ in the modeled potentials used here, because they have the largest experimentally determined FCFs. The products $f_4^{FC} \cdot f_3^{FC}$ for different excited states (within the high-FCF range) and initial vibrational states (near $|2\rangle$) are shown in Figure 6.5 on the left side. The right panel shows the FCFs for the initial state $v = 49$. From this analysis, we identify the intermediate state $|3, v' = 25\rangle$ as yielding

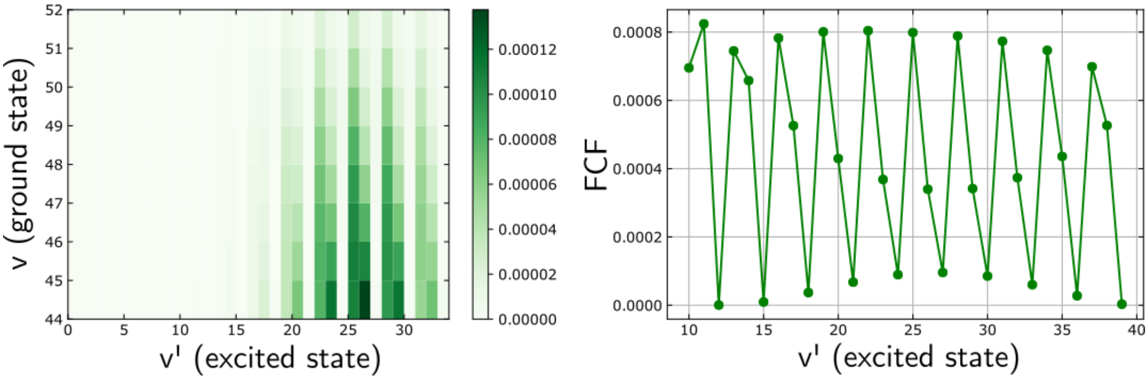

Figure 6.5.: Left: Color-coded products of FCFs for transitions from initial state v and excited state v'. Right: Franck-Condon factors for the starting state $|2, \Delta v = -5\rangle$.

the largest product $f_4^{FC} \cdot f_3^{FC}$, making it the most favorable candidate for efficient state transfer towards the absolute ground state of RbYb.

6.2.1.4 Wavelength of the Third Photon

Having determined a suitable intermediate state, we can now estimate the wavelength of the third photon required to couple the initial state $|2, \Delta v = -5\rangle$ to the selected intermediate state $|3, v' = 25\rangle$. Based on the calculated eigenenergies from our Morse potential model, this transition corresponds to a photon wavelength of

$$\lambda_3 = 1525\,\text{nm}.$$

To account for all intermediate levels ($v' = 21 - 31$) with FCFs at least 50 % of the maximum, we obtain a broader range of possible transition wavelengths. These fall within the range

$$\lambda_3 = 1445\,\text{nm to } 1585\,\text{nm},$$

which defines the relevant spectral window for the wavelength of the third laser.

6.2.1.5 Conclusion

To conclude the theoretical analysis presented above, we compare our results with predictions based on alternative models. By employing different sets of Morse parameters – or other potential forms – from Table 6.1, we obtain different transition wavelengths and corresponding optimal intermediate states. A summary of these model-dependent predictions is presented in Table 6.2. Even though Sørensen's calculation is purely theoretical, it is likely the most accurate one for the excited state. For the ground state, calculations that incorporate experimental data, such as those by Borkowski, are probably more precise and thus used here. However, the predicted wavelengths and vibrational quantum numbers vary due to differences in the underlying potentials, but these results allow us to estimate the experimental effort required to locate the transition.

	Vib. State v'	Wavelength [nm]
Castor [149]	23	1554
Münchow [57]	21	1525
Sørensen [58]	24	1518
Here	25	1525

Table 6.2.: Vibrational states $|3\rangle$ with the largest Franck-Condon overlap and corresponding wavelengths from different calculations. Data from Sørensen were received upon request.

Assuming a search range of 10 nm ($\approx$ 1300 GHz), a step size of 1 MHz, and a sequence time of 45 s per data point, a full scan would take around 2 years of continuous measurement. Even though the average Ph.D. duration in our group tends to be on the longer

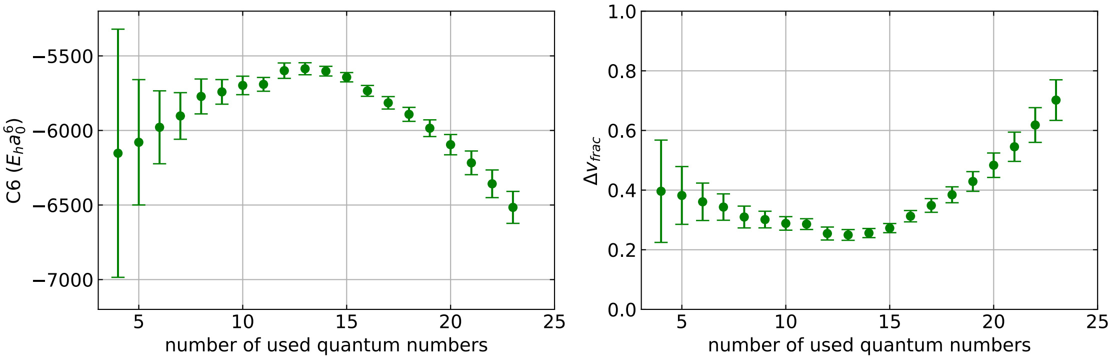

Figure 6.6.: C_6 dispersion coefficient and fractional part Δ_{frac} of the fractional quantum number v_D for varying numbers of vibrational levels used in the LeRoy-Bernstein fit for the isotope combination ^{87}Rb^{176}Yb.

side, this is still a bit excessive. Nevertheless, a laser system operating at 1520 nm – which covers a significantly broader range – is already available (see Section 6.2.5.2).

Therefore, it is indispensable to gain further information about the potential energy curves – particularly of the $^2\Pi_{1/2}$ state – as discussed in the following section.

6.2.2 Exploring the $^2\Pi_{1/2}$ Excited Potential

A crucial step toward identifying intermediate states with favorable Franck-Condon overlap is to refine our knowledge of the excited $^2\Pi_{1/2}$ potential. Improved modeling of this potential by including more deeply bound states could lead to more accurate predictions of vibrational levels.

As summarized in Table 3.3, more than 20 vibrational levels of the $^2\Pi_{1/2}$ for ^{87}Rb^{176}Yb but only one for ^{87}Rb^{170}Yb have been observed. Consequently, we will begin by searching for additional weakly bound states in ^{87}Rb^{170}Yb. Using mass scaling (see Equation (2.10)), their locations can be estimated to reduce search time. However, as shown in Table 3.3, deviations of up to 1.6 GHz have been observed between predictions and measurements, as further illustrated in Figure 6.6. Since the energy difference in the mass scaling formula depends not only on the reduced mass μ but also on the fractional part Δ_{frac} of the fractional quantum number v_D, the limitations of the LeRoy-Bernstein approach become evident.

Figure 6.6 shows the fitted C_6 coefficient and Δ_{frac} for ^{87}Rb^{176}Yb as a function of the number of experimentally determined vibrational states included in the fit. The most weakly bound levels were used in all cases. The error bars represent fit uncertainties. Clearly, C_6 and Δ_{frac} are not independent parameters.

While the smallest uncertainties in Figure 6.6 (for 15 used quantum numbers) are obtained for the values given by [57], deviations remain possible. A more accurate determination of Δ_{frac} would require locating the most weakly bound vibrational level $\Delta v' = -1$, which remains experimentally challenging due to high off-resonant scattering rates. Based on this knowledge and the mass scaling from Equation (2.9) with ^{87}Rb^{176}Yb, we can estimate the binding energies of vibrational levels (here $\Delta v' = -6$) of ^{87}Rb^{170}Yb using the values from Figure 6.6. The result is illustrated in Figure 6.7. The maximum deviation in the calculated binding energies is approximately $0.2\,\mathrm{cm}^{-1}$ ($\sim 6\,\mathrm{GHz}$). Since we expect the actual values of C_6 and Δ_{frac} to lie closer to the center of the plotted range (for vibrational quantum numbers 10 to 20), we estimate the relevant search range to be smaller. Additional levels can then help to determine a more accurate value for Δ_{frac}.

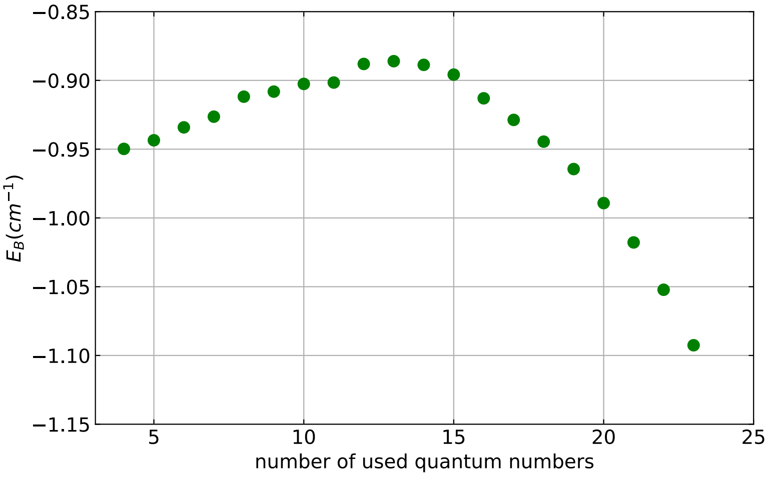

Figure 6.7.: Calculated binding energies of the $\Delta v' = -6$ vibrational state of ^{87}Rb^{170}Yb using mass scaling (Equation (2.9)) and the experimental data from ^{87}Rb^{176}Yb versus the number of used quantum numbers, which corresponds to different Δ_{frac}.

6.2.3 Light-Shift Spectroscopy

The basic principle of light-shift spectroscopy is illustrated in Figure 6.8 and the corresponding potential energy scheme in Figure 6.9, and has already been theoretically motivated in Section 2.3.3. The underlying idea is to reduce the search time by increasing the possible frequency step size. This can be achieved by using the narrow dark resonance (see Section 5.2.2) near the Yb intercombination line as a probe transition, as outlined below.

We probe a weakly bound state $|2, \Delta v = -1, -2\rangle$ by keeping both the 1-PA and 2-PA lasers (near the intercombination line of Yb) on resonance with the molecular transitions, such that the system is positioned on the narrow peak of the dark resonance. The corresponding bound-bound Rabi frequency and linewidth is $\Omega_1 = 1\,\mathrm{MHz}$ and $\gamma = 0.2\,\mathrm{MHz}$, respectively. Due to the coupling of the 2-PA laser, the free-bound laser is shifted out of

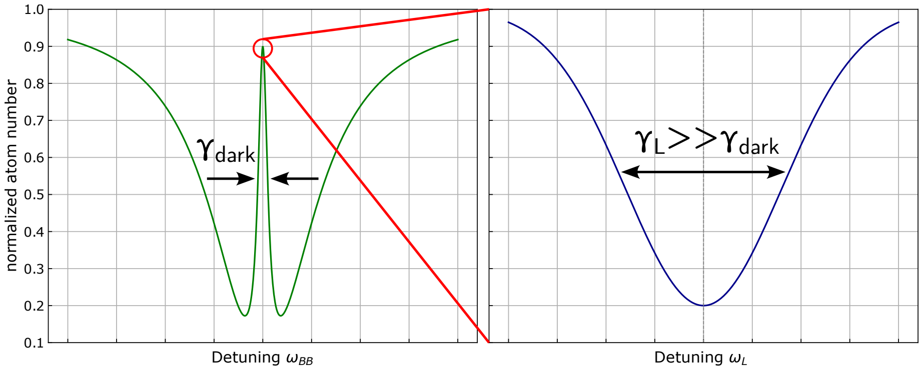

Figure 6.8.: Spectroscopic schematic of light-shift spectroscopy. Left: Typical dark-resonance signal obtained by scanning the bound-bound laser while keeping the free-bound laser on resonance. The linewidth γ_{dark} is on the order of the natural linewidth of the atomic transition (in our case, approximately 0.2 MHz). Right: When both the free-bound and bound-bound lasers are on resonance, we observe a loss-of-loss signal and atoms remain detectable. However, if the coupling laser is scanned for light-shift spectroscopy and the induced light shift ΔE_e exceeds the dark-resonance linewidth γ_{dark}, the transition shifts out of resonance. As a result, the free-bound laser becomes resonant again, leading to atom loss. This light-shift linewidth is much larger than that of the dark resonance.

1-PA resonance and we do not see a loss of atoms in absorption imaging.

Next, we couple this state – either $|2, \Delta v = -1\rangle$ (bound by $h \cdot 102\,\text{MHz}$) or $|2, \Delta v = -2\rangle$ (bound by $h \cdot 1011\,\text{MHz}$) – to a weakly bound state $|3, \Delta v'\rangle$ in the ${}^2\Pi_{1/2}$ potential near the Rb D1 line using a coupling laser with a wavelength that is larger than the Rb D1 atomic transmission wavelength of 795 nm. This configuration corresponds to a 3-level V-scheme, illustrated in Figure 6.9 b).

Since the previously observed bound-bound Rabi frequencies at the D1 line are significantly higher than those in the dark resonance configuration, we can apply the model described in Section 2.3.3 and recalling Equation (2.23), the light shift is given by: $\Delta E_e = \frac{\hbar\Omega_2^2}{4\delta}$. In this scheme, the dark resonance transition $|1\rangle \rightarrow |2, \Delta v = -1, -2\rangle$ acts as the probe transition, while $|2, \Delta v = -1, -2\rangle \rightarrow |3, \Delta v'\rangle$ serves as the coupling transition. The key advantage of the proposed method is that the required energy shift ΔE_e only needs to match the linewidth of the dark resonance to produce a measurable signal. Rearranging Equation (2.23) provides

$$\delta = \frac{\hbar\Omega_2^2}{4\Delta E_e}, \tag{6.4}$$

the detuning at which this condition is fulfilled for a given Rabi frequency. Even for relatively small Rabi frequencies (e.g. $\Omega_2 > 6\,\text{MHz}$), the induced light shift exceeds the natural linewidth of the D1 line – thus enabling larger step sizes compared to conventional 1-PA

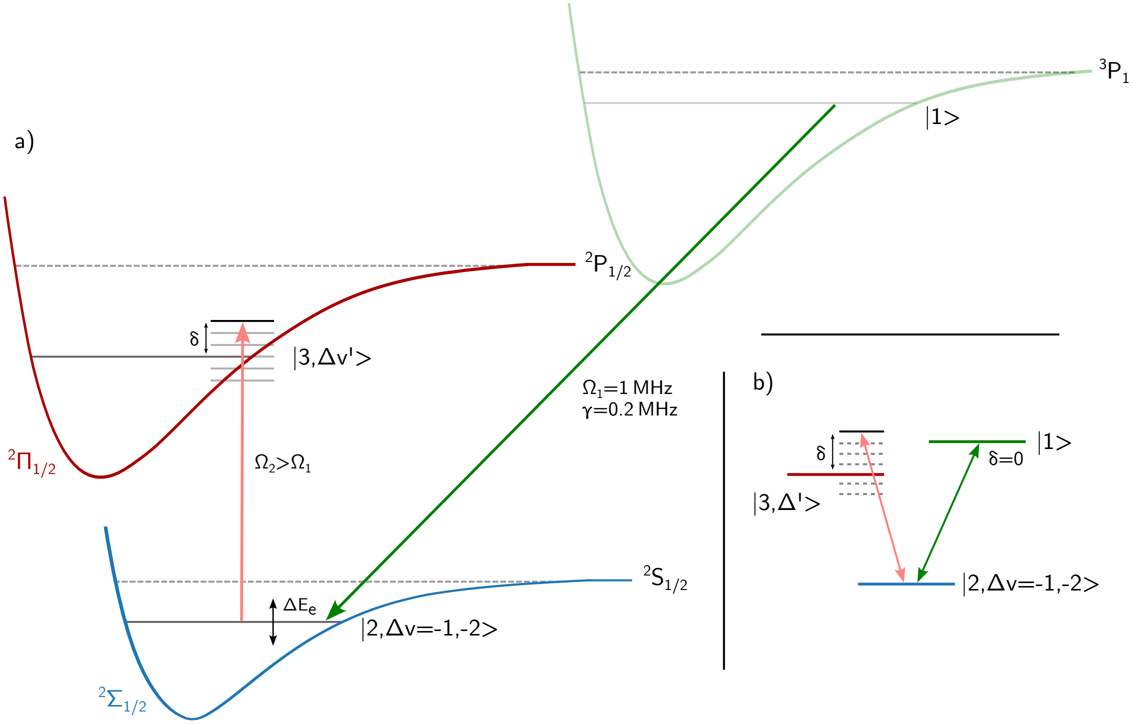

Figure 6.9.: Schematic energy diagram of light-shift spectroscopy (a) and corresponding three-level V-scheme. Transition $|1\rangle \rightarrow |2, \Delta v = -1, -2\rangle$ is driven resonantly and the coupling laser scans transition $|2, \Delta v = -1, -2\rangle \rightarrow |3, \Delta v'\rangle$. Energy spacing is not to scale.

scans. Münchow observed Rabi frequencies exceeding 100 MHz, which would correspond to a required detuning on the order of 2 GHz for shifting the dark resonance out of resonance, decreasing the above mentioned search duration dramatically.

The expected experimental signature is a loss of atoms, indicating that the 2-PA resonance has been shifted out of resonance, while the 1-PA laser is again on resonance.

Once a signal is observed, the laser intensity should be reduced to determine the precise binding energy of the vibrational state. Since the starting point is a bound level of the ground-state potential, its binding energy must also be considered.

In addition to the identification of the vibrational level energies, this technique allows for an estimation of the bound-bound Rabi frequency. By knowing the laser intensity and the detuning δ at which the signal occurs, Ω_2 can be extracted from Equation (2.23), assuming the level position is then known.

Light-shift spectroscopy therefore offers a powerful and time-efficient tool for mapping the excited $^2\Pi_{1/2}$ potential, and it presents a significant advantage over conventional 1-PA-based methods, as have been used in the past [50, 97, 124].

6.2.4 Experimental Procedure

Now we have gained initial insight, the question arises: *What is the next step toward a deeper understanding of the excited state of* $^{87}Rb^{170}Yb$*?*

The first step will be to set up a photoassociation laser system near the Rb D1 line (at 795 nm) and perform conventional 1-PA spectroscopy starting from the atomic scattering state. In this context, we aim to confirm the only 1-PA transition observed so far ($\Delta v' = -6$ at $-0.783\,\mathrm{cm}^{-1}$, see Chapter 3). With the help of a fast photodiode and a beatnote measurement, we will be able to determine the binding energies of vibrational levels up to $\Delta v' = -6$ with an accuracy on the order of the natural linewidth (see Section 6.2.5.1).

Once the exact position of this (already observed) transition is located, we will implement the light-shift spectroscopy method at this point. Based on its performance, we will then systematically explore the $^2\Pi_{1/2}$ potential across the accessible spectral range of the infrared D1-PA laser. As soon as a few additional lines are identified, we can refine the value of Δ_{frac}, allowing for improved predictions of subsequent vibrational levels and thus a reduction of the overall search range for more deeply bound levels.

Since the current D1-PA laser is tunable only within a limited spectral window (up to 805 nm), an extension of the scan range will eventually require a new laser source. Fortunately, several diode or fiber-based laser systems operating in the (near-) infrared are obtainable, enabling us to probe deeper into the potential. One of these laser sources at 1550 nm has already been setup, as described in Section 6.2.5.2.

Depending on the number and distribution of the observed transitions, it may also become worthwhile to intensify theoretical efforts and to collaborate with theory groups to develop a more accurate potential energy model. This would allow for improved predictions of the optimal target state for the third photon and its location.

Preparations for these experiments are already underway and will be described in the following section.

6.2.5 Laser Setups for Light-Shift Spectroscopy

In this section, we will have a look at the already built setups for the experimental procedure explained above. This includes the D1-PA laser, a beatnote setup, a transfer lock, and a laser system at 1520 nm, which will be used as the third photon.

6.2.5.1 PA Laser near the Rb D1 Line

The laser for photoassociation near the Rb D1 line at 795 nm is a commercial *Toptica DL PRO 780* covering a wavelength range of $765 - 805\,\mathrm{nm}$ corresponding to achievable PA detunings of approximately $\Delta_{PA} = 150\,\mathrm{cm}^{-1}$[2]. The typical linewidth is 100 kHz, the maximum output power is $> 100\,\mathrm{mW}$, and the mode-hop-free tuning-range $\sim 20\,\mathrm{GHz}$.

---

[2] Depending on the line strengths of the PA transitions, the range could be even higher.

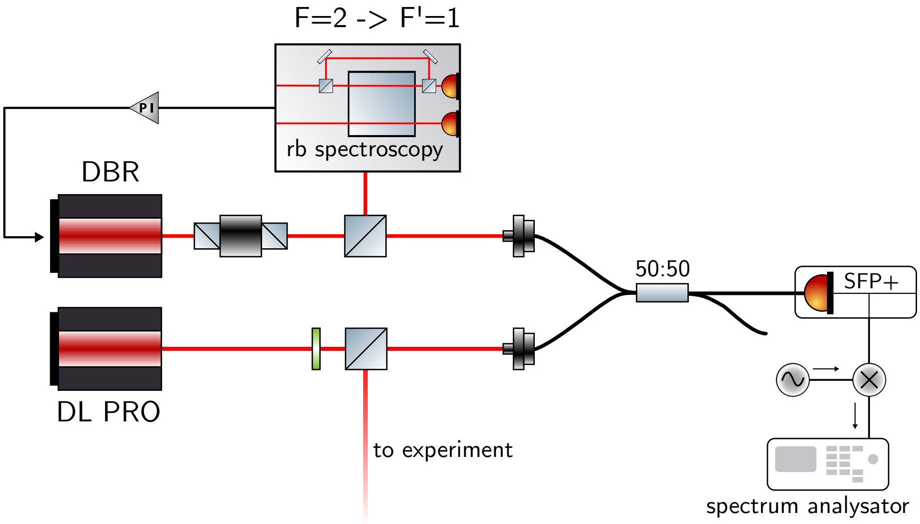

Figure 6.10.: Scheme of the beatnote measurement setup using a DBR laser diode stabilized to a compact saturated-absorption spectroscopy.

Since the intrinsic stability of this ECDL-based laser system is very high, measurements with the free-running laser can be performed as a starting point without the need for an extra stabilization system. This laser will be the coupling laser for the first light-shift experiments for the investigation of the $^2\Pi_{1/2}$ excited state potential of RbYb near the D1 line.

Wavelength Determination using a Beatnote

The previously measured binding energies were determined using a wavemeter, with an accuracy of $\pm 5 \cdot 10^{-3}\,\mathrm{cm}^{-1}$ ($\sim 150\,\mathrm{MHz}$). A more precise method, particularly suited for the very weakly bound states, involves detecting a beatnote signal between the PA laser and a wavelength-stabilized reference laser. An illustration of this method is shown in Figure 6.10. The reference laser is a commercial distributed Bragg reflector (DBR) laser diode (*Thorlabs, DBR795PN*), stabilized using a compact saturated-absorption spectroscopy setup. This stabilization scheme is similar to the one used for the Rb MOT laser system and was implemented by Antonio Buzza [151] and Anna Sopp [152] during their bachelor's theses. The typical linewidth of this laser diode is 1 MHz.

Since the PA detunings Δ_{PA} are referenced to the Rb $|F=1\rangle \rightarrow |F'=2\rangle$ transition, which has an absolute wavenumber of $12579.104\,\mathrm{cm}^{-1}$, and the $\Delta v' = -6$ transition is located at $\Delta_{PA} = -0.783\,\mathrm{cm}^{-1}$, the expected beat frequency would be $\sim 23\,\mathrm{GHz}$. However, due to the red detuning of the PA laser, it is advantageous to use the $|F=2\rangle \rightarrow |F'=1\rangle$ hyperfine transition of Rb (at $12578.848\,\mathrm{cm}^{-1}$) as the locking point for the reference laser. This reduces the expected beat frequency to around 16 GHz.

For the beat measurement, the D1-PA laser and the reference laser beams are com-

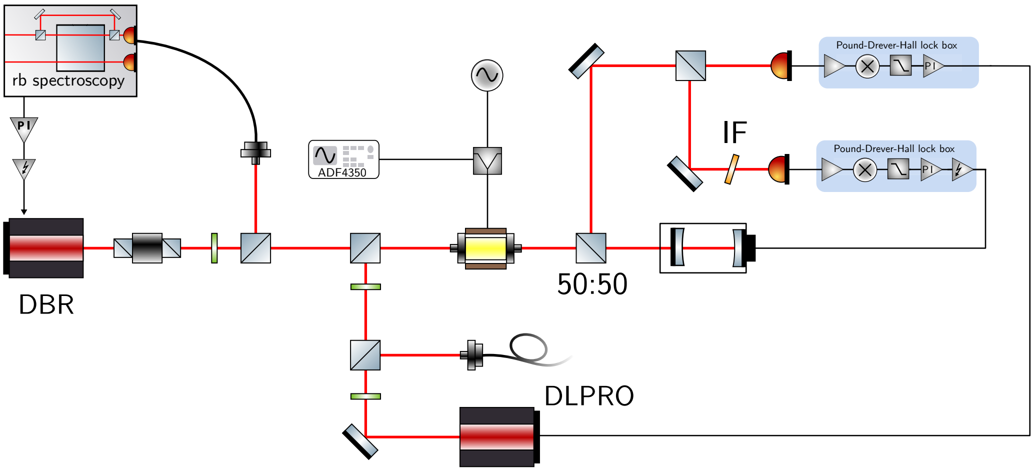

Figure 6.11.: Scheme of the cavity transfer-lock. The reference DBR laser is stabilized using a compact saturation spectroscopy setup. A transfer cavity is then locked to this reference laser, serving as a stable intermediary for the PA laser, which is subsequently locked to the cavity via the sideband locking technique.

bined using a 50:50 fiber coupler and directed onto a high-bandwidth SFP+ fiber-coupled photodiode (similar to the setup used for the Rb repumper beatnote stabilization) (see Section 4.2.2). The resulting beat signal is then down-mixed with an RF synthesizer to frequencies below 3 GHz and recorded with an RF spectrum analyzer.

Because the linewidths of both lasers are significantly narrower than the natural linewidth of Rb ($2\pi \cdot 6\,\mathrm{MHz}$), the achievable measurement accuracy is limited by the natural linewidth, representing an improvement by a factor of approximately 25 compared to the previous wavemeter-based measurements. The main limiting factors in this setup are the bandwidth of the photodiode and the maximum output frequency of the RF synthesizer, which restrict detectable beat frequencies to below 20 GHz and thus limit accessible vibrational states to $\Delta v' = -6$.

Transfer Lock

If we aim to dig deeper into the potential, the beatnote frequency exceeds the measurement capability of the beatnote setup described above. To achieve wavelength determination on the order of the natural linewidth, a cavity transfer-lock system is currently under development [153], as illustrated in Figure 6.11, based on a stabilized reference laser.

The basic principle of a cavity transfer lock is to stabilize the length of a transfer cavity to a reference laser. Provided that the cavity mirrors are compatible with both laser wavelengths, a second laser can then be locked to this cavity, enabling almost arbitrary frequency stabilization even in the absence of suitable spectroscopic lines.

In our case, the reference laser is a *Thorlabs, DBR780PN* DBR laser diode, delivering a typical output power of 45 mW and linewidth of 1 MHz. It is stabilized to a hyperfine transition of the Rb D2 line at 780 nm using the compact saturation spectroscopy setup described previously [1]. A beatnote measurement with the Rb MOT laser shows a relative linewidth of ~ 1 MHz and a standard deviation of 6 MHz, which is sufficiently stable for our intended applications. The light from the other path is passed through a fiber-coupled EOM (*Photline, NIR-MPX800*), to generate sidebands required for Pound-Drever-Hall (PDH) locking.

The transfer cavity consists of an Invar spacer with a length of 50 mm and the mirror position is adjustable via a fine-thread screw. The cavity mirrors posses a nominal reflectivity of $R > 0.99$ and radii of curvature of $r = 50$ mm, forming a confocal geometry. One of the mirrors is mounted on a piezoelectric actuator to allow fine length adjustments for locking. The calculated finesse of $\mathcal{F} \sim 300$ corresponds to a cavity linewidth of ~ 10 MHz. The entire assembly is housed inside a KF-flange vacuum chamber, which is evacuated and sealed with a valve to minimize pressure fluctuations, though not continuously pumped.

The cavity length is stabilized using the mirror-mounted piezo to the reference laser using a standard PDH locking technique, providing a stable optical reference for the photoassociation laser.

The D1-PA laser is then locked to the stabilized cavity using the same EOM. In our implementation, two independent PDH locks are employed: one for the cavity length and one for the PA laser frequency. To separate the corresponding error signals, the reflected light from the cavity is split according to wavelength, using orthogonal polarizations, a polarizing beam splitter, and an interference filter (IF).

For arbitrary offset locking, we employ the EOM sideband-locking technique, as described in Section 4.3.4.4.

By this method, we effectively transfer the frequency stability of the reference laser – on the order of the natural linewidth of Rb – to the D1-PA laser, significantly improving the precision of vibrational level measurements. For future experiments requiring precise stabilization onto specific PA resonances, such a transfer-lock system is indispensable.

6.2.5.2 Laser System at 1520 nm

As described in Section 6.2.1, the laser required for the third photon must operate at a wavelength around 1520 nm. A corresponding laser has already been set up by Castor and is ready for deployment in the experiment. The setup is described in detail in her master's thesis [149], and a publication is currently in preparation [154].

The system is based on a single-angled-facet (SAF) gain chip (*Thorlabs, SAF1550P2*), implemented in a compact fiber-coupled half-butterfly configuration using a Littrow configuration with an optical Bragg grating [155]. This ECDL is frequency-stabilized via the Pound-Drever-Hall (PDH) sideband locking technique, similar to the stabilization scheme used for the new Yb MOT laser (see Section 4.3.4.4). An overview of the setup is shown

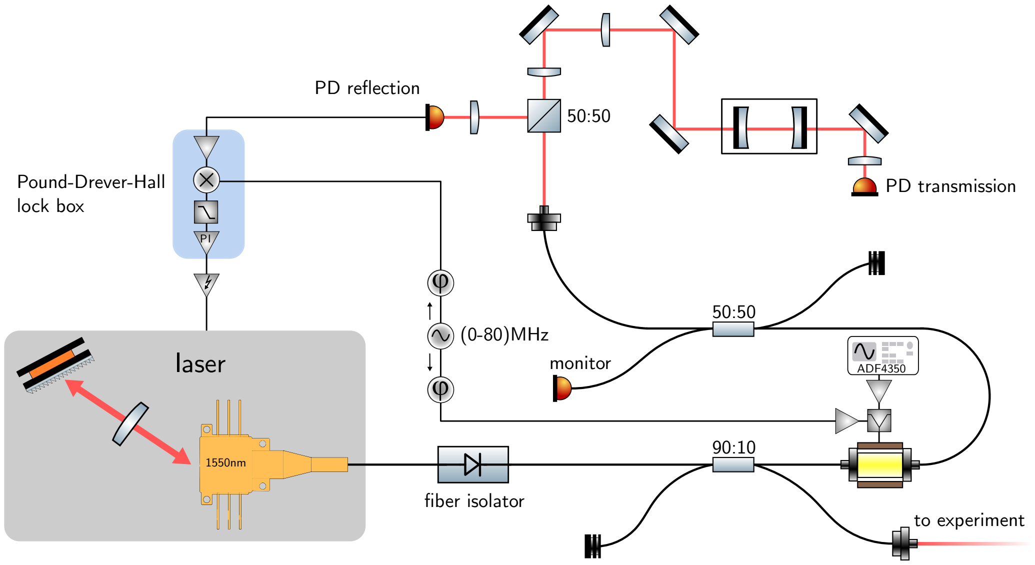

Figure 6.12.: Schematic setup of the 1520 nm ECDL system including the Pound-Drever-Hall sideband cavity lock.

in Figure 6.12.

Laser Setup

The SAF gain chip is housed in a thermoelectrically temperature-stabilized half-butterfly package, operating at the wavelength of 1550 nm. It includes an optical isolator and is directly coupled to a FC/APC single-mode fiber. The angled (26.5 °) back facet is anti-reflection coated to suppress internal feedback. The external cavity is formed by a blazed reflection grating (*Thorlabs, GR12-0616*, 600/mm), with a reflection efficiency of 78 % at 1520 nm in Littrow configuration, allowing wide-range tuning by adjusting the grating angle. The −3 dB tuning bandwidth with grating feedback is 160 nm, with a maximum output power of ∼ 40 mW, as shown in Figure 6.13.

Stabilization and Linewidth

The laser output is sent through a fiber-coupled EOM (*iXBlue, MPZ-LN-10-00-P-P-FA-FA*), which is modulated by a function generator (PDH signal) and an ADF4350 synthesizer board (sideband generation) for locking and frequency scanning. The modulated light is directed into the reference cavity setup, where the reflected signal is detected by a photodiode and used as the error signal for the PDH lock, which actuates on a piezo attached to the grating.

The cavity setup is identical in design to the Yb MOT cavity[3], but uses mirrors coated for

---

[3] The cavity spacer and vacuum system including copper shielding are the same, though no externally temperature-stabilized housing is employed.

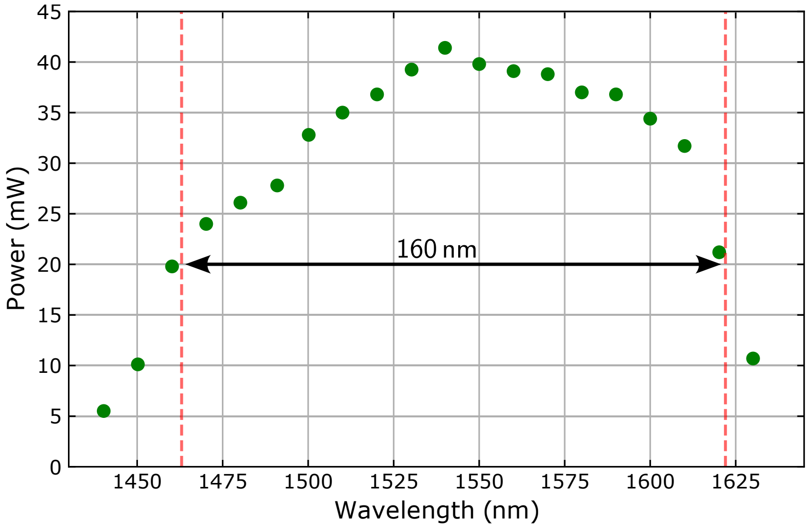

Figure 6.13.: Wavelength-dependent laser power in the ECDL configuration with a -3 dB bandwidth of 160 nm.

the wavelength range around 1520 nm[4]. The mirrors (*Layertec, 140987*) have a reflectivity of $R \approx 0.99995$, yielding a cavity linewidth of approximately 25 kHz – more than sufficient, since the expected PA linewidths lie in the MHz range. As with the Yb MOT system, the locked laser exhibits a slow frequency drift due to thermal changes of the Zerodur spacer, measured to be 0.15 kHz/s. Given that the absolute wavelength is measured with a wavemeter of ~ 100 MHz precision, this drift is not a limiting factor.

The frequency of the stabilized laser can be tuned over a range of several hundred MHz while remaining locked through adjustment of the EOM frequency. The exact tuning range depends on the chosen sideband frequency and potential interference with neighboring cavity modes. The mode-hop free tuning range of the unlocked laser is approximately 5.6 GHz, making it suitable for free-running operation during line searches, followed by locking for precise characterization.

The laser's linewidth was measured via a beatnote with a sub-10 Hz reference laser and found to be approximately 10 kHz.

For further details on the laser system, including locking techniques, frequency noise, drift measurements, and long-term stability, refer to [149] and [154].

In summary, this laser setup provides a reliable and tunable source for the third photon, representing a crucial step toward the formation of absolute ground state RbYb molecules.

---

[4] Which is identical to the telecom regime.

7

Outlook

In this chapter, I provide a brief outlook on the future prospects of our experiment. In Section 7.1, I discuss general improvements to the apparatus aimed at increasing atom numbers, thereby enhancing stability, sensitivity, and PA rates through optimized optical dipole traps and lattice configurations. Section 7.2 outlines potential strategies for the coherent formation of weakly bound molecules. Finally, in Section 7.3, I describe the envisioned route toward absolute ground-state molecules and summarize first possible experiments involving them.

7.1 General Improvements

As discussed in Section 4.9, substantial (and mostly unavoidable) atom loss occurs during the preparation process. Naturally, beginning with a higher initial atom number would improve the overall experimental performance. Another key limitation lies in the merging of both atomic species into a single trap (see Section 4.9.3.1) and in achieving higher PA rates. This section outlines possible improvements to address these challenges.

7.1.1 Enhancing Atom Numbers

A straightforward approach to enhance atom numbers is to increase laser powers, which offers several advantages:

- Higher MOT beam powers allow for larger beam sizes, leading to larger MOT volumes and enabling greater detunings due to higher capture velocities.
- Increased slower power improves the loading rate, thereby reducing the overall experimental sequence duration.
- Higher ODT powers create deeper trapping potentials, allowing for the capture of hotter atoms and increasing the trap volume. This would also improve transport efficiency and reduce transport time.

Another potential strategy to increase the initial atom number is implementing transverse cooling of the atomic beam or a 2D MOT [156], which could result in a larger MOT.

7.1.2 Optical Trap with Balanced Potential Depth

A key challenge in the entire project aiming at the production of RbYb ground-state molecules is combining and cooling both species within a single optical trap while using only one trapping wavelength. This leads, in our case, to a tenfold difference in trap depths. To overcome this issue, we can either use a bichromatic trap or precisely tune the wavelength of a monochromatic trap. In both cases, it is essential to reconsider the wavelength-dependent polarizabilities – and thus optical potentials – of Yb and Rb, as shown in Figure 2.11.

7.1.2.1 Bichromatic Traps

As the name suggests, a bichromatic trap consists of two trapping lasers with different wavelengths. If we retain the 1064 nm wavelength, the second wavelength must either be more attractive to Yb than to Rb or even repulsive for Rb.

One possible option is 532 nm, which is readily accessible at high intensities via frequency doubling of a 1064 nm source, such as a 10 W *VERDI* laser. A setup for utilizing this laser is described in [2]. The advantage of 532 nm is its relatively large detuning from any transition in Rb or Yb, minimizing scattering rates. However, this also means that high laser power is required to achieve effective potential tuning[1].

Another approach is to use wavelengths close to atomic resonances and were used in previous experiments [50]. As seen in Figure 2.11, polarizabilities vary strongly near atomic transitions, allowing for fine-tuned optical potentials. This can help compensate for the imbalance in the 1064 nm light field. However, the downside is that proximity to atomic resonances increases scattering rates, shortening trap lifetimes.

An optical trap near Yb's intercombination line was previously used by Bruni [50] to create a hybrid conservative trap, where Rb was confined in a magnetic trap. Additionally, an optical dipole trap between Rb's D1 and D2 lines at the tune-out wavelength of 790 nm was investigated in Scheidler's bachelor's thesis [157].

All these studies highlight the critical role of precisely tuning trap parameters to achieve the desired potentials. The potential depth is highly sensitive to the interplay of wavelength, beam focus, intensity, and spatial overlap – all of which are challenging to stabilize at the required precision.

Furthermore, Gaussian beams of different wavelengths but identical focus sizes have different Rayleigh lengths, making perfect spatial overlap physically impossible. Therefore, I recommend using a monochromatic optical dipole trap as the final trapping configuration after the merging sequence.

---

[1] A drawback of 532 nm is its strong absorption in optical components, which can lead to heating and damage.

7.1.2.2 Monochromatic Traps

To overcome these alignment challenges, an alternative is using a monochromatic trap, where the trapping wavelength is chosen to ensure equal trap depths for Rb and Yb, meaning their polarizabilities are matched. For an attractive potential, this requires a crossing point in Figure 2.11 where $\alpha < 0$.

Such crossings occur near the tune-out wavelengths of Rb at 420 nm and 790 nm, as well as the more detuned 457 nm. However, tune-out wavelengths inherently come with high scattering rates, which significantly reduce the trap lifetime when aiming for sufficiently deep potentials. Additionally, due to the steep slope near atomic resonances, the potentials become highly sensitive to the exact wavelength. As a result, tune-out wavelengths are more suitable as balancing beams in a bichromatic setup rather than for a standalone trap.

A more practical alternative is a far-detuned optical dipole trap at 457 nm, which offers reasonable scattering rates for both species [2] and a shallower slope, making the system less sensitive to wavelength fluctuations. Achieving sufficient trap depths for Rb and Yb, a few watts of laser power are necessary. With a beam waist ($1/e^2$ radius) of 50 µm and a power of 2 W, the trap depth of a single beam ODT would be approximately 50 µK. Unfortunately, single-mode laser sources at this wavelength remain challenging to obtain.

Nevertheless, initial steps towards realizing an ODT at 457 nm were taken by Hübbers during his bachelor's thesis [158]. He explored the use of a cost-effective multi-mode laser diode (*OSRAM PLPT9 450LB E*) with a nominal wavelength of 447 nm and an output power of 5 W. The spatially multi-mode light was coupled into a multi-mode fiber and subsequently focused to 77 µm. This proof-of-concept demonstrated that an affordable multi-mode laser diode could potentially serve as a monochromatic ODT. Future work should focus on improving fiber coupling efficiency, tuning the wavelength to higher values, and testing different opportunities for trap shape modulation. Nevertheless, this approach presents a promising pathway towards a trap with equal trap depth for both atomic species, unlocking various future applications in the experiment.

7.1.3 Improved Optical Lattice

An improvement in PA rates can also be achieved by increasing the local density of Rb and Yb atoms in a 3D optical lattice. While first PA measurements in such a lattice described in Section 5.1.3.8 demonstrated increasing PA rates, this has not been pushed to its limit so far. The reason for this is the high temperature with which the atoms are loaded into the lattice.

When this issue is solved – potentially with an optical trap setup explained above – this could increase the experimental performance significantly by avoiding thermal broadening due to discrete lattice states [159].

7.1.3.1 Mott Insulator

A particularly promising application of a 3D optical lattice is the transition to a Mott insulator at high lattice depths. The principle idea will de discussed in the following. For a more detailed treatment of Mott insulators, see [160, 161].

At shallow lattice depths, the system remains in a superfluid state, where the atoms are delocalized and can tunnel freely between lattice sites. As the lattice depth increases, the tunneling probability decreases until atoms become localized at individual lattice sites, minimizing interaction energy. Once the system reaches a state with fixed occupation number per site, it is referred to as a Mott insulator.

In the case of a dual-species Mott insulator, where a heteronuclear site occupation of lattice sites is energetically favored[2], we obtain a mixed Mott insulator – an ideal starting point for photoassociation. Not only does this configuration provide extremely high local densities, but it also allows the associated molecules to remain trapped within the lattice sites, preventing losses due to collisions.

To maximize this enhancement, a mixed Mott insulator would be highly desirable. Our experimental setup Section 4.4 is expected to support the formation of an Rb Mott insulator. While, in principle, it could also facilitate a Yb Mott insulator, achieving this is significantly more challenging. This limitation of the lattice depth could potentially be addressed by incorporating an additional amplification stage in the lattice amplifier.

Mott insulators have already been experimentally realized for Rb [160], Yb [162, 163], and even Bose-Fermi mixtures of different Yb isotopes [164]. However, a mixed Rb-Yb Mott insulator has not been reported yet.

7.2 Formation of Weakly Bound Ground-State Molecules

As we have already discussed several potential experimental enhancements that can improve the overall performance of our molecule machine in the short term in Section 7.1, as well as the next steps for exploring the potential energy curves at the Rb D1 line in Section 6.2, we now turn to a more forward-looking perspective.

While the methods described so far are primarily spectroscopic – providing information about the positions of vibrational states and the shape of potential energy curves – efficient molecule production remains a future challenge.

This chapter outlines several possible approaches toward molecular formation, including STIRAP, LASIFR, and magnetic Feshbach resonances. Finally, we will briefly touch on the last step, the formation of ground-state molecules.

---

[2] Which is the case for ^{87}Rb^{170}Yb.

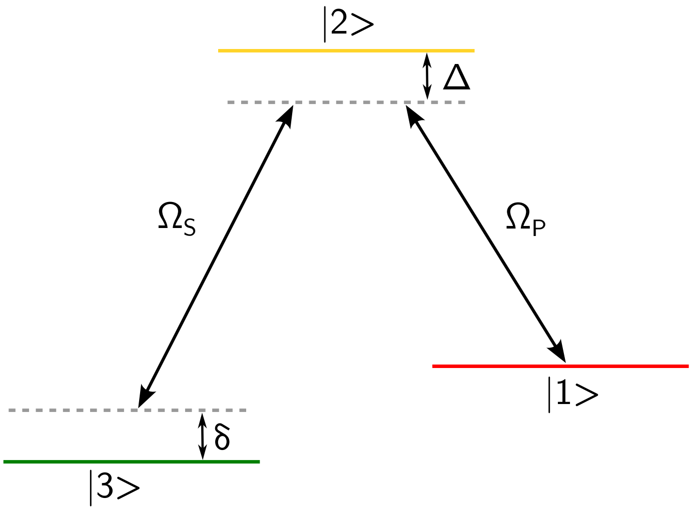

Figure 7.1.: Energy scheme of the three-level system for a STIRAP process. The pump laser couples the initial state $|1\rangle$ to the intermediate state $|2\rangle$ and the Stokes laser couple the states $|2\rangle$ and $|3\rangle$. For a STIRAP process, the one-photon detuning δ must be zero.

7.2.1 Stimulated Raman Adiabatic Passage – STIRAP

Stimulated **R**aman **a**diabatic **p**assage (STIRAP) is a highly efficient, fully optical method for transferring population between two discrete quantum states, both coupled to a common intermediate state. It is a well-established technique with broad applications in atomic and molecular physics [42, 165], chemistry [166], pp. 14–16, and quantum information [167], pp. 35–39. While the first experimental results and the basic theory were presented by Gaubatz et al. in 1990 [168], we will follow the framework outlined in the comprehensive review by Vitanov, Rangelov, Shore, and Bergmann from 2017 [167]. Several applications for STIRAP can be found in [166].

As emphasized throughout this thesis, ultracold molecule experiments suffer from a variety of loss channels, which reduce the number of atoms – and therefore the number of potentially formed molecules. One can easily imagine that starting with low atom numbers in a combined CODT (see Section 4.9.3.3), followed by a lossy four-photon process, would most likely yield no measurable molecular signal.

Fortunately, STIRAP offers a coherent and, in principle, fully efficient method of population transfer in a three-level system by coupling to an intermediate state. The concept is somewhat related to the 2-photon photoassociation described in Section 2.4.1. Since the scheme is not limited to molecular transitions, we adopt the standard notation using pump (P) and Stokes (S) coupling[1], illustrated in Figure 7.1. The pump laser couples the states $|1\rangle$ and $|2\rangle$, while the Stokes laser couples the states $|2\rangle$ and $|3\rangle$.

---

[1] Instead of free-bound and bound-bound as used in the 2-PA case.

The time-dependent Hamiltonian of this three-level system in the rotating-wave approximation is given by:

$$\hat{H}(t) = \frac{\hbar}{2} \begin{bmatrix} 0 & \Omega_P(t) & 0 \\ \Omega_P(t) & 2\Delta & \Omega_S(t) \\ 0 & \Omega_S(t) & 2\delta \end{bmatrix}, \tag{7.1}$$

where $\Omega_P(t)$ and $\Omega_S(t)$ are the time-dependent Rabi frequencies of the pump and Stokes transitions, Δ is the one-photon detuning, and δ is the two-photon detuning. Similar to the dressed-state picture explained in Section 2.3, the unperturbed states are coupled through interaction with the light fields and, for $\delta = 0$, can be written as:

$$|0\rangle = \cos\theta\ |1\rangle + \sin\theta\ |3\rangle \tag{7.2}$$

$$|+\rangle = \sin\theta \sin\Phi\ |1\rangle + \cos\Phi\ |2\rangle + \cos\theta \sin\Phi\ |3\rangle \tag{7.3}$$

$$|-\rangle = \sin\theta \cos\Phi\ |1\rangle - \sin\Phi\ |2\rangle + \cos\theta \sin\Phi\ |3\rangle, \tag{7.4}$$

with time-dependent mixing angles defined by:

$$\tan\theta(t) = \frac{\Omega_P(t)}{\Omega_S(t)} \quad \text{and} \quad \tan 2\Phi(t) = \frac{\sqrt{\Omega_P^2(t) + \Omega_S^2(t)}}{\Delta}. \tag{7.5}$$

From Equation (7.2), we see directly that $|0\rangle$ contains no contribution from the intermediate state $|2\rangle$, enabling a population transfer within the dressed-state picture as follows:

Initially, with no Stokes and probe fields, the system starts in the bare state $|1\rangle$. If we now apply the Stokes field, such that the dressed state $|0\rangle$ corresponds to this starting state, we require $\theta = 0$, which holds for $\Omega_P/\Omega_S \to 0$. To transfer population from $|1\rangle$ to $|3\rangle$, the mixing angle θ must be smoothly varied from 0 to $\pi/2$ (i.e., $\Omega_S/\Omega_P \to 0$). Once both laser fields are turned off, the system ends up in the bare state $|3\rangle$ – without ever populating the lossy intermediate state $|2\rangle$.

This mechanism leads to a counterintuitive temporal sequence: the Stokes pulse must precede the pump pulse.

During this process, the eigenenergy of $|0\rangle$ remains zero, while the eigenenergies of the adiabatic states $|+\rangle$ and $|-\rangle$ correspond to an Autler-Townes splitting and can be written as:

$$E_\pm(t) = \frac{1}{2}\left(\Delta \pm \sqrt{\Delta^2 + \Omega_P^2(t) + \Omega_S^2(t)}\right).$$

If the energy splitting between these states is sufficiently large, the system can adiabatically remain in $|0\rangle$, allowing complete population transfer from $|1\rangle$ to $|3\rangle$.

The time evolution of a STIRAP process with $\Delta = 0$ is illustrated in Figure 7.2 for two different scenarios.

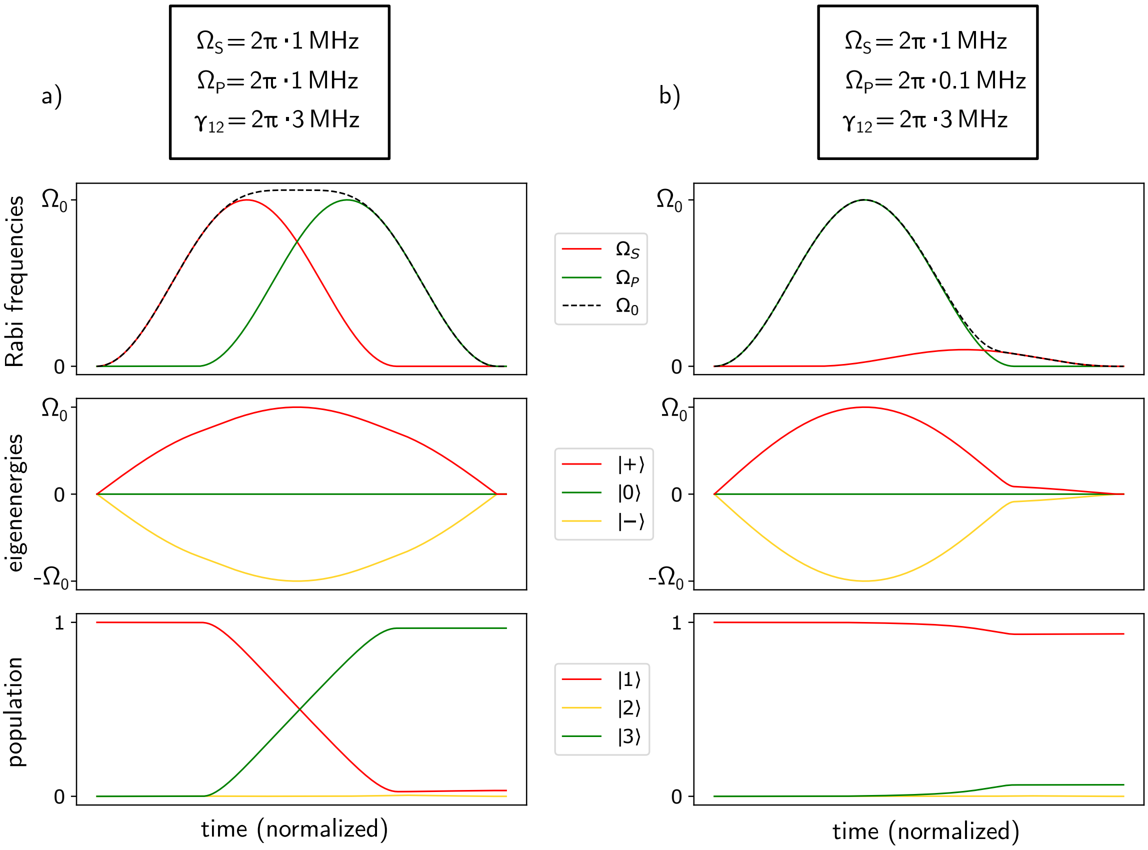

Figure 7.2.: Time evolution of a STIRAP process for different parameters. The decay rate γ_{12} is set to the observed linewidth of the 1-PA resonance at the intercombination line of Yb. a) shows an efficient case where the maximum Rabi frequencies are equal, the energy splitting of the adiabatic states $|+\rangle$ and $|-\rangle$, and the population transfer from the starting state $|1\rangle$ to $|3\rangle$. The Rabi frequencies are chosen such that the transfer is almost 100 %. b) shows the realistic case with Rabi frequencies on the order of the experimentally observed ones. It is clearly visible that the transfer is highly inefficient.

In both scenarios, the pulses follow a $\sin^2$ shape and are delayed such that the reduced Rabi frequency $\Omega_0^2 = \Omega_S^2 + \Omega_P^2$ remains constant during the crossing regime. The parameters in Figure 7.2 correspond to the free-bound transition found at the intercombination line of Yb (see Section 5.1), where the decay rate of state $|2\rangle$ is $\gamma_{12} = 2\pi \cdot 3\,\mathrm{MHz}$. In panel a), both Rabi frequencies are $\Omega_S = \Omega_P = 2\pi \cdot 1\,\mathrm{MHz}$, resulting in efficient transfer. In panel b), we use experimentally realistic values corresponding to our PA experiments close to the intercombination line, with the free-bound Rabi frequency (i.e., Ω_P in the STIRAP picture) limited to just 0.1 MHz, resulting in a very small transfer efficiency.

For $\delta = 0$, the transfer efficiency can be approximated by [169]:

$$\eta = \exp\left(-\frac{\pi^2 \gamma_{12}}{\Omega_0^2 \tau} - \frac{D}{2}\tau\right), \tag{7.6}$$

where D denotes relative linewidth of the pump and Stokes lasers and τ the STIRAP duration. As evident from this expression, high Rabi frequencies for both transitions are essential[2], explaining why efficient molecule formation using the Yb intercombination line is, for the time being, not feasible. Additionally, the relative linewidth of both coupling lasers must be small, necessitating robust laser sources and methods for phase-locking, which could require ultra-high finesse cavities and/or frequency combs.

Notably, free-bound STIRAP has already been demonstrated for Sr_2 dimers near the intercombination line, achieving transfer efficiencies of up to 30 % [142, 170]. However, to date, no such results have been reported for alkali-alkaline-earth molecular systems, highlighting an open and promising direction for further exploration. However, this would require substantial upgrades to our laser systems.

Employing a transition near the Rb D1 line may offer a more viable route toward efficient molecule formation in future experiments.

7.2.2 Laser-Assisted Self-Induced Feshbach Resonance – LASIFR

An alternative adiabatic optical method for transferring population from a scattering state to a bound vibrational state within the electronic ground-state potential was proposed by Devolder et al. in 2019 [171]. This technique, called **l**aser-**a**ssisted **s**elf-**i**nduced **F**eshbach **r**esonance (LASIFR), was specifically proposed for RbSr, but should be applicable to RbYb and uses lasers in the sub-THz regime. In contrast to STIRAP, LASIFR does not require an intermediate state; the transition is driven entirely within the ground-state potential. This eliminates losses due to spontaneous emission, which typically occur in optical Feshbach resonances involving excited molecular states leading to line broadening as discussed in Section 5.1.3.7. The LASIFR concept is illustrated in Figure 7.3 and is closely related to magnetic Feshbach resonances (see Section 7.2.3).

The process starts with a mixture of ultracold atoms colliding in the s-wave scattering regime, referred to as the open channel in Figure 7.3 a). The core idea is to tune the energy of a bound state in a different potential (the closed channel) into resonance with this scattering state. If both channels can be coupled using a laser field, an adiabatic transfer can be realized by slowly sweeping the laser detuning across this resonance.

Here the open channel corresponds to an s-wave scattering state with $l = 0$, and the closed channel to a bound state with $l = 1$, exhibiting a the p-wave centrifugal barrier.

---

[2] Note that the approximation in Equation (7.6) is valid only if Ω_0 remains constant during the crossing regime, as illustrated in Figure 7.2 a). This requires $\Omega_P \approx \Omega_S$.

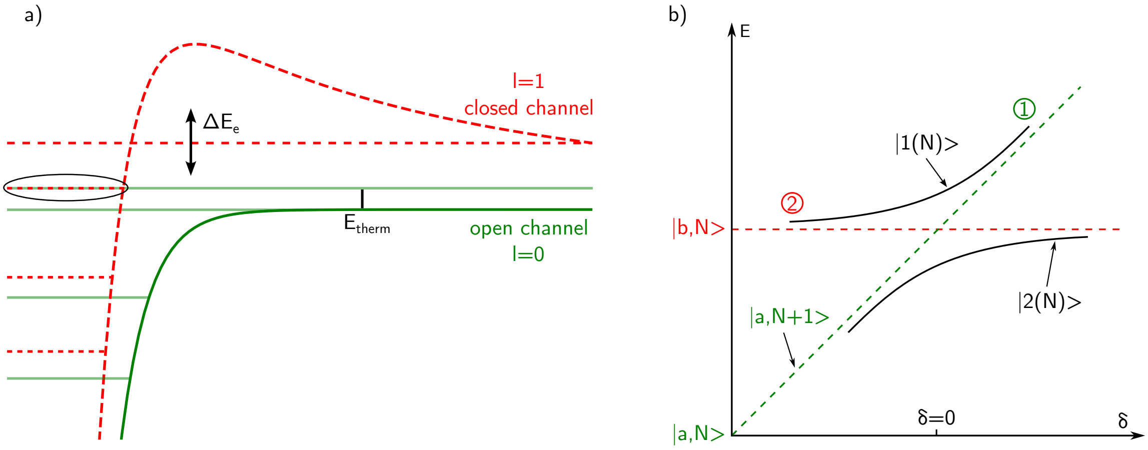

Figure 7.3.: Scheme of the LASIFR principle. a) shows the potential energy curves of the open ($l = 0$) and closed ($l = 1$) channel. The relative energy of both can be shifted into resonance due to the light shift. b) shows the energy dependence of the corresponding states versus the laser detuning in the dressed-state picture.

In the dressed-state picture, the open and closed channels correspond to the bare states $|a, N+1\rangle$ and $|b, N\rangle$, respectively. A coupling light field mixes these states, and for a two-level system, the dressed states are then given by [70]:

$$|1(N)\rangle = \sin\theta\,|a, N+1\rangle + \cos\theta\,|b, N\rangle \tag{7.7}$$

$$|2(N)\rangle = \cos\theta\,|a, N+1\rangle - \sin\theta\,|b, N\rangle\,, \tag{7.8}$$

where the mixing angle is defined as:

$$\tan 2\theta = -\frac{\Omega(t)}{\delta} \quad \text{with} \quad 0 < 2\theta < \pi, \tag{7.9}$$

with Ω being the Rabi frequency and δ the detuning from resonance.

The adiabatic process can then be explained as follows: The laser field is initially applied with large positive detuning ($\delta > 0$), corresponding to $\theta = \pi/2$, so that $|a, N+1\rangle$ corresponds to the dressed state $|1(N)\rangle$ (point ① in Figure 7.3 b). As the detuning is swept adiabatically to large negative values ($\delta \to -\infty$), the mixing angle evolves to $\theta = 0$, and $|1(N)\rangle$ corresponds to the bare state $|b, N\rangle$ (point ②). When the laser is turned off at this point, the system is left in the bound molecular state of the closed channel.

The transfer probability is given by the Landau-Zener model as [171]:

$$P = 1 - \exp\left(-\frac{\pi\,\Omega_{max}^2}{2\,|\alpha|}\right), \tag{7.10}$$

where Ω_{max} is the maximum Rabi frequency, and α is the linear chirp rate of the time-dependent detuning: $\delta(t) = \alpha\,(t - T_{pulse}/2)$. As usual, a high Rabi frequency – resulting from a large wavefunction overlap and/or high laser intensity – is beneficial for maximizing transfer.

Notably, the process may also be initiated from large negative detuning, following the evolution of the dressed state $|2(N)\rangle$ instead.

Closely related to this adiabatic population transfer is the detuning-dependent interspecies scattering length. Near resonance, it is given by [171]:

$$a = a_{BG}\left(1 - \frac{\Gamma}{\delta}\right), \tag{7.11}$$

where a_{BG} is the background scattering length, Γ is the resonance width (referred to as the reduced width Γ_{red} in [171]), and scales linearly with the laser intensity. Due to the divergence of a at resonance, a wide range of tunable scattering lengths (positive and negative) can be achieved. This tunability may be exploited for enhanced thermalization and efficient sympathetic cooling.

Devolder et al. presented numerical parameters for the ^{87}Rb^{84}Sr system, where both species are trapped in a combined Mott insulator, resulting in discrete scattering states. For this system, the strongest transition dipole moment element occurs at vibrational level $v = 56$, with a transition wavenumber of $6.6\,\mathrm{cm}^{-1}$ ($\nu = 185\,\mathrm{GHz}$) and resonance width $\Gamma_{56} = 2\pi \cdot 1.45 \cdot 10^{-4}\,\mathrm{MHz}$. Levels with $\Gamma > \Gamma_{56}/2$ range from $v = 51$ ($21.44\,\mathrm{cm}^{-1}$) to $v = 60$ ($1.20\,\mathrm{cm}^{-1}$). For a pulse duration of $T_{pulse} = 10000\,\mu\mathrm{s}$ and chirp rate $\alpha = 5 \cdot 10^{-5}\,\mathrm{MHz}/\mu\mathrm{s}$, laser intensities on the order of hundreds of $\mathrm{W/cm^{-2}}$ are required.

Although RbSr and RbYb differ in their potential energy curves – and thus the exact position of optimal vibrational states – the RbSr results provide a useful reference for estimating parameters in the RbYb system.

In principle, LASIFR can be adapted for RbYb to form weakly bound ground-state molecules. However, several challenges remain: Sub-THz laser sources are still under development [172, 173], and no suitable source is commercially available at this time. Furthermore, the relevant vibrational level must be accurately predicted for efficient implementation, since the proposed linewidths are rather small.

In conclusion, LASIFR offers a possible route for adiabatic population transfer to weakly bound vibrational states in the electronic ground state, without incurring spontaneous emission losses typical of excited-state optical Feshbach resonances. However, its experimental realization remains challenging and, at present, appears to be out of reach.

7.2.3 Magnetic Feshbach Resonances

In addition to fully optical methods of adiabatic molecule formation, magnetic Feshbach resonances (MFR) [174] offer an alternative pathway. The underlying principle of MFR is conceptually similar to the LASIFR scheme described above. As illustrated in Figure 7.4 a), an open and a closed channel, both originating from different electronic ground-state potentials, are involved, and a weakly bound molecular state is tuned into resonance with the scattering state. In the case of MFR, these states typically belong to different hyperfine manifolds, with their relative energy shifts arising from distinct Zeeman shifts in an

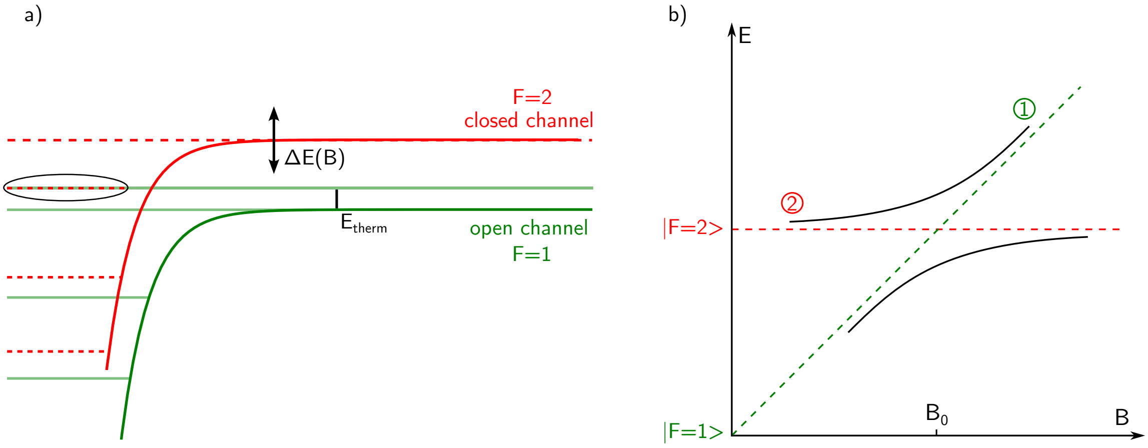

Figure 7.4.: Scheme of a magnetic Feshbach resonance. a) shows the potential energy curves of the open ($F = 1$) and closed ($F = 2$) channel. The relative energy of both can be shifted into resonance due to the Zeeman shift $\Delta E(B)$. b) shows the energy dependence and the avoided crossing of the corresponding states versus the magnetic field strength.

external magnetic field. Provided there is a coupling between these channels, adiabatic transfer can be achieved by sweeping the magnetic field across the resonance. Magnetic Feshbach resonances are the workhorse for the creation of weakly bound molecules in bi-alkali systems such as NaK [175], KCs [176], NaRb [177], RbCs [178], and, naturally, also in homonuclear bi-alkali combinations. In these systems, spin-spin interactions generate strong coupling, resulting in broad and robust MFRs that are ideally suited for efficient molecule formation.

In contrast, since Yb's ground state is spinless, such strong coupling is absent in RbYb. Nevertheless, weaker interaction mechanisms do exist, offering the possibility of magnetic Feshbach resonances. These coupling mechanisms have been explored for CsYb in [179] and are briefly summarized here.

One such mechanism involves a distortion of the Rb electron cloud in the presence of the Yb atom, which modifies the hyperfine coupling constant. This type of coupling was proposed by [180] and [181], and prompted experimental searches for corresponding resonances in RbYb [50]. Although these initial searches were unsuccessful, the discovery of narrow resonances in RbSr [182] suggests that a renewed search – particularly with improved magnetic field control and access to higher fields – could prove worthwhile. The strength of this coupling can be inferred through precision measurements of the hyperfine structure of the molecular ground state via two-photon photoassociation, as discussed in Section 5.2.

Another proposed coupling arises from the interaction between the Rb valence electron spin and the nuclear spin of a fermionic Yb isotope[3]. Such resonances have been observed for CsYb at magnetic fields of several hundreds Gauss [47], and exploring similar behavior in RbYb could be an interesting future route.

A further route to enable strong magnetic Feshbach resonances could be the use of Yb in an electronically excited triplet state. In this scenario, spin-spin interactions can give rise to significant coupling. A particularly intriguing candidate is the long-lived metastable $^3P_0$ clock state, as proposed in [146]. However, due to the lack of precise knowledge about the corresponding interaction potentials, accurate predictions of resonance locations remain challenging. Additional spectroscopic investigations, such as photoassociation or Feshbach spectroscopy, are necessary to characterize these potentials.

7.3 RbYb in the Absolute Ground State

If weakly bound RbYb molecules can be produced using e.g. one of the methods outlined above, we will be poised to address the next significant milestone: the creation of rovibronic ground-state molecules. As outlined above, the essential prerequisite for this is a robust and efficient production of molecules in a weakly bound vibrational level of the electronic ground-state potential. Once achieved, a well-established and conceptually straightforward pathway – successfully demonstrated in numerous other cold molecule experiments – is the use of a coherent two-photon STIRAP transfer to the absolute ground state.

Ground-state formation of heteronuclear bi-alkali molecules has already been realized for RbCs [40, 183], NaK [42], NaRb [43], and KRb [184], with the initial step (production of weakly bound molecules) typically relying on strong magnetic Feshbach resonances to access weakly bound molecular states.

As discussed in Section 6.2.1, the wavelength of the third photon required for the transfer process is around 1520 nm. Conveniently, the final STIRAP laser is proposed to lie near 1.3 µm [57], a technologically accessible region for laser systems.

Once the production of RbYb molecules in the rovibronic ground state is accomplished, a natural next step will be the measurement of their electric dipole moment – a fundamental property that will also enable future manipulation and control. To this end, the integration of precisely aligned electrodes into the existing experimental setup is essential. Fortunately, we can draw upon the experience and infrastructure of our lovely colleagues Alex and Nele working on the neighboring Yb Rydberg experiment, whose insights of electric field control will prove an invaluable endeavor.

For me it's now time to hand over these next steps – and the feared "10er Schlüssel[1]" – to the safe hands of Arne and Céline.

---

[3] Only ^{171}Yb and ^{173}Yb possess nuclear spin.

[1] To open the science chamber and implement new components – such as electrodes, ion detectors, or magnetic field coils – in preparation for future experiments with RbYb ground-state molecules.

Bibliography

[1] Tobias Franzen. “A RbYb ultracold mixture machine - from room temperature fo 2-photon-photoassociation on the intercombination line”. PhD thesis. Heinrich-Heine-Universität Düsseldorf, 2023.

[2] Bastian Pollklesener. “Photoassociation of ultracold RbYb in an optical lattice - a quest towards absolute ground state molecules”. PhD thesis. Heinrich-Heine-Universität Düsseldorf, 2023.

[3] W.D. Phillips and H. Metcalf. Laser deceleration of an atomic beam. Phys. Rev. Lett. 48 (1982), p. 596.

[4] EL Raab, M Prentiss, Alex Cable, Steven Chu, and David E Pritchard. Trapping of neutral sodium atoms with radiation pressure. Physical review letters 59.23 (1987), p. 2631.

[5] J. Dalibard and C. Cohen-Tannoudji. Laser cooling below the Doppler limit by polarization gradients: simple theoretical models. Journal of the Optical Society of America B: Optical Physics 6.11 (Nov. 1989), pp. 2023–2045.

[6] M. Kasevich and S. Chu. Laser Cooling below a Photon Recoil with Three-Level Atoms. Phys. Rev. Lett. 69 (1992), p. 1741.

[7] K.B. Davis. “Evaporative cooling of sodium atoms”. PhD thesis. Massachusetts Institute of Technology, 1995.

[8] Kendall B Davis, M-O Mewes, Michael R Andrews, Nicolaas J van Druten, Dallin S Durfee, DM Kurn, and Wolfgang Ketterle. Bose-Einstein condensation in a gas of sodium atoms. Physical review letters 75.22 (1995), p. 3969.

[9] Mike H Anderson, Jason R Ensher, Michael R Matthews, Carl E Wieman, and Eric A Cornell. Observation of Bose-Einstein condensation in a dilute atomic vapor. Science 269.5221 (1995), pp. 198–201.

[10] Satyendra Nath Bose. Plancks Gesetz und Lichtquantenhypothese. Zeitschrift für Physik 26.1 (1924), pp. 178–181.

[11] Albert Einstein and Daniel Simon. *Akademie-Vorträge: Sitzungsberichte der Preussischen Akademie der Wissenschaften, 1914–1932*. Edited collection of Einstein’s original academic lectures and reports. Weinheim: Wiley-VCH, 2006.

[12] J. Bardeen, L. N. Cooper, and J. R. Schrieffer. Theory of Superconductivity. Phys. Rev. 108 (5 1957), pp. 1175–1204.

[13] M. Greiner, O. Mandel, T. Esslinger, T. W. Hänsch, and I. Bloch. Quantum phase transition from a superfluid to a Mott insulator in a gas of ultracold atoms. Nature 415 (2002), p. 44.

[14] S. Ospelkaus, K.-K. Ni, D. Wang, M. H. G. de Miranda, B. Neyenhuis, G. Quéméner, P. S. Julienne, J. L. Bohn, D. S. Jin, and J. Ye. Quantum-State Controlled Chemical Reactions of Ultracold Potassium-Rubidium Molecules. Science 327.5967 (2010), pp. 853–857.

[15] K.-K. Ni, S. Ospelkaus, D. Wang, G. Quéméner, B. Neyenhuis, M. H. G. de Miranda, J. L. Bohn, J. Ye, and D. S. Jin. Dipolar collisions of polar molecules in the quantum regime. Nature 464.7293 (2010), pp. 1324–1328.

[16] K. Góral, L. Santos, and M. Lewenstein. Quantum Phases of Dipolar Bosons in Optical Lattices. Phys. Rev. Lett. 88 (17 2002), p. 170406.

[17] L. Pollet, J. D. Picon, H. P. Büchler, and M. Troyer. Supersolid Phase with Cold Polar Molecules on a Triangular Lattice. Phys. Rev. Lett. 104 (12 2010), p. 125302.

[18] B. Capogrosso-Sansone, C. Trefzger, M. Lewenstein, P. Zoller, and G. Pupillo. Quantum Phases of Cold Polar Molecules in 2D Optical Lattices. Phys. Rev. Lett. 104 (12 2010), p. 125301.

[19] Andrea Micheli, GK Brennen, and Peter Zoller. A toolbox for lattice-spin models with polar molecules. Nature Physics 2.5 (2006), pp. 341–347.

[20] T Lahaye, C Menotti, L Santos, M Lewenstein, and T Pfau. The physics of dipolar bosonic quantum gases. Reports on Progress in Physics 72.12 (2009), p. 126401.

[21] Roman Krems, Bretislav Friedrich, and William C Stwalley. *Cold molecules: theory, experiment, applications.* CRC press, 2009.

[22] M.A. Baranov. Theoretical progress in many-body physics with ultracold dipolar gases. Physics Reports 464.3 (2008), pp. 71–111.

[23] Jun-Ru Li, William G. Tobias, Kyle Matsuda, Calder Miller, Giacomo Valtolina, Luigi De Marco, Reuben R. W. Wang, Lucas Lassablière, Goulven Quéméner, John L. Bohn, and Jun Ye. Tuning of dipolar interactions and evaporative cooling in a three-dimensional molecular quantum gas. Nature Physics 17.10 (2021), pp. 1144–1148.

[24] D. DeMille. Quantum Computation with Trapped Polar Molecules. Phys. Rev. Lett. 88 (6 2002), p. 067901.

[25] S. F. Yelin, K. Kirby, and Robin Côté. Schemes for robust quantum computation with polar molecules. Phys. Rev. A 74 (5 2006), p. 050301.

[26] Jing Zhu, Sabre Kais, Qi Wei, Dudley Herschbach, and Bretislav Friedrich. Implementation of quantum logic gates using polar molecules in pendular states. The Journal of Chemical Physics 138.2 (Jan. 2013), p. 024104.

[27] Kang-Kuen Ni, Till Rosenband, and David D. Grimes. Dipolar exchange quantum logic gate with polar molecules. Chem. Sci. 9 (33 2018), pp. 6830–6838.

[28] Qi Wei, Yudong Cao, Sabre Kais, Bretislav Friedrich, and Dudley Herschbach. Quantum Computation using Arrays of N Polar Molecules in Pendular States. ChemPhysChem 17.22 (2016), pp. 3714–3722.

[29] E. S. Shuman, J. F. Barry, and D. DeMille. Laser cooling of a diatomic molecule. Nature 467 (2010), 820–823.

[30] J. Lim, J. R. Almond, M. A. Trigatzis, J. A. Devlin, N. J. Fitch, B. E. Sauer, M. R. Tarbutt, and E. A. Hinds. Laser Cooled YbF Molecules for Measuring the Electron's Electric Dipole Moment. Phys. Rev. Lett. 120 (12 2018), p. 123201.

[31] Matthew T. Hummon, Mark Yeo, Benjamin K. Stuhl, Alejandra L. Collopy, Yong Xia, and Jun Ye. 2D Magneto-Optical Trapping of Diatomic Molecules. Phys. Rev. Lett. 110 (14 2013), p. 143001.

[32] S. Truppe, H. J. Williams, M. Hambach, L. Caldwell, N. J. Fitch, E. A. Hinds, B. E. Sauer, and M. R. Tarbutt. Laser cooling of a diatomic molecule. Nature Physics 13 (12 2017), 1173–1176.

[33] Ivan Kozyryev, Louis Baum, Kyle Matsuda, Benjamin L. Augenbraun, Loic Anderegg, Alexander P. Sedlack, and John M. Doyle. Sisyphus Laser Cooling of a Polyatomic Molecule. Phys. Rev. Lett. 118 (17 2017), p. 173201.

[34] Nathaniel B. Vilas, Christian Hallas, Loic Anderegg, Paige Robichaud, Andrew Winnicki, Debayan Mitra, and John M. Doyle. Magneto-optical trapping and sub-Doppler cooling of a polyatomic molecule. Nature 606.7912 (2022), pp. 70–74.

[35] Thorsten Köhler, Krzysztof Góral, and Paul S Julienne. Production of cold molecules via magnetically tunable Feshbach resonances. Reviews of modern physics 78.4 (2006), p. 1311.

[36] Kevin M. Jones, Eite Tiesinga, Paul D. Lett, and Paul S. Julienne. Ultracold photoassociation spectroscopy: Long-range molecules and atomic scattering. Rev. Mod. Phys. 78 (2 2006), pp. 483–535.

[37] Alessio Ciamei, Jacek Szczepkowski, Alex Bayerle, Vincent Barbé, Lukas Reichsöllner, Slava M Tzanova, Chun-Chia Chen, Benjamin Pasquiou, Anna Grochola, Pawel Kowalczyk, et al. The RbSr $^2\Sigma^+$ ground state investigated via spectroscopy of hot and ultracold molecules. Physical Chemistry Chemical Physics 20.41 (2018), pp. 26221–26240.

[38] William Dowd, Richard J Roy, Rajendra K Shrestha, Alexander Petrov, Constantinos Makrides, Svetlana Kotochigova, and Subhadeep Gupta. Magnetic field dependent interactions in an ultracold Li–Yb(3P2) mixture. New Journal of Physics 17.5 (2015), p. 055007.

[39] F. Schäfer, N. Mizukami, and Y. Takahashi. Feshbach resonances of large-mass-imbalance Er-Li mixtures. Phys. Rev. A 105 (1 2022), p. 012816.

[40] Tetsu Takekoshi, Lukas Reichsöllner, Andreas Schindewolf, Jeremy M Hutson, C Ruth Le Sueur, Olivier Dulieu, Francesca Ferlaino, Rudolf Grimm, and Hanns-Christoph Nägerl. Ultracold dense samples of dipolar RbCs molecules in the rovibrational and hyperfine ground state. Physical review letters 113.20 (2014), p. 205301.

[41] Peter K Molony, Philip D Gregory, Avinash Kumar, C Ruth Le Sueur, Jeremy M Hutson, and Simon L Cornish. Production of ultracold 87Rb133Cs in the absolute ground state: complete characterisation of the STIRAP transfer.. ChemPhysChem. 17.22 (2016), pp. 3811–3817.

[42] Jee Woo Park, Sebastian A Will, and Martin W Zwierlein. Ultracold dipolar gas of fermionic Na23 K40 molecules in their absolute ground state. Physical review letters 114.20 (2015), p. 205302.

[43] Mingyang Guo, Bing Zhu, Bo Lu, Xin Ye, Fudong Wang, Romain Vexiau, Nadia Bouloufa-Maafa, Goulven Quéméner, Olivier Dulieu, and Dajun Wang. Creation of an ultracold gas of ground-state dipolar Na 23 Rb 87 molecules. Physical review letters 116.20 (2016), p. 205303.

[44] S. Ospelkaus, Avi Pe'er, Kk Ni, Josh Zirbel, Brian Neyenhuis, Svetlana Kotochigova, Paul Julienne, Jun Ye, and D. Jin. Efficient state transfer in an ultracold dense gas of heteronuclear molecules. Nature Physics 4 (June 2008), pp. 622–626.

[45] MB Shundalau and AA Minko. Ab initio multi-reference perturbation theory calculations of the ground and some excited electronic states of the RbYb molecule. Computational and Theoretical Chemistry 1103 (2017), pp. 11–16.

[46] Y. Takasu, K. Maki, K. Komori, T. Takano, K. Honda, M. Kumakura, T. Yabuzaki, and Y. Takahashi. Bose-Einstein Condensation of Yb atoms. AIP Conference Proceedings 770.1 (May 2005), pp. 254–262.

[47] Tobias Franzen, Alexander Guttridge, Kali E. Wilson, Jack Segal, Matthew D. Frye, Jeremy M. Hutson, and Simon L. Cornish. Observation of magnetic Feshbach resonances between Cs and ^{173}Yb. Phys. Rev. Research 4 (4 2022), p. 043072.

[48] N Nemitz, F Baumer, F Münchow, S Tassy, and A Görlitz. Production of heteronuclear molecules in an electronically excited state by photoassociation in a mixture of ultracold Yb and Rb. Physical Review A 79.6 (2009), p. 061403.

[49] Frank Muenchow, Cristian Bruni, Maximilian Madalinski, and Axel Goerlitz. Two-photon photoassociation spectroscopy of heteronuclear YbRb. Physical Chemistry Chemical Physics 13.42 (2011), pp. 18734–18737.

[50] Cristian Bruni. “Exploring strategies for the production of ultracold RbYb molecules in conservative traps”. PhD thesis. Heinrich-Heine-Universität Düsseldorf, 2015.

[51] Tobias Franzen, Bastian Pollklesener, Christian Sillus, and Axel Görlitz. Intercombination-line photoassociation spectroscopy of ^{87}Rb^{170}Yb. Phys. Rev. A 107 (2 2023), p. 023114.

[52] J.M. Brown and A. Carrington. *Rotational Spectroscopy of Diatomic Molecules.* Cambridge Molecular Science. Cambridge University Press, 2003.

[53] G. Herzberg. *Molecular Spectra and Molecular Structure.* Vol. I. Spectra of Diatomic Molecules. Van Nostrand Reinhold, 1950.

[54] H. Lefebvre-Brion and R.W. Field. *The Spectra and Dynamics of Diatomic Molecules: Revised and Enlarged Edition.* Elsevier Science, 2004.

[55] Jonathan Tennyson, Lorenzo Lodi, Laura K McKemmish, and Sergei N Yurchenko. The ab initio calculation of spectra of open shell diatomic molecules. Journal of Physics B: Atomic, Molecular and Optical Physics 49.10 (2016), p. 102001.

[56] F. Hund. Concerning the importance of some appearances in the molecular spectra. Zeitschrift für Physik 36 (1926), p. 658.

[57] F. Münchow. “2-Photon-Photoassociation spectroscopy in a mixture of Ytterbium and Rubidium”. PhD thesis. Heinrich-Heine-Universität Düsseldorf, 2012.

[58] Lasse Kragh Sørensen, Stefan Knecht, Timo Fleig, and Christel M Marian. Four-component relativistic coupled cluster and configuration interaction calculations on the ground and excited states of the RbYb molecule. The Journal of Physical Chemistry A 113.45 (2009), pp. 12607–12614.

[59] Daniel Comparat. Improved LeRoy–Bernstein near-dissociation expansion formula, and prospect for photoassociation spectroscopy. Journal of Chemical Physics 120.3 (2004), pp. 1318–1329.

[60] Stephan Falke, Eberhard Tiemann, and Christian Lisdat. Born-Oppenheimer approximation for mass scaling of cold-collision properties. Phys. Rev. A 76 (1 2007), p. 012724.

[61] Jean Dalibard. “Collisional dynamics of ultra-cold atomic gases”. *Bose-Einstein Condensation in Atomic Gases.* IOS Press, 1999, pp. 321–349.

[62] P. F. Bedaque, Eric Braaten, and H.-W. Hammer. Three-body Recombination in Bose Gases with Large Scattering Length. Phys. Rev. Lett. 85 (5 2000), pp. 908–911.

[63] F. Baumer, F. Münchow, A. Görlitz, S. E. Maxwell, P. S. Julienne, and E. Tiesinga. Spatial separation in a thermal mixture of ultracold ^{174}Yb and ^{87}Rb atoms. Physical Review A 83 (4 2011), p. 040702.

[64] Mateusz Borkowski, Piotr S. Zuchowski, Roman Ciuryo, Paul S. Julienne, Dariusz Kedziera, Lukasz Mentel, Pawel Tecmer, Frank Muenchow, Cristian Bruni, and Axel Goerlitz. Scattering lengths in isotopologues of the RbYb system. Physical Review A 88 (5 2013), p. 052708.

[65] Masaaki Kitagawa, Katsunari Enomoto, Kentaro Kasa, Yoshiro Takahashi, Roman Ciuryło, Pascal Naidon, and Paul S. Julienne. Two-color photoassociation spectroscopy of ytterbium atoms and the precise determinations of s-wave scattering lengths. Physical Review A 77 (1 2008), p. 012719.

[66] S. L. Cornish, N. R. Claussen, J. L. Roberts, E. A. Cornell, and C. E. Wieman. Stable ^{85}Rb Bose-Einstein Condensates with Widely Tunable Interactions. Phys. Rev. Lett. 85 (9 2000), pp. 1795–1798.

[67] John R. de Laeter, John Karl Böhlke, P. De Bièvre, H. Hidaka, H. S. Peiser, K. J. R. Rosman, and P. D. P. Taylor. Atomic weights of the elements. Review 2000 (IUPAC Technical Report). Pure and Applied Chemistry 75.6 (2003), pp. 683–800.

[68] M. J. Holland, B. DeMarco, and D. S. Jin. Evaporative cooling of a two-component degenerate Fermi gas. Phys. Rev. A 61 (5 2000), p. 053610.

[69] Florian Baumer. “Isotope dependent interactions in a mixture of ultracold atoms”. PhD thesis. Ph. D. thesis, Heinrich-Heine-Universität, Düsseldorf, 2010.

[70] “The Dressed Atom Approach”. *Atom—Photon Interactions.* John Wiley & Sons, Ltd, 1998. Chap. 6, pp. 407–514.

[71] C. Cohen-Tannoudji, J. Dupont-Roc, and G. Grynberg. *Atom-Photon Interactions.* New York: Wiley, 1992.

[72] S. H. Autler and C. H. Townes. Stark Effect in Rapidly Varying Fields. Phys. Rev. 100 (2 1955), pp. 703–722.

[73] A. Ashkin and J. M. Dziedzic. Optical Trapping and Manipulation of Viruses and Bacteria. Science 235.4795 (1987), pp. 1517–1520.

[74] Peter J. Pauzauskie, Aleksandra Radenovic, Eliane Trepagnier, Hari Shroff, Peidong Yang, and Jan Liphardt. Optical trapping and integration of semiconductor nanowire assemblies in water. Nature Materials 5.2 (2006), pp. 97–101.

[75] Waseem S. Bakr, Jonathon I. Gillen, Amy Peng, Simon Fölling, and Markus Greiner. A quantum gas microscope for detecting single atoms in a Hubbard-regime optical lattice. Nature 462.7269 (2009), pp. 74–77.

[76] W. S. Bakr, A. Peng, M. E. Tai, R. Ma, J. Simon, J. I. Gillen, S. Fölling, L. Pollet, and M. Greiner. Probing the Superfluid to Mott Insulator Transition at the Single-Atom Level. Science 329.5991 (2010), pp. 547–550.

[77] D. Jaksch, C. Bruder, J. I. Cirac, C. W. Gardiner, and P. Zoller. Cold Bosonic Atoms in Optical Lattices. Phys. Rev. Lett. 81 (15 1998), pp. 3108–3111.

[78] R. Grimm, M. Weidemüller, and Y.B. Ovchinnikov. Optical dipole traps for neutral atoms. Adv. at. mol. opt. phys 42.95 (2000), p. 130.

[79] Jérôme Beugnon, Charles Tuchendler, Harold Marion, Alpha Gaëtan, Yevhen Miroshnychenko, Yvan R. P. Sortais, Andrew M. Lance, Matthew P. A. Jones, Gaétan Messin, Antoine Browaeys, and Philippe Grangier. Two-dimensional transport and transfer of a single atomic qubit in optical tweezers. Nature Physics 3.10 (2007), pp. 696–699.

[80] Florian Schäfer, Takeshi Fukuhara, Seiji Sugawa, Yosuke Takasu, and Yoshiro Takahashi. Tools for quantum simulation with ultracold atoms in optical lattices. Nature Reviews Physics 2.8 (2020), pp. 411–425.

[81] Immanuel Bloch, Jean Dalibard, and Sylvain Nascimbène. Quantum simulations with ultracold quantum gases. Nature Physics 8.4 (2012), pp. 267–276.

[82] T. D. Ladd, F. Jelezko, R. Laflamme, Y. Nakamura, C. Monroe, and J. L. O'Brien. Quantum computers. Nature 464.7285 (2010), pp. 45–53.

[83] Ivan H. Deutsch, Gavin K. Brennen, and Poul S. Jessen. Quantum Computing with Neutral Atoms in an Optical Lattice. Fortschritte der Physik 48.9-11 (2000), pp. 925–943.

[84] M. Greiner. "Ultracold quantum gases in three-dimensional optical lattice potentials". PhD thesis. Ludwig-Maximilians-Universität München, 2003.

[85] Patrick Windpassinger and Klaus Sengstock. Engineering novel optical lattices. Reports on Progress in Physics 76.8 (2013), p. 086401.

[86] Kevin M Jones, Eite Tiesinga, Paul D Lett, and Paul S Julienne. Ultracold photoassociation spectroscopy: Long-range molecules and atomic scattering. Reviews of Modern Physics 78.2 (2006), p. 483.

[87] M. Borkowski, R. Ciuryło, P. S. Julienne, S. Tojo, K. Enomoto, and Y. Takahashi. Line shapes of optical Feshbach resonances near the intercombination transition of bosonic ytterbium. Phys. Rev. A 80 (2009), p. 012715.

[88] Peter W Atkins and Ronald S Friedman. *Molecular quantum mechanics.* Oxford University Press, USA, 2011.

[89] Michael Fleischhauer, Atac Imamoglu, and Jonathan P Marangos. Electromagnetically induced transparency: Optics in coherent media. Reviews of modern physics 77.2 (2005), p. 633.

[90] Stephen E Harris, JE Field, and A Imamoğlu. Nonlinear optical processes using electromagnetically induced transparency. Physical Review Letters 64.10 (1990), p. 1107.

[91] Christiane P. Koch and Moshe Shapiro. Coherent Control of Ultracold Photoassociation. Chemical Reviews 112.9 (2012). PMID: 22489790, pp. 4928–4948.

[92] JR Kuklinski, U Gaubatz, Foek T Hioe, and K Bergmann. Adiabatic population transfer in a three-level system driven by delayed laser pulses. Physical Review A 40.11 (1989), p. 6741.

[93] Nikolay V Vitanov, Andon A Rangelov, Bruce W Shore, and Klaas Bergmann. Stimulated Raman adiabatic passage in physics, chemistry, and beyond. Reviews of Modern Physics 89.1 (2017), p. 015006.

[94] Frank Münchow, Cristian Bruni, Maximilian Madalinski, and Axel Görlitz. Two-photon photoassociation spectroscopy of heteronuclear YbRb. Physical Chemistry Chemical Physics 13.42 (2011), pp. 18734–18737.

[95] C. Bruni, F. Münchow, and A. Görlitz. Optical Autler–Townes spectroscopy in a heteronuclear mixture of laser-cooled atoms. Applied Physics B: Photophysics and Laser Chemistry 123.1 (2017), p. 6.

[96] Markus Debatin, Tetsu Takekoshi, Raffael Rameshan, Lukas Reichsöllner, Francesca Ferlaino, Rudolf Grimm, Romain Vexiau, Nadia Bouloufa, Olivier Dulieu, and Hanns-Christoph Nägerl. Molecular spectroscopy for ground-state transfer of ultracold RbCs molecules. Phys. Chem. Chem. Phys. 13 (42 2011), pp. 18926–18935.

[97] Nils Nemitz. "Production and spectroscopy of ultracold YbRb* molecules". PhD thesis. Ph. D. thesis, Heinrich-Heine-Universität, Düsseldorf, 2008.

[98] Céline Castor. *Charakterisierung eines Yb-Kapillarofens.* Directed Study, Universität Düsseldorf. 2021.

[99] Etienne Staub. "Developing a High-Flux atomic beam source for Experiments with ultracold Strontium quantum gases". PhD thesis. University München, 2019.

[100] Ruwan Senaratne, Shankari V. Rajagopal, Zachary A. Geiger, Kurt M. Fujiwara, Vyacheslav Lebedev, and David M. Weld. Effusive atomic oven nozzle design using an aligned microcapillary array. Review of Scientific Instruments 86.2 (2015), p. 023105.

[101] Alexander Batär. “Erzeugung und Charakterisierung ultrakalter Rubidium-und Ytterbiumatome-Auf dem Weg zu einem gemischten Quantengas”. PhD thesis. Ph. D. thesis, Heinrich-Heine-Universität, Düsseldorf, 2005.

[102] Sven Kroboth. *Laserkühlung von Ytterbiumatomen.* Diplomarbeit, AG Görlitz, Universität Stuttgart. 2002.

[103] J. Huckans, W. Dubosclard, E. Maréchal, O. Gorceix, B. Laburthe-Tolra, and M. Robert de Saint-Vincent. *Note on the reflectance of mirrors exposed to a strontium beam.* 2018.

[104] D. A. Steck. *Rubidium 87 D Line Data.* accessed 23.01.2025. last revised 28 May 2024.

[105] X. Baillard, A. Gauguet, S. Bize, P. Lemonde, Ph. Laurent, A. Clairon, and P. Rosenbusch. Interference-filter-stabilized external-cavity diode lasers. Optics Communications 266.2 (2006), pp. 609–613.

[106] M. Gilowski, Ch. Schubert, M. Zaiser, W. Herr, T. Wübbena, T. Wendrich, T. Müller, E.M. Rasel, and W. Ertmer. Narrow bandwidth interference filter-stabilized diode laser systems for the manipulation of neutral atoms. Optics Communications 280.2 (2007), pp. 443–447.

[107] Fabian Türck. *Microwave spectroscopy in an ultracold mixture of Yb and Rb atoms.* Master Thesis, Universität Düsseldorf. 2018.

[108] John Daniel Kraus. *Antennas.* 2 Sub. McGraw-Hill Companies, 1988.

[109] Bastian Pollklesener. *Aufbau eines Lasersystems zur Laserkühlung von Ytterbium.* Bachelor Thesis, Universität Düsseldorf. 2014.

[110] Tobias Franzen, Bastian Pollklesener, and Axel Görlitz. A single-stage 1112 nm fiber amplifier with large gain for laser cooling of ytterbium. Applied Physics B: Photophysics and Laser Chemistry 124.12 (2018), pp. 1–7.

[111] C. Sillus, T. Franzen, B. Pollklesener, and A. Görlitz. Active position stabilization of an atomic cloud in a narrow-line magneto-optical trap using a Raspberry Pi. Review of Scientific Instruments 92.3 (2021), p. 033204.

[112] R. W. P. Drever, J. L. Hall, F. V. Kowalski, J. Hough, G. M. Ford, A. J. Munley, and H. Ward. Laser phase and frequency stabilization using an optical resonator. Applied Physics B: Lasers and Optics 31.2 (1983), pp. 97–105.

[113] F Riehle. Use of optical frequency standards for measurements of dimensional stability. Measurement Science & Technology 9.7 (1998), p. 1042.

[114] C. Bruni and A. Görlitz. Observation of hyperfine interaction in photoassociation spectra of ultracold RbYb. Physical Review A 94 (2 2016), p. 022503.

[115] Thomas H. Loftus, Tetsuya Ido, Martin M. Boyd, Andrew D. Ludlow, and Jun Ye. Narrow line cooling and momentum-space crystals. Physical Review A 70 (6 2004), p. 063413.

[116] A Guttridge, SA Hopkins, SL Kemp, D Boddy, R Freytag, MPA Jones, MR Tarbutt, EA Hinds, and SL Cornish. Direct loading of a large Yb MOT on the ${}^1S_0 \rightarrow {}^3P_1$ transition. Journal of Physics B: Atomic, Molecular and Optical Physics 49.14 (2016), p. 145006.

[117] R. V. Pound. Electronic Frequency Stabilization of Microwave Oscillators. Review of Scientific Instruments 17.11 (Nov. 1946), pp. 490–505.

[118] J. Alnis, A. Matveev, N. Kolachevsky, Th. Udem, and T. W. Hänsch. Subhertz linewidth diode lasers by stabilization to vibrationally and thermally compensated ultralow-expansion glass Fabry-Pérot cavities. Phys. Rev. A 77 (5 2008), p. 053809.

[119] Richard Roy, Alaina Green, Ryan Bowler, and Subhadeep Gupta. Rapid cooling to quantum degeneracy in dynamically shaped atom traps. Physical Review A 93 (4 2016), p. 043403.

[120] Torsten Kemmerling. *Setup of an Optical Lattice at 1064nm for Ultracold Rubidium Atoms.* Master Thesis, Universität Düsseldorf. 2019.

[121] E.P. Ippen and R.H. Stolen. Stimulated Brillouin scattering in optical fibers. Applied Physics Letters 21.11 (1972), pp. 539–541.

[122] S. Schiller, A. Görlitz, A. Nevsky, S. Alighanbari, S. Vasilyev, C. Abou-Jaoudeh, G. Mura, Tobias Franzen, U. Sterr, S. Falke, C. Lisdat, Ernst-Maria Rasel, A. Kulosa, S. Bize, J. Lodewyck, G. Tino, N. Poli, M. Schioppo, K. Bongs, Y. Singh, P. Gill, G. Barwood, Y. Ovchinnikov, J. Stuhler, W. Kaenders, C. Braxmaier, R. Holzwarth, A. Donati, S. Lecomte, D. Calonico, and F. Levi. "Towards Neutral-atom Space Optical Clocks (SOC2): Development of high-performance transportable and breadboard optical clocks and advanced subsystems". *2012 European Frequency and Time Forum.* 2012.

[123] Richarda Niemann. *Photoassociation Spectroscopy at the Intercombination Line of Ytterbium.* Master Thesis, Universität Düsseldorf. 2019.

[124] Frank Münchow. "2-Photon-Photoassociation spectroscopy in a mixture of Ytterbium and Rubidium". PhD thesis. HHU Düsseldorf, 2012.

[125] J. F. Kelly and A. Gallagher. Efficient electro-optic modulator for optical pumping of Na beams. Review of Scientific Instruments 58.4 (1987), pp. 563–566.

[126] A. Kallweit. *Aufbau eines Lasersystems bei 1112nm.* Bachelorarbeit, AG Görlitz, Universität Düsseldorf. 2010.

[127] Bastian Pollklesener. *Setup of an optical lattice for rubidium and ytterbium.* Master Thesis, Universität Düsseldorf. 2014.

[128] J. Szczepkowski, R. Gartman, M. Witkowski, L. Tracewski, M. Zawada, and W. Gawlik. Analysis and calibration of absorptive images of Bose–Einstein condensate at nonzero temperatures. Review of Scientific Instruments 80.5 (May 2009).

[129] Aviv Keshet and Wolfgang Ketterle. A distributed, graphical user interface based, computer control system for atomic physics experiments. Review of Scientific Instruments 84.1 (2013), p. 015105.

[130] Wolfgang Ketterle and N.J. Van Druten. "Evaporative Cooling of Trapped Atoms". Ed. by Benjamin Bederson and Herbert Walther. Vol. 37. Advances In Atomic, Molecular, and Optical Physics. Academic Press, 1996, pp. 181–236.

[131] G. Modugno, G. Ferrari, G. Roati, R. J. Brecha, A. Simoni, and M. Inguscio. Bose-Einstein Condensation of Potassium Atoms by Sympathetic Cooling. Science 294.5545 (2001), pp. 1320–1322.

[132] Wolfgang Petrich, Michael H. Anderson, Jason R. Ensher, and Eric A. Cornell. Behavior of atoms in a compressed magneto-optical trap. Journal of the Optical Society of America B: Optical Physics 11.8 (1994), pp. 1332–1335.

[133] David E. Pritchard. Cooling Neutral Atoms in a Magnetic Trap for Precision Spectroscopy. Physical Review Letters 51 (15 1983), pp. 1336–1339.

[134] Y-J Lin, Abigail R Perry, Robert L Compton, Ian B Spielman, and James V Porto. Rapid production of Rb87 Bose-Einstein condensates in a combined magnetic and optical potential. Physical Review A 79.6 (2009), p. 063631.

[135] K. M. O'Hara, M. E. Gehm, S. R. Granade, and J. E. Thomas. Scaling laws for evaporative cooling in time-dependent optical traps. Physical Review A 64 (5 2001), p. 051403.

[136] P Hommelhoff, W Hänsel, T Steinmetz, T W Hänsch, and J Reichel. Transporting, splitting and merging of atomic ensembles in a chip trap. New Journal of Physics 7 (2005), pp. 3–3.

[137] Ralph Vincent Brooks, Stefan Spence, Alexander Guttridge, Alexandros Chantif Alampounti, Ana Rakonjac, Lewis McArd, Jeremy M Hutson, and S L Cornish. Preparation of one 87Rb and one 133Cs atom in a single optical tweezer. New Journal of Physics (2021).

[138] SN Tohme and M Korek. Electronic structure and rovibrational calculation of the low-lying states of the RbYb molecule. Chemical Physics 410 (2013), pp. 37–44.

[139] SG Porsev, MS Safronova, A Derevianko, and Charles W Clark. Relativistic many-body calculations of van der Waals coefficients for Yb-Li and Yb-Rb dimers. Physical Review A 89.2 (2014), p. 022703.

[140] Adrien Devolder, Eliane Luc-Koenig, Osman Atabek, Michèle Desouter-Lecomte, and Olivier Dulieu. Proposal for the formation of ultracold deeply bound RbSr dipolar molecules by all-optical methods. Physical Review A 98.5 (2018), p. 053411.

[141] Piotr S. Żuchowski, R. Guérout, and O. Dulieu. Ground- and excited-state properties of the polar and paramagnetic RbSr molecule: A comparative study. Physical Review A 90 (1 2014), p. 012507.

[142] Alessio Ciamei. "Taming ultracold RbSr and Sr_2". PhD thesis. Universiteit van Amsterdam, 2018.

[143] Alex Bayerle. "Ultracold strontium and rubidium: mixtures, quantum gases and molecules". PhD thesis. Universiteit van Amsterdam, 2017.

[144] Vincent Barbé. "Ultracold RbSr: Optical and magnetic spectroscopy, Feshbach resonances and molecular structure". PhD thesis. Universiteit van Amsterdam, 2018.

[145] Satoshi Tojo, Masaaki Kitagawa, Katsunari Enomoto, Yutaka Kato, Yosuke Takasu, Mitsutaka Kumakura, and Yoshiro Takahashi. High-resolution photoassociation spectroscopy of ultracold ytterbium atoms by using the intercombination transition. Physical review letters 96.15 (2006), p. 153201.

[146] Bijit Mukherjee, Matthew D. Frye, and Jeremy M. Hutson. Feshbach resonances and molecule formation in ultracold mixtures of Rb and $\mathrm{Yb}(^3P)$ atoms. Phys. Rev. A 105 (2 2022), p. 023306.

[147] Maykel L González-Martínez and Jeremy M Hutson. Sympathetic cooling of fluorine atoms with ultracold atomic hydrogen. Physical review A 88.5 (2013), p. 053420.

[148] Pascal Naidon and Paul S. Julienne. Optical Feshbach resonances of alkaline-earth-metal atoms in a one- or two-dimensional optical lattice. Phys. Rev. A 74 (6 2006), p. 062713.

[149] Céline Castor. *A laser system for Molecular Spectroscopy of RbYb at 1500nm.* Master Thesis, Universität Düsseldorf. 2022.

[150] Edmund R. Meyer and John L. Bohn. Electron electric-dipole-moment searches based on alkali-metal- or alkaline-earth-metal-bearing molecules. Phys. Rev. A 80 (4 2009), p. 042508.

[151] Antonio Buzza. *Aufbau und Charakterisierung einer kompakten Dopplerfreien Spektroskopie für Rubidium.* Bachelor Thesis, Universität Düsseldorf. 2024.

[152] A. Sopp. *Charakterisierung und Stabilisierung einer DBR-Laserdiode bei 780 nm.* Bachelor Thesis, Universität Düsseldorf. 2025.

[153] Lea Andretzky. *Aufbau eines Resonator-Transferlocks zur Stabilisierung von Diodenlasern.* Bachelor Thesis, Universität Düsseldorf. 2025.

[154] C. Castor, A. Miethke, B. Pollklesener, C. Sillus, V. Vogt, and A. Görlitz. Tunable External Cavity Gain Chip Laser at 1.5µm Frequency-stabilized using Sideband Locking for Molecular Spectroscopy Applications. Manuscript in preparation (2025).

[155] Dong K. Shin, Bryce M. Henson, Roman I. Khakimov, Jacob A. Ross, Colin J. Dedman, Sean S. Hodgman, Kenneth G. H. Baldwin, and Andrew G. Truscott. Widely tunable, narrow linewidth external-cavity gain chip laser for spectroscopy between 1.0 - 1.1 µm. Opt. Express 24.24 (2016), pp. 27403–27414.

[156] Soeren Doerscher. “Creation of Ytterbium quantum gases with a compact 2D/3D MOT setup”. PhD thesis. Universität Hamburg, 2013.

[157] Benjamin Scheidler. *Aufbau eines Diodenlasersystems bei 790nm zur Manipulation von Atomen in einer optischen Dipolfalle.* Bachelor Thesis, Universität Düsseldorf. 2021.

[158] Laurenz Hübbers. *Realisierung und Evaluierung eines Aufbaus für eine optische Dipolfalle basierend auf einer Multimode-Laserdioe.* Bachelor Thesis, Universität Düsseldorf. 2024.

[159] T. Zelevinsky, M. M. Boyd, A. D. Ludlow, T. Ido, J. Ye, R. Ciuryło, P. Naidon, and P. S. Julienne. Narrow Line Photoassociation in an Optical Lattice. Physical Review Letters 96 (20 2006), p. 203201.

[160] Markus Greiner, Olaf Mandel, Tilman Esslinger, Theodor W Hänsch, and Immanuel Bloch. Quantum phase transition from a superfluid to a Mott insulator in a gas of ultracold atoms. Nature 415.6867 (2002), pp. 39–44.

[161] Immanuel Bloch, Jean Dalibard, and Wilhelm Zwerger. Many-body physics with ultracold gases. Reviews of modern physics 80.3 (2008), p. 885.

[162] Martin Miranda, Ryotaro Inoue, Naoki Tambo, and Mikio Kozuma. Site-resolved imaging of a bosonic Mott insulator using ytterbium atoms. Physical Review A 96.4 (2017), p. 043626.

[163] Takeshi Fukuhara, Seiji Sugawa, Masahito Sugimoto, Shintaro Taie, and Yoshiro Takahashi. Mott insulator of ultracold alkaline-earth-metal-like atoms. Phys. Rev. A 79 (4 2009), p. 041604.

[164] Seiji Sugawa, Kensuke Inaba, Shintaro Taie, Rekishu Yamazaki, Makoto Yamashita, and Yoshiro Takahashi. Interaction and filling-induced quantum phases of dual Mott insulators of bosons and fermions. Nature Physics 7.8 (2011), pp. 642–648.

[165] Johann G. Danzl, Manfred J. Mark, Elmar Haller, Mattias Gustavsson, Russell Hart, Jesus Aldegunde, Jeremy M. Hutson, and Hanns-Christoph Naegerl. An ultracold high-density sample of rovibronic ground-state molecules in an optical lattice. Nature Physics 6.4 (2010), 265.

[166] Klaas Bergmann, Hanns-Christoph Nägerl, Cristian Panda, Gerald Gabrielse, Eduard Miloglyadov, Martin Quack, Georg Seyfang, Gunther Wichmann, Silke Ospelkaus, Axel Kuhn, Stefano Longhi, Alexander Szameit, Philipp Pirro, Burkard Hillebrands, Xue-Feng Zhu, Jie Zhu, Michael Drewsen, Winfried K Hensinger, Sebastian Weidt, Thomas Halfmann, Hai-Lin Wang, Gheorghe Sorin Paraoanu, Nikolay V Vitanov, Jordi Mompart, Thomas Busch, Timothy J Barnum, David D Grimes, Robert W Field, Mark G Raizen, Edvardas Narevicius, Marcis Auzinsh, Dmitry Budker, Adriana Pálffy, and Christoph H Keitel. Roadmap on STIRAP applications. Journal of Physics B: Atomic, Molecular and Optical Physics 52.20 (2019), p. 202001.

[167] Nikolay V. Vitanov, Andon A. Rangelov, Bruce W. Shore, and Klaas Bergmann. Stimulated Raman adiabatic passage in physics, chemistry, and beyond. Rev. Mod. Phys. 89 (1 2017), p. 015006.

[168] U. Gaubatz, P. Rudecki, S. Schiemann, and K. Bergmann. Population transfer between molecular vibrational levels by stimulated Raman scattering with partially overlapping laser fields. A new concept and experimental results. The Journal of Chemical Physics 92.9 (May 1990), pp. 5363–5376.

[169] L. P. Yatsenko, V. I. Romanenko, B. W. Shore, and K. Bergmann. Stimulated Raman adiabatic passage with partially coherent laser fields. Physical Review A 65 (4 2002), p. 043409.

[170] Simon Stellmer, Benjamin Pasquiou, Rudolf Grimm, and Florian Schreck. Creation of Ultracold Sr_2 Molecules in the Electronic Ground State. Phys. Rev. Lett. 109 (11 2012), p. 115302.

[171] Adrien Devolder, Eliane Luc-Koenig, Osman Atabek, Michèle Desouter-Lecomte, and Olivier Dulieu. Laser-assisted self-induced Feshbach resonance for controlling heteronuclear quantum gas mixtures. Phys. Rev. A 100 (5 2019), p. 052703.

[172] G. Scalari, C. Walther, M. Fischer, R. Terazzi, H. Beere, D. Ritchie, and J. Faist. THz and sub-THz quantum cascade lasers. Laser & Photonics Reviews 3.1-2 (2009), pp. 45–66.

[173] Kazuue Fujita, Shohei Hayashi, Akio Ito, Masahiro Hitaka, and Tatsuo Dougakiuchi. Sub-terahertz and terahertz generation in long-wavelength quantum cascade lasers. Nanophotonics 8.12 (2019), pp. 2235–2241.

[174] Cheng Chin, Rudolf Grimm, Paul Julienne, and Eite Tiesinga. Feshbach resonances in ultracold gases. Reviews of Modern Physics 82.2 (2010), p. 1225.

[175] Torsten Hartmann, Torben A. Schulze, Kai K. Voges, Philipp Gersema, Matthias W. Gempel, Eberhard Tiemann, Alessandro Zenesini, and Silke Ospelkaus. Feshbach resonances in $^{23}\mathrm{Na} +^{39}\mathrm{K}$ mixtures and refined molecular potentials for the NaK molecule. Phys. Rev. A 99 (3 2019), p. 032711.

[176] Michael Gröbner, Philipp Weinmann, Emil Kirilov, Hanns-Christoph Nägerl, Paul S. Julienne, C. Ruth Le Sueur, and Jeremy M. Hutson. Observation of interspecies Feshbach resonances in an ultracold $^{39}\mathrm{K} -^{133}\mathrm{Cs}$ mixture and refinement of interaction potentials. Phys. Rev. A 95 (2 2017), p. 022715.

[177] Fudong Wang, Xiaodong He, Xiaoke Li, Bing Zhu, Jun Chen, and Dajun Wang. Formation of ultracold NaRb Feshbach molecules. New Journal of Physics 17.3 (2015), p. 035003.

[178] Michael P. Köppinger, Daniel J. McCarron, Daniel L. Jenkin, Peter K. Molony, Hung-Wen Cho, Simon L. Cornish, C. Ruth Le Sueur, Caroline L. Blackley, and Jeremy M. Hutson. Production of optically trapped ^{87}RbCs Feshbach molecules. Phys. Rev. A 89 (3 2014), p. 033604.

[179] BC Yang, Matthew D Frye, A Guttridge, Jesus Aldegunde, Piotr S Żuchowski, Simon L Cornish, and Jeremy M Hutson. Magnetic Feshbach resonances in ultracold collisions between Cs and Yb atoms. Physical Review A 100.2 (2019), p. 022704.

[180] Daniel A Brue and Jeremy M Hutson. Prospects of forming ultracold molecules in 2 Σ states by magnetoassociation of alkali-metal atoms with Yb. Physical Review A 87.5 (2013), p. 052709.

[181] Piotr S. Żuchowski, J. Aldegunde, and Jeremy M. Hutson. Ultracold RbSr Molecules Can Be Formed by Magnetoassociation. Physical Review Letters 105 (15 2010), p. 153201.

[182] Vincent Barbé, Alessio Ciamei, Benjamin Pasquiou, Lukas Reichsöllner, Florian Schreck, Piotr S Żuchowski, and Jeremy M Hutson. Observation of Feshbach resonances between alkali and closed-shell atoms. Nature Physics 14.9 (2018), pp. 881–884.

[183] Peter K Molony, Philip D Gregory, Zhonghua Ji, Bo Lu, Michael P Köppinger, C Ruth Le Sueur, Caroline L Blackley, Jeremy M Hutson, and Simon L Cornish. Creation of ultracold Rb 87 Cs 133 molecules in the rovibrational ground state. Physical review letters 113.25 (2014), p. 255301.

[184] K. K. Ni, S. Ospelkaus, M. H. G. de Miranda, A. Pe'er, B. Neyenhuis, J. J. Zirbel, S. Kotochigova, P. S. Julienne, D. S. Jin, and J. Ye. A High Phase-Space-Density Gas of Polar Molecules. Science 322.5899 (2008), 231.

[185] KH Leung, E Tiberi, B Iritani, I Majewska, R Moszynski, and T Zelevinsky. Ultracold $^{88}Sr_2$ molecules in the absolute ground state. New Journal of Physics 23.11 (2021), p. 115002.

[186] B. Pollklesener, T. Franzen, C. Sillus, and A. Görlitz. A new apparatus for the production of ultracold mixtures of Rb and Yb. Manuscript in preparation (2023).

[187] Many of the figures in this thesis make use of the symbols from the ComponentLibraray by Alexander Franzen. (`https://www.gwoptics.org/ComponentLibrary/`). 2023.

Danksagung

Zum Schluss noch ein paar Worte des Dankes an die ganzen lieben Menschen, die mich durch die Zeit meiner Promotion begleitet haben.

- Mein größter Dank geht an Axel Görlitz. Seit nunmehr zehn Jahren durfte ich Teil Deiner Arbeitsgruppe sein und habe in dieser Zeit eine Menge von Dir lernen können – sei es physikalisches Bauchgefühl, wo es die besten Brezn gibt oder wie man als Betreuer sein kann. Du hast ein unglaubliches physikalisches Verständnis und hast immer neue Ideen, wenn man selbst nicht mehr weiterweiß. Viel wichtiger jedoch ist, dass Du eine Arbeitsatmosphäre geschaffen hast, in der man Freund:innen finden kann und jeden Tag gerne zur Arbeit kommt. Ich hatte eine tolle Zeit in Deiner Arbeitsgruppe und würde mich jederzeit wieder dafür entscheiden, bei Dir zu promovieren. Ich danke Dir außerdem für das sorgfältige Korrekturlesen dieser Arbeit.

- Ich danke Prof. Heinzel für die freundliche Übernahme des Koreferats und besonders für die zügige Fertigstellung des Gutachtens.

- Die zweite Konstante in der AGG ist natürlich Ralf. Ohne Dich würde hier gar nichts laufen. Man kann Dir abends einen kryptischen Zettel schreiben, auf den Tisch legen und am nächsten Morgen liegt es schon fertig auf meinem Schreibtisch. Auch wenn elektronische Geräte grundsätzlich nur ohne Deckel funktionieren, können wir uns nur glücklich schätzen, dass Du immer alles für uns machst. Den einen oder anderen Wasserunfall haben wir auch schon gemeinsam mitmachen dürfen. Danke, dass Du mir so viel technische und handwerkliche Dinge beigebracht hast und immer einen Scherz auf Lager hast.

- Ein großes Dankeschön geht auf die Insel zu Tobi. Du hast das ganze Experiment aufgebaut, warst der Betreuer meiner Bachelorarbeit und hast mir alles beigebracht, was man so im Labor wissen muss. Ich hatte unglaublich viel Spaß mit Dir, Laserdinos kennengelernt und tolle Mittagspausen im Botanischen Garten gehabt. Auch nach dem zehnten Nachfragen warst Du noch geduldig und hast mir Dinge erklärt. Ich wünsche Dir alles Gute auf deinem Weg zum verrückten Professor.

- Basti, von Dir habe ich unermüdliches Justieren und vor allem den Satz: "Wir brauchen mehr Atome." gelernt. Es hat immer Spaß gemacht, mit Dir zu arbeiten, zu bouldern und Deine ruhige Art hat einen auch in Zeiten, in denen es nicht so gut lief, immer hoffnungsvoll gestimmt. Ich hoffe, dass Du weiterhin eine gute Zeit beim Laserbauen hast.

- Damit der Katastrophentourismus möglich ist, braucht es natürlich auch das Rydbergexperiment, das vom langsamsten Menschen der Welt betrieben wird. Alex, ich bin froh, dass wir so lange Zeit zusammenarbeiten konnten und uns über unsere Probleme auslassen konnten – sei es von der Arbeit oder privat. Wir haben so viel gemeinsam gelacht und auch wenn ich Dir nicht immer zuhöre, bist Du ein guter Freund geworden. Viel Erfolg bei deiner Diss. Send It!

- Meinem ersten Bachelorstudenten, dem besten Arne der Uni, möchte ich auch in vielerlei Hinsicht danken. Du warst mutig genug Teil dieses Projetks zu werden. Du hast ein unglaubliches physikalisches Verständnis, kriegst wirklich jedes Problem – meist mit unkonventionellen Mitteln – gelöst, warst schon in jedem Ort mit Deinem Fahrrad und hast es tatsächlich geschafft, mich zum Joggen zu bringen. Du strahlst immer über beide Ohren und bist motiviert. Wenn es einer schafft Moleküle im Grundzustand zu erzeugen, dann Du. Lass dich nicht ärgern.

- Ein großer Dank geht auch an die Chefin, Céline. Auch, wenn Du am Anfang Angst vor mir hattest, sind wir doch Freunde geworden. Du initiierst gemeinsame Aktivitäten in der Arbeitsgruppe und hast dafür gesorgt, dass niemand mehr Fleisch in der Mensa isst. Du gehst deinen Weg und kriegst alles hin, was du dir vornimmst.

- Nele, unser neuestes Mitglied, gebührt der Dank dafür, dass zum ersten Mal mehr Frauen als Männer in der Arbeitsgruppe sein werden und Deine ruhige und gelassene Art wird Dir dabei helfen, das Rydbergexperiment zu bändigen. Du musst mit uns einiges mitmachen, was man zum Teil an deinem Blick sehr gut ablesen kann. Du bist eine perfekte Nachfolgerin für Deinen Meister.

- Ich danke allen Bachelor- und Masterstudierenden, die ich im Laufe meiner Zeit betreuen durfte. Ihr habt mir viel beigebracht und einen nicht unerheblichen Anteil zu dieser Arbeit beigetragen.

- Besonders muss ich mich bei Dir bedanken, Fab. Wir haben seit der Erstiwoche das gesamte Studium zusammen verbracht – seien es Übungszettel, Praktika, Bachelor- und Masterarbeit oder Abende in der Altstadt. Ohne Dich hätte ich mich zu keiner Prüfung rechtzeitig angemeldet und hätte nicht gewusst, welche Module ich belegen muss. Über die Zeit bist Du einer meiner besten Freunde geworden, der mich sowohl während des Studiums als auch heute noch, immer unterstützt und mit Rat und Tat zur Seite steht.

- Als Letztes möchte ich meiner Familie und meinen Freund:innen danken. Ihr unterstützt mich immer und macht meine Zeit außerhalb der Uni so schön, dass ich glücklich bin. Ohne euch wäre ich nicht so, wie ich bin.

Publications

The following scientific papers involving work within this thesis have been published:

Reference [111]:
C. Sillus, T. Franzen, B. Pollklesener, and A. Görlitz
Active position stabilization of an atomic cloud in a narrow-line magnetooptical trap using a Raspberry Pi. in Review of Scientific Instruments, 92(3):033204, 2021.
The author led the development and optimization of the presented stabilization system and prepared the manuscript. Section 4.3.3 in this work is a reproduction of the manuscript.

Reference [51]:
T. Franzen, B. Pollklesener, C. Sillus, and A. Görlitz
Intercombination line photoassociation spectroscopy of 87Rb170Yb. in Phys. Rev. A 107, 023114 (2023)
The author participated in the development and maintenance of the laser systems, recorded data, joined in the analysis appearing in this publication and helped editing the manuscript.
Contents of this publication appear in chapters Section 5.1 and Section 5.2 of this thesis.

Reference [186]:
B. Pollklesener, T. Franzen, C. Sillus, and A. Görlitz
A new apparatus for the production of ultracold mixtures of Rb and Yb [manuscript to be submitted]
The author participated in the development and maintenance of the experimental apparatus, recorded data, joined in the analysis appearing in this publication and helped editing the manuscript.

Reference [154]:
C. Castor, A. Miethke, B. Pollklesener, C. Sillus, V. Voigt, and A. Görlitz
Tunable External Cavity Gain Chip Laser at $1.5\,\mu\mathrm{m}$ **Frequency-stabilized using Sideband Locking for Molecular Spectroscopy** [manuscript to be submitted]
The author participated and supervised the development of the laser system, joined in the

analysis appearing in this publication and helped editing the manuscript.
Contents of this publication appear in chapter Section 6.2.5.2 of this thesis.

Eidesstattliche Erklärung

Hiermit versichere ich an Eides Statt, dass die vorliegende Dissertation eigenständig und ohne unzulässige Hilfe unter Beachtung der "Grundsätze zur Sicherung guter wissenschaftlicher Praxis an der Heinrich-Heine-Universität Düsseldorf" erstellt worden ist. Zur Überprüfung von Rechtschreibung, Zeichensetzung und sprachlicher Formulierung wurden KI-basierte large-language models wie ChatGPT und DeepL verwendet. Alle Abbildungen ohne explizite Quellenangabe wurden eigenständig erstellt.

Düsseldorf, 03.07.2025
Ort, Datum

Christian David Sillus